Complex Dynamics of Ultracold Atoms

Inaugural–Dissertation

zur Erlangung der Doktorwürde
der Naturwissenschaftlich–Mathematischen Gesamtfakultät
der Ruprecht–Karls–Universität Heidelberg

vorgelegt von

Dipl.-Phys. Patrick Plötz
aus Greifswald

Tag der mündlichen Prüfung: 13. Oktober 2010

Gutachter: Dr. Sandro Wimberger

Prof. Dr. Manfred Salmhofer

Zusammenfassung

Aktuelle Experimente mit ultrakalten Atomen bilden die Motivation für das Studium komplexer Quantendynamik von Bose–Einstein-Kondensaten in optischen Gittern, das den Gegenstand dieser Arbeit bildet. Ausgehend von diesen Experimenten wird ein Gittermodell wechselwirkender Bosonen unter dem Einfluss einer externen Kraft abgeleitet und im Weiteren der Arbeit in verschiedenen dynamischen Regimen untersucht. Im ersten Teil entwickeln wir dabei ein neues Mass zur Detektion vermiedener Kreuzungen in komplexen Energiespektren und wenden es auf das quantenchaotische Regime des Ein-Band Systems an. Im zweiten und längeren Teil der Arbeit wird die Kopplung zweier Energiebänder anhand eines Zwei-Band-Modells untersucht. Die komplexe Zeitentwicklung zeigt sich hierbei schon im wechselwirkungsfreien Problem in der horizontalen und vertikalen Populationsdynamik, unter anderem in der Existenz von Resonanzen im Interband-Transport. Des Weiteren können wir zeigen, dass die interatomare Wechselwirkung zu Kollaps und Wiederkehr dieser resonanten Interband-Oszillationen führt und sind in der Lage alle Zeitskalen dieser komplexen Interband-Dynamik vorherzusagen. Letzteres erfolgt durch ein exakt lösbares effektives Modell, das durch eine Vielzahl numerischer Ergebnisse motiviert und gestützt wird.

Abstract

Motivated by current experiments with ultracold atoms, the study of complex dynamics of Bose–Einstein condensates in optical lattices forms the central subject of this work. A lattice model of interacting bosons under the influence of an external force is motivated and derived from the experimental setup. Several dynamical regimes of this model are discussed in this thesis. In a first part we will develop a new measure for detecting avoided crossings in complex energy spectra and apply it to the quantum chaotic regime of the single-band system. The second and main part of this work is dedicated to the coupling between energy bands described in terms of a two-band model. The complex time evolution is already apparent in the horizontal and vertical population dynamics of the non-interacting problem. We find resonances in the interband transport, and, in a second step, study the effect of inter-particle interactions on these resonant oscillations. We are able to predict all time scales of the complex interband dynamics even in the presence of interactions. This is possible via the introduction of an effective model that is motivated and supported by a multitude of numerical results and proves exactly solvable.

Preface

Wissenschaft wird vom Menschen gemacht.
Werner Heisenberg

The last three years passed very quickly and the work on this thesis took many, sometimes unexpected turns. Whilst working on the problems that cumulated in the present text, I experienced help and support from many sides and I would like to acknowledge the most important ones here.

First of all, I am grateful to my supervisor, Dr. Sandro Wimberger, for the possibility to work in his group and for introducing me to the fascinating topic of ultracold atoms. He provided many contacts with researchers working in this and related fields leading to stimulating discussions. I would also like to thank him for many suggestions during this whole project and his proof-reading and comments concerning this thesis.
Furthermore I would like to thank Prof. Manfred Salmhofer for being the second referee of my thesis.

Special gratitude is devoted to Andrea Tomadin for providing his code, for his help in how to use it and for several good discussions. I am also grateful to Dr. Javier Madroñero for his help in improving the speed of the numerical routines. I am indebted to Prof. Peter Schlagheck for his constant support and interest. He came up with the idea for an effective spin model in a personal discussion in Krasnoyarsk.

I profited by financial and organisational support from various sides. I would like to thank the Klaus Tschira Foundation for generously granting me a scholarship and offering several interesting events. I also wish to express my gratitude to the Graduate School of Fundamental Physics in Heidelberg and in particular to Gesine Heinzelmann and Prof. Sandra Klevansky. Both were always friendly, encouraging, and supportive. I am furthermore grateful to the Graduate Academy of the University of Heidelberg for two travel grants allowing me to learn and discuss in Krasnoyarsk and Utrecht.

Friends and colleagues, in particular Ghazal Tayebirad, Christoph Karrasch, Benedikt Probst, Tobias Paul, and Michael Henke, contributed with many chats, discussions, and support. Thank you all.

Besonders danken möchte ich meinen Eltern, Rita und Gerhard Plötz, die mich stets und in allem unterstützt haben und damit die vorliegende Arbeit erst ermöglicht haben. Meiner Mutter Rita Plötz danke ich zusätzlich für Ihre Offenheit, Toleranz und ihren wunderbaren Humor gerade in der letzten Zeit.

Die allergrößte und unschätzbare Unterstützung erhalte ich von Kerstin Klett. Ich kann ihren Beitrag sowie meine Dankbarkeit und Freude darüber nicht beschreiben.

Heidelberg, July 2010.

Contents

Introduction

Ultracold Atoms

The experimental realisation of Bose–Einstein condensation with dilute gases and the unprecedented control of these systems has created a new and fast developing field of research inspiring many scientist [Blo08b]. By combining atomic physics, condensed matter and quantum optics, various areas of physics are connected through this link and fascinating experiments have become possible to test existing theories and to develop new models. In these experiments, clouds of bosonic or fermionic atoms are cooled to very low temperatures and can be manipulated by various external fields to create, for instance, traps and lattice potentials or to address different internal degrees of freedom [Blo08b]. They offer the realisation of many different models of quantum physics ranging as far as condensed matter theory [Blo08b], quantum information [Blo08a], quantum chromodynamics [Rap07, Wil07], and cosmology [Bra08].

After a focus on weakly interacting systems in the first years, the high degree of control of almost all system parameters has allowed a study of strongly correlated quantum systems by now [Blo08b]. Prime examples of quantum effects and of the perfect control of systems of ultracold gases are the interference of matter waves [And95a, Gat07], where a large regime of parameters is accessible in a single experimental setup, and the direct study of a quantum phase transition in a cold gas realisation of the Bose–Hubbard model [Gre02a]. An extension of earlier experiments on the coupling of energy bands in weakly interacting gases of cold atoms to the regime of stronger inter-particle interactions is now possible. The required phase coherence of the time evolution in many-body systems for the complex interference effects has again been demonstrated in a recent experiment with ultracold bosons in optical lattices [Wil10].

Complex Dynamics

We take these opportunities as a motivation to study complex dynamics in quantum systems. The time evolution of a quantum state in a many-level quantum system, very often quantum many-body models, is a central topic in many fields of physics [Aku06]. The complexity arises from a large number of levels contributing to the time evolution and allowing multiple phase interference. It can also be the result of an explicit time-dependence of the Hamiltonian which can be translated into a many-level problem by Floquet analysis. Another typical feature of such complex systems is that a small perturbation can have a large effect and that the system shows completely different behaviour at different time scales. Direct signatures of an intriguing phase interference in these systems are present in the

population dynamics. We will often discuss this simple observable since it bears witness of the complex time evolution of the wave function.

There are several ways to approach a complex many-level quantum system. These approaches could be classified as statistical, analytical, and numerical. To begin with, it is natural to use a statistical description for a system of many contributing levels. The difficulty lies in finding the right degree of abstraction, i.e., to remove almost all details without removing the characteristic effects, for instance by replacing matrix elements by random numbers and keeping only the symmetries of the original problem. Historically, this proved successful in the description of complex nuclei and led to the development of a systematic theory of the spectral structure of random matrices [Meh04]. It found a large revival with the conjecture that quantum chaotic systems have the same spectral properties as random matrices [Boh84].

Secondly, complex quantum systems do usually not allow a solution in a simple analytical way, involving only known analytical functions or a small number of integrals. One is then forced to apply approximations in order to obtain an analytical understanding of the system's behaviour. The application of higher order perturbation theory and of different bases are means to capture the effect of even small perturbations. For the dynamics they might furthermore allow a separation of time-scales to find a useful approximate description which can be compared to numerical simulations for further improvement.
But even in seemingly simple cases, where an exact solution is possible, this solution may not be helpful in a better understanding of the physical system. To give a simple example, the eigenvalues and eigenvectors of any $2, 3$, or 4 dimensional matrix can always be given exactly (the characteristic polynomial is maximally of fourth order and has an explicit solution in terms of radicals). They can be found for instance with a computer algebra system and the number of bytes necessary to store such a solution can be taken as a measure for its length. This length grows very quickly with the system size and where the eigensystem of an arbitrary two-level system is only two lines long, the full four-level system takes already 18 pages (with 45 lines per page). Such a solution is thus possible, but clearly not useful and the need to find good physical approximations is apparent already for the case of solvable few-level systems.

A third approach is to immerge oneself into a complete numerical study of the system. If one is able to obtain the required matrix elements (which can be an obstacle right from the beginning on [Aku06]) and to simulate systems large enough, one faces a different problem: The vast amount of data for a many-body (or many-level) wave function is often too detailed and even veiling the relevant physical mechanisms at work which are, in the end, what we are interested in and not the individual set of data points. This means one has to distill the physical characteristics out of an abundance of numbers. However, if one manages to get a glimpse on the basic effects, one can try to build—or even guess—effective models and compare their predictions to further numerical data.

This Work

The solutions of the Schrödinger equation for a periodic optical lattice are Bloch waves and the spectrum consists of energy bands [Kit04, Blo08b]. An additional external force gives rise to interesting phenomena such as Bloch oscillations and leads to transport of atoms between the energy bands. This has been demonstrated for ultracold atoms in optical lattices in various experiments [Mor01, Sia07, Zen09]. However, the situation for deep optical lattices and the effect of interactions beyond mean-field has not yet been fully understood. Motivated by these experiments, we will study interacting bosons in optical lattices under the influence of a strong external force. If the force is much smaller than the separation between the lowest energy bands, such a situation is well described by a single-band Bose–Hubbard model. A strong coupling of many energy levels is possible in this regime and the corresponding spectrum shows many interdependent avoided crossings. Stronger forces lead to a significant coupling of energy bands and the Bose–Hubbard model needs to be extended to include at least two energy bands. The main goal of this thesis will be a non-perturbative understanding of the force-induced interband coupling of interacting bosons in deep optical lattices. We will use a two-band Bose–Hubbard model to study the interband transport comprehensively in the non-interacting case and to understand the effect of weak many-body interactions on interband oscillations. In this way, we are going to combine the two fields mentioned above in an investigation of the complex dynamics of ultracold atoms.

The detailed outline of this thesis is as follows. We will review bosonic systems of cold atoms, derive and discuss the Bose–Hubbard models relevant for this thesis in chapter 1. This will also include an overview of results forming the background for our own work. In the following chapters we will discuss different aspects of complex dynamics in the Bose–Hubbard model. The results obtained in this work are divided into two parts which can be read independently.

We are going to start by studying the regular and quantum chaotic regime of the single-band model in chapter 2. We will define a new and useful tool to detect and characterise avoided crossings in energy spectra. After its definition and an analysis of model systems, we will apply it to the complex spectrum of the single-band model and verify random matrix theory predictions very precisely allowing even the detection of spectral details. This study of a quantum chaotic system realisable with ultracold atoms provides thus an example of the statistical approach to complex quantum systems.

The following and longest part of this thesis is dedicated to the interband coupling in a two-band Bose–Hubbard model. In chapter 3, we will begin our analysis of the interband coupling with the non-interacting case. A non-interacting two-band model with external force is the simplest model system for a non-perturbative study of the interband coupling due to the external force. However, we will find that even this case does not have a simple solution in known functions, but shows very rich and complex dynamics. We are going to apply the analytical approach to complex quantum systems here, by using different bases and approximative methods to gain a sound understanding of the system's behaviour in different regimes. We will mainly study the population dynamics between the two energy bands and find resonances in this interband transport.

The additional effect of interparticle interactions on these resonant interband oscillations is at the focus of chapter 4. The interparticle interaction leads to a collapse and revival of these interband oscillations. We will collect numerical results for this phenomenon which

will guide us in finding an approximate analytical description for the mechanisms at work and we will even give an effective model that allows analytical predictions of all time scales of the interband oscillations. Chapter 4 is accordingly an example of the numerical strategy for understanding a complex many-level system and building of effective models. We are going to close this thesis by a short summary of our results and an outlook on future perspectives.

To summarise, we are going to study complex dynamics in the Bose–Hubbard model, mainly discussing the complex spectral structure of the single-band case and the interband coupling in the two-band model. Let us emphasize that the system is interesting in its own respect and that many of the results of this thesis are valid independently of their realisation. For example the tool we are going to develop for the detection and characterisation of avoided crossings can be applied to many systems and the non-interacting two-band system is equivalent to a driven two-level system with various possible applications. Nevertheless, we want to motivate our results by reference to ongoing experiments and believe that many of them can indeed be realised in systems of ultracold atoms.

Prerequisites:

Interacting Bosons in Optical Lattices

Chapter 1

Cold Quantum Gases and the Bose–Hubbard Model

Contents

1.1 Ultracold Atoms in External Fields

The experimental realisation of Bose–Einstein condensation (BEC) in 1995 [And95b, Dav95, Bra95], about 70 years after its prediction [Bos24], has opened a completely new and fast developing field of research [Blo08b]. Atoms are cooled as far down as to the nano Kelvin regime, undergo Bose–Einstein condensation and are then manipulated with additional mangetic and electric fields. The macroscopic wavefunction of the BEC allows a direct study of many different quantum phenomena. The applied experimental techniques, as e.g. optical methods, permit an amazing control of almost all parameters including the strength of the inter-particle interaction by the use of Feshbach resonances [Blo08b]. We want to

use this first chapter to give a very brief overview on experimental scales, define central quantities of this thesis and we would like to point out, how the central model of this thesis, the Bose–Hubbard model, could be realised with current experiments using ultracold atoms in optical lattice.

1.1.1 Bose–Einstein Condensation and Ultracold Gases

Let us discuss characteristics of these ultracold atomic systems. They consist of clouds of gases (usually alkali atoms) with densities of typically $10^{13} - 10^{15}\ \mathrm{cm}^{-3}$. They are often coined "dilute gases" since these density are lower than, for instance, the density of molecules in the air which is about $10^{19}\ \mathrm{cm}^{-3}$ at normal conditions (compared to $10^{22}\ \mathrm{cm}^{-3}$ in liquids and solids or $10^{38}\ \mathrm{cm}^{-3}$ in nuclei) [Pet02]. An important feature of these systems is the possibility to observe quantum phenomena at a macroscopic scale, which allows to use optical means to probe them. However, Bose–Einstein condensation in dilute gases is achieved at temperatures of $10^{-5}\ \mathrm{K}$ or less, which is much smaller than for instance the lambda point in ^{4}He, $T_\lambda = 2.17\ \mathrm{K}$, below which superfluid phenomena are observed. The exact critical temperature for the BEC transition of dilute gases in optical potentials depends on the trapping potential (see [Pet02, chap. 11]).

The regime of ultracold atomic gases is not strictly identical with a Bose-condensed dilute gas (see below). In fact, Bose–Einstein condensation is the macroscopic occupation of a quantum state [Leg01]. More precisely, a quantum system shows BEC at any given time t, if one or more of the eigenvalues $n_i(t)$ of the reduced single-particle density matrix

$$\rho(\mathbf{r}\alpha, \mathbf{r}'\alpha'; t) \equiv \langle \hat{\psi}^\dagger(\mathbf{r}, \alpha)\hat{\psi}(\mathbf{r}', \alpha')\rangle = \sum_i n_i(t)\chi_i^*(\mathbf{r}, \alpha; t)\chi_i(\mathbf{r}', \alpha'; t) \tag{1.1.1}$$

is of the order of the total number of particles N [Leg01]. In the expression above, $\hat{\psi}(\mathbf{r}, \alpha)$ denotes the standard bosonic field operator and α denotes additional quantum numbers, for instance the hyperfine index and $\chi_i(\mathbf{r}, \alpha; t)$ are the single-particle eigenfunctions of $\rho(\mathbf{r}\alpha, \mathbf{r}'\alpha'; t)$. We have further made use of the fact, that the reduced single-particle density matrix is hermitian and has real eigenvalues. The phrase "of order N" has a certain vagueness, but this does not lead to problems in practise [Leg01]. There are also rigorous mathematical results concerning the presence of BEC and the size of the condensate fraction as a function of various system parameters. We refer the reader to [Leg01, sec. III.C] and [Lie99, sec. 5] for a discussion thereof.

On the other hand (and following [Blo08b]), the regime of ultracold atoms has been reached when the dilute gas is at a temperature where only s-wave scattering occurs (typically below mK). The short-ranged two-body interaction between neutral atoms is well described by a van der Waals potential $V(r) = -C_6/r^6$ and this defines a characteristic length scale $r_0 \equiv (2M_rC_6/\hbar^2)^{1/4}$ at which the kinetic energy of the relative motion (with reduced mass M_r) equals the interaction energy [Blo08b]. The effective potential for scattering of states with angular momentum $l \neq 0$ contains a centrifugal barrier of height $E_c \approx \hbar^2/M_r r_0^2$. But at low enough temperatures (below $1\ \mathrm{mK}$) the typical energy $E = \hbar^2k^2/2M_r$ in the relative motion of two atoms is below this barrier and scattering into states with $l \neq 0$ is no longer possible (see [Blo08b] and [Leg01] for further details). Thus at very low temperatures, the inter-atomic scattering is limited to s-wave scattering. This has direct consequences for scattering of dilute atomic gases. It turns out [Blo08b], that the scattering is completely determined by the s-wave scattering length a and the scattering of

cold atoms can be described by the following pseudopotential [Blo08b]

$$V(\mathbf{r}) = \frac{4\pi\hbar^2 a}{2M_r}\delta(\mathbf{r}) \equiv g\delta(\mathbf{r})\frac{\partial}{\partial r}(r\cdots). \tag{1.1.2}$$

The last term with the partial derivative with respect to $r = |\mathbf{r}|$ can be omitted when the potential acts on a function that is regular at $r = 0$ [Blo08b]. We will use (an effective one-dimensional version of) this short ranged pseudopotential for the many-body model later in this chapter. Feshbach resonances allow additionally to change the s-wave scattering length [Blo08b], implying that external magnetic fields can be used to create attractive, repulsive or even non-interacting gases and to tune the interaction strength.
We have clarified the regime of ultracold atoms also applicable to BECs of dilute ultracold gases. Let us now describe how these can be manipulated by external fields.

1.1.2 Optical Lattices

A so-called optical lattice, that is an artificial crystal consisting of light, can be achieved by shining laser light on the atoms. The oscillating electric field induces a dipole moment in the atoms and the interaction between this dipole moment and the electric field leads to an ac-Stark shift of the atomic energy levels (provided the laser frequency is not exactly resonant with an atomic transition). If the light field $\mathbf{E}(\mathbf{r})$ of the laser with frequency ω is spatially varying, this exerts a dipole force on the atoms

$$\mathbf{F} = \frac{1}{2}\alpha(\omega)\nabla(|\mathbf{E}(\mathbf{r})|^2), \tag{1.1.3}$$

where $\alpha(\omega)$ denotes the polarisability [Blo08b]. Close too an atomic transition at frequency ω_0, the polarisability has the form $\alpha(\omega) = |\langle e|\hat{d}_{\mathbf{E}}|g\rangle|^2/[\hbar(\omega_0-\omega)]$, with the dipole operator $\hat{d}_{\mathbf{E}}$, and the direction of the force is determined by the detuning from the resonant frequency ω_0. The atoms move towards minima (maxima) of the laser intensity for blue (red) detuned light, i.e. $\omega > \omega_0$ ($\omega < \omega_0$) [Blo08b]. The potential corresponding to the dipole force (in this dipole approximation) is directly proportional to the laser intensity

$$V(\mathbf{r}) = \frac{3\pi c^2}{2\omega_0^3}\frac{\Gamma}{\omega-\omega_0}I(\mathbf{r}), \tag{1.1.4}$$

and will be used to create an optical lattice (Γ is the decay rate of the excited level). By superimposing two counterpropagating laser beams, one can create a spatially periodic intensity profile. If both lasers have a Gaussian beam profile, the resulting trapping potential is given by $V(r,z) = -\tilde{V}_0 \mathrm{e}^{-2r^2/w_0^2}\cdot\sin^2(k_L z)$, where $k_L = 2\pi/\lambda_L$ is the wave vector of the laser light and w_0 the $1/\mathrm{e}^2$ width of the laser beam [Blo08b]. This potential is a one-dimensional optical lattice in z-direction. One can create periodic optical lattices in higher dimensions by overlapping similar standing waves in different directions and at different polarisations. By choosing very deep lattice depths (by using high laser intensities) one can create a two-dimensional array of quasi one-dimensional tubes with no contact between different tubes. With a standing light field in the transversal direction one achieves a one-dimensional periodical optical potential. In the center of the trap this is well approximated as [Blo08b]

$$V(z) = \tilde{V}_0\sin^2(k_L z) = \tfrac{1}{2}\tilde{V}_0\big(1-\cos(2k_L z)\big) \sim V_0\cos(2k_L z), \tag{1.1.5}$$

where we introduced $V_0 = \tilde{V}_0/2$ and dropped a constant energy shift in the last step. We will use this realisation of a one-dimensional optical lattice throughout this thesis. It has the advantage, that the lattice depth can easily be tuned by altering the laser intensity and the lattice constant $d_L = \lambda_L/2$ is directly given by the wave length of the laser, being changeable as well. This lattice potential is made up of laser light and differs in several respects from the periodic potentials found in solids. First of all, it offers the unique feature of changing the lattice constant. Secondly, the lattice is perfect, meaning it does not show any defects or vibrations of the lattice (absence of phonon excitations). Phonons and defects or disorder give certainly rise to interesting physics, but the great advantage of optical lattices is, that these different aspects can be added at a later stage in a well-controlled manner. It is furthermore possible to add an external force to the system by introducing a frequency shift $\Delta\omega$ between the counterpropagating laser beams. If the rate of change is $\mathrm{d}\Delta\omega/\mathrm{d}t$, the lattice potential will be accelerated and the atoms of mass m in the rest frame of the lattice experience an external force [Mor06]

$$F = ma = m\frac{d_L}{2\pi}\frac{\mathrm{d}\Delta\omega}{\mathrm{d}t}. \tag{1.1.6}$$

One can thus create a periodic potential plus a controllable external force. Overall, cold atoms in optical lattices offer great possibilities to study various physical models with a high degree of control of almost all system parameters. Most important for this thesis, they allow the realisation of quasi one-dimensional periodic potentials with arbitrary lattice depth and a tuneable external force.

1.2 Wannier–Stark Systems

The energy band coupling under the influence of an external force in deep optical lattices and including interactions is the main question of this thesis. We use the present section to discuss known results for a single-particle description and related experiments with ultracold atoms in shallow lattices.

1.2.1 Overview

By accelerating the optical lattice it is thus possible to create a system with constant external force. For a weakly interacting gas of ultracold atoms, the following single-particle Hamiltonian can therefore be realised with dilute ultracold gases

$$H = \frac{p^2}{2m} + V_0\cos(2k_L x) + Fx. \tag{1.2.1}$$

Such a problem is actually well-known from solid-state physics as the Wannier–Stark Hamiltonian, see [Glü02] for a recent review, describing the motion of electrons under a constant electrical field in the otherwise periodic potential of the atoms.

There has been a long controversy about the spectrum of eq. (1.2.1). On one hand, taking any eigenstate of the untilted system with energy, say, E_0, one should obtain a full ladder of eigenstates with energies $E_l = E_0 + ld_LF$ by a translation over l periods of the lattice (with lattice constant $d_L = \pi/k_L$). This is the so-called Wannier–Stark ladder. A superposition of these states would then evolve periodically in time with the *Bloch period* $T_B = 2\pi/d_LF$. On the other hand, the Hamiltonian of eq. (1.2.1) is unbounded and proven

to have a continuous spectrum, i.e., it does not have discrete eigenvalues [Glü02]. This discrepancy is resolved as follows. The spectrum is complex and the discrete eigenstates are actually resonances embedded in the complex continuum

$$\mathcal{E}_l^\alpha = E^\alpha + l d_L F - \mathrm{i}\Gamma^\alpha/2, \tag{1.2.2}$$

where α is the band index. Put differently, we can consider the spectrum of the Wannier–Stark problem to be discrete, if we keep in mind the finite lifetime of these states. How can we understand this finite lifetime in a more intuitive way? Let us prepare the system at $F = 0$ in the lowest Bloch band and studying its time-evolution in the presence of the external force. The energetically lowest state at vanishing force is at the center of the lowest Brillouin zone (at $k = 0$). Preparing a Gaussian wave packet centered around this energy, it will undergo periodic oscillations within the lowest Brillouin zone under the influence of the external force [Glü02]. However, when the wavepacket reaches the edge of the zone, it comes in close contact with the first excited energy band and has a finite probability to tunnel to the first excited band. This process can be studied in detail experimentally [Zen09] and is usually modelled by Landau–Zener tunnelling [Glü02]. There, the tunnelling probability increases exponentially with the square of the energy gap between the initial and final state of the tunnelling process. These oscillations and partial tunnelling when the bands come close to each other repeat themselves in higher bands and the wave packet tunnels very fast to higher bands since the band gaps are quickly decreasing with the band index α. Via these repeated tunnelling processes, the particle couples effectively to the continuum. Applying only Landau–Zener theory, the expected decay rate is given by [Sia07]

$$\Gamma_{\mathrm{LZ}} = \frac{\omega_B}{2\pi} \exp\Big[-\frac{\pi^2}{32} \frac{\Delta^2}{d_L F E_R} \Big], \tag{1.2.3}$$

where Δ denotes the bandgap, the recoil energy $E_R = \hbar^2 k_L^2/2m$ is the energy scale of the system, and $\omega_B = d_L F/\hbar$ is the Bloch frequency. The decay rate has a similar structure as for α-decay: Tunnelling events can take place at a certain frequency ω_B and their probability has an exponential form.

The authors of [Glü02] also provide some simple MATLAB routine which allows to compute the Wannier–Stark resonances as scattering states. We used their method to compute the decay rate for particles from the lowest Bloch band in an optical lattice as a function of the external force. The chosen parameters correspond to a shallow optical lattice as used in experiments with ultracold atoms. The decay rate is shown as a function of the inverse external force in figure 1.1. We see that the decay rate of the lowest Bloch band is rather small for small values of the external force. The interband coupling becomes strong for large values of the force and also at specific resonant values of the force. Let us now turn to the experimental observation of this interband coupling.

1.2.2 Realisation with Ultracold Atoms

The mentioned repeated tunnelling between bands and thus an effective depletion of the lowest Bloch band has been observed in experiments with ultracold atoms [Sia07]. There, a gas of bosonic atoms has been prepared in the ground state of the field-free Hamiltonian. Then the force was switched on and the system was allowed to evolve in time. At a later time, all fields were rapidly turned off, the gas evolved freely under gravity and was measured by time-of-flight imaging. The number of atoms observed in the lowest Bloch band after a

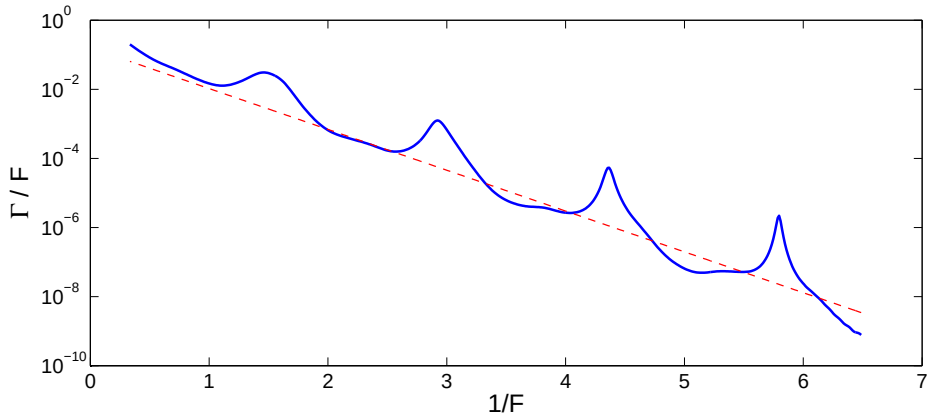

Figure 1.1: Decay rate Γ (solid line) for the lowest Bloch band in the Wannier–Stark problem as a function of the external force F for a potential $V(x) = 4E_R \cdot \sin^2(k_L x) \sim 2E_R \cos(2k_L x)$. Also shown is Landau-Zener prediction (red dashed line) given by $\Gamma_{\mathrm{LZ}} = (2\pi)^{-1} F \exp[-\pi^2 \frac{\Delta^2}{32F}]$ in dimensionless units to be defined in eq. (1.3.18). We observe that the decay becomes stronger when the external force is increased. Additionally, the decay rates are enhanced at specific values of the external force. The basic reason of this resonantly enhanced tunnelling is explained in the main text.

certain evolution time under the force was compared to the initial number of atoms in the same band. Atoms that had tunnelled to higher bands acquired higher momenta and were therefore not captured by the time-of-flight measurement. In other words, the evolution under the influence of the force leads to an effective loss of particles from the ground band. This loss could be fitted with an exponential decay to determine the decay rate. This measurement of a decay rate from the ground band was performed at different values of the external force with a gas of rubidium atoms by [Sia07].

In figure 1.2 we show the results of this experiment (details are reported in [Sia07]), where the rate of decay from the ground band is shown as a function of the external force. The straight line is the Landau–Zener prediction which gives a good account for the overall decay rate. However, on top of the mono-exponential decay one observes a slight enhancement of the decay rate for certain values of the external force. This corresponds to specific tilts of the lattice such that the band gap between the lowest and first excited Bloch band is an integer multiple of external force, $\Delta = n \cdot F$. In this case an initial state from the lower band is energetically degenerate with a level of the first excited band. This effect is called resonantly enhanced tunnelling.
In the lower panel of the same figure 1.2, we show results from the same group [Sia07], where the effect of a weak interaction onto the resonant tunnelling has been studied by increasing the density of the atomic cloud. The interactions are rather weak and can in fact be modelled by a mean-field approach (using the Gross-Pitaevskii equation). For us, it is interesting to note that the weak interaction has an effect on the interband tunnelling, already in this mean-field picture. One major question of this thesis (see chapter 4) is to study the effect of inter-particle interactions on the interband transport beyond mean-field. To describe such a situation, we will use a many-body model that will be motivated and derived in the following section.

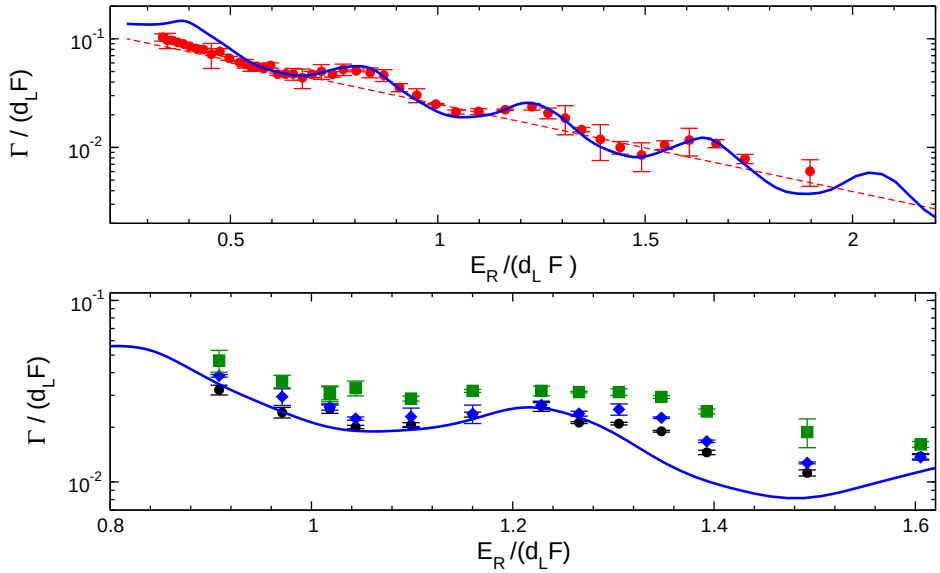

Figure 1.2: Decay rate for particles from the ground band of an optical lattice under the influence of an external force F (E_{rec} and d_L are fixed in the experiment). Shown are the non-interacting (top panel) and the weakly interacting (lower panel) case for an optical lattice $V(x) = 2.5E_R \cdot \sin^2(k_L x)$. The thin dashed line in the top panel represents the mono-exponential decay rate according to simple Landau–Zener tunnelling. The thick line correspond to numerical simulations according to [Glü02]. The theory is in good agreements with the experimental data, also reproducing the enhancement of tunnelling at resonant values of the force. The lower panel shows again the numerical results with experimental for a weakly interacting system (interaction increases from bottom to top). The data shown here has been reported in [Sia07] and is reproduced here with kind permission of one of the authors.

1.3 Derivation of the Bose–Hubbard Model

1.3.1 The Many-body Model

The general many-body Hamiltonian we need to discuss is given by [Fet71]

$$\mathcal{H} = \int \hat{\phi}^\dagger(x) \left(H_0(x) + Fx\right) \hat{\phi}(x) \mathrm{d}x + g_{1\mathrm{D}} \int \hat{\phi}^\dagger(x) \hat{\phi}^\dagger(x) \hat{\phi}(x) \hat{\phi}(x) \mathrm{d}x, \tag{1.3.1}$$

where we used the fact that the inter-particle scattering can be modelled by a contact potential $g_{1\mathrm{D}}\delta(x)$ with an effective 1D scattering coefficient $g_{1\mathrm{D}}$ [Ols98]. We are now going to derive the Bose–Hubbard model along the lines of [Tom06] from this general many-body Hamiltonian. The single-particle part of the Hamiltonian consists of kinetic energy, the periodic potential and the external Stark force. The field-free single-particle part is well-known from solid-state physics

$$H_0(x) = \frac{p^2}{2m} + V_0 \cos(2k_L x) \tag{1.3.2}$$

and the associated single-particle eigenstates are Bloch waves

$$H_0 \psi_k^\alpha(x) = E_k^\alpha \psi_k^\alpha(x) \qquad \text{with} \qquad \psi_k^\alpha(x) = \mathrm{e}^{\mathrm{i}kx} u_k^\alpha(x), \tag{1.3.3}$$

with quasimomentum k restricted to the first Brillouin zone $-\pi/d_L \leq k \leq \pi/d_L$. The functions $u_k^\alpha(x)$ have the same period as the lattice $u_k^\alpha(x+d_L) = u_k^\alpha(x)$ and are eigenstates of the Hamiltonian $H_k = \frac{1}{2m}(p+k)^2 + V_0 \cos\left(2k_L x\right)$ containing the quasimomentum as parameter. Since the quasimomenta are reduced to the first Brillouin zone, the Bloch waves are periodic functions of the quasimomentum k and can be expanded in a Fourier series. The expansion coefficients depend on the coordinate x and are the so-called *Wannier functions* (we use $x_l \equiv l \cdot d_L$)

$$\psi_k^\alpha(x) = \sqrt{\frac{d_L}{2\pi}} \sum_{x_l} w^\alpha(x-x_l) \mathrm{e}^{\mathrm{i}kx_l}, \text{ with } w^\alpha(x-x_l) = \sqrt{\frac{d_L}{2\pi}} \int_{BZ} \psi_k^\alpha(x) \mathrm{e}^{-\mathrm{i}kx_l} \mathrm{d}k. \quad (1.3.4)$$

We note that there is an ambiguity in the definition of the Bloch functions, which can be used to tune the Wannier functions. Indeed, if we consider a new Bloch function

$$\tilde{\psi}_k^\alpha(x) = \mathrm{e}^{\mathrm{i}\chi_\alpha(k)} \psi_k^n(x) \qquad \text{with} \qquad \chi_\alpha(k + 2\pi/d_L) - \chi_\alpha(k) = 2\pi m, m \in \mathbb{N} \quad (1.3.5)$$

the same physical state is described. As has been shown by Kohn [Koh59], the Wannier functions can be chosen real and exponentially decaying for all bands, i.e., $|w^\alpha(x)| \sim |x|^{-3/4} \mathrm{e}^{-h_\alpha x}$ as $x \to \infty$ with some $h_\alpha > 0$ (see [Blo08b, sec. II.C] and [Koh59, He01]). These Wannier functions are called maximally localised and it is exactly this property that makes them interesting for discussing deep lattices. Namely, a single-particle state localised around a certain lattice site l is best described by a Wannier function $w^\alpha(x - x_l)$.

We expand the field operator $\hat{\phi}(x)$ in terms of these single-particle Wannier functions to obtain a description of local single-particle states. This expansion involves the Wannier functions at all wells and all energy bands

$$\hat{\phi}(x) = \sum_{\alpha=1}^{\infty} \sum_{l \in \mathbb{Z}} w^\alpha(x - x_l)\ \hat{a}_l^\alpha. \quad (1.3.6)$$

The operator $\hat{a}_l^{\alpha\dagger}$ thus creates a boson in a Wannier function for the energy band α that is centered around $x_l = d_L l$, or for short: at site l in band α. We will truncate this expansion to the two lowest energy bands ($\alpha = 1, 2$) later in order to study the inter-band dynamics in this many-body model. But the expansion of the field operator in terms of single-particle functions like the Wannier functions is in general not an approximation, provided one keeps all terms and all bands generated by the expansion.

Using the Wannier functions as single-particle basis for a Fock basis, we can write many-body states with a finite number of particles N and lattice sites L in terms of Fock states

$$|\{n\}\rangle = |n_1^1, \ldots, n_L^1; n_1^2, \ldots; \ldots n_l^\alpha \ldots\rangle, \quad \text{such that } N = \sum_{\alpha,l} n_l^\alpha, \quad (1.3.7)$$

with $n_l^\alpha \equiv \hat{a}_l^{\alpha\dagger} \hat{a}_l^\alpha$ and the usual action of the creation and annihilation operators on Fock states

$$\hat{a}_l^\alpha |\{n\}\rangle = \sqrt{n_l^\alpha} |\ldots n_l^\alpha - 1 \ldots\rangle, \quad \hat{a}_l^{\alpha\dagger} |\{n\}\rangle = \sqrt{n_l^\alpha + 1} |\ldots n_l^\alpha + 1 \ldots\rangle. \quad (1.3.8)$$

Let us proceed and take a closer look at the expansion of the field operator in terms of Wannier functions. When inserting eq. (1.3.6) into the many-body Hamiltonian of

eq. (1.3.1), many different terms are generated. We will shortly discuss them and analyse the resulting coefficients in a moment.

The periodic part of the single-particle Hamiltonian gives rise to a coupling of different lattice sites within the same band

$$\begin{aligned} \int \hat{\phi}^\dagger(x) H_0(x) \hat{\phi}(x) \mathrm{d}x &= \sum_\alpha \sum_{l,l'} J^\alpha_{l-l'}\ \hat{a}^{\alpha\dagger}_l \hat{a}^\alpha_{l'}, \\ \text{with} \quad J^\alpha_{l-l'} &\equiv \int w^\alpha(x-x_l) H_0(x) w^\alpha(x-x_{l'}) \mathrm{d}x = \varepsilon^\alpha_{l-l'}, \end{aligned} \tag{1.3.9}$$

where we used that the Wannier functions can be chosen real and introduced $\varepsilon^\alpha_l \equiv \frac{d_L}{2\pi}\int_{BZ} E^\alpha_k \mathrm{e}^{\mathrm{i}kx_l}\mathrm{d}k$, the Fourier transform of the eigenenergies E^α_k. This contribution is usually referred to as *hopping* since it removes an atoms at a given lattice site l' in band α and creates an atom at site l in the same band. There is no hopping between different energy bands. To obtain this result, we used the fact that the Fourier transform of the Wannier functions, the Bloch waves $\psi^\alpha_k(x)$, are eigenfunctions of the single-particle Hamiltonian H_0 and that the Wannier functions obey the normalisation

$$\int w^\alpha(x-x_l) w^{\alpha'}(x-x_{l'}) \mathrm{d}x = \delta_{\alpha\alpha'}\delta_{ll'}, \tag{1.3.10}$$

which allow to derive $H_0 w^\alpha(x-x_l) = \sum_{l'} \varepsilon^\alpha_{l'}\ w^\alpha(x-x_{l+l'})$. Thus the onsite energies and the hopping terms in the Bose–Hubbard model to be derived are a consequence of the periodic single-particle part of the Hamiltonian.

The second single-particle term in the many-body Hamiltonian, eq. (1.3.1), contains the external Stark force and induces an *interband coupling*. Inserting the expansion of the field operator yields

$$\begin{aligned} F\int \hat{\phi}^\dagger(x)\cdot x \cdot \hat{\phi}(x)\mathrm{d}x &= d_L F \sum_{\alpha,l} l\cdot \hat{a}^{\alpha\dagger}_l \hat{a}^\alpha_l + d_L F \sum_{\alpha,\alpha'}\sum_{l,l'} C^{\alpha\alpha'}_{l-l'}\ \hat{a}^{\alpha\dagger}_l \hat{a}^{\alpha'}_{l'}, \\ \text{where} \quad C^{\alpha\alpha'}_{l-l'} &\equiv \int w^\alpha(x-x_l)\, x\, w^{\alpha'}(x-x_{l'})\mathrm{d}x. \end{aligned} \tag{1.3.11}$$

Here, we shifted the variable of integration by x_l and made again use of the normalisation of the Wannier functions. We see, that the force has two effects: 1) it tilts the lattice and 2) it couples different bands and lattice sites. This is of particular interest for us here. Although the Wannier functions of adjacent bands have opposite parity, the overlap integral does not vanish due to the presence of the additional factor of x. On the other hand, the parity property of the Wannier functions

$$w^\alpha(-x) = (-1)^{\alpha-1} w^\alpha(x), \quad \alpha = 1,2,\ldots \tag{1.3.12}$$

implies the absence of a force induced coupling between different sites of the *same* band.

The third term of the many-body Hamiltonian contains the *inter-particle interaction* and by inserting the expansion for the field operator we find

$$\begin{aligned} g_{1\mathrm{D}}\int \hat{\phi}^\dagger(x)\hat{\phi}^\dagger(x)\hat{\phi}(x)\hat{\phi}(x)\mathrm{d}x &= \sum_{\alpha_1\ldots\alpha_4}\sum_{l_1\ldots l_4} M^{\alpha_1\ldots\alpha_4}_{l_1\ldots l_4}\ \hat{a}^{\alpha_1\dagger}_{l_1}\hat{a}^{\alpha_2\dagger}_{l_2}\hat{a}^{\alpha_3}_{l_3}\hat{a}^{\alpha_4}_{l_4}, \\ \text{with} \quad M^{\alpha_1\ldots\alpha_4}_{l_1\ldots l_4} &\equiv g_{1\mathrm{D}}\int w^{\alpha_1}(x-x_{l_1}) w^{\alpha_2}(x-x_{l_2}) w^{\alpha_3}(x-x_{l_3}) w^{\alpha_4}(x-x_{l_4})\mathrm{d}x. \end{aligned} \tag{1.3.13}$$

The interaction thus creates and annihilates two particles at certain lattice sites in different bands and therefore yields another coupling of different energy bands. Since the Wannier functions are maximally localised on the lattice, the dominant contribution is given by onsite interactions $M_{llll}^{\alpha_1\ldots\alpha_4}$. However, the parity of the Wannier functions (they are odd (even) for even (odd) bands) will make many of these coefficients vanish.

Our general goal is to study the complex dynamics in the Bose–Hubbard model, in particular the interband coupling and the effect of the inter-particle interaction on such a coupling. We therefore restrict ourselves to a two-band system. The main effects of an interband coupling should be present there and it is the simplest non-perturbative extension of the single-band system. At that same time, a two-band system is still numerically feasible and the interpretation of results is easier when we restrict ourselves to two vertical degrees of freedom. The dimension of the Hilbert space for N bosons in B bands and L lattice sites per band is given by [Kol03b]

$$\dim \mathcal{H}(N,B,L) = \frac{(N+BL-1)!}{N!\,(BL-1)!}. \tag{1.3.14}$$

We will give examples of Hilbert space sizes below. But let us note here, that the Hilbert space of the two-band system grows roughly by a factor of 6 when increasing the number of bosons and sites simultaneously by one. Denoting henceforth operators for the lowest band as $a_l \equiv a_l^1$ and for the first excited band as $b_l \equiv a_l^2$, the many-body Hamiltonian reduced to these two energy bands and onsite interaction reads (we drop the hats over operators from now on)

$$\begin{aligned}\mathcal{H} = &\sum_{l,l'} J_{l-l'}^{(a)}\; a_l^\dagger a_{l'} + J_{l-l'}^{(b)}\; b_l^\dagger b_{l'} + d_L F \sum_l l\cdot\left(a_l^\dagger a_l + b_l^\dagger b_l\right) + d_L F \sum_{l,l'} C_{l-l'}\;\left(a_l^\dagger b_{l'} + \text{h.c.}\right)\\ &+ \sum_l \left(M_{llll}^{1111}\; a_l^\dagger a_l^\dagger a_l a_l + M_{llll}^{2222}\; b_l^\dagger b_l^\dagger b_l b_l + M_{llll}^{1122}\;\left(a_l^\dagger a_l^\dagger b_l b_l + b_l^\dagger b_l^\dagger a_l a_l + 4 a_l^\dagger a_l b_l^\dagger b_l\right)\right).\end{aligned}$$

The first two terms are the onsite energies (for $l = l'$) and hopping processes between different sites in either band, followed by a tilt of the whole lattice due to the external force. The last term in the first line is a force induced single-particle coupling of different sites of the different bands. It will move particles from the lower band to the upper band and will be of great importance for the inter-band transport to be studied in large parts of this thesis. Due to its similarity to dipole coupling in atomic physics, we will often refer to this process as *dipole coupling*, which helps to distinguish this single-particle interband coupling from the interaction induced two-body interband interaction. The different interaction terms (we already reduced our analysis to onsite interaction) for the two-band system are given in the second line. They include onsite interaction in either bands (the first two terms) and a two-particle coupling between the bands. The latter includes the creation of two particles in the lower band and annihilation of two particles in the upper band at the same time, as well as the reverse process. Finally, there is an onsite interaction between the bands (very last term) whenever a particle in the lower band and in the upper band are present at the same site. Throughout, we will mainly discuss repulsive interactions.
At this point, one needs to analyse the hopping and coupling coefficients further in order to estimate the relative strength of the different processes which requires computation of the Wannier functions.

1.3.2 Coefficients in the Hubbard Model

The different coefficients in the Bose–Hubbard model are integrals over Wannier functions. We can compute them by solving the eigenvalue problem for the Bloch waves

$$H_k u_k^\alpha(x) = \left[\frac{(p+k)^2}{2M} + V_0\cos(2\pi x/d_L)\right] u_k^\alpha(x) = E_k^\alpha u_k^\alpha(x) \tag{1.3.15}$$

and the Wannier functions are then obtained by Fourier transformation. The quasimomentum k enters as a parameter in the Hamiltonian above and the eigenstates are computed for each k independently yielding an infinite system of eigenfunctions with infinitely many eigenenergies E_k^α. Those depend on k and are referred to as *energy bands*. Since the $u(x)$ are periodic, $u(x+d_L) = u(x)$, we expand them in a Fourier series $u_k^\alpha(x) = \sum_{n\in\mathbb{Z}} c_k^\alpha(n)\mathrm{e}^{\mathrm{i}2\pi n x/d_L}$ to get a discrete eigenvalue problem for the coefficients $u_k^\alpha(n)$ that is numerically feasible

$$\sum_{n\in\mathbb{Z}} H_{mn}^{(k)} c_k^\alpha(n) = E_k^\alpha c_k^\alpha(m). \tag{1.3.16}$$

The Fourier space representation of $H^{(k)} = (k - i\partial_x)^2/2m + V_0\cos(2\pi x/d_L)$ is easily calculated by multiplication with exponentials and subsequent integration. It reads

$$H_{nn'}^{(k)} = \frac{(k+2\pi n/d_L)^2}{2m}\delta_{nn'} + \frac{V_0}{2}(\delta_{n,n'+1} + \delta_{n,n'-1}). \tag{1.3.17}$$

The eigenvalue problem is easy to handle numerically and a small basis is sufficient to obtain the lowest few bands. The Wannier functions are then obtained from $w^\alpha(x-x_l) = \sqrt{d_L/(2\pi)}\int_{BZ} u_k^\alpha(x)\mathrm{e}^{-\mathrm{i}kx_l}$. Special care has to be taken to ensure that the Wannier functions are real and maximally localised [Tom06, Blo08b, He01].

Let us now introduce dimensionless units to simplify notation. The relevant length and energy scales are determined by the parameters of the optical lattice. These are the wavevector of the laserlight k_L yielding a lattice constant $d_L = \pi/k_L$ and the recoil energy $E_R = \hbar^2 k_L^2/(2m)$ where m is the mass of atoms. We use these scales to make all parameters dimensionless, i.e., we perform the substitutions

$$\frac{k}{k_L} \to k, \qquad \frac{x}{d_L} \to x, \qquad \frac{d_L F}{E_R} \to F, \qquad \frac{V_0}{E_R} \to V_0. \tag{1.3.18}$$

We will use these dimesionless units throughout the thesis and they have also been used to implement a dimensionless version of eq. (1.3.17). All energies, like the coefficients in the Hubbard model or the depth of the optical lattice, will be given in units of the recoil energy.

Using the outlined computation of the Wannier functions, we can discuss the coefficients in our Hubbard model. The hopping coefficients are expectation values of the untilted single-particle Hamiltonian with respect to Wannier functions. They determine the onsite energies per band and thus also the band gap between the lowest and first excited band. Since the Wannier functions are exponentially localised, they decrease very rapidly when the distance between the center of the Wannier functions is increasing. But Wannier functions of neighbouring sites still have a significant overlap and yield a finite hopping coefficient. The first three hopping coefficients of the two lowest bands are depicted in figure 1.3.
As the lattice depth increases, the Wannier functions become more localised on their lattice site and the hopping decreases. Furthermore, the exponential localisation of the Wannier

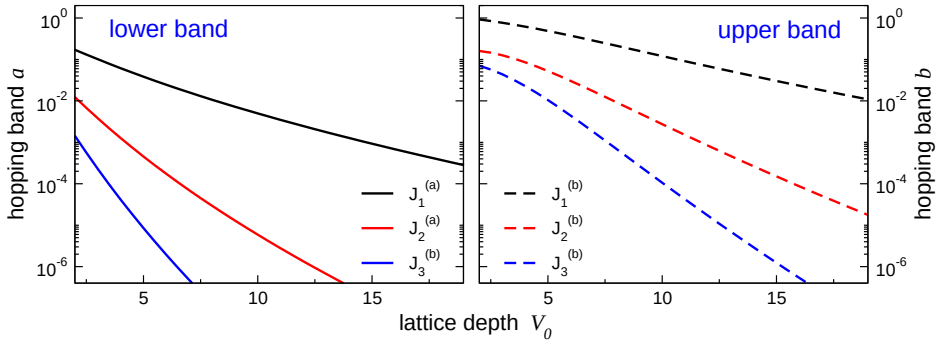

Figure 1.3: Absolute values of the hopping coefficients in Hubbard models as a function of the lattice depth. Shown are the coefficients for hopping to a neighbour that is 1, 2, or 3 sites away in the lower (*left panel*) or upper (*right panel*) band. All coefficients have been multiplied by a factor of 2 for later comparison.

function makes the coupling between next-to-nearest neighbour sites by about one order of magnitude smaller than between neighbouring sites. All this holds for the lowest and the first excited band. We will therefore neglect all hopping processes beyond nearest-neighbour hopping in the following, as is usually done in Hubbard models. Additionally, we observe that the Wannier functions in the upper band are more extended and the resulting coupling of neighbouring sites expressed in the hopping coefficient is larger than in the lower band. Please note, that we show only the absolute values of the hopping coefficients above. For example, the nearest-neighbour hopping coefficients to be kept in the following, have opposite sign in the two lowest bands. Including only nearest neighbour hopping leads (in the absence of interactions) to the well-known cosine dispersion and the more remote hopping coefficients can be used to approximate the actual band structure by a Fourier series of the form $E(k) = -2\sum_n J_n \cos(nk)$.

Besides a tilting of the whole lattice, the external force we introduced to the system leads to a coupling of sites in different bands. This coupling is proportional to the strength of the force. The constant of proportionality for coupling sites at a distance Δl is given by the integral over Wannier functions at the same distance multiplied by a factor of x allowing a single-particle coupling of adjacent bands which is otherwise forbidden by the parity of the Wannier functions. We computed the Wannier functions for the two lowest bands as outlined above and the resulting first three dipole coefficients are shown in figure 1.4.
Very much alike the case of hopping, the coefficients decrease rapidly with the distance between the lattice sites to be coupled. Furthermore, all couplings become smaller with increasing lattice depth, only the onsite coupling becoming approximately constant. This is again a consequence of the localisation of the Wannier functions. However, this does not concern the interband dipole coupling at the same site and the coefficient C_0 thus remains almost constant at about 0.1. This onsite dipole coupling C_0 is accordingly much larger (between one and three orders of magnitude) than the dipole coupling between different lattice sites, and as in the case of more remote hopping coefficients, we will neglect such a dipole coupling of distant lattice sites. It would lead to a slight enhancement of the interband coupling and we expect a small broadening of the resonance in the inter-band coupling to be discussed later in this thesis. However, since these couplings are by at least one order of magnitude smaller than the onsite dipole coupling this is a minor effect and does not change the general behaviour of the system. It would only complicate an analytical

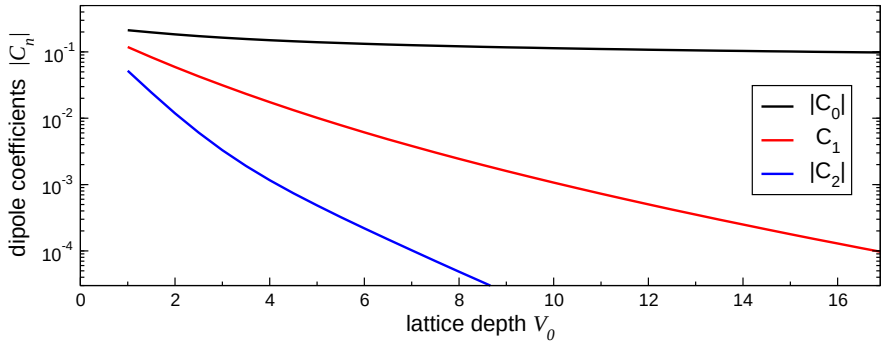

Figure 1.4: Dipole coefficients in Hubbard models as a function of the lattice depth. Shown are the absolute values of the dipole coefficients ($C_{0,2} < 0$ and $C_1 > 0$). All except the onsite dipole coupling decrease rapidly with increasing lattice depth.

understanding of the main effects to be discussed in chapter 3 and 4 of this thesis.

After discussing the different terms and coefficients in the Hubbard model, including their relative strength and dependence on the depth of the optical lattice, we are now in a position to sum up these efforts in stating the Hamiltonians that will be further investigated in this thesis. Firstly, if the lowest energy band can be considered isolated due to a weak force or very large band gap, we obtain the following single-band Bose–Hubbard model with an external force:

$$H_1 = -\frac{J}{2}\sum_l (a_{l+1}^\dagger a_l + \text{h.c.}) + \frac{U}{2}\sum_l n_l(n_l - 1) + F\sum_l l n_l,$$

with hopping between nearest neighbours only, and an onsite interaction $U = 2M_{llll}^{1111}$. The external force tilts the lattice. We will give a short overview of known results for this model in section 1.4 and we will study the complex spectrum of this interacting many-body model in the second half of chapter 2.
Secondly, we have a two-band Bose–Hubbard model with several terms that lead to a coupling of the two energy bands. Including only nearest neighbour hopping and the onsite dipole coupling of the energy bands, we obtain the following two-band model:

$$H_2 = \sum_l \Big\{ lFn_l^a - \tfrac{J_a}{2}(a_{l+1}^\dagger a_l + \text{h.c.}) + \tfrac{W_a}{2} n_l^a(n_l^a - 1) + FC_0(b_l^\dagger a_l + \text{h.c.}) + \\ (\Delta + lF)n_l^b - \tfrac{J_b}{2}(b_{l+1}^\dagger b_l + \text{h.c.}) + \tfrac{W_b}{2} n_l^b(n_l^b - 1) + 2W_x n_l^a n_l^b + \tfrac{W_x}{2}(b_l^\dagger b_l^\dagger a_l a_l + \text{h.c.}) \Big\}.$$

We have again a tilt of the lattice sites (in either band) and the bands are separated by a band gap Δ. The interaction coefficients are given by $W_a = 2M_{llll}^{1111}$, $W_b = 2M_{llll}^{2222}$, and $W_x = 2M_{llll}^{2211}$. We will discuss this Hamiltonian in two chapters of this thesis. Namely, we will analyse the interband coupling in the non-interacting system in chapter 3. The population dynamics will turn out quite complex already in this case, and we will finally study the effect of the inter-particle interaction on the dynamics in the last chapter of this thesis, chapter 4 of this thesis.

We have reviewed the derivation of the Bose–Hubbard models of [Tom06] starting from the general many-body Hamiltonian with a contact interaction. We shortly the discussed the relevant approximations in this derivation as for instance neglecting hopping between

next-to-nearest neighbours. Below in section 1.4 we are going to describe some of the many existent results for Bose–Hubbard models in one spatial dimension. But let us first discuss specific aspects of the experimental realisation with cold atoms of the two models presented here.

1.3.3 Remarks on Possible Experimental Realisation

We have derived the single-band and two-band Bose–Hubbard model for ultracold atoms in deep optical lattices in the previous section. Throughout this thesis we will discuss both systems analytically and numerically. In the derivation we used parameters for an experimental realisation with an optical lattice created by a single-frequency laser beam, i.e., a potential of $V(x) = V_0 \cos(x)$ (in dimensionless units) experienced by the atoms. The single-band Bose–Hubbard model is a good description for deep optical lattices at low temperatures (when the thermal energy is smaller than the gap to the first excited energy band) and small external forces ($F \ll \Delta$). Let us use the present section for a brief discussion of possible issues in an experimental realisation of the two-band model.

Inter-band Coupling in Optical Lattices

In section 1.2 we discussed the Wannier–Stark problem, i.e. the spectrum of a Hamiltonian of the form $\mathcal{H} = p^2 + V_0 \cos(x) + Fx$ for $x \in \mathbb{R}$. The spectrum consists of metastable resonances forming the Wannier–Stark ladder. We can compute the imaginary part of the three lowest resonances which are the decay rates of the three lowest Bloch bands. These decay rates are shown for a deep optical lattice with $V_0 = 8$ in figure 1.5.

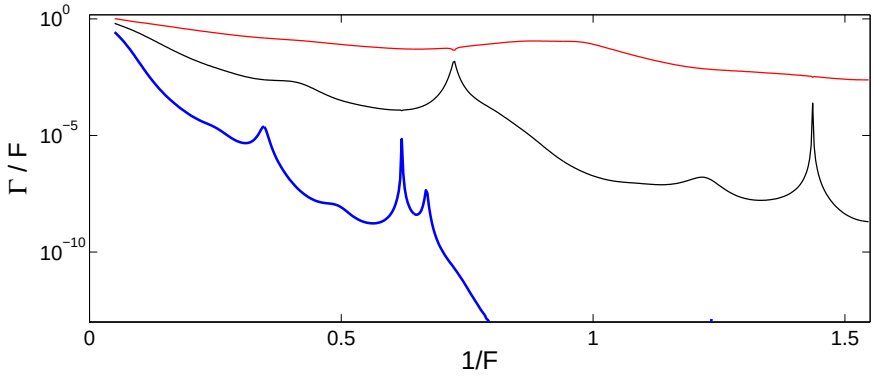

Figure 1.5: Decay rates for the three lowest Bloch bands as a function of the inverse force for a deep optical lattice with $V_0 = 8$. They have been computed similarly to section 1.2. The decay rates decrease strongly with decreasing force (and increasing $1/F$) and show differently pronounced peaks.

The decay rates in figure 1.5 decrease for smaller values of the external force and show resonances as discussed in section 1.2. We can use the decay rates as shown in the figure to estimate the lifetimes of particles in the lowest or first excited band. If we take a strong force $F \approx 2.0$ for the potential depth $V_0 = 8$ shown in figure 1.5 we find a decay rate for particles from the first excited band to leave towards higher bands of about $\Gamma/F \approx 10^{-4}$. This corresponds to a lifetime of $\tau = 1/\Gamma = (2\pi)^{-1} \cdot 10^4 \, T_B$ which is the same order of magnitude as the maximal time scales discussed in this thesis and should at least allow

an observation of the effects to be discussed. However, this is only a rough estimate, but it shows qualitatively that an observation of time-dependent phenomena in a two-band Bose–Hubbard model is not directly excluded by loss of particles to higher bands in a single optical lattice. However, future research should clearly take into account the effect of higher bands onto the two-band model, e.g. by adding finite lifetimes to the two lowest energy bands when discussing their coupling. This can for instance be done by computing decay rates perturbatively as has been shown in [Tom07, Tom08] for a single-band Bose–Hubbard model.

Isolated Two-band System: Superlattices

Another possible setup to create an isolated two-band system is to use superlattices as, e.g., in [Bar09] where a Bose–Hubbard Hamiltonian for atoms in a superlattice is discussed. A superlattice is created by adding a second lattice (with a possible phase shift) to an existing optical lattice to create a potential

$$V(x) = V_0 \cos(x) + V_1 \cos(2x + \phi). \tag{1.3.19}$$

Here we took the simple case that the second lattice has twice the lattice constant as the first optical lattice. Three examples for such superlattices and their four lowest energy bands are shown in figure 1.6. Our description of the Bose–Hubbard system in the present chapter neglected the effect of other than only two bands. Such a description is valid for a system with two energy bands that are well separated from the other energy bands. We need two neighbouring energy bands with a bandgap that is much smaller than the gap to other bands.

In the first realisation shown in figure 1.6, we see a deep superlattice with no phase shift. The four lowest energy bands corresponding to this case are also shown. The band gap between the second and third band is slightly larger, about 10%, than between the first (i.e. lowest) and second energy band. This means that the two lowest bands are closer together than the second and third band. However, the two lowest energy bands are not well separated from the others in this case.
The second example of a possible superlattice is shown in the middle panel of figure 1.6 and a phase shift of π between the two lattices has also been included. We clearly see that two lowest energy bands are well separated from the higher energy bands. The first energy gap is $\Delta_1 = 0.76$ and is about 15 times smaller than the separation between the second and third energy band. The requirements for our description as a two-band system are very well realized by this choice of lattice parameters. The present case is thereby a promising candidate for an experimental realisation of the effects discussed in chapter 3 and 4. Please note, that it is also possible to tune the band gap between energy bands by variation of the phase shift. This will serve as a motivation to vary the band gap in section 4.2.2.
In the lowest panel of figure 1.6 we show another superlattices created from the superposition of two lattices with equal lattice depth. The resulting band structure shows that it is also possible to have the second and third energy band separated from the others. For the parameters shown in the lowest panel of figure 1.6 the minimal distance between two isolated bands is 1.5 which is almost four times smaller than the gap to the lower or upper neighbouring energy level. It is thus possible to create a system with two isolated energy bands which are not the two lowest energy bands of the system.

The cases discussed in the present section clearly show that it is possible to create isolated two-band systems with optical lattices. Additionally, we would like to mention other

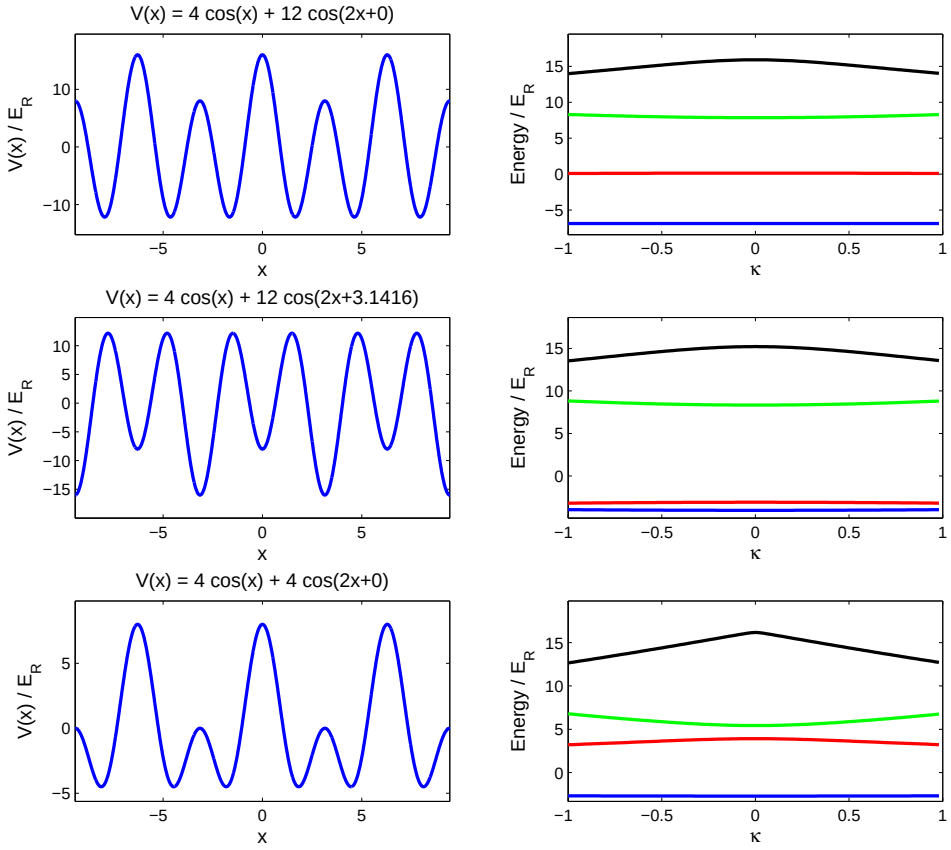

Figure 1.6: Examples for band structures of superlattices. Shown are three examples for superlattices according to eq. (1.3.19) (*left*) and their four lowest energy bands (*right*). The specific parameter values for the superlattices $V(x) = V_0 \cos(x) + V_1 \cos(2x + \phi)$ are directly given in the figure for the three cases. The middle and lower panel show two isolated energy bands.

systems that allow the realisation of two isolated energy bands. Semiconductor superlattices consist of layers of different semiconductors, e.g. GaAs or $Al_xGa_{1-x}As$ [Glü02]. The wave function of an electron travelling through the structure can be approximated by a plane wave in the transversal direction to the layers of semiconductors. In the perpendicular direction, the particle experiences a series of potential barriers. The corresponding band structure depends on the details of the system, but two minibands well separated from other energy bands can be realised. Indeed, resonances in the interband coupling similar to the ones we will find in chapter 3 have been discussed by a completely different method for semiconductor superlattices in [Abu07]. Further realisations of Wannier–Stark systems and isolated two-band systems with semiconductor superlattices can be found in [Voi88]. However, we will not discuss these systems any further. For the sake of simplicity, we will use parameters in this thesis corresponding to a setup with a single optical lattice, such that the parameters of the Hamiltonian can be characterised by a single quantity, the depth of the optical lattice V_0. This allows us to treat the single- and two-band Bose–Hubbard model on the same footing. A further study should include the computation of Wannier functions and the parameters in the Hamiltonian for a specific choice of an isolated two-band system in order to formulate a precise experimental proposal.

1.4 Some Background on Bose–Hubbard Models

The present section is devoted to a discussion of some results for Bose–Hubbard models that are needed in later parts of this thesis. The aim is to provide background in addition to the effects discussed in section 1.2 and to introduce some technical details.

1.4.1 Phase Diagram of the Single-band Bose–Hubbard model

Before discussing specific physical effects, we will review the phase diagram of the single-band Bose–Hubbard model and exploit the translational symmetry of the model to introduce a new basis of translational invariant Fock states.

In the absence of an external force and at low temperatures (such that the thermal energy is smaller than the separation between the lowest bands), only the lowest energy band needs to be taken into account. The corresponding single-band Bose–Hubbard model with possible additional external potentials reads

$$H = -\frac{J}{2}\sum_l \left(a_{l+1}^\dagger a_l + \text{h.c.}\right) + \frac{U}{2}\sum_l n_l(n_l-1) + \sum_l \epsilon_l n_l, \tag{1.4.1}$$

with a hopping strength J, the interaction coefficient $U = 2M_{llll}^{1111}$ and additional potentials ϵ_l which might contain for instance external trapping potentials or the chemical potential.

The phase diagram of this model was studied in [Fis89] and a recent review including experimental results can be found in [Blo08b]. The single-band Bose–Hubbard model of eq. (1.4.1) in one dimension is not exactly solveable although the continuum version in (the Lieb–Liniger model) is soluble and the Fermi–Hubbard model is integrable [Blo08b]. Despite this fact, the physics of the model is rather well understood. The ground state for vanishing interaction $U = 0$ is given by an occupation of the lowest Bloch band with momentum $k = 0$ by all N bosons

$$|\Psi_0(N)\rangle^{(U=0)} = \frac{1}{\sqrt{N!}}(A_{k=0}^\dagger)^N|\text{Vac}\rangle = \frac{1}{\sqrt{N!}}\left(\frac{1}{\sqrt{L}}\sum_l a_l^\dagger\right)^N|\text{Vac}\rangle, \tag{1.4.2}$$

where $A_k^\dagger$ denotes the creation operator for a particle with momentum k and L is the number of lattice sites. The system is in a superfluid phase. The particles are completely delocalised over the lattice in this ground state and the local particle number $\langle n_l\rangle$ fluctuates. For large systems, these fluctuations of the local particle number are Poissonian and the superfluid ground state is indistinguishable from a coherent state $|\Psi_0\rangle \propto \exp(A_{k=0}^\dagger)|\text{Vac}\rangle$ [Blo08b] (see also section 4.2.2). The excitation spectrum is gapless in this regime and the system has a non-vanishing compressibility κ.

In the opposite limit of strong interactions $U \gg J$, the ground state (for integer filling) is given by a product of local Fock states with one atom per site [Blo08b]

$$|\Psi_0(N)\rangle^{(J=0)} = \left(\prod_l a_l^\dagger\right)|\text{Vac}\rangle. \tag{1.4.3}$$

For $J > 0$ the atoms start to hop on the lattice, which implies a double occupancy and costs an interaction energy U. The spectrum is gapped with an energy gap $\approx U$. The system is insulating due to the interaction induced energy gap and is thus a *Mott insulator*. Increasing J leads to a gain in kinetic energy and the ground state is no longer a simple product state.

At a certain value of J/U the kinetic energy gain wins over the repulsive interaction and the system undergoes a quantum phase transition [Blo08b]. The critical value of J/U depends on the dimensionality of the system. For a one-dimensional Bose gas, the critical value for the superfluid-Mott-insulator transition is $(2J/U)_c = 0.26 \pm 0.01$ [Els99] and the transition is of Kosterlitz–Thouless type [Buo07].

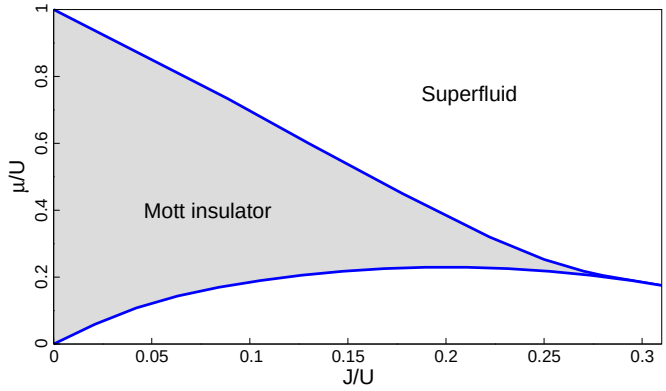

Figure 1.7: Schematical view of the phase diagram of the 1D Bose–Hubbard model for integer filling based on the results of [Els99]. The characteristic Mott lobes of higher dimensional systems become pointy in one spatial dimension.

The phase diagram of the one-dimensional Bose–Hubbard model at integer filling shows typical Mott lobes extending into the superfluid phase. At $J = 0$, the system is in the Mott insulating phase. It undergoes a quantum phase transition into the superfluid phase at finite J/U. Experimentally one can vary the ratio of hopping and interaction strength by changing the depth of the optical lattice. The dependence of both parameters on the lattice depth can be given approximately without computation of the Wannier functions. The hopping coefficient is obtained from the width of the lowest band of the Mathieu equation and the interaction coefficient can be computed by approximating the lowest band Wannier function by the harmonic oscillator ground state [Blo08b]. The result for one dimension is (all energies in dimensionless units)

$$J(V_0) \approx \frac{2}{\sqrt{\pi}} V_0^{1/4} \mathrm{e}^{-2\sqrt{V_0}} \quad \text{and} \quad U(V_0) = g_{1\mathrm{D}} \int |w^{(0)}(x)|^4 \mathrm{d}x \approx g_{1\mathrm{D}} \sqrt{\frac{\pi}{2}} \cdot V_0^{1/4}. \quad (1.4.4)$$

The harmonic oscillator functions are good approximations for the Wannier functions at one lattice site for deep lattices. However, it is not possible to use them for a computation of the hopping coefficients since they decay much faster ($\propto \mathrm{e}^{-x^2}$) than the Wannier functions ($\propto \mathrm{e}^{-x}$). In figure 1.8, we compare these approximate values for the coefficients of the single-band Bose–Hubbard model with the exact values from numerical computation of the Wannier functions. The obviously different scaling behaviour of the two parameters with the lattice depth has been used to study the superfluid-Mott-insulator phase transition experimentally by varying the lattice depth. The analytical estimates for the hopping and interaction coefficients as a function of the lattice depth reproduce the exact values fairly well. Note in particular, that the interaction strength increases with the lattice depth. For a deeper lattice the local potential walls draw closer on the Wannier function, it is squeezed and the interaction coefficient becomes larger.

The mentioned quantum phase transition between superfluid and Mott insulator has also been subject of a recent study using the overlap between the ground state to slightly

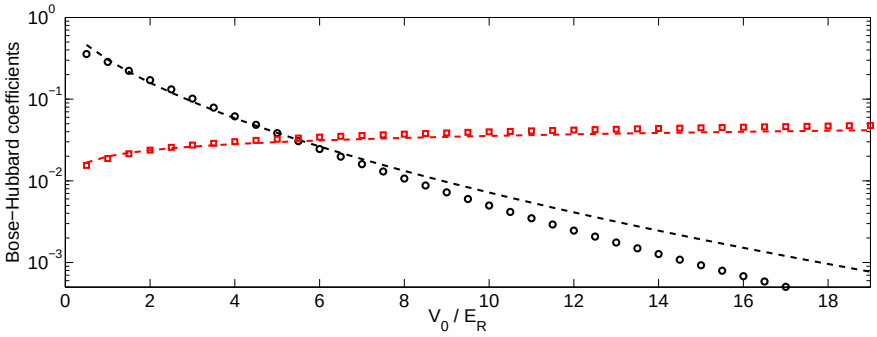

Figure 1.8: Coefficients in the single-band Bose–Hubbard model as a function of the lattice depth. Shown are the hopping coefficient (black circles) and the interaction coefficient (red squares), together with their analytical approximations, eq. (1.4.4), (dashed lines).

different parameter values [Buo07]. This overlap is denoted as fidelity

$$f(\lambda) \equiv |\langle \Psi_0(\lambda) | \Psi_0(\lambda + \delta\lambda) |, \quad \delta\lambda \ll 1 \tag{1.4.5}$$

and the authors used $\lambda = J/U$ to study the mentioned transition in the one-dimensional Bose–Hubbard model. The idea is rather intuitive: the ground state of the system changes drastically at the critical value $(J/U)_c$ and the fidelity which should usually be close to one will show a significant drop when crossing the quantum phase transition. Indeed, the authors [Buo07] were able to perform finite-size scaling of (the second derivative of) the fidelity and affirmed the critical value known from earlier Quantum Monte Carlo and Density Renormalisation Group calculations [Els99]. In many cases, a quantum phase transition can be viewed as an avoided crossing of energy levels in the spectrum of a quantum system [Sac01]. This suggests to use the fidelity in order to detect avoided crossings and we will later explore this idea in extending the applicability of the fidelity to the complete spectrum of a complex quantum systems in chapter 2.

1.4.2 Fock Space and Translational Invariant Basis

After discussing the phase diagram of the one-dimensional single-band Bose–Hubbard model, let us now have a closer look at the Fock basis. We will discuss a single-band and two-band Bose–Hubbard model with an external force in this thesis. In either cases it is possible to apply the following gauge transformation. We introduce new operators $\tilde{a}_l^\alpha = T^\dagger a_l^\alpha T$, with $T = \exp[-\mathrm{i}Ft \sum_{l,\alpha} l n_l^\alpha]$, leading to a time-dependent Schrödinger equation with a new Hamiltonian (the single-band case $\alpha = 1$ is clear from the following)

$$H(t) = -\sum_\alpha \sum_l \frac{J_\alpha}{2} \left(\mathrm{e}^{\mathrm{i}Ft} a_{l+1}^{\alpha\dagger} a_l^\alpha + \mathrm{h.c.} \right) + \text{ interaction terms.} \tag{1.4.6}$$

The gauge transformation thus removes the tilt of the lattice at the cost of a time-dependent phase factor for the hopping. The other terms in the Hamiltonian are unaffected by this transformation. The time-dependence is periodic with the *Bloch period* $T_B = 2\pi/F$.
A great advantage of this new Hamiltonian is, that it allows to reduce the numerical complexity of the problem. The new Hamiltonian is translational invariant when imposing periodic boundary conditions on the system

$$a_{L+1}^\alpha = a_1^\alpha. \tag{1.4.7}$$

There is a clear physical interpretation of this transformed Hamiltonian. The atomic cloud can be formed to a ring shape and the optical lattice is imposed on this ring, similar to a donut that is quenched along the circumference at equally spaced positions. The external force can experimentally be realised by an acceleration of the optical lattice. The atoms are sitting at the dents of the donut and experience this rotation of the ring as a force. For us, it is important to note that the quasimomentum is a conserved quantity when periodic boundary conditions are used and the different subspaces of fixed total quasimomentum can be treated independently. Since there are L possible quasimomentum subspaces of approximately equal size, the Hilbert space is reduced by a factor of order L.

To derive a representation of a translational invariant basis, we follow [Kol03b, Tom06] and introduce a shift operator that moves the occupation numbers in each band by one site to the right

$$\hat{S}|n_1^1,\ldots,n_L^1;\ldots n_i^\alpha\ldots\rangle \equiv |n_L^1,n_1^1\ldots,n_{L-1}^1;\ldots n_{i-1}^\alpha\ldots\rangle, \tag{1.4.8}$$

where the use of periodic boundary conditions ($n_0^\alpha = n_L^\alpha$) is implied. The shift operator is the lattice equivalent of the operator of translations $T_a|x\rangle = |x+a\rangle$ on the continuum which is well known to be $\mathrm{e}^{\mathrm{i}\hat{p}a}$ with the momentum operator $\hat{p}$. The shift operator allows to decompose the Fock basis into equivalence classes of states that can be obtained by subsequent application of the shift operator on one representative state. We will call these states *seed states* [Kol03b] and denote them as $|\mathbf{s}\rangle$, since they form the basis to build up all possible Fock basis states. One seed state can maximally generate L different Fock states. We call the number of different Fock states that can be obtained from a seed state $|\mathbf{s}\rangle$ the cyclicity $M(s)$ of the seed state. An $M(s)$-fold application of the shift operator onto one seed state will reproduce the original state

$$\hat{S}^{M(s)}|\mathbf{s}\rangle = |\mathbf{s}\rangle. \tag{1.4.9}$$

In other words, the cyclicity $M(s)$ of a given seed state $|\mathbf{s}\rangle$ answers the question "How many different Fock states can one create by applying the shift operator to a seed state $|\mathbf{s}\rangle$?". With the help of the seed states, one can construct eigenstates to the shift operator which form a new translational invariant basis labeled explicitly by the total quasimomentum of a given state

$$|\mathbf{s},\kappa_j\rangle = \frac{1}{\sqrt{M(s)}}\sum_{l=1}^{M(s)} \mathrm{e}^{\mathrm{i}2\pi\kappa_j l}\hat{S}^l|\mathbf{s}\rangle \qquad \text{with} \qquad \kappa_j = \frac{j}{M(s)}, \quad j=1,\ldots,M(s). \tag{1.4.10}$$

The possible values of different quasimomenta are limited by the cyclicity of the state and maximally by the number of lattice sites. Let us verify explicitly that they are eigenstates of the shift operator

$$\begin{aligned}\hat{S}^m|\mathbf{s},\kappa\rangle &= \frac{1}{\sqrt{M(s)}}\sum_{l=1}^{M(s)} \mathrm{e}^{\mathrm{i}2\pi\kappa l}\hat{S}^{l+m}|\mathbf{s}\rangle = \frac{\mathrm{e}^{-\mathrm{i}2\pi\kappa m}}{\sqrt{M(s)}}\sum_{l'=1-m}^{M(s)-m} \mathrm{e}^{\mathrm{i}2\pi\kappa l'}\hat{S}^{l'}|\mathbf{s}\rangle \\ &= \mathrm{e}^{-\mathrm{i}2\pi\kappa m}|\mathbf{s},\kappa\rangle,\end{aligned} \tag{1.4.11}$$

where we used the periodic boundary conditions. The states of eq. (1.4.10) form a new basis and we will refer to this basis as *seed basis* in opposition to the original basis which we will simply call Fock basis. Since the Hamiltonian with periodic boundary conditions

is translational invariant and thus commutes with the shift operator $\hat{S}$, both can be diagonalised simultaneously and the Hamiltonian can be decomposed into L subspaces of different total quasimomentum. The same holds for the time-evolution operator over one period ($\mathcal{T}$ denotes time-ordering)

$$U(T_B) \equiv \mathcal{T}\exp\left[-\mathrm{i}\int_0^{T_B} H(t)\mathrm{d}t\right] = \oplus_{j=1}^{L} U^{(\kappa_j)}(T_B), \tag{1.4.12}$$

the so-called *Floquet–Bloch operator*, which also decomposes into different blocks. We would like to mention that there is an additional symmetry of the time-dependent Hamiltonian, revealed by studying the instantaneous spectrum, i.e., the eigenvalues $E_n(t)$ of the time-dependent Hamiltonian as a function of time. For integer filling ($N = L$) one finds not only $E_n(t) = E_n(t+T_B)$ but also $E_n(t) = E_n(t+T_B/L)$. More generally, if M is the greatest common divisor of N and L, i.e. $M = \gcd(N, L)$, than $E_n(t) = E_n(t+T_B/M)$. This implies that the Hamiltonians corresponding to these time are related by a unitary transformation $H(t+T_B/M) = Q^\dagger H(t) Q$, with a diagonal matrix Q having elements $\exp[(-\mathrm{i}E_n T_B)^{1/L}]$ [Kol03b]. The time-evolution operator over one period can then be written as $U(T_B) = [Q^\dagger U(T_B/M)]^L$. This fact is important for a statistical analysis of the spectrum as done in quantum chaos studies, since all symmetries in the system must have been considered to compare the actual level statistics with random matrix theory predictions (see [Kol03b, Tom06] for details).

Example of Seed Basis and Hilbert Space Size

Let us discuss a specific example of how the seed state and the seed basis are constructed. We will take a single-band example, but the extension to more bands is not difficult. Consider $N = 3 = L$ with a total number of Fock states of $\dim H = 5!/(3!2!) = 10$. There are four seed states which allow to construct the whole Fock basis. They read

$$\begin{array}{lll} |\mathbf{s}_1\rangle = |111\rangle & & \\ |\mathbf{s}_2\rangle = |201\rangle & \text{creates} & |120\rangle, |012\rangle, |201\rangle \\ |\mathbf{s}_3\rangle = |210\rangle & \text{creates} & |021\rangle, |102\rangle, |210\rangle \\ |\mathbf{s}_4\rangle = |300\rangle & \text{creates} & |030\rangle, |003\rangle, |300\rangle, \end{array} \tag{1.4.13}$$

where we also gave the different Fock states that can be created by application of the shift operator. The first state has multiplicity $M(s_1) = 1$ and the others have $M(s_{2,3,4}) = 3$. Thus the new basis in terms of seed basis states is given by the following states

$$\begin{array}{lllll} |\mathbf{s}_1, 1/1\rangle & & & & \\ |\mathbf{s}_2, 1/3\rangle & \text{and} & |\mathbf{s}_2, 2/3\rangle & \text{and} & |\mathbf{s}_2, 3/3\rangle \\ |\mathbf{s}_3, 1/3\rangle & \text{and} & |\mathbf{s}_3, 2/3\rangle & \text{and} & |\mathbf{s}_3, 3/3\rangle \\ |\mathbf{s}_4, 1/3\rangle & \text{and} & |\mathbf{s}_4, 2/3\rangle & \text{and} & |\mathbf{s}_4, 3/3\rangle. \end{array}$$

These are the ten states of the translational invariant seed basis. We note, that the three subspaces are not of equal size $\dim H^{(\kappa_i)} = 3$, but the $\kappa = 1$ subspace is slightly larger $\dim H^{(\kappa=1)} = 4$. The same holds for larger systems. The reason is, that only the seed states with $M(s_i) = L$ can contribute to the seed basis states $|\mathbf{s}_i, 1/L\rangle$ but all seed states are able to give a state with $\kappa = 1$.

In the numerical simulations below we will compute the Floquet–Bloch operator for different system sizes in the single-band and the two-band case. The main limitation of this is the exponentially growing Hilbert space which requires larger amounts of working memory to store and diagonalise the Floquet–Bloch operator. Since it is in general a full matrix with complex elements, we need 16 bytes (in double precision) per matrix element. The number of matrix elements is

$$[\dim H^{(\kappa)}]^2 \qquad \text{with} \qquad \dim H^{(\kappa)} \approx \frac{(N+BL-1)!}{N!(BL-1)!L}, \tag{1.4.14}$$

the factor of $1/L$ stems from the reduction to one quasimomentum subspace. Please note, that another matrix of the same size is necessary to store the eigenvectors of the Floquet–Bloch operator. We give a few examples for the size of the Hilbert spaces for a single-band and a two-band system below in table 1.1, together with the memory needed to store only the Floquet–Bloch operator. If we are only interested in a specific solution of the time-dependent Schrödinger equation, as we will discuss in chapter 4, we only need the non-zero matrix elements of the Hamiltonian for an integration of the Schrödinger equation. This has the advantage that the required memory scales only linear with the dimension of the Hilbert space and physically larger systems are computable. This and the numerical procedures are explained in more detail in appendix A.

1.4.3 Quantum Chaos in the Bose–Hubbard Model

The single-band Bose–Hubbard with and without external force exhibits quantum chaotic behaviour in certain parameter regimes [Kol04, Kol03b]. This might be somewhat surprising, since its fermionic counterpart, the Fermi–Hubbard model, is integrable [Ess91, Pon08]. Let us discuss this in more detail after a short general review of quantum chaos.

What is Quantum Chaos?

Centuries of study of classical physics have flourished in an understanding that there are two distinct types of motion in Hamiltonian systems: regular motion of integrable systems and chaotic motion of non-integrable systems [Haa91]. They can be distinguished by studying the time evolution of a set of neighbouring phase space trajectories. In a chaotic system, any such bunch of trajectories will divert quickly, with the distance between two trajectories growing exponentially in time at a rate called *Lyapunov exponent*. This distance of trajectories can also grow very quickly in regular systems but never exponentially, the corresponding Lyapunov exponent vanishes [Haa91]. With the birth of quantum mechanics, the natural question arose how this classical cleavage translates into the quantum realm. The answer is not obvious since the notion of trajectory and thus of Lyapunov exponent is not applicable in quantum mechanics. There are different approaches to think of chaos in quantum mechanical systems. Since many aspects of quantum mechanics are wave phenomena, it proved rewarding to study classical wave equations. In many cases, this has direct consequences for our understanding of quantum mechanics, as for instance the two-dimensional Helmholtz equation is mathematically the same as a two-dimensional Schrödinger equation [Stö99]. Independent of the field (classical or quantum), the non-separability of the Hamilton–Jacobi equations shows up in the short wave length limit [Haa91]. A quantum mechanical system is then called quantum chaotic, when its classical counterpart ($\hbar \to 0$) is chaotic. This notion is very useful in various contexts [Haa91, Stö99], but what should be

$\dim H_{B=1}^{(\kappa=1)}$	single–band Bose–Hubbard model				
memory [GB]	$L=2$	$L=5$	$L=8$	$L=9$	$L=10$
$N=2$	2	3	5	5	6
	$6.0\cdot10^{-8}$	$1.3\cdot10^{-7}$	$3.7\cdot10^{-7}$	$3.7\cdot10^{-7}$	$5.4\cdot10^{-7}$
$N=5$	3	26	99	143	201
	$1.3\cdot10^{-7}$	$1.0\cdot10^{-5}$	$1.5\cdot10^{-4}$	$3.0\cdot10^{-4}$	$5.8\cdot10^{-4}$
$N=8$	5	99	810	1430	2438
	$3.7\cdot10^{-6}$	$1.5\cdot10^{-4}$	$3.9\cdot10^{-2}$	0.12	0.35
$N=9$	5	143	1430	2704	4862
	$3.7\cdot10^{-6}$	$3.0\cdot10^{-4}$	0.12	0.11	0.35
$N=10$	6	201	2438	4862	9252
	$5.4\cdot10^{-6}$	$5.8\cdot10^{-4}$	0.35	0.35	1.27

$\dim H_{B=2}^{(\kappa=1)}$	two–band Bose–Hubbard model				
memory [GB]	$L=2$	$L=5$	$L=8$	$L=9$	$L=10$
$N=2$	6	11	18	19	22
	$5.4\cdot10^{-7}$	$1.8\cdot10^{-6}$	$4.8\cdot10^{-5}$	$5.4\cdot10^{-6}$	$7.2\cdot10^{-6}$
$N=5$	28	402	1938	2926	4252
	$1.2\cdot10^{-5}$	$2.4\cdot10^{-3}$	0.06	0.13	0.27
$N=8$	85	4862	61334	120175	222079
	$1.0\cdot10^{-4}$	0.35	56.0	215	734
$N=9$	110	9724	163438	347186	$6.9\cdot10^{5}$
	$1.8\cdot10^{-4}$	1.41	398	$1.8\cdot10^{3}$	$7.1\cdot10^{3}$
$N=10$	146	18478	408694	$9.4\cdot10^{5}$	$2.0\cdot10^{6}$
	$3.0\cdot10^{-4}$	5.09	$2.5\cdot10^{3}$	$1.3\cdot10^{4}$	$6.0\cdot10^{4}$

Table 1.1: Hilbert space size for the $\kappa=1$-subspace of the single-band (*upper table*) and two-band (*lower table*) Bose–Hubbard model. Also shown is the memory needed to store the Floquet–Bloch operator for the same subspaces and parameters in units of GB. Increasing the number of particles and lattice sites at the same time leads to an increase of the Hilbert space size by a factor of approximately 4 in the single-band case and of 6 in the two-band case.

understood as classical counterpart remains unclear for many quantum systems, for instance the Hubbard models.[1] A second approach attacks the problem from a different perspective and translates integrability into quantum mechanics by using the correspondence between

[1] Besides the classical limit of $\hbar\to0$ one can consider the limit of large particle number $N\to\infty$ and effectively replace creation and annihilation operators by complex numbers. Writing the time evolution for amplitudes and phases separately one can derive classical Hamiltonian equations for amplitudes and phases, which are interpreted as action and angle variables. This has been done for the Bose–Hubbard model in [Kol07] yielding a chaotic classical system.

the classical Poisson brackets and the commutator. More precisely, classical integrability consists in the existence of as many mutually independent conserved quantities as degrees of freedom in the system [Tab89]. A quantum system could then be called integrable if the number of mutually commuting constants of motion equals the number of degrees of freedom. However, there is no clear definition of the latter for an arbitrary quantum system. In fact, it has been shown that there is an infinite number of conserved quantities in the Fermi–Hubbard model [Sha86].

A different characterisation of many quantum systems with classically chaotic counterpart came from nuclear physics and led to the Bohigas-Giannoni-Schmit conjecture: Spectral fluctuations of quantum chaotic systems follow the predictions of Random Matrix Theory (RMT) [Boh84]. Important features shared by both types of spectra are a universal level repulsion, that is a tendency to avoid level crossings (the degree of repulsion depends on the symmetries of the system) and spectral rigidity (small fluctuations around the average number of levels found in a interval of given length) and many more. This universality of spectral fluctuations is widely supported by a vast amount of numerical data [Haa91] in very diverse types of systems [Stö99]. Additionally, progress has recently been made towards a semiclassical justification of these universal level fluctuations [Mül04, Heu07]. This characterisation of quantum chaos, that the universal features of the system's spectrum behave as those of an ensemble of Gaussian random matrices (with the appropriate fundamental symmetries) has the great advantage of being applicable to any discrete quantum system and numerically testable. It stimulated an abundance of research and has been accepted as a different characterisation of quantum chaos [Haa91].

To give a short example, the strong coupling of many levels leading to a repulsion of energy levels when approaching each other, results in the following behaviour. The statistical distribution $P(s)$ of normalised level spacings $s_j \equiv (E_{j+1} - E_j)/\langle \Delta E \rangle$ can be computed for an ensembles of random matrices. The results for a regular system and for a quantum chaotic system with time-reversal symmetry, described by the so-called Gaussian Orthogonal Ensemble (GOE) of random matrices, read [Haa91]

$$P(s) = \begin{cases} \mathrm{e}^{-s} & \text{Poissonian for regular systems} \\ \frac{\pi}{2}\, s\, \mathrm{e}^{-\pi s^2/4} & \text{Wigner–Dyson for GOE systems.} \end{cases} \tag{1.4.15}$$

These show that the repulsion of levels for small s in chaotic systems is in contrast to the possibility to approach each other arbitrarily close in regular systems where $P(0)$ has a finite value. The level spacing distribution is a measure that can be applied when one set of energy levels is given. However, to visualise the level repulsion characteristic in chaotic spectra, one studies the change of the spectrum under variation of an external parameter like magnetic or electric field, for instance. Then, the levels move as the parameter changes, some of them approach and are then repelled from each other as the parameter varies further. This happens for many levels and leads to a characteristic shape of a quantum chaotic spectrum showing many avoided crossings. There are also predictions for the distribution of minimal distances at avoided crossings in random matrices. We restate the derivation given by Zakrzewski and Kus [Zak91] as an illustration. Two levels undergoing an avoided crossings can be described by an effective Hamiltonian $\left(\begin{smallmatrix} a & g \\ g & b \end{smallmatrix}\right) + \lambda \left(\begin{smallmatrix} v_1 & 0 \\ 0 & v_2 \end{smallmatrix}\right)$ where the basis is chosen such that the perturbation is diagonal. All parameters are real numbers and the minimal distance at the avoided crossing is easily computed to be $c = 2g$. Since all parameters are Gaussian distributed random numbers, g is also normally distributed. Then, the normalised

probability to find an avoided crossing of width c is given by [Zak91]:

$$P(c) = \frac{2}{\pi \bar{c}} \exp\left[-\frac{c^2}{\pi \bar{c}^2}\right], \tag{1.4.16}$$

where $\bar{c} = \int_0^\infty cP(c)\mathrm{d}c$ denotes the mean width of avoided crossings. In a regular system on the other hand the levels do not show a strong repulsion and are allowed to come very close. Compared to the mean level spacing, the minimal distances of avoided crossings will be tiny and the corresponding probability distribution for the width of avoided crossings is given by $P(c) = \delta(c)$ [Yan93], where the delta function has to be understood as "much, much smaller than the mean level spacing". We will give an example for this behaviour in the following chapter.

Known Results for Quantum Chaos in Bose–Hubbard Models

The latter understanding of quantum chaos is applicable to the Bose–Hubbard model. Kolovsky and Buchleitner studied an untilted Bose–Hubbard model at integer filling $N = L$ and found the statistical distribution of level spacings for $J \approx U$ to be in accordance with RMT predictions (when reduced to one symmetry subspace) [Kol04]. In particular, the Bose–Hubbard model is invariant under time reversal and the level spacing distribution follows RMT the prediction for the corresponding GOE. This is an indication of quantum chaotic behaviour. In quantum chaotic systems, it is a consequence of a strong coupling of many different levels. Therefore, the authors tested two "generic" bases for the system, Fock states with Wannier functions and Bloch waves as single particle basis. They found that the coefficients for an expansion of the system's eigenstates in either basis show a broad distribution (quantised by the information entropy). The authors concluded that the system exhibits a strong coupling of many different levels in either basis and is thus quantum chaotic [Kol04].

In a second study, the same authors extended their results to the single-band Bose–Hubbard model with an additional external force [Kol03b]. They applied the gauge transformation we described earlier to obtain a periodically time-dependent Hamiltonian and used periodic boundary conditions. Then, it is not the spectrum that shows the characteristic avoided level structure (since the eigenvalues are not meaningful in a time-dependent system), but the quasienergy spectrum, i.e., the eigenphases of the Floquet–Bloch operator. Studying again integer filling $N = L$ the authors where able to show by analysing the spectral structure, that the Floquet spectrum of the tilted Bose–Hubbard model is chaotic when all parameters of the system are of comparable strength $J \approx U \approx F$, but becomes regular for large values of the external force, i.e., when $J \approx U \ll F$ [Kol03b]. It is thus possible to study the crossover between regular and chaotic dynamics in the tilted Bose–Hubbard model by varying the external force [Tom06].

Interband Coupling in Bose–Hubbard Models

As mentioned already, the external force does not only lead to the expected change of the eigenstates and energy spectrum, but also induces transitions to higher energy bands. In a single-particle picture the eigenvalues in the well-known Wannier–Stark problem acquire a non-zero complex part, i.e., they have a finite lifetime. Tomadin *et al.* computed decay rates for the tilted many-body Bose–Hubbard model by including the strongest interband couplings perturbatively [Tom08, Tom07]. They opened the tilted single-band Bose–Hubbard

model to the second energy band and found the complex eigenvalues of this open problem by numerical diagonalisation. Quite remarkably, the presence of the regular-chaotic transition is also visible in the statistics of decay rates of the open system [Tom06, Tom07, Tom08]. This is a first result for the interband coupling in the complex Bose–Hubbard model and large part of this thesis is dedicated to the study of the interband coupling in different regimes including the influence of the interparticle interaction.

Summary

This chapter is intended to serve as a background for the results in the main parts of this thesis. We shortly reviewed ongoing experiments with ultracold atoms and the amazing possibilities they give in controlling and manipulating bosonic gases in optical lattices. From this starting point, we derived the Bose–Hubbard model which will be at the focus of all following chapters. This included a short discussion of the coefficients in the Hubbard model and the effect of an external force. We found that the force effectively tilts the optical lattice and leads to an additional single-particle coupling of the different energy bands. The Bose–Hubbard model with external force is thus the lattice counterpart of continuous Wannier–Stark problem taking also inter-particle interactions into account. The complex spectral structure triggered by the external force has shortly been reviewed and will be at the center of our discussion in the following part of this thesis. The largest part will later be dedicated to the complex dynamics in the interband coupling induced by the external force and the additional effect of interactions.

Single-band Bose–Hubbard Model:

Quantum Chaos

Chapter 2

Fidelity and Avoided Crossings in the Bose–Hubbard Model

Contents

2.1 Fidelity and Avoided Crossings

The present chapter provides an example for complex spectral dynamics and we are going to study the quantum chaotic behaviour of the single-band Bose–Hubbard model under the influence of an external force. We will develop a tool to detect avoided crossings in complex spectra and apply it to the Bose–Hubbard model in order to characterise the system. The applied approach to complex dynamics will be statistical in this chapter, i.e., we are going to compare the complex spectrum of our model with predictions from random matrix theory.

This chapter is organised as follows: We start with the development of a new tool to detect and characterise avoided crossings in quantum spectra. This will be the overlap of one and the same eigenstate to slightly different Hamiltonians—the fidelity. It has previously been used for the ground state of systems undergoing quantum phase transitions. We are going to extend its use to the complete spectrum showing how and why it is useful. We will demonstrate and analyse this for several model systems. The second part of this chapter will deal with the application of this measure to the Bose–Hubbard model. We will study the crossover from regular to chaotic spectral dynamics by variation of the external force and will be able to resolve remarkable details in the statistics of avoided crossings.

2.1.1 Introduction: The Quantum Fidelity Measure

The fidelity of a quantum state—the overlap of a state with itself at slightly different parameter values—has been used in recent years as a tool to detect quantum phase transitions, i.e., an abrupt qualitative change of the system's ground state when varying an external parameter.[1] This is rather intuitive since the ground state before and after the phase transition differ strongly (often they belong to different symmetry classes) and thus their overlap should be minimal or even zero in the thermodynamic limit. However, systems in nature and in numerical simulations are finite and the overlap will not vanish completely. Instead, a phase transition in a finite system appears as an avoided crossing between the ground state and the first excited state [Sac01].[2] On the other hand, it should be possible to apply the same idea not only to the ground state but also to higher states in order to detect avoided crossings anywhere in the spectrum of a quantum system.
For instance, quantum chaotic systems intrinsically show many avoided crossings with a broad distribution of widths [Haa91, Zak91, Wan00], a manifestation of a strong coupling of many energy levels. Such a behaviour has been found in numerical studies of example systems, such as interacting spins [Ber01] or Hubbard type models [Mon93, Kol04, Kol03b]. The applicability of fidelity can indeed be lifted from pure ground-state analysis to detect and characterise avoided crossings in the entire spectrum of a complex quantum system. To do this in detail will be our agenda for this chapter. We are going to introduce the quantum fidelity measure and will study its behaviour and ability to characterise avoided crossings in simple systems and in more complex ones. We will show that it is reliable in detecting avoided crossings and can be applied locally, that is using only a small fraction of the complete spectrum. We will apply it to the one-dimensional Bose–Hubbard model with external force in the second part of this chapter to emphasize its value in application to complex systems.

Major Definitions

Let us start with a proper definition of the systems and main quantities under consideration. We consider a Hamiltonian depending on a real-valued parameter λ:

$$H(\lambda) = H_1 + \lambda H_2 \qquad \text{with} \qquad H(\lambda)|n(\lambda)\rangle = E(\lambda)|n(\lambda)\rangle, \tag{2.1.1}$$

acting on a finite-dimensional Hilbert space $\mathcal{H}$ of dimension $\dim \mathcal{H}$. To simplify the formal discussion, we assume that the levels do not show any degeneracy in the whole parameter range. This can be achieved by taking one symmetry subspace. By *fidelity* we denote the absolute value of the overlap between the n-th eigenstate of $H(\lambda)$ and $H(\lambda + \delta\lambda)$:

$$f_n(\lambda, \delta\lambda) \equiv |\langle n(\lambda)|n(\lambda + \delta\lambda)\rangle|. \tag{2.1.2}$$

The fidelity thus depends on both the value of the external parameter λ and the distance in parameter space $\delta\lambda$ between the two eigenstates to be compared. Here and in the following, we want to focus on "nearby" eigenstates, i.e., on $\delta\lambda \ll 1$. Here we assume

[1] By quantum phase transition we mean a non-analyticity of the ground state energy as a function of an external parameter in the thermodynamical limit [Sac01].

[2] This is true if the parameter-dependent and -independent part of the Hamiltonian (H_2 and H_1 in eq. (2.1.1)) do not commute [Sac01] which we will always assume in the following. If they were commuting, real crossings were possible. This can also lead to a quantum phase transition (non-analyticity of the ground state energy) in the infinite system, but the case of non-commuting parts is more common [Sac01].

that the parameter λ has been made dimensionless by an appropriate choice of units. The fidelity is an overlap between slightly different states and will thus usually be very close to one. It will differ from one only in the vicinity of an avoided crossing where the state changes abruptly.

In order to detect and characterise avoided crossings, the change of the fidelity as a function of λ is actually more interesting. Since the fidelity is usually close to one and—as we will see in a moment—is proportional to $(\delta\lambda)^2$, we introduce a function

$$S_n(\lambda, \delta\lambda) \equiv \frac{1 - f_n(\lambda, \delta\lambda)}{(\delta\lambda)^2} \tag{2.1.3}$$

which measures the change of the state $|n\rangle$. We denote S_n as *fidelity change* and we will mainly study this function instead of the fidelity, since it contains the relevant information about avoided crossings. S_n will be usually very small and differ significantly from zero only near an avoided crossing. It is also well suited for numerical studies, since one can directly compute the overlap of two states and for $\delta\lambda \ll 1$ the fidelity change is only a function of λ. Expanding the fidelity around $\delta\lambda = 0$ we see that

$$f_n(\lambda, \delta\lambda) = 1 - (\delta\lambda)^2 \frac{\partial^2 f_n}{\partial(\delta\lambda)^2} + \mathcal{O}(\delta\lambda^3). \tag{2.1.4}$$

The fidelity must have this form since the wavefunction is normalised and the fidelity must always be smaller than one. The latter excludes a linear term and forces the correction to have a negative sign. Thus, for two nearby parameter values, the newly introduced function S_n mainly gives the change of the fidelity.

The principal effect of the fidelity change S_n can be understood from perturbation theory. We simply use the second order expression for the states to expand the wave function $|n(\lambda + \delta\lambda)\rangle$ up to second order in $\delta\lambda$ [Lan81, §38]. The according textbook expression is given by

$$\begin{aligned} |n^{(2)}(\lambda + \delta\lambda)\rangle = \delta\lambda \sum_{m\neq n} \frac{H_{2,mn}}{\omega_{nm}} |m(\lambda)\rangle + (\delta\lambda)^2 \sum_{m\neq n} \sum_{k\neq n} \frac{H_{2,mk} H_{2,kn}}{\omega_{nk}\omega_{nm}} |m(\lambda)\rangle \\ - (\delta\lambda)^2 \sum_{m\neq n} \frac{H_{2,nn} H_{2,mn}}{\omega_{nm}^2} |m(\lambda)\rangle - \frac{(\delta\lambda)^2}{2} |n(\lambda)\rangle \sum_{m\neq n} \frac{|H_{2,mn}|^2}{\omega_{nm}^2}, \end{aligned} \tag{2.1.5}$$

where $H_{2,nm} = \langle m|H_2|n\rangle$ and $\omega_{nm} = E_n - E_m$ for short. Please note that there is no first order contribution to the state $|n(\lambda + \delta\lambda)\rangle$ from $|n(\lambda)\rangle$. This appears only in second order and the contribution is given by the very last term in eq. (2.1.5). Therefore only this term gives a non-zero contribution to the perturbative calculation of the fidelity $f_n = |\langle n(\lambda)|n(\lambda + \delta\lambda)\rangle|$. The expressions of ordinary perturbation theory are valid, since we assumed no actual degeneracy in the system and all of the denominators are accordingly non-zero. We compute the fidelity and thus find the first non-vanishing contribution to the fidelity change is given by

$$S_n(\lambda) = \frac{1}{2} \sum_{m\neq n} \frac{|\langle m(\lambda)|H_2|n(\lambda)\rangle|^2}{[E_n - E_m]^2} \approx \frac{|\langle n'(\lambda)|H_2|n(\lambda)\rangle|^2}{2\,[E_n - E_{n'}]^2}, \tag{2.1.6}$$

where we reduced the sum near an isolated avoided crossing to the nearest neighboring level n'. The denominator in this expression is usually large and makes S_n a small quantity.

Only close to an avoided crossing, two energy levels become nearly degenerate and the fidelity change takes on large values. The above expression for the fidelity change close to an avoided crossing has been given to serve as an illustration of how the fidelity change works. We will use it in only one situation and in all other cases compute the fidelity change numerically or fully exactly. We will furthermore give an example of nearly degenerate perturbation theory for the minimal width of an avoided crossing when discussing an extended two-level system below.

To summarise, a quantum system showing a strong coupling of levels will have many avoided crossings as a parameter λ is varied. The fidelity as the overlap between two neighbouring eigenstates will usually be close to one except at avoided crossings. The fidelity change $S_n(\lambda)$ will likewise differ from zero at these avoided crossings for a large number of λ-values in a given interval. We have now defined the main quantities of our discussion and will study them in specific systems in the following.

Connection to Loschmidt Echo

Another, closely related quantity to the fidelity introduced above is the *Loschmidt echo*, which itself is often called fidelity. We will stick to the name Loschmidt echo here, in order to distinguish it from the fidelity as defined above. The Loschmidt echo has originally been introduced in an attempt to translate the classical understanding of chaos to quantum mechanics. In classical chaotic systems, a small difference in initial states will show an exponential increase in distance between the corresponding trajectories. This cannot be directly translated to quantum mechanics, since the unitary time-evolution fixes the initial overlap for all times

$$\langle\psi(t)|\phi(t)\rangle = \langle\psi_0|U^\dagger(t)U(t)|\phi_0\rangle = \langle\psi_0|\phi_0\rangle \quad \forall t.$$

Peres introduced the Loschmidt echo in [Per84] to avoid this but at the same time transferring the idea of stability or instability against small perturbations into quantum mechanics. The idea is not to use a slight change of the initial state but of the system, i.e. the Hamiltonian. The Loschmidt echo is thus defined as the overlap between two states evolving in time according to slightly different Hamiltonians

$$M_\epsilon(t) \equiv |\langle\psi|\mathrm{e}^{\mathrm{i}H_0 t}\cdot\mathrm{e}^{-\mathrm{i}(H_0+\epsilon V)t}|\psi\rangle|^2. \tag{2.1.7}$$

However, it turned out that things are more involved and that the Loschmidt echo of chaotic systems does not generally decay faster or to lower values than of regular systems. But this quantity is still widely used and, for the sake of completeness, we would like to mention the relation to the fidelity measure used in this thesis. This can be done by either interpreting the parameter λ as a ficticious time (or take it as linearly time-dependent) or by treating it as an additional parameter and considering the time evolution of two slightly different parameter dependent Hamiltonians. The first approach would actually mean to compare one and the same wave function at different instants (t and $t+\delta t$) of its time evolution. We will not discuss this further, but the interpretation of energy levels as ficticious particles moving in time and undergoing scattering events (i.e. showing avoided crossings) is very interesting and the levels can be treated as a low dimensional gas of interacting particles, the so-called Pechukas-Yukawa gas [Haa91].

To discuss the second interpretation, we shortly rewrite our Hamiltonian and the Loschmidt echo. The small parameter should be $\delta\lambda$, such that we consider a Hamiltonian $\tilde{H}(\lambda) = H(\lambda+\delta\lambda) = H(\lambda)+\delta\lambda H_2$. The corresponding Loschmidt echo is then given

by

$$M_{\lambda,\delta\lambda}(t) \equiv |\langle\psi|\mathrm{e}^{\mathrm{i}H(\lambda)t}\cdot\mathrm{e}^{-\mathrm{i}H(\lambda+\delta\lambda)t}|\psi\rangle|^2 = \Big|\sum_{nm} c_n^*(\lambda)c_m(\lambda+\delta\lambda)\mathrm{e}^{-\mathrm{i}[E_m(\lambda+\delta\lambda)-E_n(\lambda)]t}F_{nm}(\lambda,\lambda+\delta\lambda)\Big|^2, \tag{2.1.8}$$

where $c_m = \langle m|\psi\rangle$ and we see that the overlap of any two eigenstates of the Hamiltonian at different parameter values

$$F_{nm}(\lambda,\lambda') = \langle n(\lambda)|m(\lambda')\rangle \tag{2.1.9}$$

is needed. This quantity is surely not expressable solely by the fidelity $f_n = |\langle n(\lambda)|n(\lambda+\delta\lambda)\rangle|$ introduced above. It is another measure of correlation between different eigenstates and has been studied for the three-site Bose–Hubbard model in [Hil06]. Using a diagonal approximation $\langle n|m\rangle \approx \delta_{nm}$ (as e.g. in [Per84] but see also [Hil06] for the size of off-diagonal elements) one can establish links between the overlap of any two eigenstates and the fidelity, but the fidelity and the Loschmidt echo are clearly not equivalent. For the rest of this thesis, we will not discuss the Loschmidt echo any further but focus exclusively on the fidelity $f_n(\lambda)$ and the fidelity change $S_n(\lambda)$.

2.1.2 Detection and Characterization of Avoided Crossings

Let us now apply the fidelity and the fidelity change to study avoided crossings in specific systems. We start with a simple, yet instructive two-level system and increase complexity afterwards.

Two-level System

The close encounter of two energy levels in a spectrum can be described by nearly degenerate perturbation theory, leading to an effective 2×2 system. It is also the simplest system showing an avoided crossing. We take a real symmetric Hamiltonian

$$H(\lambda) = \begin{pmatrix} -\lambda\alpha & V \\ V & \lambda\alpha \end{pmatrix} = \alpha\begin{pmatrix} -\lambda & g \\ g & \lambda \end{pmatrix} \tag{2.1.10}$$

with a real coupling $V = V^*$ between the unperturbed levels and a dimensionless coupling strength $g = V/\alpha$. Such a two-level system is also used for the RMT prediction of the width of avoided crossings (see section 1.4.3 and [Zak91]) and is therefore also an excellent starting point for our discussion. The eigenenergies are given by $E_\pm = \pm\alpha\sqrt{\lambda^2+g^2}$, and show an avoided crossing at $\lambda = 0$ of width $c = 2\alpha|g| = 2|V|$. The normalised and λ-dependent eigenstates read

$$|E_\pm(\lambda)\rangle = \frac{1}{\sqrt{(\lambda\pm\sqrt{\lambda^2+g^2})^2+g^2}}\begin{pmatrix}\lambda\pm\sqrt{\lambda^2+g^2}\\ g\end{pmatrix}. \tag{2.1.11}$$

Note that the normalization factor shows a more involved λ-dependence than the components of the vector themselves. As is well known, without requiring further symmetries, the eigenvectors can be expressed in closed analytical form for any matrix of dimension up to

four. However, the expressions become more involved for higher dimensional systems and render analytical expressions for the fidelity change very cumbersome and less useful.

To continue with the two-level system, we use the eigenstates to compute the fidelity and fidelity change. For the fidelity we can directly compute the overlap $\langle E_\pm(\lambda)|E_\pm(\lambda+\delta\lambda)\rangle$ from eq. (2.1.11) to obtain the fidelity for the two-level system:

$$f_\pm(\lambda,\delta\lambda) = \frac{g^2+\lambda(\lambda_+-\lambda)+\lambda^2+\lambda_+\sqrt{g^2+\lambda^2}+\lambda\sqrt{g^2+\lambda_+^2}+\sqrt{[g^2+\lambda^2][g^2+\lambda_+^2]}}{2\sqrt{\left[g^2+\lambda\left(\lambda\pm\sqrt{g^2+\lambda^2}\right)\right]\left[g^2+\lambda_+\left(\lambda_+\pm\sqrt{g^2+\lambda_+^2}\right)\right]}},$$

where we used the shorthand $\lambda_+ \equiv \lambda+\delta\lambda$. To obtain the fidelity change in the limit $\delta\lambda \ll 1$, we need to expand the expression for the fidelity in a power series for $\delta\lambda$ and keep only the leading term proportional to $(\delta\lambda)^2$. The final expression is the same for both eigenstates and has a surprisingly simple form [Plö10b]:

$$S_\pm(\lambda) = \frac{1}{8}\left(\frac{g}{g^2+\lambda^2}\right)^2. \tag{2.1.12}$$

This is the square of a Lorentzian and differs significantly from zero only near the avoided crossing at $\lambda = 0$. This simple analytic formula allows a closer understanding of isolated avoided crossings. For example the peak width is easily computed as $\sigma^{\mathsf{FWHM}} = 2g\sqrt{\sqrt{2}-1} \approx 1.287\ g$. The peak is of height $S_{\mathsf{max}} = 1/8g^2 = \alpha^2/2c^2$. The peak height is thus directly related to the width (i.e., the minimal distance of the levels) of the avoided crossing c. But only the dimensionless coupling strength g enters the peak height, and for the actual width $c = 2|V| = 2\alpha|g|$, the local slope of the levels α is needed. However, the peak height is still a good indicator of the actual width of the avoided crossing as we will see in further examples below. Furthermore, we see that the minimal width of an avoided crossing that can be resolved numerically, is proportional to the numerical step size δ when we sample the possible parameter values as $\lambda_l = \lambda_0 + l\cdot\delta$. The possible minimal value of the fidelity is zero, and correspondingly the maximum value for the fidelity change is $S_{\mathsf{max}} = (1-0)/\delta^2$ and the smallest width of an avoided crossing is then $c_{\mathsf{min}} = 1/\sqrt{2S_{\mathsf{max}}} = \delta/\sqrt{2}$.

Besides the minimal distance between the repelling levels, an avoided crossing can also be characterised by the ratio between the local energy level curvature $\partial_\lambda^2 E(\lambda)$ and the λ-dependent distance between the two repelling energy levels $\Delta(\lambda) = 2\alpha\sqrt{\lambda^2+g^2}$. We call the absolute value of this ratio *renormalised curvature* $C_n(\lambda)$ and find by direct computation

$$C_\pm(\lambda) \equiv \left|\frac{1}{\Delta(\lambda)}\frac{\partial^2 E_\pm(\lambda)}{\partial\lambda^2}\right| = 4S_\pm(\lambda) \tag{2.1.13}$$

for the two-level system. This means, that the fidelity change of isolated avoided crossings is determined by the ratio of the local energy level curvature and the energy level distance. For higher-dimensional systems, we expand the wave function in second order perturbation theory as before and obtain for the renormalised curvature [Pec83, Plö10b]

$$C_n(\lambda) = \left|\frac{2}{\Delta(\lambda)}\sum_{m\neq n}\frac{|\langle m(\lambda)|H_2|n(\lambda)\rangle|^2}{E_n-E_m}\right| \approx 2\frac{|\langle n'(\lambda)|H_2|n(\lambda)\rangle|^2}{[E_n-E_{n'}]^2} = 4S_n(\lambda), \tag{2.1.14}$$

where we reduced the sum near the avoided crossing to include only the next neighbour as before. The simple relation $C_n \approx 4S_n$ thus holds as long as the effect of other levels

can be neglected close to a single avoided crossing. But even in larger system this relation is approximately valid in the vicinity of avoided crossings. Below we will show both quantities for a joint avoided crossing of three energy levels. This cannot be described by an effective two-level system, but the validity of the latter relation is rather good close to the avoided crossing. It holds furthermore in the vicinity of avoided crossings of large and complex systems as was verified numerically for the Bose–Hubbard model to be discussed below [Lub09].
The two-level system will often be used as a cornerstone in the following discussion, since it allows a complete understanding of the fidelity and fidelity change and represents a good model for isolated avoided crossings in higher-dimensional systems.

Extended Two-level System

Avoided crossings in higher dimensional systems are not totally isolated, but other levels do also contribute to the evolution of a quantum state as the parameter λ is varied. Let us therefore study the effect of other levels onto a more or less isolated avoided crossing.

Consider two energy levels approaching each other as $\lambda \to 0$ and a third level being separated by a distance ε in energy and weakly coupled to the first two levels. The Hamiltonian for such a situation reads

$$H(\lambda) = \begin{pmatrix} -\lambda & g & g_{13} \\ g & \lambda & g_{23} \\ g_{13} & g_{23} & \varepsilon \end{pmatrix}, \quad g_{ij}, \varepsilon \in \mathbb{R}, \tag{2.1.15}$$

where we limited ourselves to real couplings. Since the first two levels become nearly degenerate and are well-separated from the third one, we can write this in degenerate perturbation theory (see appendix D) close to the crossing as

$$H_{\mathrm{PT}}(\lambda) = \begin{pmatrix} -\lambda + \frac{g_{13}^2}{\varepsilon} & g + \frac{g_{13}g_{23}}{\varepsilon} \\ g + \frac{g_{13}g_{23}}{\varepsilon} & \lambda + \frac{g_{23}^2}{\varepsilon} \end{pmatrix} + \mathcal{O}(\varepsilon^{-2}). \tag{2.1.16}$$

This reduces the three-level system to an effective two-level system taking the effect of the distant level perturbatively into account. The same procedure can be applied for higher dimensional systems as explained in appendix D. The result in first order is analogous for higher dimensional systems: The n-th level contributes to the diagonal elements of the encountering levels $1, 2$ with a term g_{in}^2/ε_n, where $i = 1, 2$ and ε_n is the distance to the distant n-th level, and the contribution to the off-diagonal of the effective 2×2-system is given by $g_{1n}g_{n2}/\varepsilon_n$.
The minimal distance c between the two levels of eq. (2.1.16) is thus changed by the influence of the distant third level in first order to

$$c_{\mathrm{PT}} = 2|g|\sqrt{\left(1 + \tfrac{g_{13}g_{23}}{2g\varepsilon}\right)^2 + \left(\tfrac{g_{23}^2 - g_{13}^2}{2g\varepsilon}\right)^2} \approx 2|g|\left(1 + \frac{g_{13}g_{23}}{2g\varepsilon}\right), \tag{2.1.17}$$

where we kept only the leading order behaviour. The minimal distance in an isolated avoided crossing is accordingly only slightly changed, provided that the coupling to the third level is not much larger than between the two encountering levels and that the third level is well-separated from them.

The effect on the fidelity change by inclusion of a neighbouring level can also be computed. We need to compute the eigenstates $|E_\pm(\lambda+\delta\lambda,\varepsilon)\rangle$ of eq. (2.1.16), which is easily done, and then take their overlap for slightly different parameter values to obtain the fidelity, i.e., $f_\pm(\lambda,\delta\lambda,\varepsilon) = |\langle E_\pm(\lambda,\varepsilon)|E_\pm(\lambda+\delta\lambda,\varepsilon)\rangle|$. However, their normalisation leads to very long and cumbersome expressions and refrain from showing the explicit formula here. Nevertheless, the fidelity change can be computed by taking the second derivative of the fidelity at $\delta\lambda = 0$. The full expression is very long and difficult to grasp. We therefore expand it in inverse powers of the distance to the third level ε. Including the first order correction to the simple two-level system, the fidelity change under the influence of a third not too close level is given by

$$S^{\pm}_{\mathrm{PT}}(\lambda,\varepsilon) = \frac{1}{8}\frac{g^2}{(g^2+\lambda^2)^2}\left[1 - \frac{2}{\varepsilon}\frac{(gg_{13}+\lambda g_{23})(gg_{23}-\lambda g_{13})}{g(g^2+\lambda^2)} + \mathcal{O}\left(\varepsilon^{-2}\right)\right]. \tag{2.1.18}$$

The correction due to the third level is also λ-dependent and changes the peak height at $\lambda = 0$. Let us also include the second order correction to the fidelity change at $\lambda = 0$ here

$$S^{\pm}_{\mathrm{PT}}(\lambda=0,\varepsilon) = \frac{1}{8g^2}\left[1 - \frac{2}{\varepsilon}\frac{g_{13}g_{23}}{g} - \frac{1}{2\varepsilon^2}\frac{g_{13}^4 - 8g_{13}^2g_{23}^2 + g_{23}^4}{g^2} + \mathcal{O}(\varepsilon^{-3})\right]. \tag{2.1.19}$$

If all off-diagonal matrix elements are of similar magnitude (as can be expected for instance in random matrices), the effect of the third level is characterised by its inverse distance to the avoided crossing. This underlines our claim that the effect of a third level on an avoided crossing is not too strong, provided that the level is not very close. But the latter does not take place when three levels undergo a joint avoided crossing, i.e., if there were no off-diagonal matrix elements coupling the levels they would all cross in one point. Such a situation cannot be reduced to an effective two-level system. We will study the behaviour of the fidelity change in exactly this case, where the third level cannot be considered a simple perturbation to the two-level system, i.e., when the approximation of an *isolated* avoided crossing breaks down, in the next section.

Three-level System

For very dense spectra and coupling between many levels, one can encounter a situation where three levels come together and undergo a joint avoided crossing. In an interpretation as a gas of moving particles, this corresponds to a three-body collision. Three crossing levels can be generated, e.g., by the following real symmetric Hamiltonian

$$H(\lambda) = \begin{pmatrix} -\lambda & a & b \\ a & 0 & c \\ b & c & \lambda \end{pmatrix}, \quad a,b,c \in \mathbb{R} \tag{2.1.20}$$

which generalises the above two-level system and contains already features of more complex systems. When studying spectra changing under variation of an external parameter, such an encounter of three energy levels may arise in particular in systems where many energy levels are coupled, as in quantum chaotic systems. The fidelity and fidelity change can be computed exactly, but the expressions are very long (several pages) and do not help much in understanding the fidelity's behaviour. We stick to a discussion of numerical results here.

Figure 2.1 shows that the fidelity change, defined in eq. (2.1.3), is able to detect and to distinguish two nearby avoided crossings in this system. Furthermore it resembles specific features of an avoided crossing in the shape of its peak, i.e., when two coupled levels get very close, $S_n(\lambda)$ shows a narrow peak of height $S(\lambda = 0) = 1/(8g^2)$. We see already

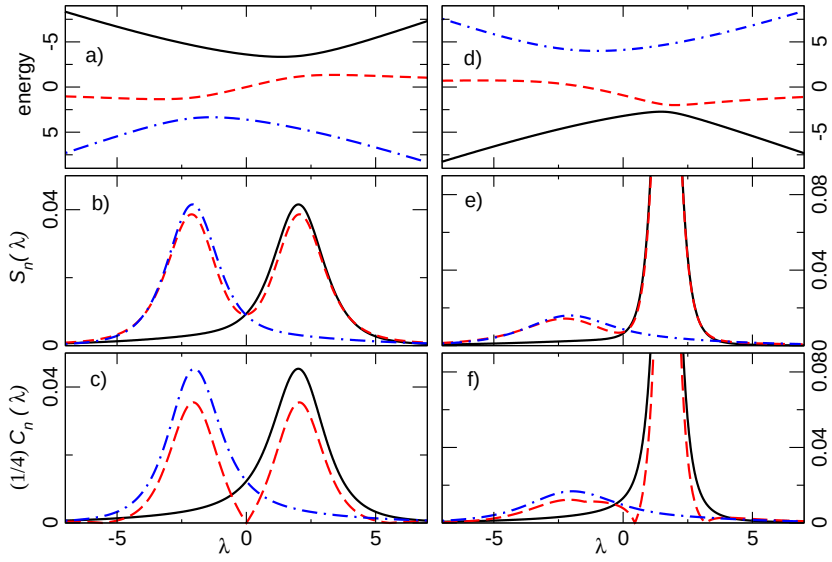

Figure 2.1: (a) Energy spectrum of eq. (2.1.20) for $a = 0, b = 2, c = 3$. All levels are coupled and the spectrum shows two close avoided crossings; (b) Fidelity change $S_n(\lambda)$ for the energy levels of (a); (c) Renormalised curvature $C_n(\lambda)$ for the energy levels of (a). (d) Energy spectrum of eq. (2.1.20) for $a = 1, b = 2, c = 3$. All three levels are now directly coupled and the spectrum shows two close avoided crossings. (e) $S_n(\lambda)$ for the energy levels of (d). (f) $C_n(\lambda)$ for the energy levels of (d).

in this simple example that the renormalised curvature captures the form of the fidelity change $S_n(\lambda)$ close to an avoided crossing [Plö10b]. Deviations arise from the admixture of a further level, which mainly effects the local curvature, i.e., the numerator in eq. (2.1.13). But it also demonstrates that the fidelity change $S(\lambda)$ itself is still effective in detecting and characterising the avoided crossings. Note again, that the three levels come very close and that the fidelity change works well in detection of avoided crossings and also that the relation $C_n = 4S_n$ is approximately valid as in two-level systems. We see that the fidelity change behaves in the vicinity of the avoided crossings as in a two-level system.

What is an Avoided Crossing?

We have not yet clearly defined what is to be understood by avoided crossing. It will turn out, that this is not completely clear and we are not aware of an unambiguous definition in the literature that could be applied under all circumstances. Usually, one speaks of a "close encounter of two energy levels without actual degeneracy" (e.g., in [Haa91]). The same idea is expressed in the definition of avoided crossing given by the compendium of chemical terminology:

> Frequently, two [...] states change their energy order as molecular geometry is changed continuously along a path. In the process their energies may become

> equal at some points (the surfaces are said to cross [. . .]), or only come relatively close (the crossing of the surfaces is said to be avoided). [McN97]

Which strongly resembles the qualitative discussion of [Haa91]. Such a prototypical situation is depicted in figure 2.2 below. On the other hand, avoided crossings appear frequently in the discussion of quantum chaotic spectra when an external parameter is varied and an example is shown in the right panel of the same figure 2.2.

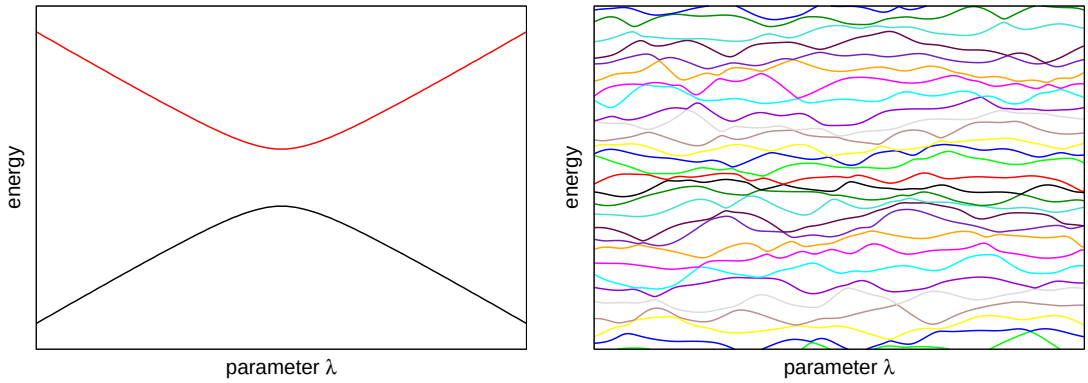

Figure 2.2: Two generic examples of avoided crossings. *Left:* Two isolated levels come close and repel each other. *Right:* Part of a quantum chaotic spectrum with many coupled energy levels showing many interacting (i.e. interdependent) avoided crossings.

An important feature seems the close approach and repulsion of both levels. But, "close" cannot mean to have a minimal distance that is smaller than the mean energy level spacing (which is the characteristic scale of for level distances). The reason is that quantum chaotic spectra typically show many avoided crossings with a broad range of distances some of them even broader than the mean level spacing (see below). Given a complex and involved spectrum of many interacting levels, it is difficult to judge by the eye, what exactly constitutes an avoided crossing.

Let us have a look at an example system and compare different definitions for avoided crossing. In the top panel of figure 2.3, we show the central part of a quantum chaotic spectrum with the central level (marked in red) undergoing several different avoided crossings. The details of the system are not important for our current discussion but will be given in the following section 2.1.3. Please note, that all level encounters in the system are avoided crossings, some not resolved on the scale of the figure.

Such pictures are typical of quantum chaotic spectra [Haa91, Zak91] but a clear definition of what constitutes an avoided crossing or how to detect it numerically are not given. We want to show that the fidelity change is useful and reliable in the numerical detection of avoided crossings. To this end, we compare two methods for detecting avoided crossings in figure 2.3. An avoided crossing is detected as

1. local maximum of the fidelity change $S_n(\lambda)$ of a state $|n(\lambda)\rangle$. This is marked by a red circle in the central panel of figure 2.3 (some beyond the scale of the figure).

2. local minimum of the energy level distance $\Delta_n(\lambda)$, where we consider $\Delta_n(\lambda) := \min\{E_{n+1}(\lambda) - E_n(\lambda), E_n(\lambda) - E_{n-1}(\lambda)\}$. This is marked by red triangles in the lower panel of figure 2.3 with the triangle pointing upwards for an avoided crossing with the upper neighbouring level and downwards for the lower neighbouring level.

In most cases (cf. figure 2.3), both criteria detect the same avoided crossings. Take for example, the very first ($\lambda \approx \pi/16$) or very last ($\lambda \approx \pi$) avoided crossings in the figure. Furthermore, they characterise the widths of the avoided crossings similarly: very narrow avoided crossings yield a very high and narrow peak in the fidelity change and a small minimal distance of the energy levels. And, inversely, broad avoided crossings lead to very small and broad peaks in the fidelity change. This is in full agreement with the expectations from the analytical treatment of the two-level system and the numerical results for the three-level system.

But the two criteria do not coincide for all possible avoided crossings. There is a minimum in the energy level distances around $\lambda \approx 5.7\,\pi/8$ where the central red level and its lower neighbour run almost parallel for some parameter values of λ. Numerically, we detect a minimum in this distance but cannot find any level repulsion in the spectrum itself. That is to say, the search for minima in the energy level distances can "detect" false avoided crossings when two levels run almost parallel for some λ-values. We observed in similar and larger spectra, that the second criterion detects usually a larger number of minima than can be attributed to actual avoided crossings in the spectrum. The fidelity, on the other hand, is not sensitive to these minima in energy level distance and detects only real avoided

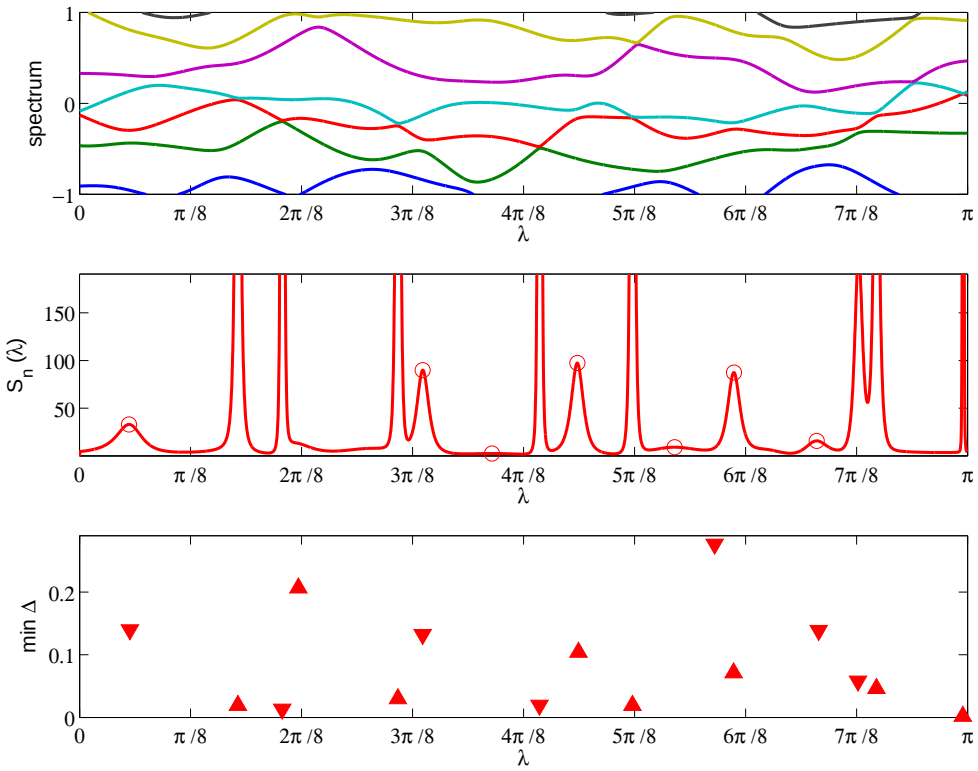

Figure 2.3: What is an avoided crossing? The upper panel shows the central part of quantum chaotic spectrum, according to eq. (2.1.21) to be defined below. The central panel shows the fidelity change $S_c(\lambda)$ for the central level in the upper spectrum (also in red). Avoided crossings undergone by the central level show up as maxima of the fidelity change (additionally marked by circles). The lower panel shows the positions and widths of minima in the energy level distance (defined in the main text) of the central level. The triangles point up- or downwards for avoided crossings with the upper or lower level, respectively.

crossings, that is when the state of the system actually changes. Taking into account that the broad avoided crossing at $\lambda = 2\,\pi/8$ is not seen by the fidelity change of the central level (since it is suppressed by the strong neighbouring peak) but by the fidelity change of the upper cyan-coloured level (its fidelity change S_{n+1} is not shown in the figure), we conclude that the fidelity change detects all actual avoided crossings that are found by the energy level distances.

The fidelity also detects avoided crossings with more remote levels. Namely, we observe two maxima in the fidelity change in figure 2.3, where the level under consideration (the red central level in the figure) has no obvious avoided crossing with any of its two nearest neighbours. This is at values of $\lambda \approx 3.7\,\pi/8$ and $5.3\,\pi/8$ in figure 2.3. Taking a closer look at the spectrum, we find that the central level is repelled from its next-to-nearest neighbour. Particularly at the first of the two instances ($\lambda \approx 3.7\,\pi/8$), the red and magenta level repel each other while the cyan level between them is changing only very slowly. It is clear that there is a significant coupling in this quantum chaotic spectrum not only between neighbouring levels but also others and this leads to avoided crossings also between these levels in the energy spectrum. Since there is a finite coupling between these levels and they repel each other, i.e., they also interchange their role slightly when encountering, we suggest to consider this as an avoided crossing too. We would like to mention that this could clearly not be detected by considering minima in the distances of neighbouring energy levels. However, one could include a search for minima between any two levels, but only at the cost of more false detections. At this point, the fidelity change presents itself as a good detector of avoided crossings in even complex energy spectra.[3] We will therefore identify avoided crossings by maxima in the fidelity change.

Summary

We introduced the fidelity as the overlap between the same eigenstate to slightly different Hamiltonians in the first part of the present chapter. We discussed it explicitly for small model systems here. It turned out, that the fidelity change is a useful quantity to detect and characterise avoided crossings numerically in these model systems, even in the case of many coupled neighbouring levels. It is more reliable than considering the minima of energy level distances. We will thus go on by studying avoided crossings as maxima of the fidelity change and will apply it to larger complex systems now.

[3] One could think of other definitions for avoided crossing, e.g. including a sign change in the first derivative of the level curvature. However, we do not want to discuss more definitions here. We mainly wanted to point at the surprising difficulties in this seemingly simple notion of avoided crossing.

2.1.3 Application to Random Matrix Model

Definition and RMT Predictions

A *highly dense* spectrum with many and possibly overlapping avoided crossings is encountered in quantum chaotic systems as described by Random Matrix Theory (RMT) [Haa91]. A prime example having such a dense complex spectrum is the parameter dependent combination of two random matrices drawn from the Gaussian orthogonal ensemble (GOE) [Haa91, Yan93]

$$H(\lambda) = H_1 \cos\lambda + H_2 \sin\lambda, \quad H_1, H_2 \in \text{GOE}. \tag{2.1.21}$$

Such a distribution is well-known in comparing RMT predictions to numerical simulations, cf. [Haa91]. Numerically, the matrices $H_{1,2}$ are obtained by creating large matrices with Gaussian distributed random numbers as entries and adding the transpose of each matrix to itself (to ensure the right symmetry). We focus on Gaussian orthogonal matrices solely since the quantum chaotic behaviour of the Bose–Hubbard model to be studied later in this chapter belongs to this universality class. The numerical implementation of other universality classes is easily possible, but does not concern the Bose–Hubbard model. Note, however, that the situation is different to the Fermi–Hubbard model with an additional external force, where other universality classes play also a role [Pon08].

We normalise the widths of avoided crossings $c \to c/\langle c\rangle$, such that $\int_0^\infty cP(c)\mathrm{d}c = 1$. The statistical distribution of widths of avoided is then given by the following Gaussian distribution (see [Zak91] and chapter 1) and the cumulative distribution function by the error function:

$$P(c) = \tfrac{2}{\pi}\,\mathrm{e}^{-c^2/\pi} \qquad \text{and} \qquad \mathrm{CDF}(c) = \mathrm{erf}\big(\tfrac{c}{\sqrt{\pi}}\big), \tag{2.1.22}$$

with $\mathrm{erf}(x) \equiv \frac{2}{\sqrt{\pi}} \int_0^x \mathrm{e}^{-t^2}\mathrm{d}t$ and $P(c)$ has also been normalised ($\int_0^\infty P(c)\mathrm{d}c = 1$).

Using our fidelity measure, we are able not only to detect the avoided crossings in such a highly correlated system but also to estimate their widths. In this way we can check the RMT prediction with high accuracy. In the vicinity of a local maximum, the fidelity change $S(\lambda)$ has a Lorentzian shape as in eq. (2.1.12) even in very dense quantum chaotic spectra. This has been demonstrated explicitly for a joint avoided crossing of three levels and in the last section, when we discussed what should be counted as an avoided crossing. The example spectrum shown, was actually produced with the model of equation (2.1.21). We can thus extract the width of the avoided crossing as $c = \sqrt{2S_{\max}}$ from the local maximum $S_{\max}$ of the fidelity change $S(\lambda)$. Again, the local slope of the levels is in principle needed to obtain the absolute value of the width, but since we normalise the widths with respect to their mean, this is not necessary to obtain the correct distribution. By averaging over many avoided crossings, the fidelity allows the verification of the RMT prediction with high accuracy [Plö10b]. In figure 2.4 we show the results from numerical diagonalisation and detection of avoided crossings for large random matrices. We observe an excellent agreement between the numerically obtained distribution of widths of avoided crossings with the help of the fidelity and the RMT prediction. This supports our use of the fidelity in order to detect and characterise avoided crossings in complex quantum systems.

Comparison of Methods

In a previous section we discussed the problems of defining and detecting avoided crossings in complex spectra (cf. figure 2.3). To further support our method in using the fidelity

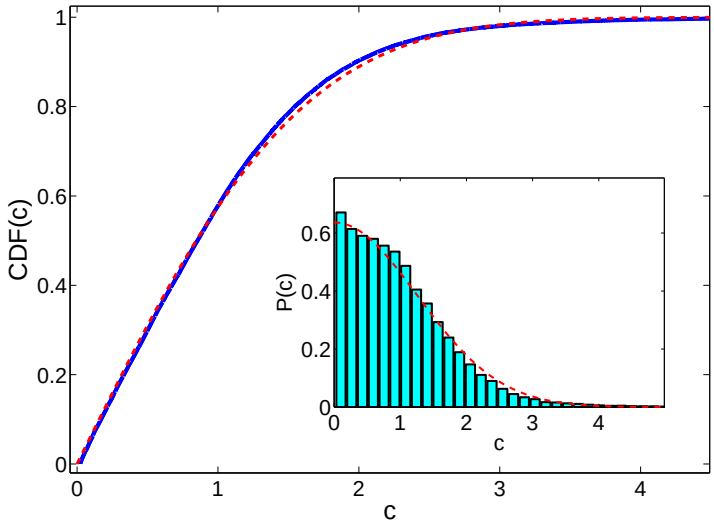

Figure 2.4: Cumulative distribution of avoided crossings determined from the fidelity change maxima for a RMT model as in eq. (2.1.21) with $\dim H_{1,2} = 1024$ and $\lambda \in [0, \pi[$ showing approx. $30,000$ avoided crossings. Shown is the numerical distribution (thick solid line) in almost perfect agreement with the RMT prediction (dashed line) $\mathrm{CDF}(c) = \int_0^c P(x)\mathrm{d}x = \mathrm{erf}(c/\sqrt{\pi})$. *Inset:* Distribution of widths of avoided crossings for the same model (histogram) and the RMT prediction (dashed line).

as a tool for both detection and characterisation of avoided crossings, we are going to compare different methods to reproduce the results from the last paragraph. As already mentioned, one can directly (and completely independent of the eigenstates) search for minima in the distance between neighbouring levels. This will, however, lead to many false detections, whenever two neighbouring levels are running more or less parallel for some λ-values. Additionally, let us compare these two methods with a third one, combining both. This consists in deciding about the presence of an avoided crossing by looking for maxima of the fidelity change as before, but taking the direct distance in the spectrum in case of detection. This has the advantage that it does not make any further assumptions concerning the distribution of local level slopes as necessary for the fidelity.

We used the same RMT model as in the last section and the results of all three methods are compared in figure 2.5. We observe the very same result with all three methods, the data closely follows the RMT prediction. There is a slight difference in the number of detected avoided crossings as expected from our earlier analysis. In the example shown in figure 2.5, there are 3614 minima in the energy level distances, but the fidelity detects only 3451 avoided crossings. We assign the difference of 4% to a false detection of avoided crossings via the energy level distances, as already seen in the example above. Particularly interesting is the comparison between the first and third method, i.e., between using only the fidelity for detection and characterisation of the crossings together with determining the width of the crossings directly from the spectrum (after detection with the fidelity). Both methods behave very similarly: the numerical data lies slightly above the RMT prediction and crosses it around $c = 1$, to lie slightly below until $c \approx 2.5$. This means that using the fidelity for determination of the (normalised) distribution of widths yields the same distribution as taking the spectral information directly. It again supports the assumptions made before and underlines the use of the fidelity in charaterising avoided crossings.

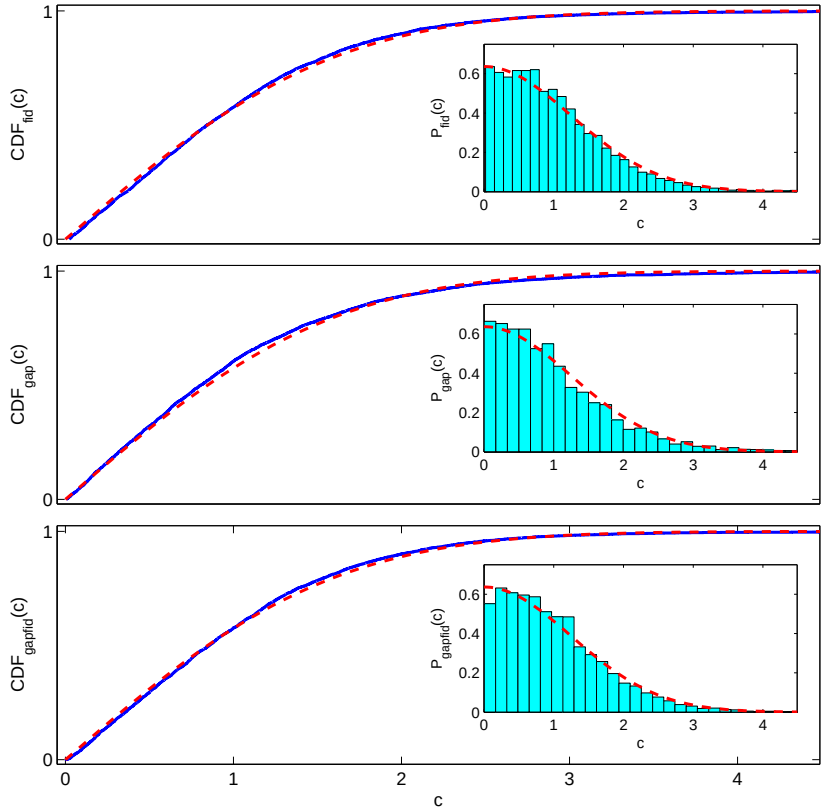

Figure 2.5: Cumulative distributions of avoided crossings detected and characterised by different methods. Shown are (top to bottom) the distribution of avoided crossings using only the fidelity change for detection and characterisation (top), using only minima in distances between neighbouring energy levels (center), and combining both methods in detecting the avoided crossings with the fidelity change but taking their width directly from the spectrum (bottom). This has been done for a RMT model as in eq. (2.1.21) with $\dim H_{1,2} = 2^8 = 256$ and $\lambda \in [0, \pi[$ (solid lines). Also shown is the RMT prediction (dashed lines) $\mathrm{CDF}(c) = \int_0^c P(x)\mathrm{d}x = \mathrm{erf}(c/\sqrt{\pi})$. *Insets:* Distribution of widths of avoided crossings for the same models (histogram) and the RMT prediction (dashed line).

Summary

In the first part of this chapter, we introduced the fidelity as overlap between one and the same eigenstate to a Hamiltonian at slightly different parameter values. We showed for different model systems that it can be used to detect avoided crossings in complex spectra. Most relevant in this context proved to be the fidelity change, which is mainly given by the second derivative of the fidelity with respect to the distance in parameter space. This quantity shows well-pronounced peaks when the eigenstate under consideration undergoes an avoided crossing. The case of a two-level system could be solved analytically and is an important cornerstone, since a near degeneracy of energy levels can be described as a two-level system in degenerate perturbation theory. Likewise, it is the basis of RMT predictions for avoided crossings. We also discussed the influence of a third level and of a joint avoided crossing by three levels. Up to now, we have established the usefulness and reliability of the fidelity when extended to the full spectra for model systems. In the following, we are going to apply it to the more complex Bose–Hubbard model.

2.2 Application to the Bose–Hubbard Model

2.2.1 Introduction

To further exemplify the value of our fidelity measures, we apply it to study the complex spectral dynamics of the one-dimensional Bose-Hubbard Hamiltonian with additional external Stark force. This example of a many-body Wannier–Stark system can be realised with ultracold atoms in optical lattices and the relevant parameters may be changed using well-known experimental techniques [Blo08b] as explained in chapter 1 of this thesis.

The tilted Bose–Hubbard model can be implemented with different boundary conditions. One can either apply a gauge transformation into the force accelerated frame of reference to restore translational invariance or keep the original reference frame and use fixed boundary conditions (also known as hard-wall boundary conditions.). The corresponding Hamiltonians read

$$H_{\text{fbc}} = -\frac{J}{2}\sum_{l=1}^{L-1}(a_{l+1}^{\dagger}a_l + \text{h.c.}) + \frac{U}{2}\sum_{l=1}^{L} n_l(n_l-1) + F\sum_{l=1}^{L} l n_l \tag{2.2.1}$$

for the case of fixed boundary conditions, and applying the gauge transformation as explained in chapter 1, the time-dependent Hamiltonian allowing periodic boundary conditions is given by

$$H_{\text{pbc}}(t) = -\frac{J}{2}\sum_{l=1}^{L}(\mathrm{e}^{\mathrm{i}Ft}a_{l+1}^{\dagger}a_l + \text{h.c.}) + \frac{U}{2}\sum_{l=1}^{L} n_l(n_l-1), \tag{2.2.2}$$

with $a_{L+1} = a_1$. In both cases $a_l^{\dagger}$ (a_l) creates (annihilates) a boson at site l and $n_l = a_l^{\dagger}a_l$ is the number of bosons at site l. The parameter J is the hopping matrix element, U the interaction energy for two atoms occupying the same site, and F the additional external force. If periodic boundary conditions are imposed for $H(t)$, the Hamiltonian and the one-period Floquet Bloch operator

$$U(T_B) = \mathcal{T}\exp\left(-\mathrm{i}\int_0^{T_B} H_{\text{pbc}}(t)\mathrm{d}t\right) \tag{2.2.3}$$

($\mathcal{T}$ denotes time-ordering) decompose into a sum of operators for specific quasimomenta κ (see [Kol03b] and section 1.4.2). The different subspaces can then be treated separately.

We will discuss the spectra of both Hamiltonians in the following and would like to point out several differences between the two. First, for fixed boundary conditions we are discussing the actual spectrum, i.e., the eigenvalues of the Hamiltonian. In the case of periodic boundary conditions we will instead use the quasienergy spectrum, that is to say, the eigenphases of the Floquet-Bloch operator. The latter are periodic and always fall into an interval $[-F/2, F/2]$. Furthermore, the number of quasienergies for a given number of atoms N and lattice sites L is smaller than the total dimension of the Hilbert space, since only a single quasimomentum subspace is discussed.

In the following, we treat the force as a parameter, independent of the original system and keep the hopping and interaction coefficients fixed. We use values $J = 0.038$ and $U = 0.032$, for which the spectrum of the Bose–Hubbard model without external force is known to be quantum chaotic [Kol04] (provided the N and L are large enough). Turning on a small external force F leads to a reordering of the (quasi-) energy levels. If all three parameters are of comparable strength, the spectrum is also chaotic [Kol04, Kol03b]. Only when the force is much larger than the other parameters ($J \approx U \ll F$) the (quasi-) energy

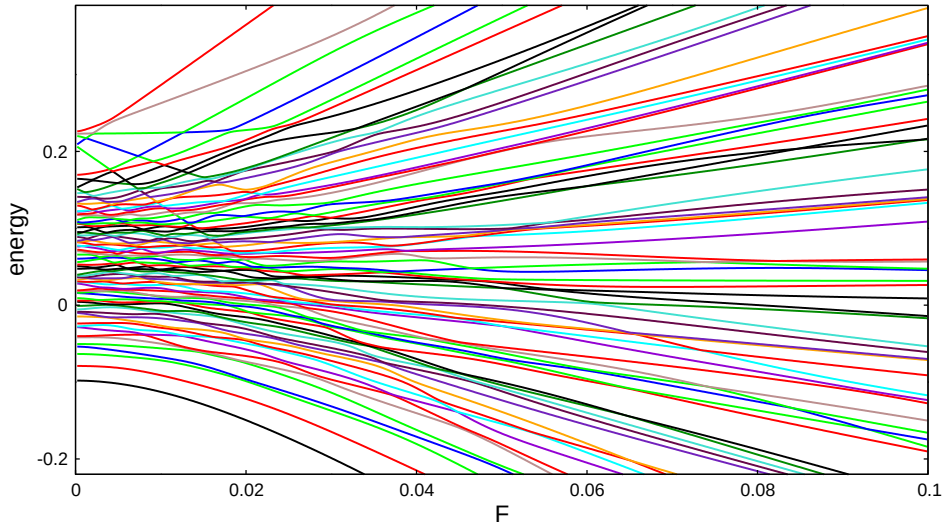

Figure 2.6: Spectrum of the Bose–Hubbard model with fixed boundary conditions, eq. (2.2.1), as a function of the external force F. For increasing force, the spectrum reorganises with single levels undergoing many avoided crossings until the force is completely dominating the spectrum. $N = 4$, $L = 5$, $J = 0.038\,, U = 0.032$.

spectrum is dominated by the external force F and the system is regular. Varying F, one observes an increasing number of avoided crossings as the spectrum is changing and additionally many broad avoided crossings as F is varied within the quantum chaotic region for either boundary conditions. Let us now have a closer look at the spectra for both types of boundary conditions.

Spectra of the Tilted Bose–Hubbard Systems

Starting with fixed boundary conditions and the spectrum of the Hamiltonian itself, we give an example of a spectrum in figure 2.6. Starting from vanishing external force, the spectrum is already quantum chaotic, i.e., it follows Wigner-Dyson statistics. An increasing external force leads to a reorganisation of the energy levels. Along this process, they come very close and show many avoided crossings of different widths (cf. the central part of the spectrum in figure 2.6 for small F). For very large values of the external force, it dominates the spectrum, no further avoided crossings take place in the spectrum of the Hamiltonian eq. (2.2.1). The reorganisation is complete. The spectrum is than given by different overlapping Wannier–Stark ladders. The total number of energy levels equals the total dimension of the Hilbert space $\dim \mathcal{H} = (N + L - 1)!/(N!(L - 1)!)$ since there is no decomposition into quasimomentum subspaces for fixed boundary conditions.

The quasienergy spectrum in the case of periodic boundary conditions is different from this. Energy levels with different slopes cannot avoid each other as the force is varied since they are restricted to a finite interval. However, since we are treating a single quasimomentum subspace, all states have the same symmetry and do not show any real crossing but only avoided crossings. We show the quasienergy spectrum of a small example system for three different ranges of the external force in figure 2.7. Note that we show the quasienergy spectrum as a function of $1/F$ to study the effect of small forces in more detail. At very

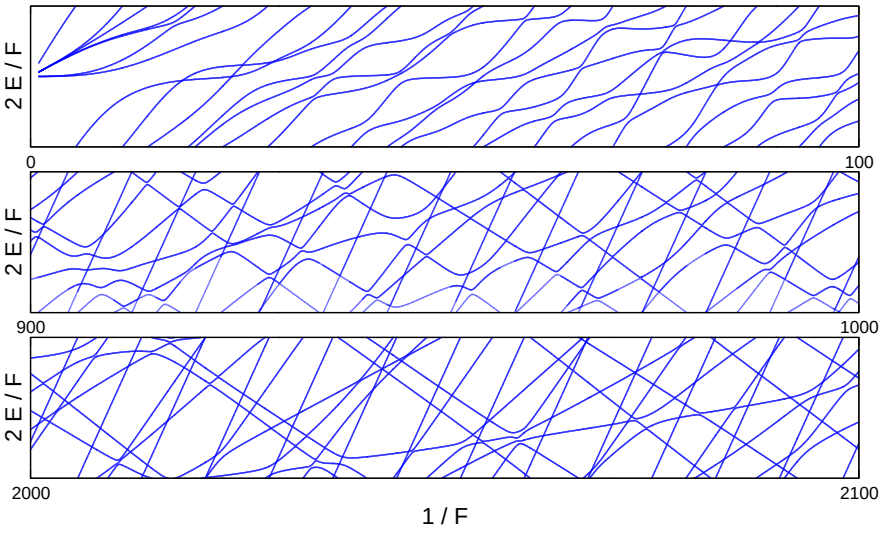

Figure 2.7: Quasienergy spectrum of the tilted Bose–Hubbard model with periodic boundary conditions, eq. (2.2.2), as a function of the external force $1/F$. Note that three very different intervals of the inverse force are shown: $1/F \in \{[0, 100], [900, 1000], [2000, 2100]\}$. For increasing force, the spectrum reorganises with single levels undergoing many avoided crossings until the force is completely dominating the spectrum. $N = 3, L = 5, \kappa = 1/5$, $J = 0.038\,, U = 0.032$. Please note, that all crossings in the figure are avoided crossings, some of them not resolved on the scale of the figure.

large force, the quasienergies are dominated by the external force as expected. When the force is further reduced, the interaction and hopping play a stronger role and the spectrum reorganises showing several avoided crossings. When the force is very small (second to third panel in figure 2.7) this reorganisation is basically completed and one observes several straight lines showing rather small avoided crossings when approaching each other. Again, since all levels have the same symmetry but are restricted to traverse a finite region periodically, they cannot avert undergoing small avoided crossings. Surprisingly, and in contrast to the tilted Bose–Hubbard model with fixed boundary conditions, the spectrum thus shows many avoided crossings even for very small values of the external force, i.e. for large $1/F$. An even further reduction of the force (increase of $1/F$) leads to smaller avoided crossings but the spectrum stays qualitatively the same. This difference will become clearer when studying the number of avoided crossings in a given interval below.

Comparing both spectra leads to the conclusion, that the number of avoided crossings in the spectra should go to zero when the external force is decreasing for fixed boundary conditions but not for periodic boundary conditions. This means, we should observe avoided crossings in the quasienergy spectrum for arbitrary small forces. This will be shown in the next section by using the fidelity to detect avoided crossings in both cases. But first we would like to discuss the detection of avoided crossings in the tilted Bose–Hubbard model with either boundary conditions.

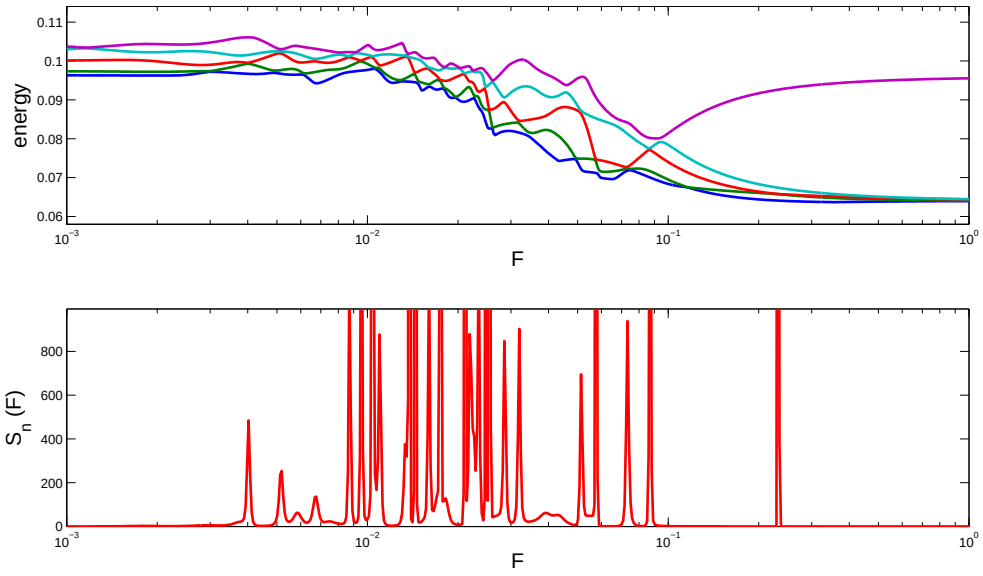

Figure 2.8: Detection of avoided crossings in the tilted Bose–Hubbard model with fixed boundary conditions. Shown is the central part of the spectrum of at tilted Bose–Hubbard model with $N = 5 = L$ for varying external force (top panel). The fidelity change detects the avoided crossings of the central level. Parameters: $J = 0.038$, $U = 0.032$

Detection of Avoided Crossings

In section 2.1.2, we showed how the fidelity or the fidelity change are able to detect avoided crossings in small model systems and in large complex random matrix models. We are now going to do the same for our complex many-body system: the tilted Bose–Hubbard model. In the case of fixed boundary conditions the implementation is straightforward and one simply needs to compute the overlap between an eigenstate to slightly different Hamiltonians in order to obtain the fidelity and fidelity change of the given eigenstate. An example for a level from the central part of the energy spectrum is shown over a broad range of external forces in figure 2.8. As discussed already, the level undergoes many avoided crossings as the spectrum is reorganising along the transition from vanishing to dominating external force F. As before, the fidelity change readily detects avoided crossings and the height of the peak corresponds to the widths of the specific avoided crossing. The spectrum shows a large number of avoided crossings for intermediate values of the external force, when the reordering concerns many levels simultaneously.

The situation is more involved for the quasienergy spectrum of the Floquet-Bloch operator. Since the eigenphases are periodic with period $\omega_B = F$ they do not have a clear order and one cannot speak of the n-th eigenstate in general. However, when varying the external parameter slowly, one can follow a given state, since its quasienergy will also vary only slowly. It that sense, one always has to look for close quasienergies at neighbouring parameter values in order to follow a certain state and compute the fidelity or fidelity change of that state. Specific care has to be taken, when the state under consideration approaches the boundary of the accessible energy interval and jumps by F. We demonstrate that this is possible in figure 2.9, where we follow one quasienergy level of the tilted Bose–Hubbard model undergoing avoided crossings. These are detected by the fidelity change, shown in

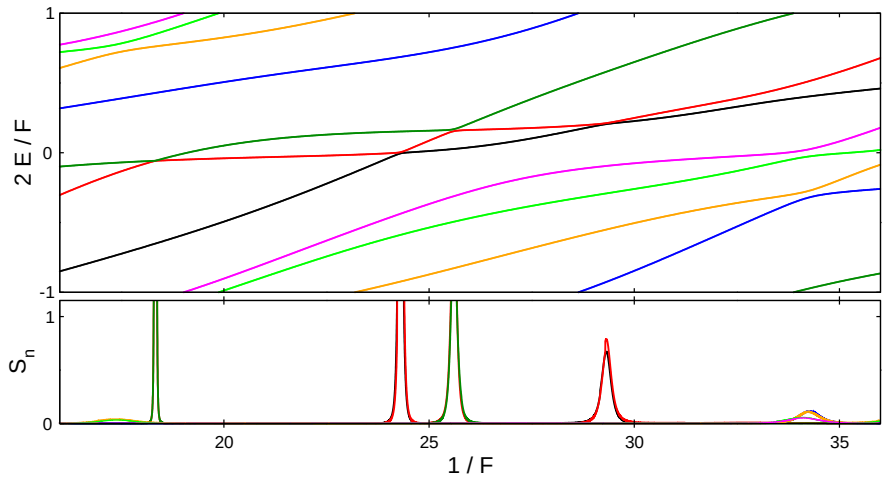

Figure 2.9: Detection of avoided crossings in the quasienergy spectrum of the tilted Bose–Hubbard model with periodic boundary conditions. The upper panel shows the quasienergy spectrum normalised to the interval $[-1, 1]$. The different levels are marked by their colour and undergo avoided crossings. The lower panel shows the fidelity change for each level in the same colour as the level in the top panel. Avoided crossings in the spectrum lead to clear peaks in the fidelity change. We are able to follow a single level, even when it crosses the interval boundary and the order of levels changes. Parameters: $J = 0.038$, $U = 0.032$, $N = 3$, $L = 5$, $\kappa = 1/5$.

the same figure. We see that the fidelity is able to detect avoided crossings in the spectrum of the tilted Bose–Hubbard model. We are now going to use this to test our expectations concerning the number of avoided crossings for different strengths of the external force for either boundary conditions.

2.2.2 Density of Avoided Crossings

To illustrate the crossover between regions with few and many avoided crossings, we study the density of avoided crossings as detected by the fidelity change S_n, when changing the system parameter λ. In a histogram, the density of avoided crossings $\rho_{\mathrm{AC}}(\lambda)$ is defined via

$$\rho_{\mathrm{AC}}(\lambda) \cdot d\lambda = N_{\mathrm{AC}}(\lambda)/\dim\mathcal{H}, \tag{2.2.4}$$

comparing the number of avoided crossings $N_{\mathrm{AC}}(\lambda)$ in the interval $[\lambda, \lambda + d\lambda]$ to the total number of energy levels $\dim\mathcal{H}$. This is shown for the tilted Bose–Hubbard model with periodic boundary conditions in the main part of figure 2.10. We observe no avoided crossings at large F, i.e., small values of $1/F$, and an increasing number of avoided crossings that saturates around $1/F \approx 20$.

The transition between regular and chaotic spectral properties for $J \approx U$ and $F \ll J$ and approximately integer filling in the tilted system can be visualised by comparing the actual level spacing distribution to a Wigner-Dyson distribution using a standard statistical χ^2-test as described in appendix A (see also [Tom07]). This is displayed in the inset of figure 2.10 along with the density of avoided crossings in figure 2.10. The fidelity change $S(1/F)$ detects avoided crossings and marks the crossover from regular to chaotic dynamics, showing the same qualitative behaviour as the spectral statistics: in regions of good Wigner-Dyson statistics we find a high density of avoided crossings compared to a

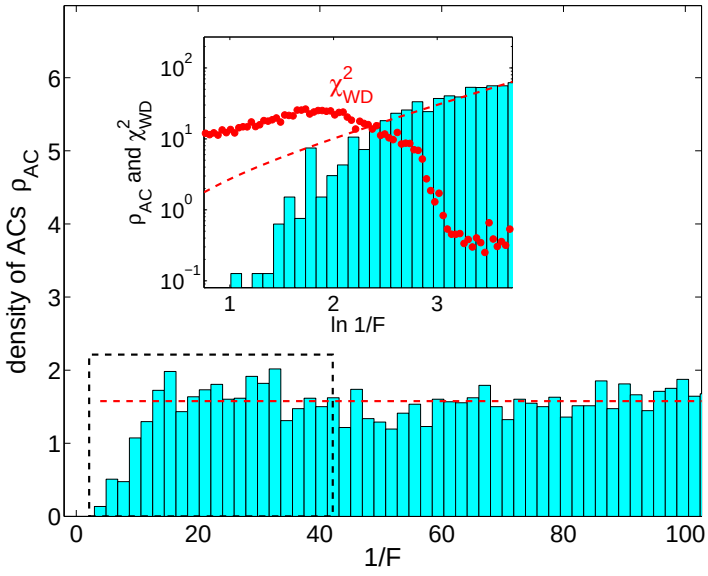

Figure 2.10: Density of avoided crossings ρ_{AC} in the quasienergy spectrum of the Floquet operator for varying external force F. Parameters: $J = 0.038$, $U = 0.032$, $N = 6, L = 6$. The number of avoided crossings as detected by the fidelity change increases with $1/F$ and saturates around $1/F \approx 20$ to an average value which is shown by the dashed line. *Inset:* Magnification of the region marked by the box on logarithmic scale with a comparison to a χ^2-test (with small values for good Wigner-Dyson statistics).

smaller number of avoided crossings in the regular regime. Please be aware that *a large number of avoided crossings alone is not a criterion for quantum chaotic behaviour*, instead the avoided crossings need to follow RMT predictions as we will discuss below. We show the density of avoided crossings here, only to illustrate the crossover from few to many avoided crossings and to exemplify our fidelity measure.

The mentioned crossover begins for $\log(1/F) \approx 2$, where the density of avoided crossings rises above unity, i.e., on average each energy level undergoes more than one avoided crossing in the unit interval. The transition is complete for $\log(1/F) \approx 3$ where the χ^2-test saturates around a low value. Let us emphasize again that the density of avoided crossings itself is *not* a criterion to distinguish regular level dynamics from chaotic. We only show the density of avoided crossings to underpin the successful detection of avoided crossings by the fidelity and to understand how the spectrum changes when the external force is varied.

In figure 2.10, we compare histrograms with equally spaced binning for a linear (main figure) and logarithmic (inset) abscissa. Note, that the difference between the two: A constant density in equally spaced bins on a linear abscissa will be exponentially growing when shown on a logarithmic abscissa. This can be understood by a short calculation. If the number of avoided crossings in an interval of length Δf, with $f \equiv 1/F$ is given by a constant value N_{AC}, the density of avoided crossings in that interval will also be constant:

$$\bar{\rho}_{\mathsf{AC}} = \frac{1}{\dim \mathcal{H}} \frac{\Delta N_{\mathsf{AC}}(f)}{\Delta f} \longrightarrow \frac{\mathrm{d}N_{\mathsf{AC}}}{\mathrm{d}f} = \frac{1}{f} \frac{\mathrm{d}N_{\mathsf{AC}}}{\mathrm{d}\ln f} = \mathrm{e}^{-l} \frac{\mathrm{d}N_{\mathsf{AC}}}{\mathrm{d}l}, \text{ with } \quad l \equiv \ln f. \tag{2.2.5}$$

To obtain the density as a function of $l = \ln f$, we simply solve this differential equation and

obtain an *increasing* density of avoided crossings when plotted as a function of $l = \ln 1/F$:

$$\int_0^l \bar{\rho}_{\mathrm{AC}}\, \mathrm{e}^{l'}\, \mathrm{d}l' = \int_0^{N_{\mathrm{AC}}} \mathrm{d}N_{\mathrm{AC}} \qquad \Longrightarrow \qquad N_{\mathrm{AC}}(l) = \bar{\rho}_{\mathrm{AC}} \cdot (\mathrm{e}^l - 1). \tag{2.2.6}$$

In this way, we have translated the approached constant density of avoided crossings to a logarithmic abscissa in figure 2.10. The density is increasing for large values of $\ln 1/F$, but follows the predicted value very closely.

Turning to the Hamiltonian we fixed boundary conditions we expect a different behaviour of the density of avoided crossings for very large or very small values of the external force: it should vanish, since the spectrum does not show any avoided crossings in either regime. This is demonstrated in the top left panel of figure 2.11.

An additional advantage of the fidelity change compared to spectral statistics is that it can be applied *locally* in the spectrum. This means that, if one is interested only in local spectral properties of a system (concerning only a limited number of states), it is sufficient to follow a small number of levels to characterise the system's behaviour and to obtain the same information as encoded in other methods, e.g., spectral statistics. To support this idea, we have studied the density of avoided crossings in the tilted Bose–Hubbard model with fixed boundary conditions of the complete spectrum and within different parts of the spectrum. Figure 2.11 shows the different densities of avoided crossings.

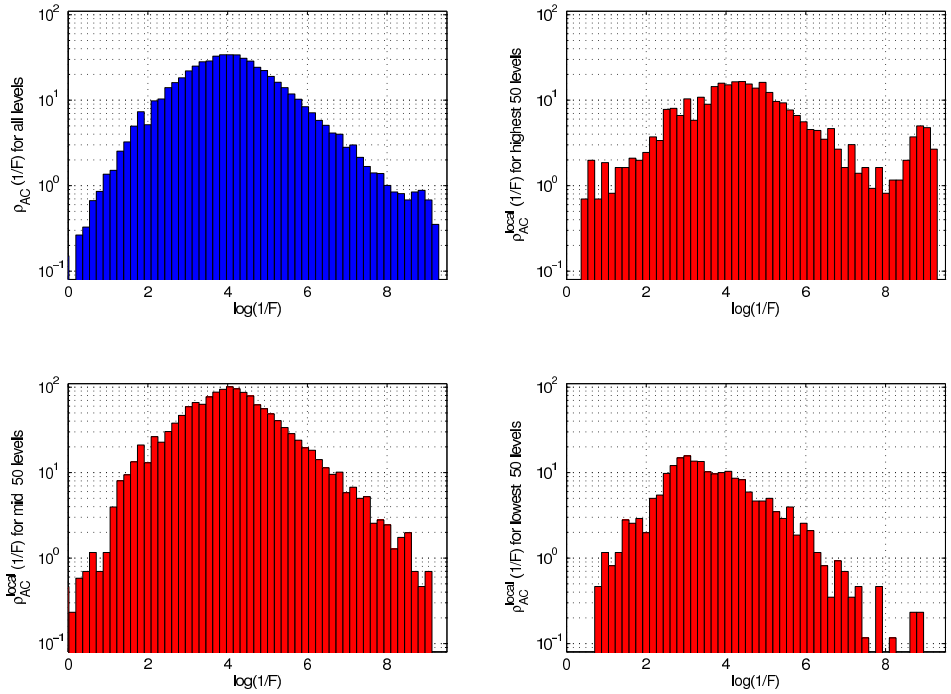

Figure 2.11: Density of avoided crossings in the tilted Bose–Hubbard model with fixed boundary conditions as a function of $0 < \log(1/F) < 10$ (corresponding to $1 > F > 10^{-5}$) for $L = 6 = N$. *upper left:* Density of avoided crossings for the whole spectrum; *upper right:* for the highest 50 levels; *lower left:* for 50 levels from the center of the spectrum; *lower right:* for the lowest 50 levels. We see that the total density of avoided crossings is dominated by the center of the spectrum. It is therefore possible to learn a lot about the system by studying a relatively small number of levels from the center.

We compare the densities of avoided crossings in a system of size $L = 6 = N$ (i.e. $\dim \mathcal{H} = 1716$) within different regions of the spectrum. First of all, one recognizes the expected effect from the reorganisation of the spectrum in the density of avoided crossings in the whole spectrum and in all parts of it: For completely dominating force ($1/F$ close to zero) and for almost vanishing force ($1/F \gg 1$) there are no avoided crossings in the energy spectrum. In between, the spectrum reorganises and the single levels undergo many avoided crossings in this process. The density starts to increase around $\log(1/F) \approx 0$ (corresponding to $F \approx 1$), where the Wannier–Stark ladder begins to get disturbed. There is a maximum in the density of avoided crossings at $\log(1/F) = 4.2$ or $F = 0.015 \approx U/2 \approx J/2$, after which the density starts to decrease again. This is clearly visible in the density of avoided crossings for the total spectrum (top left panel of the figure). The other panels show the density of avoided crossings for only 50 levels from the center, the bottom or the top of the spectrum. We observe that the highest contribution to the density of avoided crossings is clearly from the center of the spectrum where the spectral density is also the highest.

However, one can clearly say that the overall behaviour of the density of avoided crossings in this complex many-body model is strongly indicated already by a very limited number of states from the center: 50 out of 1716, i.e., only 3% in the example shown in the figure. This property can be useful in different contexts or possible applications. Experimentally, not the complete spectrum might be accessible, but only a few states. Then it is interesting to gain as much knowledge as possible from the evolution of a limited number of states. Furthermore, it can be of numerical advantage to consider only a few states. Using, e.g., the Lanczos-algorithm, one can quickly diagonalise a small part of a given Hamiltonian for different parameter values and thus compute the fidelity of even large systems to gain a good understanding of the overall spectral behaviour.

2.2.3 Characterising the System by Avoided Crossings

In the previous section, we discussed the density of avoided crossings in the tilted Bose–Hubbard model as detected by our fidelity measure. But the density itself does not yet tell us whether the system is chaotic or regular. The densities are clearly interesting in order to understand how the system evolves from one dynamical regime into an other and they showed that the fidelity is well able to detect avoided crossings in a dense and complex spectrum. However, in this section we are going to use the information contained in the fidelity to characterise the overall spectral behaviour of the different systems. The tilted Bose–Hubbard model is regular for an arbitrary number of particles when limited to only two lattice sites [Lin06]. On the other hand, it is known to be quantum chaotic for a higher number of lattice sites and approximately integer filling [Kol04]. The two regimes can also be distinguished by studying the distribution (of widths) of avoided crossings. We are going to show that it is possible to do this by using the fidelity when applied to the complete spectrum.

Integrable Double Well

The Bose–Hubbard model restricted to two lattice sites $L = 2$ is also known as the Bose–Hubbard dimer and is in fact integrable [Mil97, Lin06]. The Hamiltonian reads

$$\mathcal{H} = \frac{1}{2}\Big[U(n_1^2 + n_2^2) + (2\epsilon_1 - U)n_1 + (2\epsilon_2 - U)n_2 - J(a_1^\dagger a_2 + a_2^\dagger a_1)\Big] \tag{2.2.7}$$

and can be mapped to a spin system by introducing the Jordan-Schwinger realisation of the $SU(2)$ algebra [Fra01]:

$$S_1 = \frac{a_1 a_2^\dagger + a_2 a_1^\dagger}{2}, \quad S_2 = \frac{a_1 a_2^\dagger - a_2 a_1^\dagger}{2}, \quad S_3 = \frac{n_1 - n_2}{2}. \tag{2.2.8}$$

Introducing a fourth operator $S_4 = (n_1 + n_2)/2$ which corresponds to the total angular momentum according to $S_1^2 + S_2^2 + S_3^2 = S_4(S_4 + 1)$, we see that $n_1 = S_4 - S_3$ and $n_2 = S_4 + S_3$. In terms of these spin operators, the Hamiltonian takes the nonlinear form

$$\mathcal{H} = 2US_4(S_4 - 1) + 2US_3^2 - 2TS_1 + \frac{\epsilon_2 + \epsilon_1}{2} S_4 + \frac{\epsilon_2 - \epsilon_1}{2} S_3, \tag{2.2.9}$$

and the integrability by Bethe ansatz methods can be shown rigorously [Lin06, Fra01] with the help of these spin operators. The dimension of the Hilbert space is $N + 1$, where N is the total number of particles. The Fock basis is easily written down, by starting with all particles in the left well, and successively transferring particles to the other well.

The integrability of this many-body system is particularly interesting for our study of avoided crossings. Namely, the pure absence of avoided crossings is not necessarily a characteristic feature of an integrable system. Instead, an integrable system can have avoided crossings, but they appear in a regular fashion and the width of the avoided crossings will always be very small [Zak91]. Here small means to be smaller than the mean level spacing.

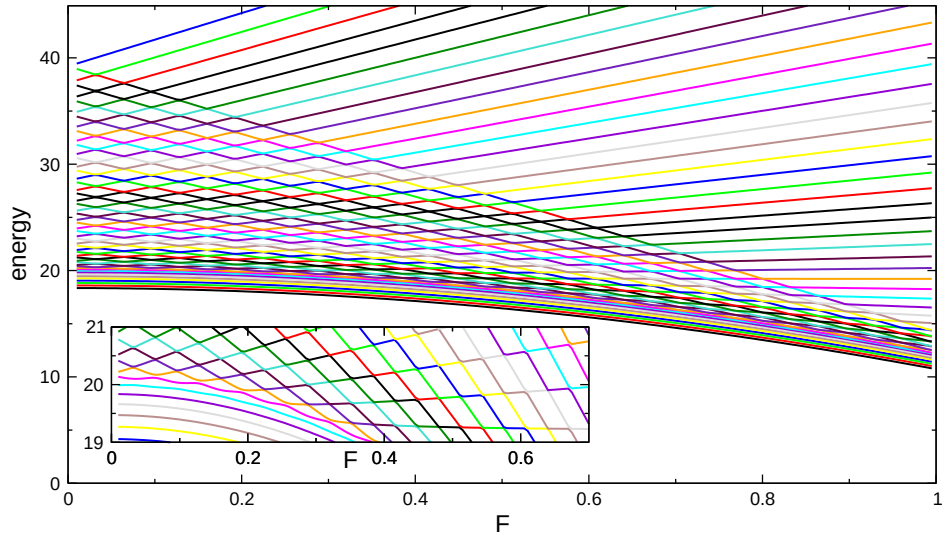

Figure 2.12: Regular spectrum of integrable double well Bose–Hubbard system as a function of the external force F. The spectrum consists of $N + 1$ levels that show a very regular structure with many tiny avoided crossings. Parameters: $N = 50$, $J = 0.038$, $U = 0.032$.

We show an example spectrum of the integrable Bose–Hubbard dimer in figure 2.12. We chose a spectrum for 50 particles (and 51 energy levels) to make the spectrum not too involved and show it as a function of the external force. We find that the spectrum of the tilted doublewell system is indeed very regular. It shows many small avoided crossings that are distributed in a regular fashion. For very large values of the external force these crossings cease and the spectrum is given by the Wannier–Stark ladder.

One observes that the structure of the spectrum changes for fixed F above certain energy values. Below an energy E_c the levels are well separated and do not show avoided crossings (cf. the inset of figure 2.12), whereas above, they attract and repel each other alternatingly when the external force is varied. A part of this crossover in the spectral structure is shown in the inset of the main figure. This crossover is a remainder from the spectral structure of the integrable dimer without external force, the so-called symmetric dimer [Aub96]. The energy eigenvalues come in pairs $E^{\pm}$ that are degenerate for $J \to 0$ [Aub96]. By increasing J, this degeneracy is lifted and the structure of the spectrum changes around a certain J-dependent energy [Fra01]. Since the system is integrable for arbitrary values of N, it is natural to treat the limit of high filling by a mean-field analysis. It turns out that the related classical system (as defined in [Aub96]) has a separatrix at the same energy value. Interestingly, reminiscents of this integrable behaviour are also present in this case of three lattices sites, in the Bose–Hubbard trimer [Buo04] and one finds a similar transition in the spectrum even for higher numbers of lattice sites which to our knowledge has not yet been analysed in the literature.

Having found avoided crossings in the spectrum of the integrable dimer, we can analyse them using the fidelity in order to compare the distribution of widths with the RMT predictions. Since the avoided crossings all have a width that is smaller than the average level spacing, one expects a δ-like distribution. This is verified for the integrable double well with the help of our fidelity measure in figure 2.13.

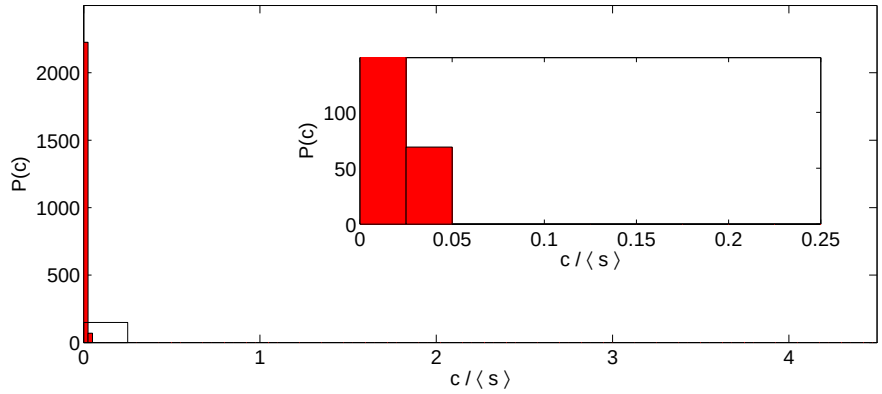

Figure 2.13: Distribution of avoided crossings in the integrable Bose–Hubbard dimer. The width of the avoided crossings c is very small compared to the mean level spacing $\langle s \rangle$ such that their distribution is δ-like with a sharp peak at zero. This distribution has been obtained for a double well Bose–Hubbard model with $N = 100$, $J = 0.038$, $U = 0.032$ and $F \in [0, 1]$. The histrogram reveals that over 2000 avoided crossings were found. The tiny fraction of larger c's stems from avoided crossings close to the levels not showing any avoided crossings at all (see the inset of figure 2.12).

The widths of avoided crossings are tiny compared to the mean level spacing and all of the same value except for a very small fraction that is slightly broader. Their contribution is shown in the inset of figure 2.13 and stems from the avoided crossings shown in the magnification of the double well spectrum above (figure 2.12). We conclude that the integrable double well shows avoided crossings that follow the corresponding RMT prediction. The fidelity is able to detect them and to verify the RMT prediction. Let us now come to the more complex case of the chaotic regime for the tilted Bose–Hubbard model.

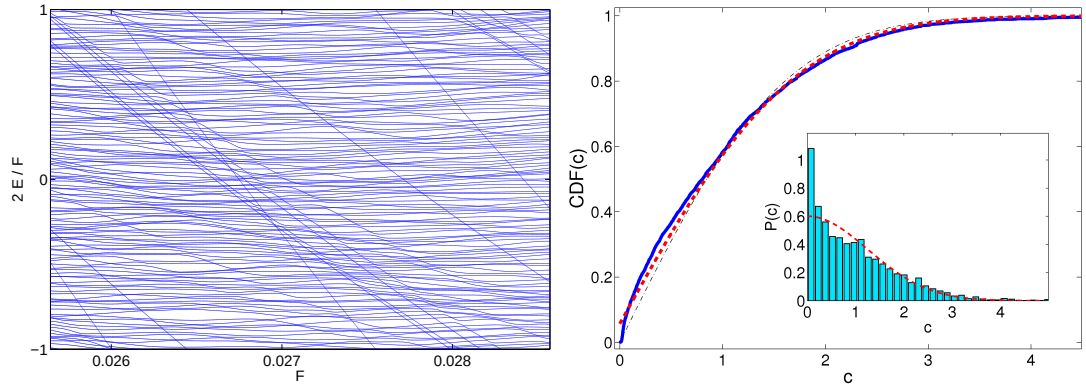

Figure 2.14: *Left:* Solitonic levels in the complex spectrum of the tilted Bose–Hubbard model with periodic boundary conditions. Shown is the spectrum at small F for $N = 6$ bosons in $L = 7$ lattice sites ($J = 0.038$, $U = 0.032$, $\kappa = 1/7$). Within the chaotic sea of energy levels are a few straight lines traversing the chaotic background.
Right: Cumulative distribution of avoided crossings determined from the fidelity change maxima for the model of eq. (2.2.2). Shown is the numerical distribution (thick solid line), the best fit for a mixed RMT spectrum (thick dashed line, and chaotic part $\gamma = 0.943$), and the RMT prediction for a purely chaotic spectrum (thin dashed dotted line). Parameters: $N = 6, L = 7, J = 0.038, U = 0.032, F = 1/39 \ldots 1/35 = 0.0256 \ldots 0.0286$. *Inset:* Distribution of widths of avoided crossings for the same model (histogram) and the best fit for a mixed RMT prediction (dashed line). The enhancement peak close $c = 0$ arises from the regular "solitonic" states in the spectrum.

Chaotic Regime and Detection of Solitonic Levels

As found by [Kol03b] and discussed in chapter 1, the tilted Bose–Hubbard (for approximate unit filling) shows quantum chaotic behaviour whenever hopping, interaction and the external force are of comparable strength. We will verify RMT predictions for this quantum chaotic regime in this section by making use of our fidelity measure.

In the left panel of figure 2.14, we show another example of the chaotic spectrum with many levels undergoing avoided crossings of different widths as the external force is varied. For better visibility we have removed an overall linear trend in the figure and shifted the quasienergies to the interval $[-F/2, F/2]$. As discussed earlier, the fidelity allows to follow levels through the spectrum and to study the spectrum locally. On the other hand, it means if we follow all energy levels over a certain parameter range, we can resolve remarkable details in the full spectrum. This is done by using the fidelity change in order to detect and characterise avoided crossings. With this method we are able to resolve the small number of regular states [Ven10] moving on top of the chaotic background and crossing it unperturbed [Plö10b]. These levels are clearly visible in the spectrum and have been coined "solitonic" by Venzl *et al.* [Ven10]:

> "In analogy to solitonic water waves that run through other waves without loosing their shape, we call the states that correspond to these levels solitonic states [Ven10]."

The corresponding distribution of avoided crossings is shown in the right panel of figure 2.14. It has been obtained by detecting and characterising the avoided crossings by the fidelity. The distribution is very close to the RMT prediction for a purely chaotic system but it

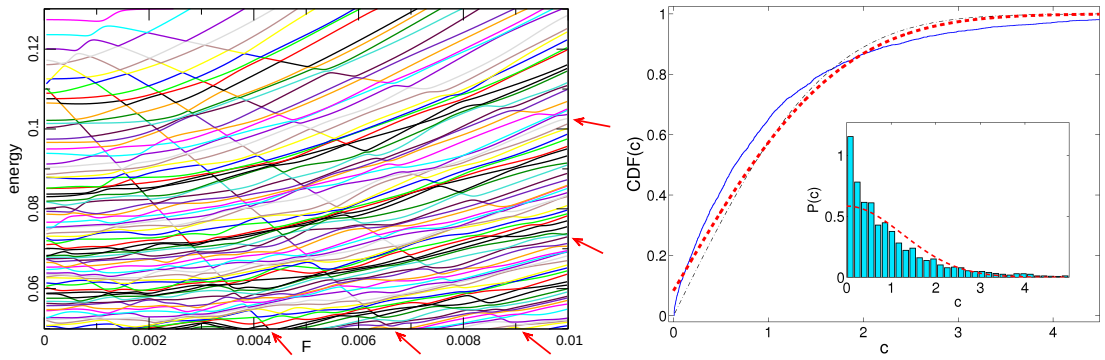

Figure 2.15: *Left:* Solitonic levels in the complex spectrum of the tilted Bose–Hubbard model with fixed boundary conditions. Shown is a section of the highest part of the spectrum at small F for $N = 3$ bosons in $L = 11$ lattice sites ($J = 0.038, U = 0.032$). Within the chaotic sea of energy levels are a few straight lines (marked by the red arrows) traversing the chaotic background.
Right: Cumulative distribution of avoided crossings determined from the fidelity change maxima for the titled Bose–Hubbard model. Shown is the numerical distribution (thick solid line), the best fit for a mixed RMT spectrum (thick dashed line, and chaotic part $\gamma = 0.884$), and the RMT prediction for a purely chaotic spectrum (thin dashed dotted line). Parameters: $N = 5, L = 6, J = 0.038, U = 0.032, F = 0.01 \ldots 0.02$. *Inset:* Distribution of widths of avoided crossings for the same model (histogram) and the best fit for a mixed RMT prediction (dashed line). The enhancement peak close $c = 0$ arises from the regular "solitonic" states in the spectrum.

shows a slight deviation from the purely chaotic case coming from the admixture of regular levels. In this case the distribution of widths of avoided crossings is the mixture between the regular and quantum chaotic distributions

$$P(c) = (1-\gamma)\delta(c) + \frac{2\gamma^2}{\pi\bar{c}} \exp\left[-\frac{\gamma^2 c^2}{\pi\bar{c}^2}\right], \tag{2.2.10}$$

with a chaotic part of weight $0 \leq \gamma \leq 1$ [Yan93]. A finite regular component makes it self visible as a strong enhancement of $P(c)$ close to zero, cf. the inset of figure 2.14. We are also able to estimate the size of this component by analysing the cumulative distribution function

$$\mathrm{CDF}(c) = 1 - \gamma + \gamma \,\mathrm{erf}\left(\frac{\gamma c}{\sqrt{\pi}}\right). \tag{2.2.11}$$

The result is shown in the right panel of figure 2.14 where we plot the numerically obtained distribution and the best χ^2-fit including a finite regular component. We obtain a chaotic part of $\gamma = 0.943$, in good agreement with counting only 8 regular levels out of 132 by direct inspection of the spectrum. Except for the identification of single regular levels [Ven10], this has so far not been detected in the tilted Bose–Hubbard model by other statistical measures and underlines the value of the fidelity change as a quantity to detect avoided crossings with high resolution in complex energy spectra [Plö10b].

We can perform a similar analysis in the tilted Bose–Hubbard model with fixed boundary conditions. A section of the spectrum of this system is shown in the left panel of figure 2.15 where the solitonic levels have been marked by arrows for better identification. Again, one observes a few number of levels moving almost unperturbed on top of a chaotic background. These can again be detected using the fidelity by studying the distribution of avoided

crossings. This is shown in the right panel of figure 2.15 where we observe a deviation from the purely chaotic distribution due to the finite regular component of the spectrum. Using a statistical χ^2-test we can estimate the size of this regular component. The best χ^2-fit yields $\gamma = 0.884$ which amounts to 11.6% of regular levels.

There is a difficulty in comparing the statistically detected number of regular levels to a direct inspection of the spectrum. There, the regular levels can be identified by their ability to traverse the other levels without being altered. According to [Ven10], these levels are almost identical to Fock basis states with all particles occupying the same lattice site, e.g. $|00003\rangle$ for three atoms on five sites (meaning that one coefficient is dominating the expansion of this eigenstate). These levels have a high energy and show a strong linear behaviour when varying the external force (cf. figure 2.15). However, since they are located above most of the other levels for $F = 0$ and some of them have positive slope (not shown in the figure), they will only move away from the large number of chaotic levels and will not cross them. This means they are neither detectable by the eye nor by the shape of the avoided crossings as detected, e.g., by the fidelity. In the example shown above, there are $\dim \mathcal{H} = 286$ levels altogether, such that the spectrum should contain 33 regular levels. Some of them are easily identified and have been marked by arrows in the figure. A closer inspection reveals more levels showing very small crossings and a straight traversing of other levels. There are several energy levels starting at $F = 0$ with energies between 0.09 and 0.11 that show such a behaviour. We expect that these levels should also show higher occupancy of single lattice sites as the solitonic levels identified in [Ven10] do. This could be tested by analysing their distribution over the Fock basis (e.g. by studying the expansion coefficients or measures as the inverse participation ratio in the Fock basis) and by studying their properties before and after avoided crossings. Nevertheless, we obtain qualitatively the same results for either boundary conditions: When all parameters are of comparable size, the system exhibits quantum chaotic behaviour with a few regular levels on top.

2.3 Summary

We showed that quantum fidelity is perfectly suited to detect and characterise avoided crossings in the energy spectrum. It therefore connects information about the wave function of a system with its spectrum, without direct reference to the energy levels by using only the overlap of wavefunctions. The fidelity of eq. (2.1.3) can be applied to characterise the system's behaviour locally in energy space, i.e., parts of spectrum only, as is the typical situation in experiments where the complete spectrum is not accessible in most cases. Since fidelity detects avoided crossings as a local measure without need of large statistics—as would be required for testing predictions of random matrix theory on spectral lines or wave functions [Haa91]—it is more attractive for experiments. The use of our fidelity measure has been exemplified for simple models and for random matrix systems showing many avoided crossings [Plö10b]. Since avoided crossings play an important role in many physical situations, it should be useful in a broad range of applications and will hopefully be applied to detect and charaterise avoided crossings in different systems.

The single-band Bose–Hubbard model is realisable with ultracold atoms in optical lattices and we studied its complex spectral structure with statistical methods. We mainly focused on the fidelity and avoided crossings, and were able to compare the behaviour of this complex many-body system with RMT predictions at very high resolution. This revealed a small number of regular levels that had so far been identified only by a direct analysis of a

few single eigenstates.

The statistical approach is nevertheless limited in discussing singular features of a complex system but is quite often the only possible route to characterise a system. In the following chapter, we are going to study a system, which shows complexity in the time evolution of the single-particle wave function, but has the advantage of being understandable by analytical means.

Two-band Bose–Hubbard model:

Complex Dynamics

Chapter 3

Complex Dynamics in the Non-interacting Two-band Model

Contents

3.1 Introduction and Review of Single-Band Case

After our study of the single-band Bose-Hubbard model with an external Stark force, we now turn to the two-band system. In Wannier–Stark systems generally, there is a finite coupling between the states from the ground band to higher bands. Or to be more precise, the eigenstates of the Wannier–Stark Hamiltonian have complex eigenvalues with a finite imaginary part, i.e., they have a finite lifetime. How does this coupling of energy bands translate into our lattice system? This is this main physical question we will address in this and the following chapter. In our two-band system, the band coupling is induced by the external force and the inter-particle interaction. To this end, we need to understand the

interband coupling in the non-interacting system and connect it to the single-band case. We start with the non-interacting two-band system which turns out to show surprisingly rich and complex behaviour. We will try to solve the time-dependent Schrödinger equation exactly, using different bases and different types of perturbation theory. This will give us a good overview and understanding of different time-scales and physical regimes present in the non-interacting two-band system. After a careful analysis of the band coupling and time evolution in this system, we will study the effect of inter-particle interaction in the later chapter 4.

The present chapter furthermore provides a beautiful example of complex dynamics in quantum systems. We will find that many energy levels contribute to the time evolution of the single-particle wave function and that it displays a complex interference. This is mirrored in the population dynamics of the two energy bands with a superposition of many different frequencies, resonances and different behaviour on different time-scales. Before starting with actual calculations, we will give a short motivation and restate the Hamiltonian as derived in chapter 1.

3.1.1 Motivation and Hamiltonian

In the present chapter, we consider a two-band tight-binding model with an additional tilting force and study the force-induced coupling between the two Bloch bands. This has been an active area of research for quite some time, although mainly focused on non-interacting electrons [Fuk73, Rot95, Zha96, Bre06, Abu07]. For ultracold atoms in optical lattices [Blo08b, Mor06], nearly closed two-band systems are also realisable using different techniques as explained in section 1.3.3. Besides the possibility of experimental realisation, a closed two-band model is interesting as a simple yet rich model system to study the coupling between energy bands.

In addition to these direct realisations, the results of the present chapter extend much further. A non-interacting system of two energy bands with an external force is equivalent to a driven two-level system and this has applications in many areas of physics and is still studied in different contexts [Lon10, Hau10]. The main reasons seem the richness of possible phenomena on one hand and the possibility of analytical results on the other hand. The long studied Rabi problem with all its extensions, as e.g. the Jaynes–Cummings model (for both see appendix B), is a well-known example.

As discussed in chapter 1, we consider the two lowest energy bands of the non-interacting Bose–Hubbard model introduced there. Since the interaction is zero, we have only a limited number of terms in the Hamiltonian, which are: on-site energies, hopping between neighbouring sites, and a coupling of the two energy bands. The Hamiltonian we will discuss in this chapter reads explicitly

$$\begin{aligned}\mathcal{H} = &-\tfrac{J_a}{2}\sum_{l\in\mathbb{Z}}\left(|a_{l+1}\rangle\langle a_l| + \text{h.c.}\right) - \tfrac{J_b}{2}\sum_{l\in\mathbb{Z}}\left(|b_{l+1}\rangle\langle b_l| + \text{h.c.}\right)\\ &+\sum_{l\in\mathbb{Z}}\epsilon_l^-|a_l\rangle\langle a_l| + \epsilon_l^+|b_l\rangle\langle b_l| + V\left(|a_l\rangle\langle b_l| + \text{h.c.}\right)\end{aligned} \tag{3.1.1}$$

with on-site energies $\epsilon_n^{\pm} = \pm\Delta/2 + nF$ and $V = C_0F$ the local coupling between the energy bands. $J_{a(b)}$ denote the hopping strength in band $a(b)$. In a realisation with optical lattices, the parameters Δ, C_0, J_a, J_b depend on the depth of the lattice V_0. In the following, we consider the external Stark force F as a free parameter. The Hamiltonian in the Wannier basis, eq. (3.1.1), is schematically depicted in figure 3.1.

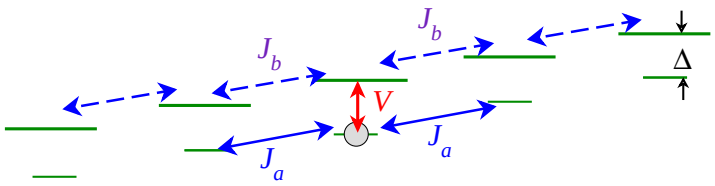

Figure 3.1: Graphical representation of the non-interacting two-band Hamiltonian. Shown is the tilted double ladder and coupling between the bands (V) and between neighbouring sites (J_a, J_b).

The original Wannier-Stark problem (see section 1.2) has actually a spectrum with finite imaginary part. Including an infinite number of bands and keeping all couplings, the Hubbard model with external force is equivalent to the continuous Wannier–Stark problem and must therefore also show complex eigenvalues. However, the truncated version we are considering has purely real eigenvalues. Using second quantisation and a vector notation $\gamma_l = (a_l, b_l)^{\mathrm{T}}$, we see explicitly that the Hamiltonian is quadratic with a real symmetric coefficient matrix

$$\mathcal{H} = \sum_{l,n} \gamma_l^\dagger (A_l \delta_{ln} + B_{ln}) \gamma_n. \tag{3.1.2}$$

It has thus real eigenvalues and is integrable [Lie61], although the unitary transformation necessary for a diagonalisation might be hard to find. Namely, as we will see later, solving this (seemingly simple) non-interacting problem is equivalent to a second order differential equation where no exact solution in terms of elementary functions is known.

This chapter is organised as follows. We start be reviewing the single-band case, including the spectrum and interesting effects in the time evolution, such as Bloch oscillations (sec. 3.1.2). We will then approach the two-band system first in momentum space (sec. 3.2), where we can reduce the Schrödinger equation to a known type of differential equation of second order. Perturbative computations of the eigenstates and time evolution operator in momentum space (sec. 3.2.3) and real space (sec. 3.3) will be given. We will find resonances analogous to resonantly enhanced tunnelling in the Wannier–Stark problem and will discuss these resonances in detail (sec. 3.4).

3.1.2 Single Band Case

We start with a short review of the single band results, as e.g. found in [Har04, Fuk73]. It is easily solved and we will discuss the wave function and its time evolution. This is very instructive since the horizontal dynamics on the lattice in the two-band case can partially be understood from the single-band dynamics.

Exact Solution

The single band Hamiltonian for a non-interacting particle on a lattice under a constant external force reads

$$\mathcal{H}_1 = -J/2 \sum_{l\in\mathbb{Z}} (|a_{l+1}\rangle\langle a_l| + \mathrm{h.c.}) + F \sum_{l\in\mathbb{Z}} l |a_l\rangle\langle a_l|, \tag{3.1.3}$$

where $J > 0$ and $|a_l\rangle$ is a Wannier-state localised at site number l. To find the eigenvalues of this Hamiltonian we make the very general ansatz

$$\mathcal{H}_1|\phi\rangle = E|\phi\rangle \qquad \text{with} \qquad |\phi\rangle = \sum_{l\in\mathbb{Z}} c_l|a_l\rangle,$$

leading to the following secular equation

$$(lF - E)\, c_l = J/2\, (c_{l+1} + c_{l-1}).$$

This strongly resembles the recursion relation for ordinary Bessel functions $\frac{2n}{x}J_n(x) = J_{n+1}(x) + J_{n-1}(x)$ (see Appendix C). The coefficients for solving the single band Hamiltonian are therefore Bessel functions $c_l = A \cdot J_{l-E/F}(J/F)$ with a normalisation constant A. Using this ansatz $|\alpha_n\rangle = \sum_l J_{l-n}(x_a)|a_l\rangle$, with $x_a = J/F$ and its inversion $|a_n\rangle = \sum_l J_{n-l}(x_a)|\alpha_l\rangle$ we can compute matrix elements

$$\langle\alpha_{n'}|\mathcal{H}_1|\alpha_n\rangle = -J/2\left(\delta_{n,n'+1} + \delta_{n,n'-1}\right) + F\sum_{l\in\mathbb{Z}} l J_{l-n'}(x_a)J_{l-n}(x_a). \tag{3.1.4}$$

The second term can be simplified by changing the summation $l \to l+n$ and using relations for Bessel functions

$$\begin{aligned} F\sum_l (l+n)J_l(x_a)J_{l+n-n'}(x_a) &= nF\delta_{nn'} + xF/2\sum_l J_{l+n-n'}\,(J_{l+1} + J_{l-1}) \\ &= nF\delta_{nn'} + J/2\left(\delta_{n,n'+1} + \delta_{n,n'-1}\right). \end{aligned}$$

The second term cancels the hopping term in eq. (3.1.4) and we obtain the eigenenergies

$$\mathcal{H}_1 = \sum_n E_n|\alpha_n\rangle\langle\alpha_n| \qquad \text{with} \qquad E_n = nF, \quad |\alpha_n\rangle = \sum_l J_{l-n}(J/F)|a_l\rangle. \tag{3.1.5}$$

We have thus computed the eigenenergies and eigenvectors. The spectrum is given by an equidistant ladder of energy values, the so-called Wannier–Stark ladder. Quite surprisingly, the energy spacing is independent of the hopping strength J. Here and in the following we will denote hopping coefficients and Bessel function by capital J. This should not lead to any misunderstanding since the Bessel functions will usually have integer indices for their order and the hopping strengths will have indices a, b indicating the band.

We see, that the external force breaks the translational symmetry of the hopping term and for any (arbitrary small) value of the force, one finds a Wannier–Stark ladder and no sign of the free electron band structure. But when $F = 0$, the energy levels coincide and the hopping couples them to obtain the lowest Bloch band $\epsilon(k) = -J\cos(k)$ with Bloch waves $|k\rangle = \sum_l \mathrm{e}^{\mathrm{i}kl}|a_l\rangle$ as eigenstates. This is further discussed in [Glü02, p. 108].

Single-band Wave Function

For vanishing force, the eigenstates are delocalised Bloch waves, occupying the whole lattice. Any finite external force leads to a localisation of the eigenstates, according to eq. (3.1.5). The extension over the lattice is shown for different ratios of hopping strength and external force in figure 3.2. The single-particle wave function is occupying very few lattice sites for large forces, i.e. $F \gg J$. The n-eigenstate $|\alpha_n\rangle$ is mainly localised in the interval $|l - n| < x_a = J/F$.

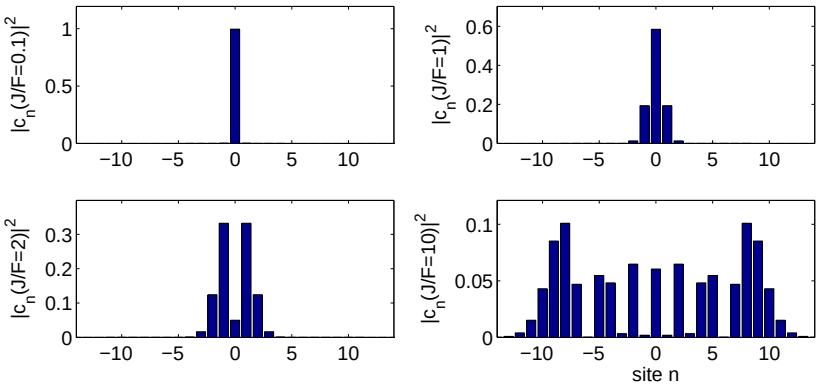

Figure 3.2: Delocalisation of the single-band wave function in real space for various values of the external force. Shown are the (absolute squares of the) expansion coefficients. Note that the expansion coefficients are Bessel functions and are thus all real but not all positive.

Time evolution and Bloch Oscillations

The knowledge of the eigenstates enables us to compute the time evolution operator and to discuss the time evolution of simple initial states. The matrix elements of the time evolution operator read [Har04]

$$\begin{aligned}\langle a_l|U(t)|a_{l'}\rangle &= \sum_n \langle a_l|\alpha_n\rangle \mathrm{e}^{-\mathrm{i}E_n t}\langle \alpha_n|a_{l'}\rangle \\ &= J_{l-l'}\left(x\sin(\tfrac{Ft}{2})\right)\mathrm{e}^{\mathrm{i}(l-l')(\pi-Ft)/2-\mathrm{i}l'Ft}.\end{aligned} \tag{3.1.6}$$

The time evolution operator is periodic in time with the Bloch period $T_B \equiv 2\pi/F$. Figure 3.3 shows the results of the time evolution for two initial wave functions in real space. On the left hand side for an initial state occupying only a single site $|\psi(0)\rangle = |a_0\rangle$ and on the right for a Gaussian wave packet $|\psi(0)\rangle \propto \sum_n \mathrm{e}^{-\beta(n-n_0)^2}|a_n\rangle$ with $\beta = 0.01$ and $n_0 = 10$.

The single-site initial wave function spreads symmetrically in both direction of the lattice and returns to its initial state after one Bloch period. The Gaussian wave packet on the other hand starts to move down the lattice, according to the tilt of the lattice as determined by the external force. But it does not "move down the hill" as a classical particle would, instead it is moving slower and stops eventually, only to move up against the external force back to its initial state. This counter-intuitive behaviour is termed *Bloch oscillations*.

This concludes our brief review of the single-band case. The external force leads to well-known but noteworthy effects in this simple lattice system. Firstly, the external force leads to a localisation of the eigenstates (Stark localisation) and, secondly, wave packets show periodic oscillatory behaviour in the form of breathing modes or Bloch oscillations. Let us now turn to the two-band system and start our analysis in momentum space.

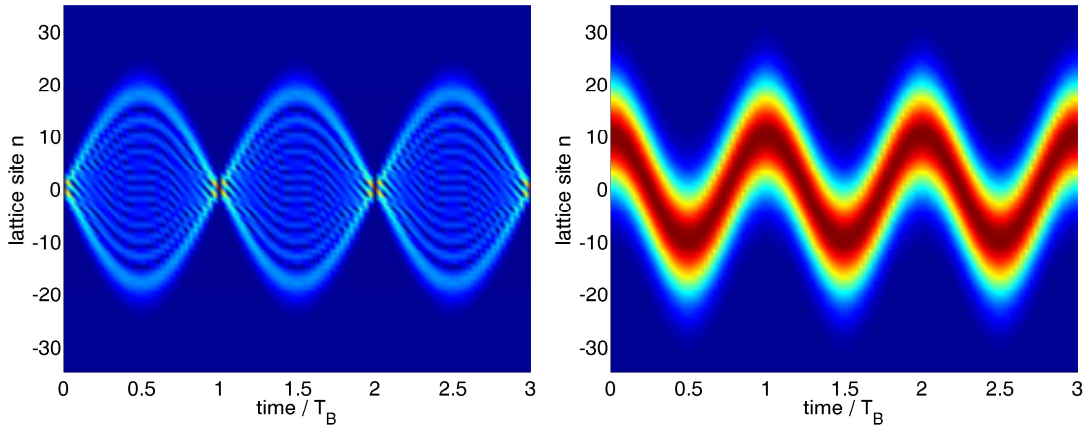

Figure 3.3: Time evolution in the one band system. Shown is the modulus of the single-band wave function over time for $x_a = J/F = -10$ and two different initial states. *Left*: A completely localised initial state occupying only one site $|\psi(0)\rangle = |a_0\rangle$ leads to a breathing mode in the time-evolution. *Right*: A Gaussian wave packet $|\psi(0)\rangle \propto \sum_n \mathrm{e}^{-\beta(n-n_0)^2}|a_n\rangle$ with $\beta = 0.01, n_0 = 10$ remains a Gaussian of nearly fixed width in the time-evolution. These are the famous Bloch oscillations in real space.

3.2 Momentum Space Analysis

3.2.1 Hamiltonian and Absence of Explicit Solution

We are generally interested in the coupling between the two energy bands, independent from the actual lattice site. We therefore go to momentum space: first we remove the force term in the time-dependent Schrödinger equation by performing a gauge transformation and secondly we introduce an expansion in Fourier components.

The applied force breaks the translational invariance of the system and can be removed by a gauge transformation

$$\psi(x,t) = \mathrm{e}^{-\mathrm{i}Ftx}\tilde{\psi}(x,t) \tag{3.2.1}$$

such that the time-dependent Schrödinger equation for the new wave function reads

$$\mathrm{i}\partial_t\tilde{\psi}(x,t) = \tilde{\mathcal{H}}(t)\tilde{\psi}(x,t) \tag{3.2.2}$$

where the Stark term is absent but the momentum p is replaced by $p - Ft$ [Kol03b] as is easily seen by making use of $p = -\mathrm{i}\partial_x$ and $\partial_x \mathrm{e}^{f(x)} = \mathrm{e}^{f(x)}(\partial_x + f'(x))$. We regain translational invariance, such that quasimomentum is a good quantum number, but the Hamiltonian is now time-dependent. This appears as a trick at this moment, but an experimental realisation can be easily imagined. A one-dimensional optical lattice needs to be produced in a ring shaped geometry, i.e. the cigar-like geometry is folded to a torus forming an explicit implementation of periodic boundary conditions. Feasible experimental parameters are discussed in [Ami05, Cou06] and the lattice tilt is achieved by a phase difference as described in chapter 1.

Since the time-dependent system is translationally invariant, we introduce Fourier components for the expansion of the wave function $|\psi\rangle = \sum_l a_l|a_l\rangle + b_l|b_l\rangle$, such that

$$a(k) = \sum_l \mathrm{e}^{\mathrm{i}lk}a_l \qquad \& \qquad b(k) = \sum_l \mathrm{e}^{\mathrm{i}lk}b_l.$$

We obtain from the original non-interacting two-band model the following time-periodic two-level Hamiltonian [Zha96]

$$\mathcal{H}(k,t) = \begin{pmatrix} -\frac{\Delta}{2} - J_a \cos(k+Ft) & V \\ V & \frac{\Delta}{2} - J_b \cos(k+Ft) \end{pmatrix}. \tag{3.2.3}$$

We find that both unperturbed energy bands have a cosine dispersion, as expected for a tight-binding model. They are separated by a bandgap Δ and coupling via V, where the band coupling is momentum-independent. Furthermore the periodicity of the Hamiltonian in time

$$\mathcal{H}(k, t+T_B) = \mathcal{H}(k,t) \qquad \text{with} \qquad T_B = 2\pi/F$$

is clearly visible in the momentum representation. Such a time-dependent two-level system can show very rich behaviour, for instance multi-photon resonances, the Rabi-problem is a typical example (see appendix B). Other time-dependent two-level systems like the Landau–Zener problem are still subject to ongoing research [Zen09, Roj10] despite their exact solution.

The time-dependent two-level system of eq. (3.2.3) appears very similar to the unquantised Rabi problem $H(t) = \left(\begin{smallmatrix} -\Delta & V\cos\omega t \\ V\cos\omega t & \Delta \end{smallmatrix}\right)$. However, it will turn out that our system is more complicated. The Rabi problem is actually equivalent to the Mathieu equation whereas the time-dependent Schrödinger equation to the Hamiltonian of eq. (3.2.3) is equivalent to an extension of the Mathieu equation. It is called Hill's equation and no solutions in terms of elementary functions are known (see eq. (3.2.12) below). In fact, applying a rotation around the y-axis by $\pi/2$ to the Rabi problem, one obtains $\tilde{H}(t) = \left(\begin{smallmatrix} -V\cos\omega t & -\Delta \\ -\Delta & +V\cos\omega t \end{smallmatrix}\right)$. The difference between the Rabi problem and our driven two-level system is the constant gap of Δ between the unperturbed levels in eq. (3.2.3).

The unperturbed energy bands for this two-level system are shown in figure 3.4. If the

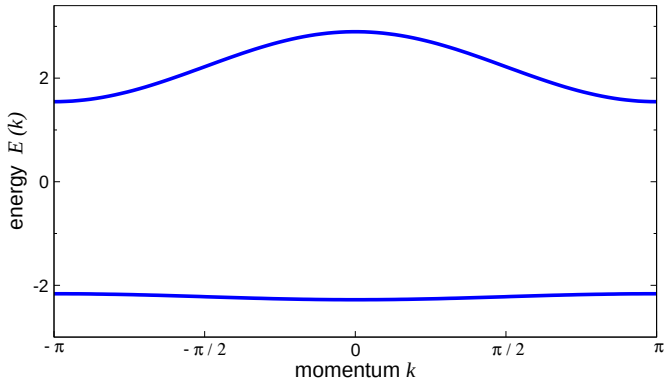

Figure 3.4: The unperturbed energy bands of Eq. (3.2.3) in momentum space at $t = 0$. A non-zero force F leads to periodic motion within the energy bands. Parameters as for an optical lattice of depth $V_0 = 4$: $\Delta = 4.39, J_a = 0.062, J_b = -0.62$.

system was prepared in an initial state of zero momentum and the interband coupling was negligible, it would perform periodic oscillations along the cosine dispersion of the lowest band. Reaching the edge of the Brillouin zone, it would be reflected and return to its initial state. This is the momentum space picture of Bloch oscillations.

We are mainly going to study the population dynamics in this and the following chapter. We will usually start from an initial state in the lower band and solve the time-dependent

Schrödinger equation. The main observable will then be the *occupation of the upper band* given by

$$\mathcal{N}_b(t) \equiv \langle\psi(t)|\sum_l b_l^\dagger b_l|\psi(t)\rangle = \sum_k |b(k,t)|^2. \tag{3.2.4}$$

This definition does not specify the initial state, but it will usually be a state occupying only the lower energy band. In the context of time-dependent two-level systems, this quantity is then also referred to as transition probability $P_{a\to b}(t)$. The above definition will also be used in the many-body problem in the following chapter. This is the observable we are aiming at and try to obtain expressions for this quantity as well as solutions of the time-dependent Schrödinger equation, e.g., in form of the time evolution operator.

The time dependent Schrödinger equation for the momentum space amplitudes reads

$$\mathrm{i}\partial_t \begin{pmatrix} a(k,t) \\ b(k,t) \end{pmatrix} = \begin{pmatrix} -\frac{\Delta}{2} - J_a\cos(k+Ft) & V \\ V & \frac{\Delta}{2} - J_b\cos(k+Ft) \end{pmatrix} \begin{pmatrix} a(k,t) \\ b(k,t) \end{pmatrix}. \tag{3.2.5}$$

This corresponds to a set of two coupled ordinary differential equations of first order. To simplify these, we follow [Zha96] and apply the following transformation in order to obtain a purely off-diagonal Schrödinger equation

$$\begin{aligned} \tilde{a}(k,t) &= a(k,t)\,\exp\Big[-\mathrm{i}\Delta\cdot t/2 - \mathrm{i}J_a\int_0^t \cos(k+Ft')\mathrm{d}t'\Big] \\ \tilde{b}(k,t) &= b(k,t)\,\exp\Big[+\mathrm{i}\Delta\cdot t/2 - \mathrm{i}J_b\int_0^t \cos(k+Ft')\mathrm{d}t'\Big] \end{aligned} \tag{3.2.6}$$

This removes the diagonal terms and we obtain an equivalent Schrödinger equation for the transformed amplitudes

$$\mathrm{i}\partial_t \begin{pmatrix} \tilde{a}(k,t) \\ \tilde{b}(k,t) \end{pmatrix} = \begin{pmatrix} 0 & V\mathrm{e}^{-\mathrm{i}\phi(k,t)} \\ V\mathrm{e}^{\mathrm{i}\phi(k,t)} & 0 \end{pmatrix} \begin{pmatrix} \tilde{a}(k,t) \\ \tilde{b}(k,t) \end{pmatrix}, \tag{3.2.7}$$

where $\phi(k,t) = \Delta\cdot t - \Delta x[\sin(k+Ft) - \sin(k)]$ is the phase between the two Bloch bands and $\Delta x = (J_a - J_b)/F$. Where the pure existence of two energy bands allows phenomena like Rabi oscillations, it is the non-trivial phase difference for the time-evolution in both bands, related to $\Delta x \neq 0$, that gives rise to interesting, non-trivial phenomena to be discussed below. That is, the difference in the curvature $J_a - J_b$ allows to collect different phases during the time evolution in the upper or lower band. From the theoretical point of view, it is $\Delta x \neq 0$ leading to differential equations which are not solvable in simple functions as we will see below. Please note, that our model is slightly different from a tight-binding superlattice, as e.g. in [Bre06, Bre07], since we include a local on-site coupling of the bands.

Let us discuss the special case $J_a = J_b$ first. The non-linear time dependence of $\phi(k,t)$ vanishes and we write the system of differential equations as a linear differential equation of second order. Differentiating the second equation and inserting it into the first one, we arrive at the simple equation

$$\ddot{\tilde{a}} + \mathrm{i}\Delta\dot{\tilde{a}} + V^2\tilde{a} = 0. \tag{3.2.8}$$

This is a linear second order equation with constant coefficients and independent of k and is easily solved. Using the initial conditions $\tilde{a}(0) = 1$ and $\dot{\tilde{a}}(0) \propto b(0) = 0$ the solution

translates to the original amplitudes as

$$\begin{aligned} a(t) &= \cos\omega_0 t + \mathrm{i}\tfrac{\Delta}{\sqrt{\Delta^2+4V^2}}\sin\omega_0 t \\ b(t) &= -\mathrm{i}\frac{2V}{\sqrt{\Delta^2+4V^2}}\sin\omega_0 t, \quad \omega_0 = \tfrac{1}{2}\tilde{\Delta} \equiv \tfrac{1}{2}\sqrt{\Delta^2+4V^2} \end{aligned} \tag{3.2.9}$$

and $|a(t)|^2 + |b(t)|^2 = 1$ as necessary. For this simple case, we find sinusoidal oscillations, $\mathcal{N}_b(t) = \frac{4V^2}{\Delta^2+4V^2}\sin^2(\tilde{\Delta}t/2)$, with an amplitude $\frac{4V^2}{\Delta^2+4V^2}$ and period $T/T_B = F/\tilde{\Delta}$. We will come back to this result later and compare it to numerical simulations.

The same procedure to derive a second order differential equation can of course be applied to the general problem. But the differential equation to be solved has now time-dependent coefficients

$$0 = \ddot{\tilde{a}} + \mathrm{i}\dot{\phi}(k,t)\dot{\tilde{a}} + V^2\tilde{a} = \ddot{\tilde{a}} + \mathrm{i}\Big[\Delta + (J_a - J_b)\cos(k+Ft)\Big]\dot{\tilde{a}} + V^2\tilde{a}. \tag{3.2.10}$$

We make an ansatz $a = y\exp[\mathrm{i}\Omega(t)]$ and choose $-2\frac{\mathrm{d}}{\mathrm{d}t}\Omega = \Delta + (J_a - J_b)\cos(k+Ft)$, in order to remove the second term in eq. (3.2.10). We finally arrive at

$$\begin{aligned} 0 = 2\ddot{y} + y\Big[&2V^2 - \mathrm{i}F(J_a - J_b)\sin(k+Ft) \\ &-3\big(\Delta + (J_a - J_b)\cos(k+Ft)\big)^2\Big]. \end{aligned} \tag{3.2.11}$$

We have transformed the initial equation to one that is of the *Hill* type [Plö10a]

$$0 = y'' + \big[A + Bf(x)\big]y, \qquad \text{with} \qquad f(x+2\pi) = f(x) \tag{3.2.12}$$

described in [Olv10, Urw70, Mag69]. It is an extension of the well known Mathieu equation. Unfortunately, solutions in closed form are not known. We have thus shown that the time-dependent Schrödinger equation for the non-interacting two-band problem is equivalent to an ordinary differential equation without known solutions in elementary functions. Of course one can see differential equations as defining new functions, but we are seeking an explicit solution expressable in known functions or a small number of integrals of known functions here. For the rest of this chapter, we are going to study different approximate solutions of the problem, as determined by the Hamiltonian of eq. (3.1.1) and the Schrödinger equation (3.2.7).

3.2.2 Perturbative Solution and Existence of Resonances

Having established the absence of exact solutions in closed form in the last section, we now turn to approximate solutions. We will use some simple approximations combined with numerical results in this section to gain some insight in the physics of the non-interacting two-band system. In the following sections we will perform more systematic calculations.

Following [Zha96], the time-evolution operator of the non-interacting two-band system is approximately (ignoring the time-ordering) given by

$$U(t) \approx \exp\left[-\mathrm{i}\int_0^t \mathcal{H}(t')\mathrm{d}t'\right] \tag{3.2.13}$$

valid to first order in V. This yields an approximate but explicit solution of the Schrödinger equation (3.2.7), namely

$$\begin{pmatrix}\tilde{a}(k,t)\\ \tilde{b}(k,t)\end{pmatrix} = \exp\left[-\mathrm{i}V\int_0^t \sigma_x\cos\phi(k,t') + \sigma_y\sin\phi(k,t')\mathrm{d}t'\right]\begin{pmatrix}\tilde{a}(k,0)\\ \tilde{b}(k,0)\end{pmatrix}. \tag{3.2.14}$$

Choosing, as before, occupation in the lower band as initial state, i.e. $a(k,0)=1$ and $b(k,0)=0$, one obtains with $\mathrm{e}^{\pm\mathrm{i}\vec{a}\cdot\vec{\sigma}} = \mathbf{1}\cos|\vec{a}| \pm \mathrm{i}|\vec{a}|^{-1}\vec{a}\cdot\vec{\sigma}\sin a$ for the occupation of the upper band

$$|b(k,t)|^2 = \sin^2\left|V\int_0^t \mathrm{e}^{\mathrm{i}\phi(k,t')}\mathrm{d}t'\right|, \tag{3.2.15}$$

with $\phi(k,t) = \Delta\cdot t - \Delta x[\sin(k+Ft)-\sin(k)]$ as above. We will encounter this integral again later and discuss it extensively there. At the moment, we only want to state that it can not be expressed by a finite number of elementary functions. We thus want to treat it approximately. It is easy to check the same special case as above. For equal hopping strength in both bands ($\Delta x = 0$) the integral is easily performed and one finds oscillations between the bands

$$|b(k,t)|^2 = \sin^2\left|V(\mathrm{e}^{\mathrm{i}\Delta t}-1)/\Delta\right| = \sin^2(2V/\Delta)\sin^2\tfrac{\Delta t}{2} \tag{3.2.16}$$

with an amplitude of $\sin^2(2V/\Delta)\approx 4V^2/\Delta^2$ and period $T = 2\pi/\Delta = F/\Delta\cdot T_B$. This is similar to earlier results. A typical example of such oscillations for our parameters is depicted in figure 3.5. The amplitude of these direct on-site oscillations is much smaller than one, usually a few percent for realisations with optical lattices, and the period is smaller than the Bloch period T_B.

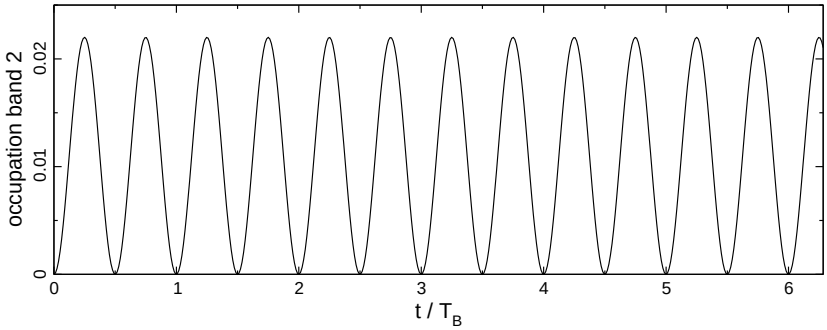

Figure 3.5: Occupation of the upper band for equal band widths ($J_a = J_b$) according to the approximate result eq. (3.2.16) for $F = 2.22$ and $V_0 = 4$, i.e. $V = -0.15F$ and $\Delta = 4.39$.

To obtain an idea of further physics contained in the above expression eq. (3.2.16), we stick to some simple approximations and set $k = 0$. Writing $\mathrm{e}^{\mathrm{i}\phi} = \cos\phi + \mathrm{i}\sin\phi$ and using the addition theorems we find integrands of the form $\cos(\Delta x\sin t)$ and $\sin(\Delta x\sin t)$ which are not accessible. We therefore expand the functions in a Fourier series

$$\cos(\Delta x\sin Ft) = J_0(\Delta x) + \sum_{n=1}^{\infty} 2J_{2n}(\Delta x)\cos(2nFt) \tag{3.2.17}$$

$$\sin(\Delta x\sin Ft) = \sum_{n=0}^{\infty} 2J_{2n+1}(\Delta x)\sin\left[(2n+1)Ft\right] \tag{3.2.18}$$

where $J_l(x)$ denotes the ordinary Bessel function of order l. Taking only the first terms

$$\begin{aligned}\cos(\Delta x \sin t) &\approx J_0(\Delta x) + 2J_2(\Delta x)\cos 2t + \mathcal{O}(\cos 4t)\\ \sin(\Delta x \sin t) &\approx 2J_1(\Delta x)\sin t + \mathcal{O}(\sin 3t),\end{aligned}$$

the integrals can be solved analytically and expressions of the following form ($m = 1, 2$) appear

$$\mathcal{N}_b(t) \propto \sin^2\left| V \sin^m(\tfrac{\Delta x}{m}) \, \frac{\sin[(\Delta - mF)\, t]}{\Delta - mF} \right|.$$

The higher order terms in the the expansion lead to similar terms, indicating special behaviour of the system when the denominator vanishes. Thus, a truncated Fourier expansion indicates the existence of resonances in the occupation of the upper band for $\Delta \approx mF$, i.e., whenever the tilt between sites of different bands equals the band gap.

To test this expectation, we evolved an initial state with $a(k, 0) = 1$ and $b(k, 0) = 0$ in time for a resonant value and the resulting occupation of the upper band $\mathcal{N}_b(t)$ is shown in figure 3.6. We observe small Rabi oscillations with a high frequency, and on top of these are Rabi oscillations of large amplitude and long period $T \gg T_B$. The latter oscillations only take place near resonances $\Delta \approx mF$. But the actual maximum of these large amplitude oscillations is not exactly at values $F_m = \Delta/m$, with $m \in \mathbb{N}$, instead they are slightly shifted. For figure 3.6 below, we searched for the largest amplitude oscillations of a resonance of order 2. For the parameters given there, the maximum is located at $F = 2.2207$ instead of $F = \Delta/2 = 2.195$, a shift of about one percent. Later, we will derive a simple expression for the actual position of the resonance.

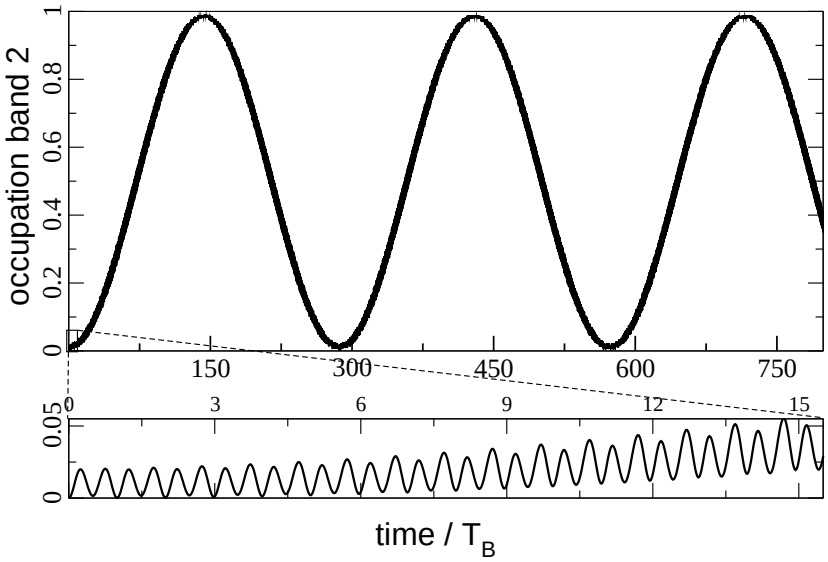

Figure 3.6: Occupation of band 2 as a function time in resonance. We observe long period and large amplitude Rabi oscillations with smaller and much faster oscillations on top. Parameters as in figure 3.4 and $F = 2.2207$.

We performed similar time evolutions for various values of the external force F and studied the long time average of $\mathcal{N}_b(t)$ [Plö10a]. The result is depicted in figure 3.7. It clearly demonstrates the existence of resonances in our system whenever the bandgap is an integer multiple of the external force. The occupation of the upper band is usually very

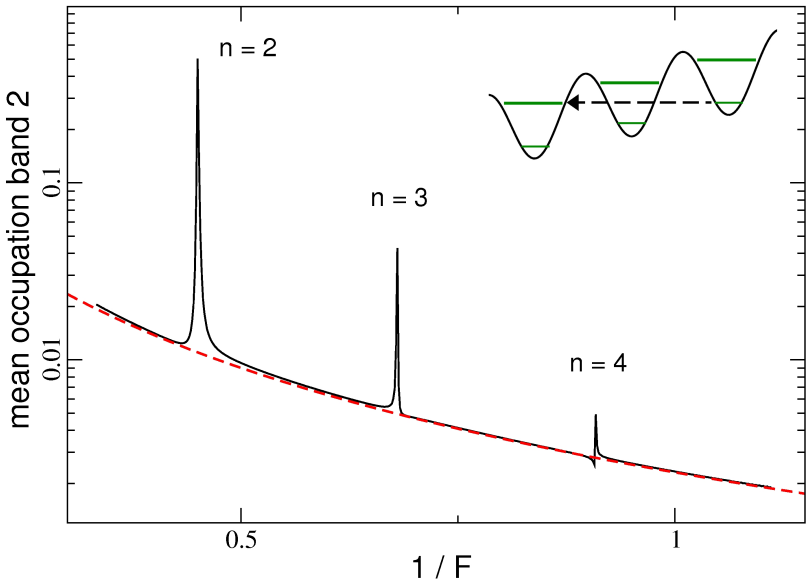

Figure 3.7: Long time averages of the occupation of band 2 as function of the inverse force. There is a clear signature of resonant behaviour when the band gap equals an integer multiple of the force: $nF = \Delta$. The dashed line shows the average occupation of band 2 as expected from eq. (3.2.19) and the inset schematically shows an $n = 2$ resonance. Parameters as in figure 3.4.

small, of the order of a few percent, but shows sharp resonances for $mF \approx \Delta$. A closer numerical study (not shown here) shows a Lorentzian shape for the lower order resonances and the possibility of more complicated, Fano-like [Fan61] shapes for the narrower higher order resonances. The non-resonant oscillations are well described by eq. (3.2.9). Specifically, if the system is not in resonance, the mean occupation of the upper band should follow

$$\overline{\mathcal{N}_b} = \frac{1}{2}\frac{4V^2}{\Delta^2 + 4V^2} = \frac{1/2}{1 + [\frac{\Delta}{2C_0}]^2 (1/F)^2}. \tag{3.2.19}$$

This is shown by the red dashed line in figure 3.7 which is in good agreement with the numerically obtained curve. We chose to show the mean occupation of the upper band as a function of the inverse force to make the resonances equidistant. Below we will derive an effective model for the system in resonance that allows a quantitative prediction of the resonance width. Similar resonant behaviour has been observed in extensive numerical studies of the occupation of minibands for electronic motion in superlattices [Abu07]. It is furthermore the lattice equivalent of resonantly enhanced tunnelling as discussed in section 1.2.2.

This section aimed at introducing the general physical picture of the band coupling in the non-interacting system. We will now turn to a more detailed and systematic analysis of the system in and out of resonance.

3.2.3 Magnus Expansion

This section is devoted to a systematic perturbation theory for solving the Schrödinger equation. The expansion technique we use is called Magnus expansion and will give us a systematic way of calculating unitary solutions to the time-dependent Schrödinger equation, perturbative in the inter-band coupling.

Introduction

Instead of solving the time-dependent Schrödinger equation directly, one can try to solve the equivalent differential equation for the time evolution operator with corresponding initial condition

$$\mathrm{i}\frac{\mathrm{d}}{\mathrm{d}t}U(t) = H(t)U(t), \qquad U(0) = \mathbf{1}. \tag{3.2.20}$$

A formal solution to this matrix differential equation is given by

$$U(t) = \mathcal{T}\exp\left[-\mathrm{i}\int_0^t \mathcal{H}(t')\mathrm{d}t'\right], \tag{3.2.21}$$

where the time-ordering $\mathcal{T}$ can only be dropped if the Hamiltonian commutes with itself at different times, i.e. $[\mathcal{H}(t), \mathcal{H}(t')] = 0 \ \forall t, t'$. The simplest approximation is to drop the time-ordering, and one would expect corrections to this in terms of more and more nested commutators. Such an expansion is actually well established and known as Magnus expansion [Mag54]. A recent review with many examples can be found in [Bla09].

The approach proposed by Magnus is to express the solution to eq. (3.2.20) as the exponential of an infinite series

$$U(t) = \exp\left[\Omega(t)\right] = \exp\left[\sum_{k=1}^{\infty}\Omega_k(t)\right], \tag{3.2.22}$$

with each term containing an increasing number $(k-1)$ of nested different time commutators. This is well-suited for time-dependent quantum mechanical problems and the Magnus expansion has the big advantage (compared to Dirac perturbation theory) that the obtained time evolution operator is unitary at any order of the expansion. Furthermore, the expansion is proven to be finite when $[\mathcal{H}(t), \int_0^{t'}\mathcal{H}(t'')\mathrm{d}t''] = 0 \ \forall t, t'$ and there are clear mathematical results concerning the convergence of the Magnus expansion [Bla09]. The first three terms of this series read explicitly (valid in both Schrödinger and interaction picture [Pec66, Kla08])

$$\Omega_1(t) = -\mathrm{i}\int_0^t \mathcal{H}(t_1)\ \mathrm{d}t_1 \tag{3.2.23a}$$

$$\Omega_2(t) = \frac{1}{2}\int_0^t \mathrm{d}t_1 \int_0^{t_1} \mathrm{d}t_2\ \left[\mathcal{H}(t_1), \mathcal{H}(t_2)\right] \tag{3.2.23b}$$

$$\Omega_3(t) = \frac{\mathrm{i}}{6}\int_0^t \mathrm{d}t_1 \int_0^{t_1} \mathrm{d}t_2 \int_0^{t_2} \mathrm{d}t_3 \Big\{\big[\mathcal{H}_1, \big[\mathcal{H}_2, \mathcal{H}_3\big]\big] + \big[\mathcal{H}_3, \big[\mathcal{H}_2, \mathcal{H}_1\big]\big]\Big\} \tag{3.2.23c}$$

with the obvious short-hand $\mathcal{H}_m = \mathcal{H}(t_m)$ in the last line. There are recursion formulae to construct higher-order commutators recursively [Bla09] and the Magnus expansion has also been used to implement fast and efficient numerical integration routines [Bla00]. All

orders could be summed in a recent work for a new derivation of the transition probability in the Landau–Zener problem [Roj10]. Unfortunately, this beautiful and clear tool does not yet appear in quantum mechanics textbooks.

Results within the Magnus Expansion

Applying the Magnus expansion to our time-dependent problem, eq. (3.2.7), we observe that the commutator at different times does not vanish

$$\begin{aligned}[\tilde{\mathcal{H}}(k,t),\tilde{\mathcal{H}}(k,t')] &= V^2\left[\sigma_x\cos\phi(t)+\sigma_y\sin\phi(t),\sigma_x\cos\phi(t')+\sigma_y\sin\phi(t')\right]\\ &= 2\mathrm{i}V^2\sigma_z\sin[\phi(t')-\phi(t)],\end{aligned} \tag{3.2.24}$$

where $\phi(t)=\Delta\cdot t-\Delta x\left[\sin(k+Ft)-\sin(k)\right]$ and $\Delta x=(J_a-J_b)/F$ as before. Dropping the time ordering operator in the formal solution of the Schrödinger equation is thus only an approximate solution. Let us now turn to a clearer analysis of the first and higher order results of the Magnus expansion.

First order Magnus Expansion Let us give the explicit expressions for our two-band system. Without loss of generality, we restrict our discussion to $k=0$, which can always be achieved by shifting the time zero. In the transformed basis, the according Hamiltonian reads

$$\tilde{\mathcal{H}}(t)=V\begin{pmatrix}0 & \mathrm{e}^{-\mathrm{i}\phi(t)}\\ \mathrm{e}^{\mathrm{i}\phi(t)} & 0\end{pmatrix}\qquad\text{with}\qquad\phi(t)=\Delta\cdot t-\Delta x\sin(Ft). \tag{3.2.25}$$

To compute the terms in the Magnus expansion explicitly, we have to integrate the Hamiltonian and commutators of it over time. We will need the integral

$$\chi(t)\equiv\int_0^t\mathrm{e}^{\mathrm{i}\phi(t')}\mathrm{d}t'=\int_0^t\mathrm{e}^{\mathrm{i}(\Delta\cdot t'-\Delta x\,\sin Ft')}\mathrm{d}t'. \tag{3.2.26}$$

First of all we observe that the other needed integral is given by

$$\int_0^t\mathrm{d}t'\mathrm{e}^{-\mathrm{i}\phi(t')}=\int_0^t\mathrm{d}t'\cos\phi(t')-\mathrm{i}\int_0^t\mathrm{d}t'\sin\phi(t')=\chi^*(t) \tag{3.2.27}$$

Using the the generating function of the Bessel function $\exp[u(\tau-1/\tau)]=\sum_{n\in\mathbb{Z}}J_n(2u)\tau^n$ for $\tau=\mathrm{e}^{-\mathrm{i}Ft}$, we can write the $\sin$ in the exponent as a sum over Bessel functions

$$\chi(t)=\sum_{n\in\mathbb{Z}}J_n(\Delta x)\int_0^t\mathrm{d}t'\mathrm{e}^{\mathrm{i}(\Delta-nF)t'}.$$

After integration and minor manipulations, we obtain a closed expression with the explicit time dependence for the highly oscillatory function

$$\chi(t)=2\sum_{n\in\mathbb{Z}}J_n(\Delta x)\,\mathrm{e}^{\mathrm{i}\omega_nt/2}\,\frac{\sin\left(\omega_nt/2\right)}{\omega_n}\qquad\text{with}\qquad\omega_n=\Delta-nF. \tag{3.2.28}$$

We observe that the same result can be obtained by keeping all terms in the Fourier expansion in the previous section 3.2.2. Applying the same procedure for similar integrals of the same type, one finds generally

$$\Phi_{\alpha,\beta,\pm\omega}(t)=\int_0^t\mathrm{e}^{\mathrm{i}(\alpha t'\pm\beta\sin\omega t')}\mathrm{d}t'=2\sum_{n\in\mathbb{Z}}J_n(\beta)\,\mathrm{e}^{\mathrm{i}(\alpha\pm n\omega)t/2}\,\frac{\sin\left[(\alpha\pm n\omega)t/2\right]}{\alpha\pm n\omega}. \tag{3.2.29}$$

With the explicit expression for the integral defining $\chi(t)$, the first term in the Magnus expansion is given by $\Omega_1(t) = -\mathrm{i}\int_0^t \mathrm{d}t' \mathcal{H}(t') = -\mathrm{i}V\left(\begin{smallmatrix} 0 & \chi^* \\ \chi & 0 \end{smallmatrix}\right)$ and the time evolution operator in first order reads correspondingly [Plö]

$$U_1(t) = \mathrm{e}^{\Omega_1(t)} = \begin{pmatrix} \cos(V|\chi(t)|) & -\mathrm{i}\mathrm{e}^{\mathrm{i}\arg\chi}\sin(V|\chi(t)|) \\ -\mathrm{i}\mathrm{e}^{-\mathrm{i}\arg\chi}\sin(V|\chi(t)|) & \cos(V|\chi(t)|) \end{pmatrix}. \tag{3.2.30}$$

This is the result in first order and the occupation of the upper band is given by

$$\mathcal{N}_b(t) = \sin^2\left(V|\chi(t)|\right) = \sin^2\left[2V\Big|\sum_n J_n(\Delta x)\mathrm{e}^{\mathrm{i}\omega_n t/2}\,\frac{\sin\left(\omega_n t/2\right)}{\omega_n}\Big|\right]. \tag{3.2.31}$$

But since $\chi(t)$ is a rather involved function, we want to discuss this in more detail and give some examples. Nevertheless, this result from first order Magnus expansion indicates some of the complexity of this time-dependent single-particle problem eq. (3.2.3).

First of all, we observe that the time evolution operator is unitary, as expected from the form of the Magnus expansion. Furthermore, we can again consider the limiting case of vanishing band curvature, i.e. $\Delta x = 0$, where we should find simple Rabi oscillations of small amplitude. In that case, only the zero-order Bessel function survives and the oscillating argument of the sine and cosine function in the time evolution operator reduces to

$$\chi(t) \overset{\Delta x=0}{=} 2/\Delta \cdot \mathrm{e}^{\mathrm{i}\Delta\cdot t/2}\,\sin\left(\Delta\cdot t/2\right).$$

Such that the occupation of the upper band reads

$$\mathcal{N}_b(t) = \sin^2\left(\tfrac{2V}{\Delta}\sin(\Delta\cdot t/2)\right) = 4\left(\sum_{n=0}^{\infty} J_{2n+1}\left(\tfrac{2V}{\Delta}\right)\sin\left[\tfrac{(2n+1)\Delta\cdot t}{2}\right]\right)^2.$$

It is a superposition of many frequencies with rapidly decreasing amplitudes already in this simple limit $\Delta x = 0$. The leading term has an amplitude of $(2V/\Delta)^2$ and is much smaller than one. An example of these oscillations for short times is shown in figure 3.8.

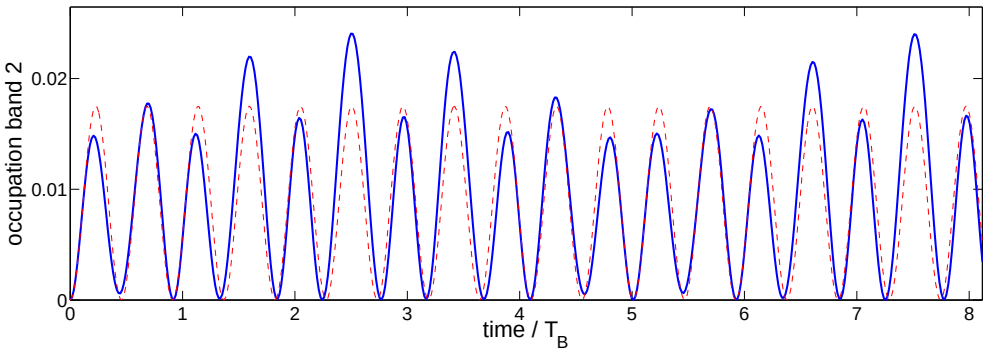

Figure 3.8: Occupation of the upper band as function of time for a non-resonant force from the first order Magnus expansion, eq. (3.2.31). Shown are the full first order solution (solid line) and the reduced solution keeping only the leading term (dashed line). Parameters correspond to $V_0 = 4$ and $F = 2.0$. A comparison with a numerical solution will be given in the following figure.

Coming back to the full expression for the time-dependent integral needed in first order, eq. (3.2.28), we can take a closer look at the resonances $\Delta = mF$. The vanishing

denominator can be treated separately since $\lim_{x\to 0} \frac{\sin xt}{x} = t$, and for a resonance of order m, this oscillatory function reads

$$\chi(t) = J_m(\Delta x)\, t + 2 \sum_{n\neq m} J_n(\Delta x)\, \mathrm{e}^{\mathrm{i}(\Delta - nF)t/2}\, \frac{\sin\left[(\Delta - nF)t/2\right]}{\Delta - nF}\,. \tag{3.2.32}$$

For large times the first term will be dominating and the overall short-time averaged occupation of the upper band shows large sinusoidal oscillations with unit amplitude

$$\mathcal{N}_b^{\mathrm{res}}(t) = \sin^2[V J_m(\Delta x)\, t]. \tag{3.2.33}$$

This is exactly the resonant behaviour we observed earlier. The other high-frequency and non-resonant terms will lead to small amplitude oscillations on top of this overall resonant inter-band oscillations. Let us now compare the complete first order Magnus expansion with a numerical simulation. This is shown in figure 3.9 for the occupation of the upper band as a function of time and a resonance of order $m = 2$.

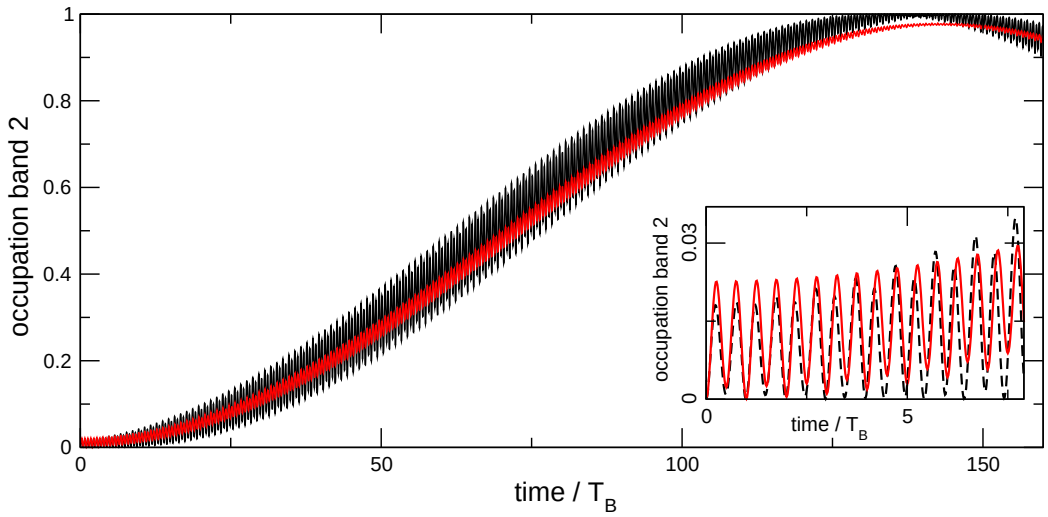

Figure 3.9: Occupation of the upper band as function of time for resonant force from the first order Magnus Expansion. Shown are the full first order solution (black line) and a numerical solution of the full problem (red line). Parameters as in figure 3.6. The resonant force for the Magnus expansion is $F = \Delta/2 = 2.195$, but $F = 2.2207$ is the numerically found resonance position and has been used in the simulation.

The first order Magnus expansion captures the most important features of the numerical result. These are small amplitude oscillations with a superposition of various frequencies (shown in the inset of figure 3.9) and an overall increase for long times, giving rise to long period sinusoidal oscillations of amplitude one. However, the amplitude of the minor oscillations is significantly larger than in the numerical result. Furthermore, the first order Magnus expansion predicts resonances exactly at $\Delta = mF$, it does not reproduce the small shift observed numerically. But besides these deficiencies, the first order gives a good overview of the complex dynamics contained in the non-interacting two-band problem and allows to capture the different dynamical regimes in a simple closed expression.

SECOND ORDER MAGNUS EXPANSION For the second order contribution we need the commutator computed earlier and integrate over it:

$$\begin{aligned}\Omega_2(t) &= \mathrm{i}V^2\sigma_z \int_0^t \mathrm{d}t_1 \int_0^{t_1} \mathrm{d}t_2 \sin[\phi(t_1)-\phi(t_2)] \\ &= \tfrac{1}{2}V^2\sigma_z \left\{ \int_0^t \mathrm{d}t_1 \mathrm{e}^{\mathrm{i}\phi(t_1)}\chi^*(t_1) - \int_0^t \mathrm{d}t_1 \mathrm{e}^{-\mathrm{i}\phi(t_1)}\chi(t_1) \right\}.\end{aligned}$$

Using the results for $\chi(t)$, eq. (3.2.28), we can rewrite this as

$$\Omega_2(t) = -\mathrm{i}V^2\sigma_z \sum_{n\in\mathbb{Z}} \frac{J_n(\Delta x)}{\Delta - nF} \left\{ \mathrm{Re}\,\chi(t) - \mathrm{Re}\,\Phi_{nF,\Delta x,F}(t) \right\},$$

where we used the fact that $\Phi_{-\alpha,\beta,-\omega}(t) = \Phi^*_{\alpha,\beta,\omega}(t)$. If we abbreviate the complicated integral as $\Omega_2(t) \equiv -\mathrm{i}V^2\sigma_z\psi(t)$, we obtain the time evolution operator in second order

$$U_2(t) = \exp\left[-\mathrm{i}V \begin{pmatrix} V\psi(t) & \chi^*(t) \\ \chi(t) & -V\psi(t) \end{pmatrix}\right] =$$

$$\begin{pmatrix} \frac{\cos(V\sqrt{\chi^*\chi+V^2\psi^2})}{\sqrt{\chi^*\chi+V^2\psi^2}} - \mathrm{i}V\psi\,\frac{\sin(V\sqrt{\chi^*\chi+V^2\psi^2})}{\sqrt{\chi^*\chi+V^2\psi^2}} & -\chi^*\,\frac{\sin(V\sqrt{\chi^*\chi+V^2\psi^2})}{\sqrt{\chi^*\chi+V^2\psi^2}} \\ -\chi\,\frac{\sin(V\sqrt{\chi^*\chi+V^2\psi^2})}{\sqrt{\chi^*\chi+V^2\psi^2}} & \frac{\cos(V\sqrt{\chi^*\chi+V^2\psi^2})}{\sqrt{\chi^*\chi+V^2\psi^2}} + \mathrm{i}V\psi\,\frac{\sin(V\sqrt{\chi^*\chi+V^2\psi^2})}{\sqrt{\chi^*\chi+V^2\psi^2}} \end{pmatrix}. \tag{3.2.34}$$

As expected, this result reduces to the time-evolution operator in first order for $\psi = 0$ and is unitary. Keeping in mind the structure of the time-dependent function $\chi(t)$ discussed earlier, we see that the result of the Magnus expansion in second order is already rather complicated. But we can still give a closed expression for the occupation of the upper band

$$\mathcal{N}_b(t) = \frac{|\chi_t|^2}{|\chi_t^*\chi_t + V^2\psi_t^2|} \sin^2\left(V\sqrt{\chi_t^*\chi_t + V^2\psi_t^2}\right), \tag{3.2.35}$$

although the functions $\chi(t)$ and $\psi(t)$ have been given only as integrals or infinite sums. Let us compare the results from both orders of the Magnus expansion. In figure 3.10 we show the occupation of the upper band as a function of time in first and second order Magnus expansion. The difference between the two orders is not discernible by the eye. Thus, the second order Magnus expansion leads only to minor corrections in the inter-band coupling.

THIRD AND HIGHER ORDERS Nested commutators have to be computed for the third order magnus expansion. This is easily done and the result is (we write $\phi_j \equiv \phi(t_j) = \Delta\cdot t_j - \Delta x \sin(Ft_j)$ for short)

$$\left[\tilde{\mathcal{H}}_1, [\tilde{\mathcal{H}}_2, \tilde{\mathcal{H}}_3]\right] = 4(\sigma_y\cos\phi_1 - \sigma_x\sin\phi_1)\sin[\phi_2-\phi_3]. \tag{3.2.36}$$

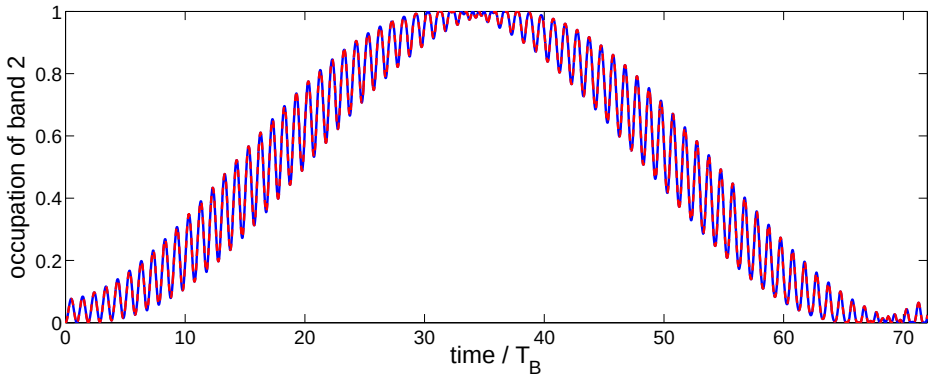

Figure 3.10: Results for the occupation of the upper band as function of time in first (blue solid line) and second order (red dashed line) Magnus expansion. We use results from a numerical integration of the functions $\chi(t)$ and $\psi(t)$ explained in the text. Parameters for $V_0 = 5$ and $m = 1$. There is no visible difference between the orders.

This means that the third order contribution has the same structure as the first order matrix Ω_1, but the integrals are now over three variables and more complicated

$$\Omega_3(t) = \frac{\mathrm{i}V^3}{6}\int_0^t \mathrm{d}t_1 \int_0^{t_1} \mathrm{d}t_2 \int_0^{t_2} \mathrm{d}t_3 \Big\{ 4\sin[\phi_2 - \phi_3](\sigma_y \cos\phi_1 - \sigma_x \sin\phi_1) + 4\sin[\phi_2 - \phi_1](\sigma_y \cos\phi_3 - \sigma_x \sin\phi_3) \Big\} \equiv -\mathrm{i}V^3 \begin{pmatrix} 0 & \theta^*(t) \\ \theta(t) & 0 \end{pmatrix}. \tag{3.2.37}$$

where we abbreviated the complicated integral by

$$\theta(t) \equiv -\frac{2}{3}\int_0^t \mathrm{d}t_1 \int_0^{t_1} \mathrm{d}t_2 \int_0^{t_2} \mathrm{d}t_3 \Big\{ \mathrm{e}^{\mathrm{i}\phi_1} \sin[\phi_2 - \phi_3] + \mathrm{e}^{\mathrm{i}\phi_3} \sin[\phi_2 - \phi_1] \Big\}$$

similar to the procedure in first order. The time evolution operator has the same form as in second order, only with the substitution $\chi(t) \to \chi(t) + V^2\theta(t)$. We will not discuss the function $\theta(t)$ any further. One could compute it numerically, but the direct numerical integration of the Schrödinger equation requires the same numerical effort but has the advantage of giving the (numerically) exact result.

Having computed the first three terms of the Magnus expansion (up to integrations), we make a remarkable observation for the non-interacting two-band problem. The nested commutators seem to have a clear structure in the sense, that even orders are proportional to σ_z and odd orders consist of off-diagonal elements made up from a time-dependent function and its complex conjugate. This could be checked by analysis of recursion formula for nested commutators as given in [Bla09]. The time evolution operator would then be of the form given above for second order and contain infinite sums of functions $\bar{\chi}(t) = \sum_n V^{2n}\chi_{2n}(t)$ and $\bar{\psi}(t) = \sum_n V^{2n+1}\psi_{2n+1}(t)$. In consequence, the solution to Hill's equation would be expressable in infinitely many sums over Bessel functions. In a similar expansion for the simpler Landau–Zener Problem (where the explicit solution of the time-dependent Schrödinger equation can be given) the resummation of the Magnus expansion has been achieved for $t \to \infty$ by [Roj10], yielding the well-known Landau–Zener result for the transition probability. We will not follow this line of investigation here, but instead try to find perturbative solutions that involve simple functions and have a clear physical interpretation.

Summary

We used the Magnus expansion for a systematic expansion of the solution of the time-dependent Schrödinger equation in commutators of the Hamiltonian with itself at different times. We gave closed analytical expressions for the first and second order results and discussed their behaviour. We found that the first order result for the occupation of the upper band shows already a very rich and complex time-dependence: A superposition of many frequencies with different amplitudes and the existence of resonances. This first order result eq. (3.2.31) gives a good overview of the possible dynamics within a single expression.

However, we have arrived at a stage, where it seems not desirable to go to higher order terms in solving the non-interacting two-band model with the Magnus expansion. We are not only interested in a solution in a single analytical expression as such, but we need to compute expectation values. This is only reasonable with not too involved analytical expressions. Therefore, we will follow another route: From the understanding we gained so far, it is possible to distinguish different physical situations for our system exhibiting resonances. In the subsequent sections, we will find approximate solutions away from resonance and directly in resonance.

3.3 Real Space Analysis

We saw that the first order Magnus expansion gives good results for the overall behaviour of the system but that the next orders do not lead to a significant improvement, as for example in giving better estimates for the correct resonance position. We thus go back to real space and analyse the system's behaviour there. This has often the advantage that the physical content of the relevant expressions is more transparent and approximations are easy to comprehend.

3.3.1 Transformation of Hamiltonian

We will now rewrite the non-interacting two-band Hamiltonian in a way that is well-suited for approximate solutions in and out of resonance.

Coordinate Transformation

Starting from the original Hamiltonian in coordinate space, eq. (3.1.1), we apply the transformation that diagonalises the single-band problem [Fuk73]. We introduce a new basis

$$|\alpha_n\rangle = \sum_l J_{l-n}(J_a/F)|a_l\rangle \qquad \text{and} \qquad |\beta_n\rangle = \sum_l J_{l-n}(J_b/F)|b_l\rangle, \tag{3.3.1}$$

and will always write $x_{a(b)} \equiv J_{a(b)}/F$ and $\Delta x = x_a - x_b$ as before. Inserting the inverse transformation into the original problem, eq. (3.1.1), and using relations for Bessel functions, we arrive at the Hamiltonian in the transformed basis [Fuk73]:

$$\mathcal{H} = \sum_l \left[\epsilon_l^- |\alpha_l\rangle\langle\alpha_l| + \epsilon_l^+ |\beta_l\rangle\langle\beta_l| + V \sum_n J_{l-n}(\Delta x)\left(|\alpha_l\rangle\langle\beta_n| + \text{h.c.}\right)\right], \tag{3.3.2}$$

where $\epsilon_n^\pm = \pm\Delta/2 + nF$, as in the original basis. We have thus removed the hopping terms at the cost of a direct coupling between any two sites of the two different bands, weighted by Bessel functions. This means the coupling between different and possibly remote sites, which is originally mediated by on-site coupling and subsequent hoppings, can be considered a higher order process in the original basis. But in the transformed basis, eq. (3.3.2), this coupling is now direct with a strength modified by the factor $J_{l-n}(\Delta x)$. This is schematically depicted in figure 3.11.

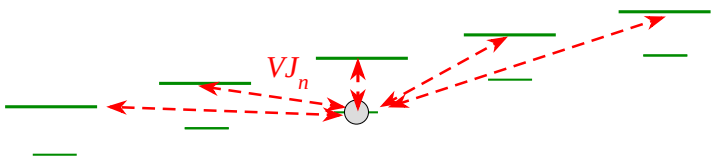

Figure 3.11: Graphical representation of the transformed non-interacting two-band Hamiltonian. Coupling between any sites of different bands is now directly possible instead of on-site transitions and subsequent hoppings. The coupling matrix elements are weighted by Bessel functions.

This transformed Hamiltonian will be discussed in the following sections. It has been derived earlier by Fukuyama *et al.* [Fuk73], but they concentrated on proving the existence of a Wannier–Stark ladder in the two-band problem. Furthermore, they mentioned the solveability of the $\Delta x = 0$ case but did not discuss resonances or the inter-band coupling in more detail. We will do both below.

Floquet Theory

Interestingly, the same matrix representation can be found by application of Floquet theory to the time-periodic Hamiltonian eq. (3.2.7). We start again with the observation, that the Hamiltonian under consideration is periodic in time and can thus be expanded in a Fourier series

$$\tilde{\mathcal{H}}(t) = \tilde{\mathcal{H}}(t+T_B) = \sum_{n\in\mathbb{Z}} H^n \mathrm{e}^{\mathrm{i}\omega_B t} \qquad \text{with} \qquad \omega_B = \frac{2\pi}{T_B} = F, \tag{3.3.3}$$

with coefficients H^n that are themselves 2×2 matrices. Floquet theory as we want to apply it here consists in the statement that the solution of the time-dependent problem is equivalent to solving a larger but stationary problem [Shi63, Shi65]. Indeed, one has to solve the eigenvalue problem for the *Floquet operator* $\mathcal{H}_F$ with matrix elements

$$(\mathcal{H}_F)^{n,k}_{\alpha\gamma} = H^{n-k}_{\alpha\gamma} + n\omega_B \delta_{\alpha\gamma}\delta_{nk} \qquad \text{with} \qquad n,k\in\mathbb{Z};\ \ \alpha,\gamma = a,b. \tag{3.3.4}$$

Instead of a small but time-dependent problem, the Floquet matrix to be diagonalised is infinitely large but constant in time. Rewriting the exponentials in sine and cosine functions, we make again use of the Fourier expansions (see appendix C)

$$\begin{aligned} \cos\left(\Delta x \sin Ft\right) &= J_0(\Delta x) + \sum_{n=1}^{\infty} 2J_{2n}(\Delta x)\cos(2nFt) \\ \sin\left(\Delta x \sin Ft\right) &= \sum_{n=0}^{\infty} 2J_{2n+1}(\Delta x)\sin\left((2n+1)Ft\right). \end{aligned} \tag{3.3.5}$$

We obtain the Fourier components for the Floquet operator

$$\begin{aligned} H^0 &= \begin{pmatrix} -\frac{\Delta}{2} & V \\ V & \frac{\Delta}{2} \end{pmatrix} \qquad \text{and} \qquad H^{2n} = VJ_{|2n|}(\Delta x)\begin{pmatrix} 0 & 1 \\ 1 & 0 \end{pmatrix} = VJ_{|2n|}(\Delta x)\sigma_x \\ H^{2n+1} &= \mathrm{sgn}(n)VJ_{|2n+1|}(\Delta x)\begin{pmatrix} 0 & -1 \\ +1 & 0 \end{pmatrix} = -i\mathrm{sgn}(n)VJ_{|2n+1|}(\Delta x)\sigma_y. \end{aligned} \tag{3.3.6}$$

Let us write the Floquet operator in matrix representation to see its structure more clearly:

$$\begin{pmatrix} \ddots & \vdots & & & & & \vdots & \\ \cdots & -\Delta/2 - F & VJ_0 & . & VJ_{-1} & . & VJ_{-2} & \cdots \\ & VJ_0 & \Delta/2 - F & VJ_1 & . & VJ_2 & & \\ & . & VJ_1 & -\Delta/2 & VJ_0 & . & VJ_{-1} & \\ & VJ_{-1} & . & VJ_0 & \Delta/2 & VJ_1 & & \\ & . & VJ_2 & . & VJ_1 & -\Delta/2 + F & VJ_0 & \\ \cdots & VJ_{-2} & . & VJ_{-1} & . & VJ_0 & \Delta/2 + F & \cdots \\ & \vdots & & & & & \vdots & \ddots \end{pmatrix}.$$

Instead of the time-dependent problem we now have a stationary problem but the corresponding matrix is infinite. But we find that this is the same matrix as the transformed Hamiltonian from the last section, eq. (3.3.2) in $\{|\alpha_n\rangle, |\beta_n\rangle\}$-representation. The transformation applied in the last section and the off-diagonal representation in momentum space derived earlier correspond to the same physical transformation.

3.3.2 Non-resonant Regime

We applied a non-local transformation in the previous section, that led to a direct coupling of any two sites in the different bands and removed the hopping terms. The Hamiltonian in the transformed basis reads (with on-site energies $\epsilon_l^{\pm} = lF \pm \Delta/2$ as before)

$$\mathcal{H} = \sum_l \Big[\epsilon_l^- |\alpha_l\rangle\langle\alpha_l| + \epsilon_l^+ |\beta_l\rangle\langle\beta_l| + V \sum_n J_{l-n}(\Delta x)\left(|\alpha_l\rangle\langle\beta_n| + \text{h.c.}\right)\Big].$$

For the specific system under consideration, i.e., atoms in optical lattices, both hopping coefficients J_a, J_b are smaller than unity and (since we are interested in strong inter-band coupling), the external Stark force F is much larger than the hopping coefficients: $\Delta x = (J_a - J_b)/F \ll 1$. This means that the coupling to remote sites can be neglected for non-resonant values of the force, since the zeroth order Bessel function is dominating. Thus, using $\Delta x \ll 1$ and $J_0(\Delta x) \approx 1$, the Hamiltonian away from resonance reduces to

$$\mathcal{H} \approx \sum_l \Big[\epsilon_l^- |\alpha_l\rangle\langle\alpha_l| + \epsilon_l^+ |\beta_l\rangle\langle\beta_l| + V\big(|\alpha_l\rangle\langle\beta_l| + \text{h.c.}\big)\Big]. \tag{3.3.7}$$

It is sum of independent two-level systems and easily diagonalised. The eigenvalues and eigenvectors read explicitly:

$$\omega_n^{\pm} = n \cdot F \pm \sqrt{\Delta^2/4 + V^2} \equiv n \cdot F \pm \tilde{\Delta}/2 \tag{3.3.8}$$

$$\begin{pmatrix} |\omega_n^+\rangle \\ |\omega_n^-\rangle \end{pmatrix} = \begin{pmatrix} \cos(\Theta/2) & \sin(\Theta/2) \\ -\sin(\Theta/2) & \cos(\Theta/2) \end{pmatrix} \begin{pmatrix} |\alpha_n\rangle \\ |\beta_n\rangle \end{pmatrix} \tag{3.3.9}$$

where $\Theta = \arctan(2V/\tilde{\Delta})$. The eigenstates are orthonormal $\langle\omega_l^\sigma|\omega_{l'}^{\sigma'}\rangle = \delta_{ll'}\delta_{\sigma\sigma'}$. For non-resonant values of the force, we have reduced the system to many independent two-level systems, all exhibiting simple Rabi oscillations for non-vanishing force. Such a simple behaviour was shown in figure 3.5. Inverting the eigenbasis transformation we find $|\alpha_n\rangle = \cos(\Theta/2)|\omega_n^+\rangle - \sin(\Theta/2)|\omega_n^-\rangle$ and $|\beta_n\rangle = \sin(\Theta/2)|\omega_n^+\rangle + \cos(\Theta/2)|\omega_n^-\rangle$ and for the occupation of the upper band when initially zero:

$$|\langle\beta_m|U(t)|\alpha_n\rangle|^2 = \frac{1}{4}\delta_{mn}\sin^2\Theta\left|\mathrm{e}^{-\mathrm{i}\omega_n^+} - \mathrm{e}^{-\mathrm{i}\omega_n^-}\right|^2 = \delta_{mn}\sin^2\Theta\cdot\sin^2\tfrac{\tilde{\Delta}t}{2}.$$

In the transformed basis, the inter-band coupling is purely local and there is accordingly no transport between different sites of the same band. On the other hand, there certainly is horizontal transport within the bands in the original real space basis. To see this, we compute the matrix elements of the time evolution operator in the original basis. They are easily computed by inserting eigenstates

$$\langle s_n|U(t)|s'_{n'}\rangle = \sum_l \sum_{\sigma=\pm} \langle s_n|\omega_l^\sigma\rangle\langle\omega_l^\sigma|s'_{n'}\rangle \mathrm{e}^{-\mathrm{i}\omega_l^\sigma t}, \qquad \text{with} \qquad s, s' = a, b. \tag{3.3.10}$$

Expressing $|\alpha_n\rangle$ and $|\beta_n\rangle$ in the original basis, we find

$$\langle a_n|\omega_l^+\rangle = \cos(\Theta/2)\cdot J_{n-l}(x_a) \qquad \langle a_n|\omega_l^-\rangle = -\sin(\Theta/2)\cdot J_{n-l}(x_a) \tag{3.3.11a}$$

$$\langle b_n|\omega_l^+\rangle = \sin(\Theta/2)\cdot J_{n-l}(x_b) \qquad \langle b_n|\omega_l^-\rangle = \cos(\Theta/2)\cdot J_{n-l}(x_b) \tag{3.3.11b}$$

Together with the eigenenergies and Graf's addition formula (see appendix C)

$$\sum_l \tau^l J_l(x) J_{n+l}(y) = \left(\frac{y - x/\tau}{y - x\tau}\right)^{n/2} J_n\left(\sqrt{x^2 + y^2 - xy(\tau + 1/\tau)}\right)$$

the matrix elements of the time evolution operator in the original basis read explicitly [Plö]

$$\begin{aligned}
\langle a_n|U|a_{n'}\rangle &= \left(\cos\tfrac{\tilde{\Delta}t}{2} - \mathrm{i}\cos\Theta\sin\tfrac{\tilde{\Delta}t}{2}\right)\mathrm{e}^{-\mathrm{i}(n'-n)(Ft-\pi)/2} J_{n'-n}(2x_a\sin(Ft/2))\mathrm{e}^{-\mathrm{i}nFt} \\
\langle b_n|U|b_{n'}\rangle &= \left(\cos\tfrac{\tilde{\Delta}t}{2} + \mathrm{i}\cos\Theta\sin\tfrac{\tilde{\Delta}t}{2}\right)\mathrm{e}^{-\mathrm{i}(n'-n)(Ft-\pi)/2} J_{n'-n}(2x_b\sin(Ft/2))\mathrm{e}^{-\mathrm{i}nFt} \\
\langle b_n|U|a_{n'}\rangle &= -\mathrm{i}\sin\Theta\sin(\tfrac{\tilde{\Delta}t}{2})\mathrm{e}^{\mathrm{i}(n'-n)\Phi(x_a,x_b,F,t)/2} J_{n'-n}\left(\sqrt{x_a^2 + x_b^2 - 2x_a x_b\cos Ft}\right), \\
&\text{where } \tan\Phi(x_a,x_b,F,t) = -\frac{x_a^2\sin 2Ft - 2x_a x_b\sin Ft}{x_a^2\cos 2Ft - 2x_a x_b\cos Ft + x_b^2}.
\end{aligned} \tag{3.3.12}$$

We see that there is a clear coupling to neighbouring sites within the same band, similar to the single-band case we reviewed at the beginning of this chapter. This force induced motion to other sites in the same band works in the same fashion in both bands, it is proportional to a Bessel function whose argument is the ratio between hopping strength in the respective band and the external force multiplied with a time-dependent factor inducing the Bloch oscillations. But in contrast to the single band case, there is finite coupling of the bands, leading to an occupation of both bands and present in the time evolution operator in form of prefactors $\sin\Theta = \sin(\arctan(2V/\Delta))$ depending on the band-coupling $V = C_0 F$. As before, these non-resonant inter-band oscillations have a period $T = 2\pi/\tilde{\Delta}$. The inter-band transition matrix element of the time evolution operator $\langle a_n|U|b_n\rangle$ shows the same time- and coupling-dependent prefactors. But it features furthermore a complicated phase factor $\mathrm{e}^{\mathrm{i}\Phi(x_a,x_b,F,t)}$ and the argument of the Bessel function is more complicated than before.

Interesting and complex structures are found in the the time evolution of wave packets. This is shown below in figure 3.12. As in the single band case, we study two different initial states: a single-site wave function (part (a) of figure 3.12) and a Gaussian wave packet (part (b) of figure 3.12). Shown are the time evolution within the lower band (when initially occupying the lower band, shown in the upper panel), the same for the upper band (when initially occupying the upper band, middle panel) and the coupling to the second band in time and real space, when starting in the lower band (lower panel in subfigure (a) and (b), respectively). In the time evolution of an initial single-site wave packet we observe breathing modes and a very weak coupling between the bands as expected in the regime of weak coupling. But the inter-band transitions (lower panel of subfigure (a)) have a rich structure of horizontal and vertical transport in real space. We observe a combination of breathing modes, inter-band oscillations and the effect of the time-dependent argument of the Bessel functions. The time evolution of the Gaussian wave packet is dominated by Bloch oscillations with an additional vertical inter-band coupling. The amplitude of the Bloch oscillations depends on the ratio between hopping strength and external force, just as in the single-band case, and is thus different in the two bands.

We see that the non-interacting two-band model is far from being simple, but shows a rich and complex time evolution present in real space and momentum space, even in the non-resonant regime. We will study the system in resonance now which will be central for the the following chapter.

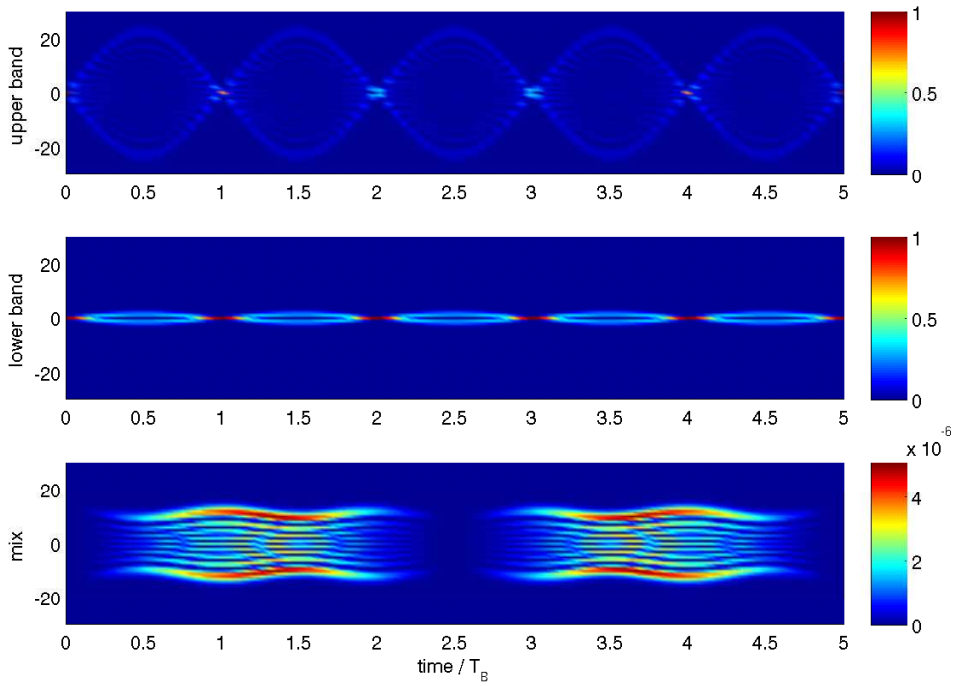

(a) Time evolution of single-site initial state in the upper band $|\langle b_n|U(t)|b_0\rangle|^2$ (top), lower band $|\langle a_n|U(t)|a_0\rangle|^2$ (middle) and transition amplitudes $|\langle b_n|U(t)|a_0\rangle|^2$ (bottom).

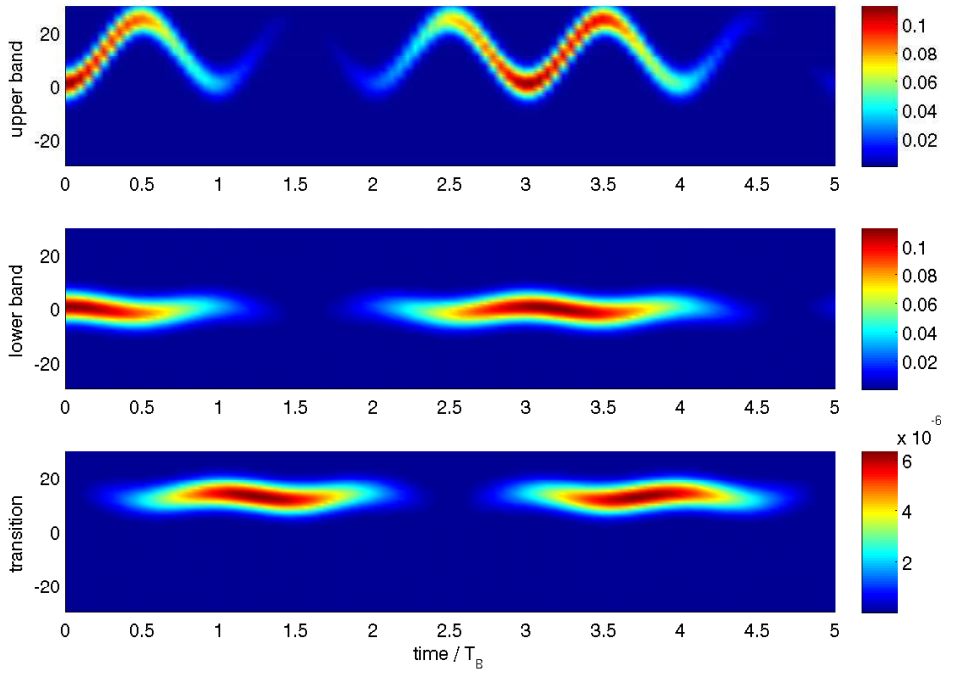

(b) Time evolution of Gaussian wave packet in the upper band $|\langle b_n|U(t)|\psi_0^b\rangle|^2$ (top), lower band $|\langle a_n|U(t)|\psi_0^a\rangle|^2$ (middle), and transition amplitudes $|\langle b_n|U(t)|\psi_0^a\rangle|^2$ (bottom).

Figure 3.12: Time evolution of two initial wave functions in the non-interacting two-band system.

3.4 System in Resonance

Having found resonances in the system in section 3.2, we are now going to study the resonant behaviour in more detail. We found numerically that the resonances are close to but not exactly at $\Delta = mF, m \in \mathbb{N}$ and that the system shows long time sinusoidal oscillations at resonance. The aim of this section is to find better theoretical estimates for the resonance position and the periods of the resonant oscillations.

3.4.1 Effective Model and Analysis of Resonances

Effective Hamiltonian

The Hamiltonian in the transformed basis, eq. (3.3.2), contains a direct coupling of any two sites from different bands, weighted by Bessel functions.

$$\mathcal{H} = \sum_l \left[\epsilon_l^- |\alpha_l\rangle\langle\alpha_l| + \epsilon_l^+ |\beta_l\rangle\langle\beta_l| + V \sum_n J_{l-n}(\Delta x) \left(|\alpha_l\rangle\langle\beta_n| + \text{h.c.} \right) \right],$$

with $\epsilon_l^\pm = lF \pm \Delta/2$ as in the original basis. Written in matrix form it reads

$$\begin{pmatrix}
\ddots & \vdots & & & & & \vdots & \\
\cdots & -\Delta/2 - F & VJ_0 & . & VJ_{-1} & . & VJ_{-2} & \cdots \\
 & VJ_0 & \Delta/2 - F & VJ_1 & . & VJ_2 & & \\
 & . & VJ_1 & -\Delta/2 & VJ_0 & . & VJ_{-1} & \\
 & VJ_{-1} & . & VJ_0 & \Delta/2 & VJ_1 & & \\
 & . & VJ_2 & . & VJ_1 & -\Delta/2 + F & VJ_0 & \\
\cdots & VJ_{-2} & . & VJ_{-1} & . & VJ_0 & \Delta/2 + F & \cdots \\
 & \vdots & & & & & \vdots & \ddots
\end{pmatrix}.$$

When the system is exactly in resonance, there is a degeneracy (or near degeneracy) between two energy levels of the two bands and the most relevant coupling in the transformed basis is the direct one between these two levels. We marked the two nearly degenerate energy levels and their couplings in the matrix above for a resonance of order $m = 2$. Reducing the matrix to this coupling corresponds to lowest order nearly degenerate perturbation theory. Such a reduction to an effective Rabi problem has for instance been applied by [Nak01] in a different context concerning Josephson junctions (see [Nak01]). In a resonance of order m, we can thus reduce the large matrix shown above to a system of independent 2×2-matrices, keeping only the nearly degenerate levels and their direct coupling [Plö10a]:

$$\mathcal{H}_{\text{res}}^{(m)} = \begin{pmatrix} \epsilon_{l-m}^+ & VJ_m(\Delta x) \\ VJ_m(\Delta x) & \epsilon_l^- \end{pmatrix}. \tag{3.4.1}$$

This will be our effective Hamiltonian for the system in resonance. We will compare the results from this approximate effective model to numerical simulations and higher order corrections of nearly degenerate perturbation theory (compare also appendix D on nearly degenerate perturbation theory).

Position of Resonances

Before discussing the physics contained in this reduction, let us point out that we still need better values for the resonant positions. As mentioned earlier, the simple relation $\Delta = mF$ is not precise enough, since it brings us close to the resonance, but does not yield inter-band oscillations of amplitude unity. The exact position of the resonances is given at values of the external force, where the band gap of a full diagonalisation is an integer multiple of the applied force

$$E_l^+(F) - E_l^-(F) = mF, \quad m \in \mathbb{N} \qquad \text{with} \qquad \mathcal{H}\,|E_l^\pm\rangle = E_l^\pm(F)|E_l^\pm\rangle.$$

Note that this is an implicit equation for the resonant values of the force since the eigenenergies will clearly depend on the force themselves. But the exact eigenstates of the system are not known. However, in the regime we are interested in $\Delta x \ll 1$ and we can use the approximate solution, eq. (3.3.8). Thus the position of a resonance of order m is approximately given by

$$mF \stackrel{!}{=} \tilde{\Delta} = \sqrt{\Delta^2 + 4C_0^2F^2} \quad \Longrightarrow \quad F_m = \frac{|\Delta|}{\sqrt{m^2 - 4C_0^2}} \tag{3.4.2}$$

where the index m indicates a resonant value of the force of order m. Note that this approximation breaks down for $|C_0| > m/2$. This has never been a problem in our calculations since $|C_0| < 0.20$ for atoms in shallow optical lattices and decreases with growing lattice depth V_0. We used this formula for all numerical computations in resonance below and found it sufficient to determine the resonance position. To give an example, the maximum in the mean occupation for lattice depth $V_0 = 4$ in the vicinity of $F = \Delta/2$ is located at $F = 2.2207$ and the approximate formula, eq. (3.4.2) predicts $F_{m=2} = 2.2201$ (compare to $\Delta/2 = 2.195$). This agreement is sufficient since the resonances have a finite width, as will be discussed below. However, higher precision can be obtained by calculating corrections from other couplings using nearly degenerate perturbation theory. We will do this in section 3.4.2 below and obtain a nonlinear equation for F_m. The above result has the advantage that it gives an explicit formula for the resonance position and numerical values that have been used in this and the following chapter of this thesis are summarised in appendix A.

Resonant Oscillations

The independent 2×2 matrices from eq. (3.4.1) are straightforwardly diagonalised and the occupation of the upper band (when initially zero) follows a simple Rabi formula [Plö10a]

$$\mathcal{N}_b^{\text{res}}(t) = \frac{4V^2J_m^2(\Delta x)}{(mF-\Delta)^2 + 4V^2J_m^2(\Delta x)}\,\sin^2\left(\Omega_{\text{res}}^{(m)}t\right), \quad \text{with } \Omega_{\text{res}}^{(m)} = |VJ_m(\Delta x)| \tag{3.4.3}$$

where we used the resonance condition $\epsilon_{l-m}^+ - \epsilon_l^- \approx 0$. The frequency of the resonant oscillations is given by $\Omega_{\text{res}}^{(m)}$ and is much smaller than the Bloch frequency $\omega_B = 2\pi/T_B$. The periods corresponding to the resonant oscillations are thus given by

$$T_{\text{res}}^{(m)} = \frac{F}{2|VJ_m(\Delta x)|}\,T_B. \tag{3.4.4}$$

To summarise, the system in resonance exhibits oscillations between the two bands of an amplitude close to unity and on a time scale much larger than the direct on-site oscillations. Numerical values for the periods of the resonant oscillations are given in table 3.1 below. The periods increase quickly with the order of the resonance m and also with the lattice

T_{res}/T_B	$m=1$	$m=2$	$m=3$	$m=4$	$m=5$
$V_0=2$	16.09	43.25	106.39	250.18	572.84
$V_0=3$	27.44	113.91	429.43	1544.55	5404.77
$V_0=4$	45.11	284.82	1626.25	8849.97	46835.47
$V_0=5$	71.66	676.50	5760.15	46716.18	368359.33

Table 3.1: Periods of resonant oscillations of the non-interacting two-band system. Numerical values are given in units of Bloch periods for different lattice depths V_0 and orders of resonance m. The periods increase rapidly with the order of resonance.

depth. The reason for this behaviour is the following. Since $\Delta x \ll 1$, the Bessel functions can be approximated as $J_m(\Delta x) \propto (\Delta x)^m/(2^m m!)$. All parameters depend on the depth of optical lattice, such that we obtain

$$T_{\text{res}}^{(m)}/T_B = \frac{2^{m-1}m!\,F}{(\Delta x)^m} = \frac{2^{m-1}m!}{m^{m+1}}\frac{\Delta^{m+1}}{|J_a - J_b|^m}. \tag{3.4.5}$$

The band gap Δ increases with growing lattice depth, but only slowly for our not too shallow lattices (the Wannier functions can be approximated by harmonic oscillator functions and the energy gap grows as $\sqrt{V_0}$). It therefore cannot compensate the exponential decrease of the hopping coefficients J_a, J_b with growing lattice depth (see eq. (1.4.4) in chapter 1), leading to an overall increase of the resonant periods with increasing V_0.

We compared the predictions for the periods of the resonant oscillations to numerical simulations. The results are summarised in figure 3.13. We observe a very good agreement on the logarithmic scale of figure 3.13. Additionally, the inset shows the relative error between the predicted and numerically observed values. It is approximately 5% for the widest resonance $m=1$, but smaller than 3% for higher resonances and slightly decreasing with increasing potential depth. The reason is that higher order corrections are proportional to Bessel functions and their argument $\Delta x = (J_a - J_b)/F$ decreases with increasing lattice depth, making these corrections smaller. Our results can be improved by using nearly degenerate perturbation theory (cf. appendix D) in the transformed basis as we will discuss in section 3.4.2 below.

Width of Resonances

The prediction for the occupation of the upper band in resonance, eq. (3.4.3), also allows us to estimate the width of the resonances. Indeed, considering the prefactor we expect a Breit-Wigner shape for the resonance as seen also numerically in related systems [Abu07]. The Breit-Wigner form of resonance of order m becomes obvious when averaging the occupation of the upper band, eq. (3.4.3), over time (F_m denotes the resonant force)

$$\overline{\mathcal{N}_b^{\text{res}}} = \frac{1}{2}\frac{\Gamma_m^2}{(1/F_m - 1/F)^2 + \Gamma_m^2}, \quad \text{with } \Gamma_m = 2\frac{|V J_m(\Delta x)|}{F_m \Delta}. \tag{3.4.6}$$

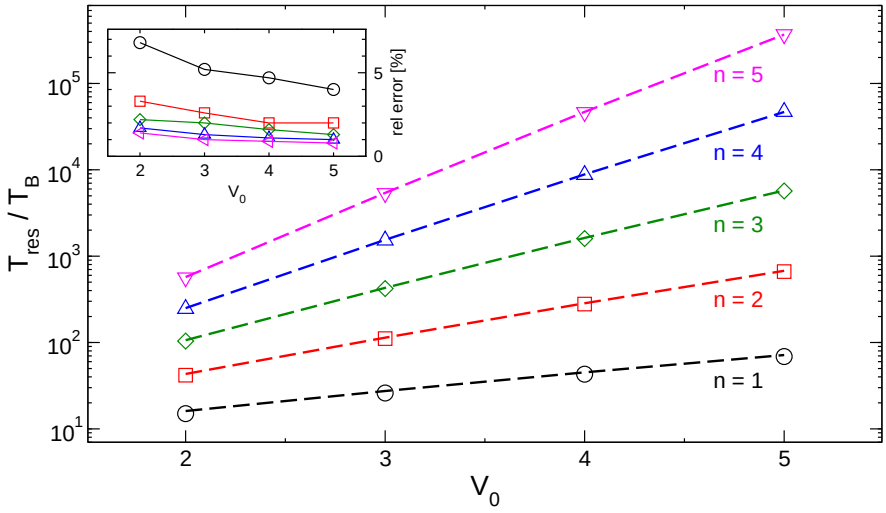

Figure 3.13: Periods of resonant oscillation exactly in resonance as predicted by the mapping on a two-level Rabi problem, eq. (3.4.3), (dashed lines) and compared to periods from numerical time evolution at resonant values of the force, according to eq. (3.4.2) (data points). The inset shows the relative error between the two values.

The width (as full width at half maximum) of the resonances is accordingly given by $2\Gamma_m$. Comparing to numerical simulations (see below), the effective model presented here gives a good estimate for the width of resonances. In particular, the width decreases very quickly with the order of the resonance or the depth of the optical lattice, since

$$2\Gamma_m \approx \frac{4|C_0|}{\Delta} \frac{m^m}{2^m m!} \left(\frac{J_a - J_b}{\Delta} \right)^m \tag{3.4.7}$$

where the factor $m^m/2^m m!$ is of the order one (for $m = 1, \ldots, 10$). Using $(J_a - J_b) \ll \Delta$, we see that the last factor decreases very rapidly. Numerical values are given in the following table and summarised in figure 3.14. Higher accuracy can be obtained by degenerate perturbation theory in the resonant basis, but we will not compute them here.

width $2\Gamma_m$	$m = 1$	$m = 2$	$m = 3$	$m = 4$	$m = 5$
$V_0 = 2$	$2.28 \cdot 10^{-2}$	$8.42 \cdot 10^{-3}$	$3.49 \cdot 10^{-3}$	$1.53 \cdot 10^{-3}$	$6.87 \cdot 10^{-4}$
$V_0 = 3$	$1.05 \cdot 10^{-2}$	$2.50 \cdot 10^{-3}$	$6.65 \cdot 10^{-4}$	$1.86 \cdot 10^{-4}$	$5.39 \cdot 10^{-5}$
$V_0 = 4$	$5.31 \cdot 10^{-3}$	$8.25 \cdot 10^{-4}$	$1.44 \cdot 10^{-4}$	$2.65 \cdot 10^{-5}$	$5.03 \cdot 10^{-6}$
$V_0 = 5$	$2.88 \cdot 10^{-3}$	$3.00 \cdot 10^{-4}$	$3.50 \cdot 10^{-5}$	$4.326 \cdot 10^{-3}$	$5.48 \cdot 10^{-7}$

Table 3.2: Widths of resonances as predicted by the effective model for different lattice depths V_0 and orders of resonance m. The width decreases rapidly with the order of resonance.

We are now in a position where we have reliable predictions for the off-resonant and resonant oscillations of the system. Combining both results, we can compare them with numerical simulations over a wide range of force values, i.e. inter-band couplings. In figure 3.15 below, we performed time evolutions of an initial state occupying only the lower band over very long times to ensure the system is beyond the onset of resonant

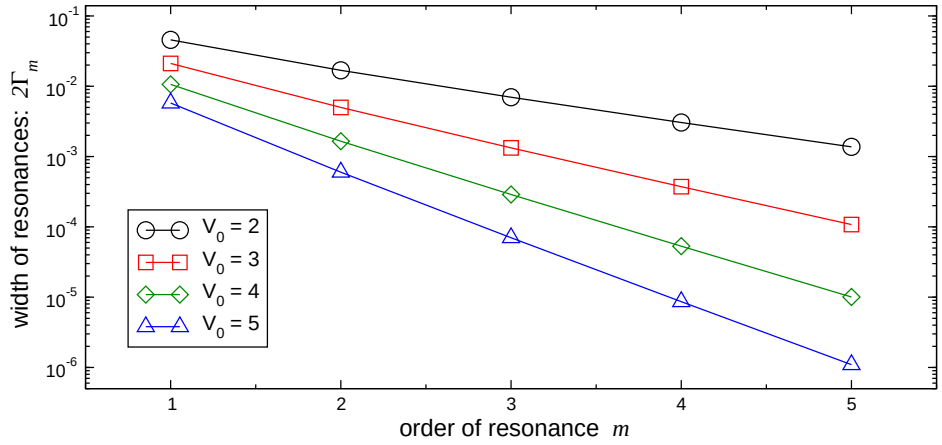

Figure 3.14: Width of first five resonances in the occupation of the upper band for the non-interacting two-band system as predicted by the effective model. The widths $2\Gamma_m$, as given by eq. (3.4.6), are shown as a function of the order of the resonance m and for different potential depths V_0. For a comparison with numerical data, see the following figure 3.15 below.

oscillations and afterwards averaged the occupation of the upper band over time. The resultant average occupation of the upper band is shown as function of the external force. These are compared to our theoretical predictions by summing both the contributions from the average occupation in the off-resonant regime eq. (3.2.19) as well as the resonant contribution eq. (3.4.6) described above. For the latter we could note simply sum over the different resonances, but had to ensure that they are only taken into account close to resonance, i.e., only in the range of near degeneracy. This was done by using an additional cut-off.

We see that the theoretical prediction, within the approximations made above, describes the numerical results to high degree of accuracy. The off-resonant average oscillation match very well. Please note, that even a small deviation of the order of 10^{-3}, such as contributions from far-away resonances, would be visible in this logarithmic plot. The insets show a zoom at the different resonances and confirm that the widths of the resonances are in good agreement with our theory. The resonances show, as mentioned earlier, a more complex structure than only Breit-Wigner shape, especially at higher resonances. They are asymmetric there, including a dip, and more reminiscent of Fano-shaped resonances. Our simple theory does not capture this additional structure, but still gives good estimates for the widths, even at higher order resonances.

3.4.2 Perturbation Theory

So far we have used the lowest order nearly degenerate perturbation theory for the system in resonance. This reduction to a two-level model enabled us to compute several observables in a simple fashion. These were in good agreement with our numerical results. Nevertheless, to underline the validity of our effective model, we want to compare with perturbation theory in the untransformed basis and will also compute higher order corrections within the transformed basis to ensure that such corrections play only a minor role.

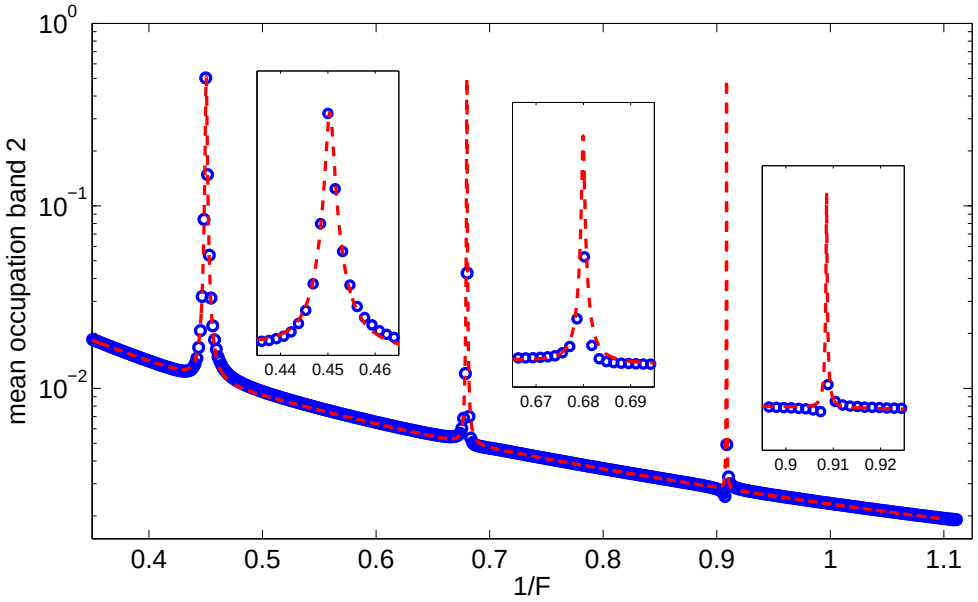

Figure 3.15: Mean occupation of the upper band as a function of the inverse force. Shown are the results of numerical simulations (blue data points) together with our theoretical prediction (red dashed line). The latter consists of a non-resonant background and Breit-Wigner resonances according to the effective model valid near resonance. We find excellent agreement between theory and numerics, only the asymmetry of higher order resonances is not reproduced.

Perturbation Theory in the Original Basis

We want to compare our results to nearly degenerate perturbation theory in the original basis. Here, the resonances of different order have to be treated separately. Starting with the first order resonance ($\Delta \approx F$), one block of the Hamiltonian in the original basis $\{|a_l\rangle, |b_l\rangle\}$ reads

$$\begin{pmatrix} \ddots & \vdots & & & \\ \dots & -\Delta/2 - F & V & -J_a/2 & . \\ & V & \Delta/2 - F & . & -J_b/2 \\ & -J_a/2 & . & -\Delta/2 & V \\ & . & -J_b/2 & V & \Delta/2 & \dots \\ & & & \vdots & \ddots \end{pmatrix}.$$

When the two central levels are nearly degenerate, it can be reduced in second order to

$$\begin{pmatrix} -\Delta/2 - F + \frac{V^2 - J_b^2/4}{\Delta} & V\frac{J_b - J_a}{2\Delta} \\ V\frac{J_b - J_a}{2\Delta} & -\Delta/2 - \frac{V^2 + J_a^2/4}{\Delta} \end{pmatrix} \tag{3.4.8}$$

giving a Rabi frequency of $\Omega = \frac{1}{2}|V(J_b - J_a)/\Delta|$ or, using $\Delta \approx F$, to a period of

$$\frac{T}{T_B} = \frac{F^2}{|V(J_b - J_a)|} \quad \text{vs.} \quad \frac{T_{\text{res}}^{(m=1)}}{T_B} = \frac{F}{2|VJ_1(\Delta x)|} \approx \frac{F^2}{|V(J_a - J_b)|}, \tag{3.4.9}$$

where we kept only the leading order behaviour of the Bessel function. We see that perturbation theory in the original basis leads to the same leading behaviour as the effective model. But the effective model has certainly the advantage of giving an immediate result for any order of resonance, whereas higher order resonances need to be treated in higher order perturbation theory when using the original basis.
We show this explicitly for the second order resonance ($\Delta \approx 2F$), where one bigger block of the Hamiltonian in the original basis $\{|a_l\rangle, |b_l\rangle\}$ reads

$$\begin{pmatrix}
\ddots & \vdots & & & & & & \\
\dots & -\Delta/2 - F & V & -J_a/2 & . & & & \\
 & V & \Delta/2 - F & . & -J_b/2 & & & \\
 & -J_a/2 & . & -\Delta/2 & V & -J_a/2 & . & \\
 & . & -J_b/2 & V & \Delta/2 & . & -J_b/2 & \\
 & & & -J_a/2 & . & -\Delta/2 + F & V & \\
 & & & . & -J_b/2 & V & \Delta/2 + F & \dots \\
 & & & & & & \vdots & \ddots
\end{pmatrix}.$$

We marked the second and second last level as being nearly degenerate. Now, using third order nearly degenerate perturbation theory, this system can be reduced to

$$\begin{pmatrix}
\Delta/2 - F + \frac{V^2}{\Delta} - \frac{J_b^2}{4F} & \frac{V}{8F^2}(J_b^2 + J_a^2) \\
\frac{V}{8F^2}(J_b^2 + J_a^2) & -\Delta/2 - F - \frac{V^2}{\Delta} + \frac{J_a^2}{4F}
\end{pmatrix}. \tag{3.4.10}$$

It yields a Rabi frequency of $\Omega = \frac{1}{2}|V(J_b^2 + J_a^2)/(8F^2)|$ or, using $\Delta \approx 2F$, the period of the resonant oscillations in perturbation theory reads

$$\frac{T}{T_B} = \frac{8F^3}{|V(J_b^2 + J_a^2)|} \quad \text{vs} \quad \frac{T_{\text{res}}^{(m=2)}}{T_B} \approx \frac{4F^3}{|V(J_a^2 + J_b^2 - 2J_aJ_b)|}. \tag{3.4.11}$$

It differs slightly from the leading order behaviour of the transformed basis result. Higher order resonances can be computed in a similar fashion, but the resonant basis, eq. (3.3.1), is clearly a better starting point for further calculations.

Perturbation Theory in the Transformed Basis

The effective model derived at the beginning of this section, consisted in reducing a large matrix with pairs of diagonal elements being nearly degenerate and directly coupled, to a system of independent 2×2 matrices with these elements and their couplings only. As mentioned before, this is lowest order nearly degenerate perturbation theory, as described in appendix D. We found very good agreement for the periods of the resonant interband oscillations and the width of the resonances between this simplified description and numerical simulations of the full problem. In this section we want to discuss the corrections to our effective model by higher orders of nearly degenerate perturbation theory.

The full problem in the transformed basis $\{|\alpha_l\rangle, |\beta_l\rangle\}$ reads

$$\mathcal{H} = \sum_l \left[\epsilon_l^- |\alpha_l\rangle\langle\alpha_l| + \epsilon_l^+ |\beta_l\rangle\langle\beta_l| + V \sum_n J_{l-n}(\Delta x)\,(|\alpha_l\rangle\langle\beta_n| + \text{h.c.})\right],$$

with $\epsilon_l^{\pm} = lF \pm \Delta/2$ as before. A level of the lower and upper band are nearly degenerate when $\epsilon_{l-m}^{+} \approx \epsilon_l^{-}$ or $mF \approx \Delta$. Using degenerate perturbation theory, we can find an two-level system with corrections from higher order processes. Keep in mind that we have coupling only between states from different bands. Therefore, only even orders perturbation theory enter the diagonal elements in the effective two-level system (for second order, the initial state couples to an unperturbed state in a different band and goes directly back to the initial state). For the same reason only odd orders of perturbation theory contribute to the off-diagonal elements. Following directly the expressions derived in appendix D we obtain the following effective two-level system including contributions up to third order

$$\begin{pmatrix} \epsilon_{l-m}^{+} + \sum_{i\neq l} \frac{|V_{l-m-i}|^2}{\epsilon_{l-m}^{+} - \epsilon_l^{-}} & V_{-m} + \sum_{i\neq l} \sum_{j\neq l-m} \frac{V_{l-m-i}V_{i-j}V_{j-l}}{(\epsilon_{l-m}^{+} - \epsilon_l^{-})(\epsilon_l^{-} - \epsilon_j^{+})} \\ V_{-m} + \sum_{i\neq l} \sum_{j\neq l-m} \frac{V_{l-m-i}V_{i-j}V_{j-l}}{(\epsilon_{l-m}^{+} - \epsilon_l^{-})(\epsilon_l^{-} - \epsilon_j^{+})} & \epsilon_l^{-} + \sum_{i\neq l-m} \frac{|V_{l-i}|^2}{\epsilon_l^{-} - \epsilon_i^{+}} \end{pmatrix}. \tag{3.4.12}$$

where we abbreviated $VJ_m \equiv V_m$ and the resonant terms ($mF = \Delta$) have been excluded from the summation. This reduced two-by-two system is valid in third order perturbation theory. How large is the correction by these additional terms? The $V_m = C_0 F J_m(\Delta x)$ are all proportional to C_0 and F, the only difference stems from the different Bessel functions. Since $\Delta x \ll 1$ for our parameters, it is sufficient to discuss the leading order behaviour of the Bessel functions, $J_m(x) = x^m/(2^m m!)$, showing that they decrease rapidly with increasing order.

We can use the above expression to find an improved estimate for the resonance condition. In resonance the diagonal elements in the effective two-level system are exactly degenerate and we obtain as new resonance condition

$$\Delta = mF - 2\sum_{i\neq m} \frac{|V_i|^2}{\Delta - iF}. \tag{3.4.13}$$

This is a nonlinear equation for the resonant value of the external force F_m since the coupling matrix elements also depend on the force $V_m = C_0 F J_m((J_a - J_b)/F)$. One can find numerical solutions in the vicinity of $\Delta = mF$ to obtain better values for the resonance condition. We did that for the already mentioned case of $V_0 = 4$ and $m = 2$. The simplest estimate is $F_2^{(0)} = \Delta/2 = 2.195$, compared to $F_2^{(3)} = 2.22067$ in third order perturbation theory as just described. The result from a direct integration of the Schrödinger equation is $F_2^{\text{num}} = 2.2207$. Remembering the finite width of the peak in the mean occupation of the upper band (it is $2\Gamma_2 = 3.0 \cdot 10^{-4}$ for $V_0 = 4$ and $m = 2$), the agreement is excellent.

It is also possible to compute the time evolution of an initial state in third order perturbation theory or the occupation of the upper band. The eigenstates in third order perturbation theory are given by

$$\begin{aligned} |E_l^{+}\rangle^{(3)} &= -\sin[\Theta_m/2]|\alpha_l\rangle + \cos[\Theta_m/2]|\beta_{l-m}\rangle \\ |E_l^{-}\rangle^{(3)} &= \quad \cos[\Theta_m/2]|\alpha_l\rangle + \sin[\Theta_m/2]|\beta_{l-m}\rangle \end{aligned} \tag{3.4.14}$$

where the angle between the different unperturbed state reads in third order

$$\Theta_m = \arctan\left[\frac{2\left|V_{-m} + \sum_{i\neq l}\sum_{j\neq l-m} \frac{V_{l-m-i}V_{i-j}V_{j-l}}{(\epsilon_{l-m}^{+} - \epsilon_l^{-})(\epsilon_l^{-} - \epsilon_j^{+})}\right|}{\Delta - mF + 2\sum_{i\neq m} \frac{|V_m|^2}{\Delta - iF}}\right]. \tag{3.4.15}$$

The occupation of the upper band can now be computed similar to our earlier results for the off-resonant system and should be compared to numerical simulations.[1] Taking a closer look at the terms in the effective two-level system, we observe that the expressions are the same as found earlier by using the Magnus expansion, i.e. we would observe resonant oscillations of large amplitude with many smaller oscillations on top of it. We will not shown an explicit comparison between numerical and analytical data here, since it is clear that the physical mechanism is well understood by now and that we are able to obtain high accuracy by using degenerate perturbation theory. We gave an example for the mentioned accuracy by computing the resonance position.

3.5 Summary

This chapter was devoted to the dynamics in an isolated two-band system under the driving of a strong external force. In momentum space it is simply a two-level system with a strong time-dependent driving. This has applications in many areas of physics since two-level systems can still be discussed analytically to a large extent. Our study was motivated by experiments in with cold gases in optical lattices, but the results should be valid in different contexts. To understand other periodically driven two-level system, we suggest the following procedure as exemplified in the present chapter. First, introduce new amplitudes to obtain a purely off-diagonal two-level system. Second, use Floquet theory to find the stationary equivalent of the driven two-level system. This enables us to use nearly degenerate perturbation theory, which forms the third and last step. This route allowed us the computation of transition amplitudes with very high accuracy and should be extendible to other driven two-level systems.

We found that the external force couples the two bands, and can lead to resonant interband oscillations. We showed that solving the time-dependent Schrödinger equation for our system under strong and time-dependent driving is equivalent to a specific ordinary differential equation for which analytical solutions in closed form are not known. We thus turned to a perturbative analysis of the system. We applied a Magnus expansion in momentum space that showed how the interband oscillations consist of a multitude of frequencies, and that one of these dominates the long-time behaviour in case of resonance. The physical origin of the resonances is clear in real space: whenever the tilt by the external force is such that a lower and upper band level become energetically degenerate, the interband transport is enhanced. This process is also known as resonant tunnelling [Glü99, Sia07]. Reducing the system in nearly degenerate perturbation theory to independent two-level system for both the resonant and non-resonant case, we were able to give approximate expressions for the periods and amplitudes of the interband coupling in good agreement with numerical simulations.

Alltogether, the dynamics of transport in horizontal and vertical direction of this non-interacting two-band system is surprisingly rich and complex. Not only is it a beautiful example of complex quantum dynamics, it is also one of the few cases where a comprehensive analytical understanding is possible. With the addition of interactions to the system, the dynamics becomes even more sumptuous. This will be focused on in the next chapter.

[1] While working on the present text, a recent publication [Hau10] discussing a driven two-level system came to our attention. The authors apply a combination of Floquet and Van Vleck perturbation theory up to second order. They obtain similar results and find very good agreement between second order and full numerical simulations.

Chapter 4

The Interacting Two-band Model: Collapse and Revival

Contents

4.1 Collapse and Revival of the Interband Oscillations

4.1.1 Introduction

We studied a non-interacting two-band Bose–Hubbard model in the previous chapter and found well-pronounced resonances in the coupling between the two bands when the external force is varied. We found a sound theoretical description of the interband oscillations by the help of a basis transformation and nearly degenerate perturbation theory. It turned

out that the time evolution is surprisingly rich with horizontal and vertical transport taking place on the lattice simultaneously. The current chapter deals with the effect of weak inter-particle interactions on the interband oscillations. Our main questions is: What is the effect of inter-particle interactions on the occupation of the upper band? We will study the dynamics of the interband oscillations as a function of time and limit ourselves to the regime of weak interactions.

Quite generally, the interaction induces new time scales into this many-body system leading to a dephasing or revival of the resonant interband oscillations. Surprisingly, this bunch of new frequencies is organized such that the resonant interband oscillations show revivals with the time of the revival depending on the details of the system under investigation. The aim of this chapter is to study this effect in detail and to derive an (approximate) analytical description for all time scales of this interacting many-body system.

At the same time, this chapter deals with a complex quantum many-body system. The time evolution of the wave function depends on the interference between phases from several energy levels of the system. In contrast to the last chapter, it will not be possible to reduce this time evolution to an effective two-level system, not even approximately. The collapse and revival effect to be studied turns out to be a real many-body effect in this system. To arrive at such an understanding we will be forced to use numerical simulations in order to isolate possible physical mechanisms at work. This will later help us to formulate effective models which themselves will be tested against numerical experiments. In this respect, we will be applying the third approach to complex dynamics (numerics for model building) as outlined in the introduction of this thesis.

This chapter is organized as follows. We will start by a short motivation in giving an example for collapse and revival in a coherent time evolution in a many-body system realised with optical lattices. Then, we are going to discuss the Hamiltonian and the relevant scales of the system. This will be followed by a numerical study of the collapse and revival in the resonant interband oscillations. This numerically obtained understanding of the effect will be used to find and analytical description in the following section which will also be compared to numerical results. In a second step it will be possible to find finite-size corrections to our analytical model by introducing an effective spin system. We will close this chapter with a short summary.

Collapse and Revival of a BEC in an optical lattice

The collapse and revival of a many-body wave function of interacting bosons in optical lattices has been reported in an experiment by Greiner *et al.* [Gre02b]. We will shortly describe their work and the explanation of the collapse and revival effect found there. The effect reported in their work concerns a different system (single-band) and a different observable (matter wave interference pattern) and is thus not directly related to our effect to be shown later. However, we will use their method and discuss their collapse and revival effect as an illustration here.

In the experiments of Greiner *et al.* [Gre02b], bosonic atoms where loaded into a deep optical lattice (without external force), such that the system is well-described by the Hamiltonian

$$\mathcal{H} = \frac{U}{2}\hat{n}(\hat{n}-1), \qquad \hat{n} = a^\dagger a,$$

for each lattice site. Here $\hat{n}$ is the number operator, and the dynamics in the system is determined by the interaction between the atoms. The eigenstates are Fock states $|n\rangle$ and

the eigenenergies read $E_n = Un(n-1)/2$. The time evolution of a n-particle state is given by $|n\rangle(t) = \exp[-\mathrm{i}E_n t]|n\rangle(0)$ in units of $\hbar = 1$. If one prepares a coherent state

$$|\alpha\rangle = \mathrm{e}^{-|\alpha|^2/2} \sum_n \frac{\alpha^n}{\sqrt{n!}} |n\rangle$$

with amplitude α and mean number of atoms $\bar{n} = |\alpha|^2$ as initial state, the different Fock states evolve independently and the time evolution of the coherent state reads

$$|\alpha(t)\rangle = \mathrm{e}^{-|\alpha|^2/2} \sum_n \frac{\alpha^n}{\sqrt{n!}} \mathrm{e}^{-\mathrm{i}Un(n-1)t/2} |n\rangle.$$

Experimentally, a coherent state is prepared by loading the condensate into a shallow optical lattice first (such that the hopping is dominating $J \gg U$), the ground state for large systems is then superfluid and basically given by a coherent state. After this initial state preparation the lattice depth is strongly increased and only the interaction needs to be considered $U \gg J$. The authors now discuss the time evolution of a matter field $\psi = \langle\alpha(t)|\hat{a}|\alpha(t)\rangle$. Initially at time zero, such a matter wave has a well defined phase and one observes a good interference pattern in a time-of-flight measurement. But since the different Fock states acquire different phases, the coherent state dephases and the interference pattern will be washed out. However, for any given number of atoms n, the quantity $n(n-1)/2$ is always a (non-negative) integer and the different contributions will have an equal phase (modulo 2π) after a time $t_R = 2\pi/U$. In other words, the time evolution of the signal has a t_R-periodicity. Indeed, such a revival of the interference pattern at multiples of t_R has been observed experimentally as reported in [Gre02b] (cf. figure 4.1).

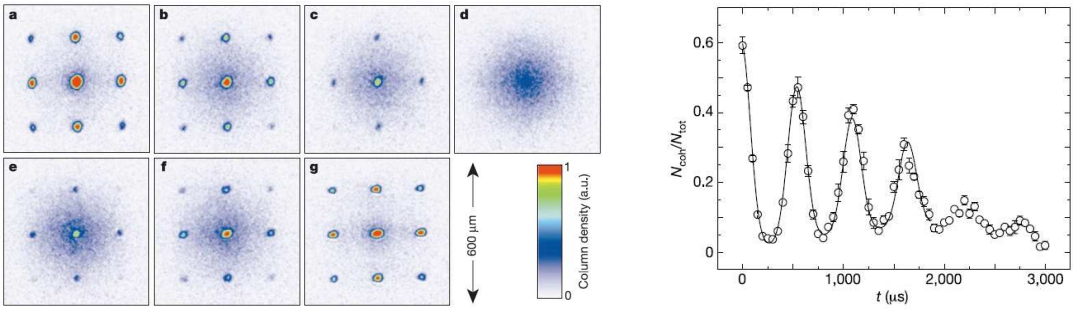

Figure 4.1: Collapse and revival in the dynamical evolution of the multiple matter wave interference pattern as observed experimentally by Greiner *et al.* [Gre02b]. *Left:* The interference pattern after different evolution times (a-g: $0, 100, 150, 200, 250, 350, 400,$ and 550μs). *Right:* Number of coherent atoms relative to the total number of atoms over time. Pictures taken from [Gre02b] and reproduced here by courtesy of the Nature Publishing Group.

From a theoretical point of view, the given description completely neglects the existence of various lattice sites. The reason is that, for very deep lattices as used for the experiments, there is no overlap between neighbouring wells (at least on the time-scales of the observed phenomena) and the site-index l in the Hubbard model can well be dropped. The many-sites coherent state $|\boldsymbol{\alpha}\rangle$ is simply a product of the local coherent states $\prod_l |\alpha\rangle_l$, all sites evolving independently. Later in this chapter, we will adopt a similar reasoning for collapses and revivals in the tilted two-band Bose–Hubbard model observed numerically.

4.1.2 The Hamiltonian

Real Space Respresentation

Let us start our discussion by restating the Hamiltonian to be studied and the relevant parameters. We want to describe interacting bosonic atoms in deep optical lattices under an external force. This is well described by the Bose–Hubbard model as explained in chapter 1. The force leads to coupling of the different energy bands and we therefore use a two-band Bose–Hubbard model. Applying a gauge transformation to the force accelerated frame of reference, the total Hamiltonian (cf. chapter 1) reads:

$$\begin{aligned} H(t) = \epsilon_a \sum n_l^a + \epsilon_b \sum n_l^b + FC_0 \sum (b_l^\dagger a_l + \text{h.c.}) - \tfrac{1}{2} J_a \sum (\mathrm{e}^{\mathrm{i}Ft} a_{l+1}^\dagger a_l + \text{h.c.}) \\ - \tfrac{1}{2} J_b \sum (\mathrm{e}^{\mathrm{i}Ft} b_{l+1}^\dagger b_l + \text{h.c.}) + \frac{1}{2} W_a \sum n_l^a (n_l^a - 1) + \frac{1}{2} W_b \sum n_l^b (n_l^b - 1) \\ + 2W_x \sum n_l^a n_l^b + \frac{1}{2} W_x \sum (b_l^\dagger b_l^\dagger a_l a_l + \text{h.c.}) \end{aligned} \tag{4.1.1}$$

It consists of the onsite energies per band which are given by either plus or minus half the band gap $\epsilon_{a,b} = \pm\Delta/2$. There is hopping between neighbouring lattice sites with strength $J_{a(b)}$ and the onsite interaction with strength $W_{a(b)}$ for band $a(b)$. The two bands are coupled by a force-induced coupling having the form of a dipole coupling (with dimensionless coupling strength C_0) and by two interactions terms (both proportional to W_x).[1] The processes in this model are schematically illustrated in figure 4.2.

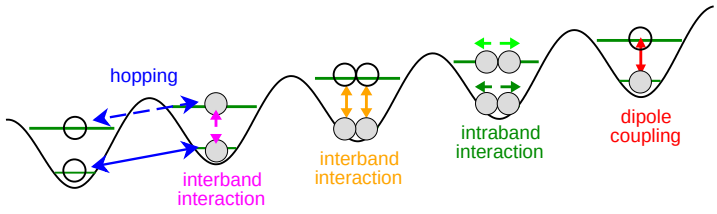

Figure 4.2: Schematical illustration of the interacting two-band Bose–Hubbard model. The different processes include hopping (blue) between neighbouring sites and onsite interaction in either bands (green), as well as an onsite coupling (red) between the bands and two terms with interband interaction (orange and magenta).

As a guiding line, we will use experimentally relevant values for the parameters appearing in the two-band model, determined by the depth of the optical lattice V_0. The external force will be taken as easily adjustable parameter. We will also vary the general strength of the interaction to study interaction effects. Table 4.1 gives values for the parameters for a given potential depth as we have used them in numerical simulations and figure 4.3 summarises

[1] We can reduce this expression by noting that the total particle number is the sum of the number of particles in the lower and upper band $N^a + N^b = N$, namely:

$$\epsilon_a \sum_l n_l^a + \epsilon_b \sum_l n_l^b = \epsilon_a N + (\epsilon_b - \epsilon_a) N^b = \epsilon_a N + \Delta \cdot N^b.$$

We drop the term proportional to N since it leads only to a constant shift of energy (and likewise for the quasienergies). This Hamiltonian is actually implemented in our numerical simulations and therefore only the bandgap Δ is shown in table 4.1.

this dependence. All parameters for the Hamiltonian used in numerical simulations can be found in appendix A.

V_0	Δ	C_0	J_a	J_b	W_a	W_b	W_x
2.0	2.97	-0.184	0.171	-0.924	0.023	0.014	0.010
3.0	3.68	-0.164	0.102	-0.769	0.027	0.016	0.011
4.0	4.39	-0.150	0.062	-0.620	0.030	0.018	0.012
5.0	5.05	-0.140	0.038	-0.487	0.032	0.020	0.014
10.0	7.77	-0.114	0.005	-0.121	0.040	0.027	0.018

Table 4.1: Parameters of the Bose–Hubbard model for different depths of the optical lattice. The band gap Δ is much larger than the hopping and interaction coefficients. The hopping coefficients have opposite sign reflecting the different curvature of the energy bands. The absolute values of both hopping coefficients are decreasing with growing lattice depth. All three interaction coefficients are of comparable size (with the interband interaction slightly smaller) and increase with growing lattice depth. All parameters are given in recoil energies E_R.

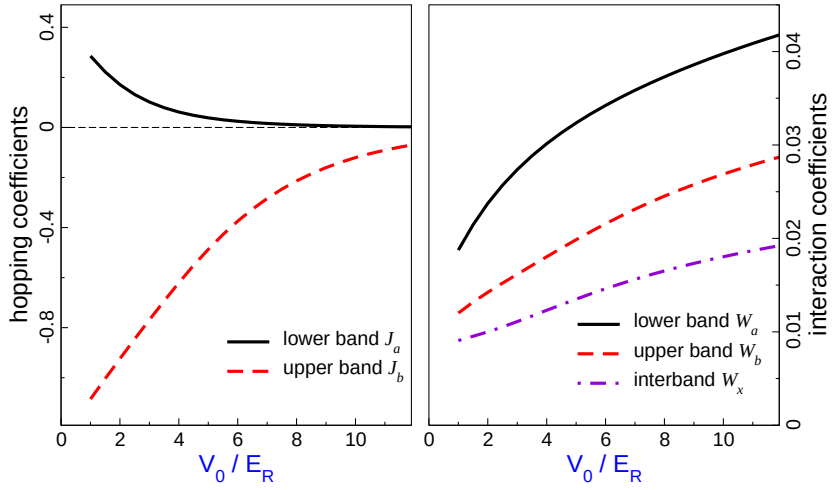

Figure 4.3: Dependence of the coefficients for the two-band Bose–Hubbrad model on the depth of the optical lattice. The Bose–Hubbard model is a good approximation for not to shallow potentials. All energies in units of the recoil energy E_R. Note that W_x appears in two processes in the Hamiltonian with different prefactors.

Our aim is to study the effect of a weak interaction on the resonant interband oscillations. We are thus dealing with a regime of strong interband dipole coupling and visible, i.e. not too narrow, resonances. The hierarchy of scales in this regime is characterised by the relations

$$\text{bandgap } \Delta \quad \gtrsim \quad \text{force } F \quad \gg \quad \text{hoppings } J_i, \text{interactions } W_i. \tag{4.1.2}$$

These relations should set only the general scene, since the details depend on the specific potential depth and order of resonance. For example, the hopping coefficients in the different bands usually differ by approximately one order of magnitude. However, we will always study sets of parameters as fixed by the depth of the optical lattice, such as given

in table 4.1 above, and kindly ask the reader to return to this table or appendix A when interested in numerical values of the parameters or scales in the system.

To study the effect of the interaction in total and motivated by the tunability of the scattering length (cf. section 1.1.1), we introduce a general coupling strength g via the replacement

$$W_i \longrightarrow gW_i, \quad i = a, b, x \tag{4.1.3}$$

such that $g = 0$ is the case without any of the interactions. We will use g in the following to compare different interaction strengths without the need to give all the different interaction coefficients. When studying the effect of only some of them, we will indicate their values separately.

Fourier Space Representation

Let us also give the momentum space representation of the two-band model by introducing Fourier components of the operators

$$A_k = \frac{1}{\sqrt{L}} \sum_l \mathrm{e}^{\mathrm{i}lk} a_l \qquad \& \qquad B_k = \frac{1}{\sqrt{L}} \sum_l \mathrm{e}^{\mathrm{i}lk} b_l.$$

After some standard manipulation, the Hamiltonian (up to some constant terms) reads

$$\begin{aligned} H(t) \;=\; & \sum_k \Big(-\frac{\Delta}{2} - J_a \cos(k + Ft) \Big) A_k^\dagger A_k + \Big(\frac{\Delta}{2} - J_b \cos(k + Ft) \Big) B_k^\dagger B_k \\ & + FC_0 \sum_k \Big(A_k^\dagger B_k + \mathrm{h.c.} \Big) + \frac{gW_a}{2L} \sum_{kk'q} A_{k'+q}^\dagger A_{k-q}^\dagger A_k A_{k'} + (a, A \to b, B) \\ & + \frac{2gW_x}{L} \sum_{kk'q} A_{k'+q}^\dagger B_{k-q}^\dagger A_k B_{k'} + \frac{gW_x}{2L} \sum_{kk'q} \Big(A_{k'+q}^\dagger A_{k-q}^\dagger B_k B_{k'} + \mathrm{h.c.} \Big). \end{aligned}$$

The hopping part of the Hamiltonian becomes obviously diagonal in momentum space and the gauge transformation $\psi \to \psi\, \mathrm{e}^{-\mathrm{i}Ftx}$ caused the effective substitution $k \to k + Ft$. The price to pay is the off-diagonal form of the interaction terms. The interaction is local in real space and therefore non-local in momentum space with the standard interpretation of an interaction process: two incoming particles with momenta k and k' scatter with momentum transfer q, leading to two new particles with momenta $k - q$ and $k' + q$ respectively. Setting all interaction terms to zero via $g = 0$, we recover the momentum space representation of the non-interacting two-band model as discussed in the previous chapter.

The momentum space version of the two-band Hamiltonian can be used as a starting point for different approximations, or, quite generally, for an application of many-body techniques from condensed matter theory. However, we saw that the momentum space treatment of the system in resonance is not as transparent as the resonant real space picture developed at the end of the previous chapter.[2] We will therefore not follow this momentum space version, but stick to the resonant real space basis. This will prove successful during the course of this chapter.

[2] Additionally, we are dealing with a non-equilibrium situation (at temperature $T = 0$) in the present chapter where quantum field theoretical methods are available but face additional complications. See [Ram07] for an introduction to field theoretical methods in non-equilibrium quantum systems.

4.1.3 Collapse and Revival of the Interband Oscillations

Observable and First Example

Let us recall the presence of resonances in the interband coupling from the previous chapter. We are studying the occupation of the upper band as a function of time where the interband coupling is introduced by the external force into the system. Fixing all parameters as being determined by the depth of the optical lattice, we choose the force as a free parameter. When varying the force, we found a strong increase of the mean occupation of the upper band for certain values of the force. These correspond to the case, when two energy levels of the lower and upper band are nearly degenerate and is analogous to the effect of resonantly enhanced tunnelling in the continuous Wannier–Stark system [Glü99, Sia07]. Our aim is now to study the effect of interactions on these resonant interband oscillations.

Our observable is again *the occupation of the upper band* $\mathcal{N}_b$ given by

$$\mathcal{N}_b(t) = \frac{1}{N}\langle\psi(t)|\sum_l n_l^b|\psi(t)\rangle, \tag{4.1.4}$$

which is normalised by the total particle number N and depends on the chosen initial state $|\psi_0\rangle$. This is exactly the same quantity as has been studied in the non-interacting two-band model and defined in eq. (3.2.4). It allows a direct connection to the results obtained there. We will only discuss approximately unit filling, $N \approx L$, and focus on the following situation: The system is prepared in an initial state $|\psi(0)\rangle$ with particles being delocalised over the lattice and occupying the lower band only, e.g. $|1,\ldots,1;0,\ldots,0\rangle$ for an equal number of particles and holes per band (and similarly for non-unit filling). This state is then evolved in time[3] according to the time-dependent Schrödinger equation and the occupation of the upper band is computed as expectation value according to eq. (4.1.4). Please recall that this observable showed a surprisingly rich behaviour even in the single-particle case. It is given by a superposition of many frequencies and shows large scale oscillations for resonant values of the force (cf. chapter 3).

Let us come to a specific example. We choose a system for a lattice depth $V_0 = 4$ which fixes the coefficients in the Hamiltonian. We consider a resonance of order two, i.e. $F \approx 2.2207$, and take five particles on five lattice sites per band, i.e. $N = 5 = L$. We choose an initial state that is equally distributed over the lower band, as is easily prepared experimentally, specifically we take $|\psi(0)\rangle = |11111;00000\rangle$. The exact form of the initial state can be varied without destroying the effect (see section 4.1.4). The occupation of the upper band is now computed for many time steps. This has been performed for a non-interacting many-body system ($g = 0$) and a weakly interacting system ($g = 0.1$). The result is shown in figure 4.4. For the non-interacting case, we find the behaviour known from the previous chapter: On short time scales the two bands are only weakly coupled, the occupation of the upper band occurring as a superposition of several oscillation frequencies with an amplitude of a few percent only (lower panel of the figure). On longer time scales,

[3] The time evolution is performed numerically and we used different algorithms to check the validity of our results. In most of the cases we used an adaptive step-size fifth order Runge–Kutta algorithm (taken from [Pre92, chap. 16.2]) for a direct integration of the time-dependent Schrödinger equation. This contains an adjustable parameter to tune the obtained accuracy. We checked, that the results obtained are sufficiently converged with respect to a variation of this numerical parameter. A second method used was to compute the Floquet–Bloch operator by the same algorithm and to use an eigenbasis expansion to obtain the wave function at integer multiples of the Bloch period.

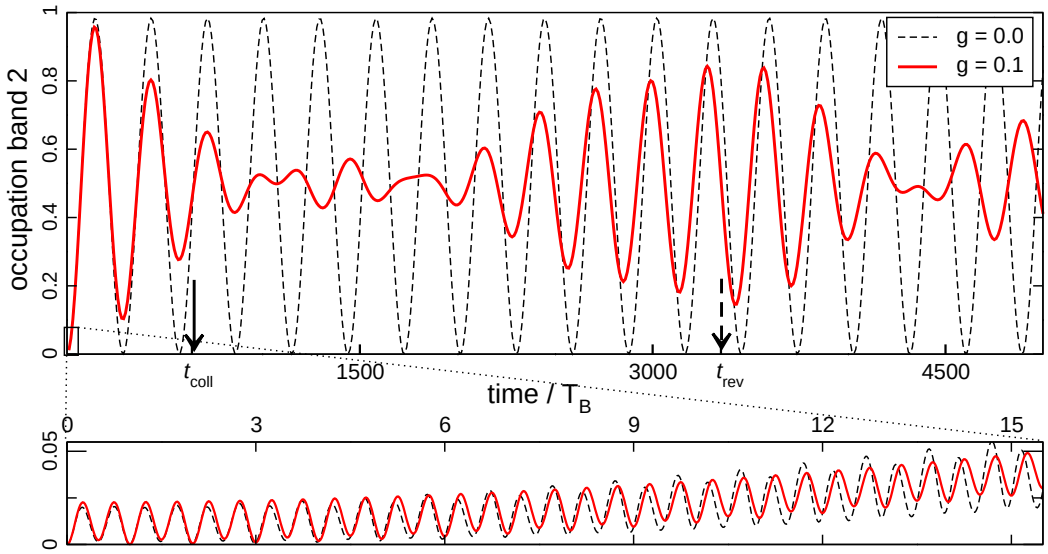

Figure 4.4: Occupation of the upper band as a function of time for a resonance of order $m = 2$. Shown are the cases of vanishing two-body interaction ($g = 0$, thin dashed line) and weak two-body interaction with all interaction terms ($g = 0.1$, thick line). We observe a collapse and revival with the collapse and revival times, t_{coll} and t_{rev}, indicated by arrows. *Lower panel:* Magnification of the initial oscillation showing small non-resonant oscillations (cf. section 3.2.2 and 3.2.3) on top of the resonant oscillations with a much longer period T_{res}. Parameters correspond to $V_0 = 4$, $N = 5 = L$.

the resonant behaviour is dominating leading to sinusoidal oscillations with a period much larger than the Bloch period and an amplitude of approximately 100%, i.e., the particles undergo complete interband transitions. As the interaction is turned on, we observe a similar behaviour on short time scales, with slight deviations from the non-interacting case, showing the presence of additional frequencies in the interband coupling. However, the inter-particle interaction leads to a striking effect on longer time scales: The resonant interband oscillations decay quickly and have collapsed after a few periods, but show a prominent revival at a later time. This first revival is then followed by several later revivals not shown in the figure (but present in figure 4.7 and 4.8 below). We also note, that the oscillations in the interacting system are not always in phase with the non-interacting case. There is, e.g., a clear phase shift of π at around $t = 1500\,T_B$. We interpret figure 4.4 as follows: the new frequencies introduced to the system by the interaction lead to a dephasing of several close-to-resonant interband oscillations but partly rephase at a later time to show a clear but not complete revival. This interpretation will be further explained and supported in the following sections. The time when the first revival shows its maximum will always be denoted as *revival time* and has been marked by an arrow in the example of figure 4.4. The corresponding time scale for the collapse is given by the time when the amplitude of the original oscillation has dropped to $1/\mathrm{e}$ of its initial value, which is at $\mathcal{N}_b(t_{\text{coll}}) \equiv (1+1/\mathrm{e})/2$ and is also marked by an arrow in the figure. Please note again, that the observed effect is clearly different from the one observed by Greiner *et al.* They studied a single-band system without external force, where resonant oscillations between the energy bands are not possible and the observable discussed by them was the interference pattern of the many-body wave function and not the occupation of the upper band.
Our main goal in this chapter will be to understand this revival phenomenon and to find

a theoretical model allowing its prediction in similar systems and an understanding of the dependence on all parameters. The main effect has been presented in the figure above and we are now going to compare it to other systems as well as check its dependence on the variation of several of the system's parameters.

Comparison to Quantum Optics

The dynamics in the interband oscillations under a weak repulsive interaction shown above strongly resembles the phenomenon of dephasing and revival being found paradigmatically in quantum optics. It appears in different contexts when several oscillations with close frequencies are superimposed [Mey91]. Let us discuss the effect and the theoretical description of the revival as it appears in the Jaynes–Cummings model (see also appendix B).

The dynamics of a two-level atom in a single-mode light field is well described by the Jaynes-Cummings model, taking into account the discrete, photonic nature of the light field. For not too strong fields, one can apply the rotating wave approximation ignoring non-energy conserving contributions and the system is easily diagonalised. One obtains a frequency $2g\sqrt{n+1}$ for induced Rabi floppings between two levels of the atom that depends on the photon number n of the light-state driving the transition and the coupling strength g between the two-level atom and the quantised light-field. The probability for an initially excited atom to be excited at a later time t when exposed to a beam of coherent light is then given by a sum of Rabi floppings weighted by the coherent state photon number distribution (characterised by an amplitude α)

$$p(t) = \sum_n p_n |b(t)|^2 = \mathrm{e}^{-|\alpha|^2} \sum_n \frac{|\alpha|^{2n}}{n!} \cos^2(g\sqrt{n+1}\, t). \tag{4.1.5}$$

As figure 4.5 illustrates, this probability collapses with $\mathrm{e}^{-(t/t_c)^2}$ (see [Mey91, chap. 13-2] for details) and shows a revival after a time t_r. This collapse is a result of a dephasing of

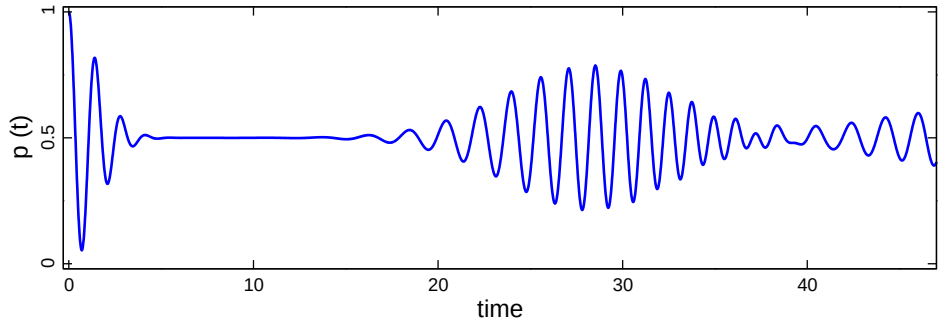

Figure 4.5: Collapse and revival for the probability to find the two-level atom stimulated by a coherent light field in an excited state, as described by eq. (4.1.5). This is a typical example for the collapse and revival phenomenon for a two-level atom in an external field as discussed in quantum optics. Parameters: amplitude $\alpha = 3$ and coupling $g = 0.7$.

oscillations at different frequencies and happens on a time scale directly connected to the range of dominant frequencies. The revival, on the other hand, is due to the discreteness of the frequency distribution, i.e., the sum of frequencies has a finite period. Both time scales turn out to be inversely proportional to the coupling strength [Mey91]

$$t_c^{-1} \propto g \quad \text{and} \quad t_r^{-1} \propto g. \tag{4.1.6}$$

Comparing this behaviour to the interaction-induced decay of the resonant oscillations in the two-band Bose–Hubbard model discussed above, the observed decay and revival times should show the same behaviour with respect to the interaction strength. This conjecture has been verified for different potential depths and the most stable resonance $m = 1$, the result is shown in figure 4.6. We find exactly the same behaviour for higher order resonances.

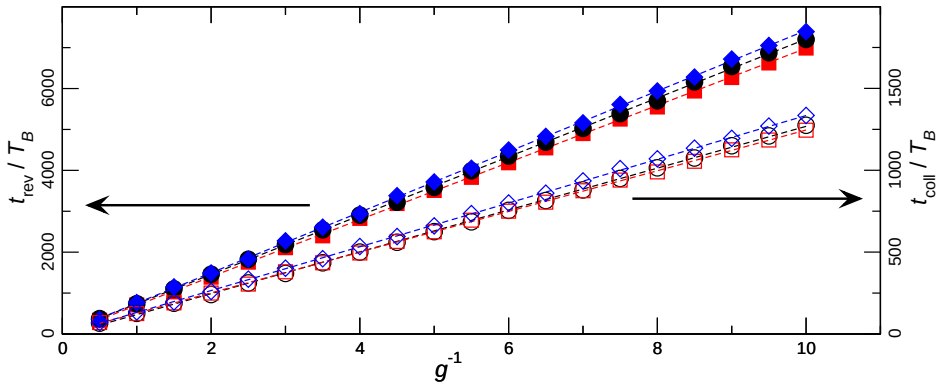

Figure 4.6: Collapse times (open symbols) and revival times (filled symbols) versus the inverse many-body interaction strength $1/g$ for the resonant interband oscillations in the two-band Bose–Hubbard model. Parameters $N = 5 = L$ and $V_0 = 4$ (squares), $V_0 = 5$ (circles), $V_0 = 6$ (diamonds). Order of the resonance: $m = 1$. The collapse time is defined via $\mathcal{N}_b(t_{\text{coll}}) = (1 + \mathrm{e}^{-1})/2$ and the revival time is chosen as the first maximum in the oscillations after initial decay $t > t_{\text{coll}}$, as indicated in figure 4.4.

This means, that the collapse and revival effect bears some similarity to the one observed in the interaction between a quantised light-field and a two-level system. However, it is not obvious how this analogy is to be seen in detail: The two states of the atom clearly correspond to the two bands in our Bose–Hubbard setup, but there is not a second degree of freedom like the light-field being characterised by simple bosonic Fock states. Instead we have bosonic atoms occupying a tilted lattice. The difference in the systems is further highlighted by considering the different Hilbert spaces and the absence of a simple solution in case of the interacting two-band Bose–Hubbard model. With the help of an effective model to be introduced in section (4.3.3) below, we will find that the analogy is indeed limited and that the revival times behave differently in both models. Nevertheless, the idea of a coherent state describing the light field will turn out to be useful later in an approximate description for the scaling of the revival time. But let us first study the stability of the effect in more detail.

4.1.4 Stability of the Collapse and Revival Effect

We found a clear collapse and revival effect in the occupation of the upper band when the system is in resonance and weakly interacting. In the present section, we are going to study the stability of this effect against variation of several parameters and would like to understand the frequencies present in the system. This will be done numerically and will guide us in the next section where we will derive an analytical expression for the revival time.

Variation of the Initial State

Let us first test the stability of the effect versus a slight variation of the initial state. The initial state should contain particles in the ground band only and they should be delocalised over the lattice. We performed numerical simulations using different seed states as initial states. Seed basis states with $\kappa = 1$, i.e. translational invariant states (cf. section 1.4.2), have been created from the following seed states for time evolutions:

$$|s_{19}\rangle = |30110; 00000\rangle \qquad |s_{20}\rangle = |21110; 00000\rangle$$
$$|s_{21}\rangle = |12110; 00000\rangle \qquad |s_{22}\rangle = |20210; 00000\rangle$$
$$|s_{23}\rangle = |11210; 00000\rangle \qquad |s_{24}\rangle = |12020; 00000\rangle$$
$$|s_{25}\rangle = |11120; 00000\rangle \qquad |s_{26}\rangle = |11111; 00000\rangle.$$

These are seed basis states enumerated by their position within the seed basis and they all have multiplicity $M = 5$ except for the last state $|s_{26}\rangle$ with $M = 1$ (cf. chapter 1 for details). Below we show the results for the occupation of the upper band with these states as initial states.

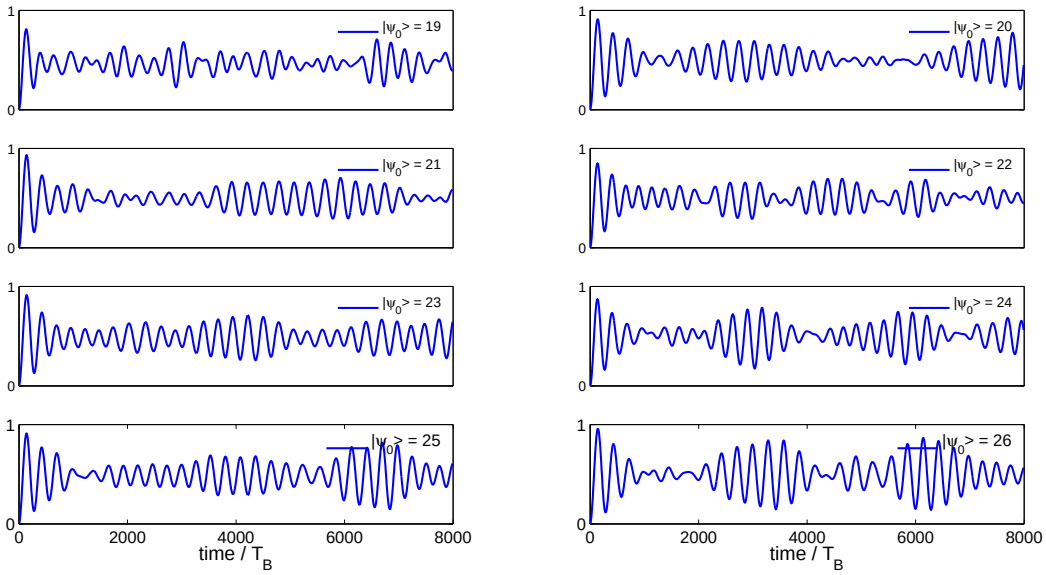

Figure 4.7: Occupation of the upper band as a function of time for different initial states $|\psi_0\rangle = |s_{19}, \kappa = 1\rangle, \ldots, |s_{26}, \kappa = 1\rangle$ (the number of the specific initial state is indicated in the legend) and $N = 5 = L$ for $V_0 = 4, m = 2$ and $g = 0.1$. We observe the presence of a collapse and revival effect as long as the initial states is mainly delocalised over the lattice. The specific position of the revival fluctuates with the initial state.

We observe a very clear collapse of the inter-band oscillations and also the presence of a revival as long as the particles are mainly delocalised in the lower band initially. The actual form and position slightly changes depending on the specific initial state. We also used linear combinations of these states and found similar results, i.e., the presence of collapse and revival with the details depending on the specific state under consideration. The delocalisation of the initial state over the lattice appears to be important for the revival phenomenon and will guide us in the theoretical modelling later. Note that the initial states

that have been used are translational invariant combinations of the states given above, such that an occupation of two atoms at a single site is also "smeared out" over the real space lattice. Altogether, we find that the collapse and revival effect in the two-band Bose–Hubbard model is stable against a variation of the initial state as long as the atoms are delocalised over the lattice.

Variation of the Total Particle Number

A second point to be tested is the stability of the effect against a variation of the total particle number. We performed numerical simulations for a fixed number of lattice sites and increased the number of atoms in the system. The result is shown for $V_0 = 4$, $m = 2$ and $g = 0.1$ in figure 4.8. The initial states were chosen with the largest possible delocalisation over the lower band, as e.g. $|10101, 00000\rangle$ for $N = 3$, $L = 5$.

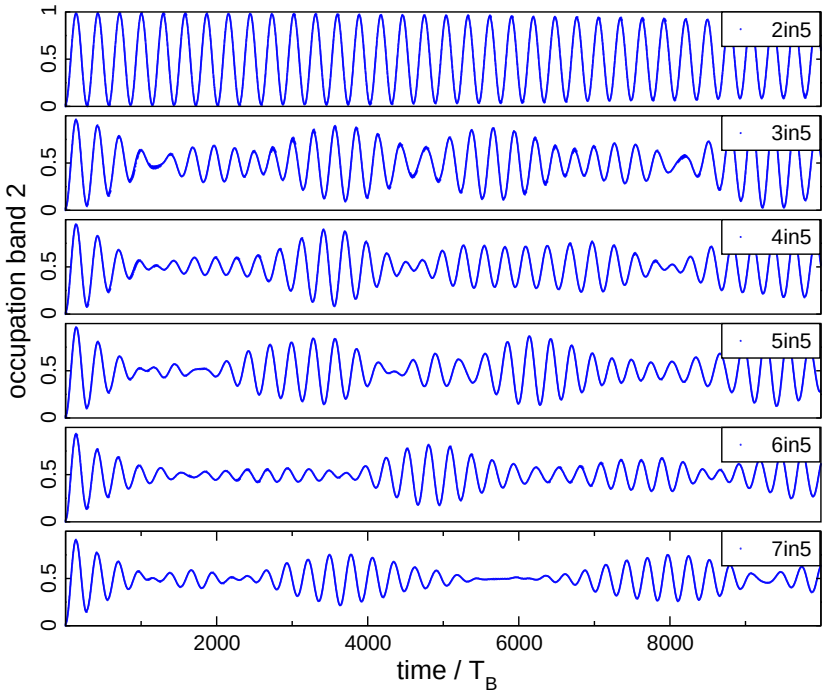

Figure 4.8: Occupation of the upper band as a function of time for different total particle number $N = 2, \ldots, 7$ and $L = 5$ for $V_0 = 4, m = 2$ and $g = 0.1$. We observe a clear collapse and revival effect for more than two particles with the specific position of the revival fluctuating with the particle number. The two particle case exhibits a beating of two frequencies at a very long time scale, much larger than the collapse or revival time in systems with higher particle number.

We find a good collapse and revival signal in the occupation of the upper band, provided the number of particles is not too small. The specific position of the revival depends again on the details of system, i.e. on the combination of N and L. However, the time of the first revival is of the same order of magnitude $t_{\text{rev}} \approx 4000\, T_B$ in all examples of figure 4.8. A clear exception is the case of two atoms. There is not collapse and revival, but instead a *beating* of two frequencies. It leads to a very slow dephasing and to a complete rephasing (beyond the scale of the figure) at a time much later than the revival time in systems with higher particle number. We will always distinguish between oscillations involving only two

nearby frequencies and showing a complete rephasing by calling it *beating* as opposed to a fast collapse and partial revival as present for higher particle numbers. The latter includes the superposition of near-resonant oscillations at several frequencies.

The examples above show that the collapse and revival effect is stable against a variation of the particle number. The exact time of the revival depends on the details of the system, but the order of magnitude is comparable for different combinations of N, L. However, it indicates that the collapse and revival observed in our system is a many-body effect since it appears only for a larger number of atoms when several (not only one) new frequencies are induced by the interaction. We will take a closer look at these frequencies in the following section.

Identification of time-scales via Fourier analysis

Given any oscillating signal, one can identify the contributing frequencies by a simple Fourier analysis. We will use this to shed light on the frequencies in the our signal for the occupation of the upper band. Our specific interest lies on the new energy scales introduced by the inter-particle interaction.
Let us start with the simplest case: no inter-particle interaction and off-resonant band coupling. The main contribution in the oscillation between the bands stems from the direct onsite coupling in the Hamiltonian of eq. (4.1.1). Figure 4.9 shows the Fourier spectrum of the occupation of band 2 for potential depth $V_0 = 4$ and different non-resonant forces. The corresponding time signals are similar to the ones in figure 3.5 and 3.8. We evolved a delocalised initial state in time, computed the occupation of the upper band and calculated the Fourier spectrum using a discrete Fourier Transform [Pre92, chap. 12-1]. We observe that

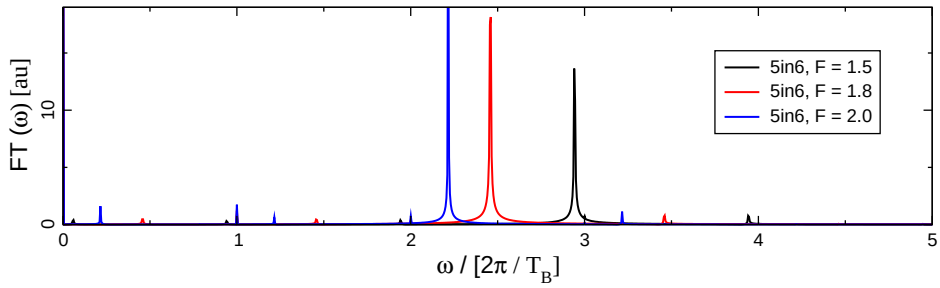

Figure 4.9: Fourier spectrum of the occupation of band 2 for an non-interacting system and different non-resonant forces. To each force, there is one clear peak for the direct onsite oscillation of period $T_0 = 2\pi/\sqrt{\Delta^2 + 4V^2}$ and minor peaks (very small but clearly visible in the figure) at the integer resonance frequencies as well as combinations of these frequencies. Parameters: $V_0 = 4, N = 5, L = 6, g = 0, T_{\text{max}} = 200\,T_B$ and $2^{14} = 4096$ data points for DFT (Discrete Fourier Transform).

the Fourier spectra of the non-interacting off-resonant interband oscillations are dominated by a single frequency. By closer inspection of the shown spectra, one identifies more but much smaller peaks at linear combinations of this dominant frequency with integer multiples of the Bloch frequency $\omega = 2\pi/T_B$. For each value of the force, the dominant frequency is exactly $\omega_0 = 2\pi/T_0$ corresponding to the non-resonant on-site coupling discussed in the previous chapter

$$\frac{\omega_0}{2\pi/T_B} = (T_0/T_B)^{-1} = (F/\tilde{\Delta})^{-1} = \sqrt{\Delta^2 + 4V^2}/F. \tag{4.1.7}$$

The corresponding frequencies of these oscillations are easily computed and are given by $\omega_0/(2\pi/T_B) = 2.9420,\ 2.4573$, and 2.2154 for $F = 1.5,\ 1.8$, and 2.0 respectively. We find a very good agreement between these theoretical values for the non-interacting off-resonant oscillations with the peaks in the Fourier spectrum shown above. This is just a result of our understanding of the non-interacting system, as developed in chapter 3.

Let us now turn to the collapse and revival effect in the resonant interacting system. We are going to analyse the time-scales or frequencies in the signal for the occupation of the upper band. We evolve the system in time up to $20,000\ T_B$ and perform a Fast Fourier Transform (FFT) for $2^{20} \approx 10^6$ data points. This long time signal is needed, since the revival occurs at a time scale much larger than the Bloch period T_B. The number of data points in the time signal if also quite large, but needed to obtain a good resolution. We will use these numerical parameters throughout in the following Fourier spectra.
From studying the non-interacting system in resonance in section 3.4.1, we expect an additional frequency for a resonance of order m in the Fourier spectrum at a frequency

$$\Omega_{\text{res}}^{(m)} = 2\pi/T_{\text{res}}^{(m)} = \frac{2|V|J_m(\Delta x)}{F} \cdot \frac{2\pi}{T_B}. \tag{4.1.8}$$

Figure 4.10 confirms this expectation. There is peak for the onsite oscillations at an integer frequency $2\pi m/T_B$ (since $\omega/(2\pi/T_B) = \tilde{\Delta}/F \approx m \in \mathbb{N}$ in resonance) and, additionally, a peak in the spectrum at Ω_{res}, yielding $3.51 \cdot 10^{-3}$ for the parameters of the figure. Again, linear combinations of these frequencies, are also present in the spectrum.

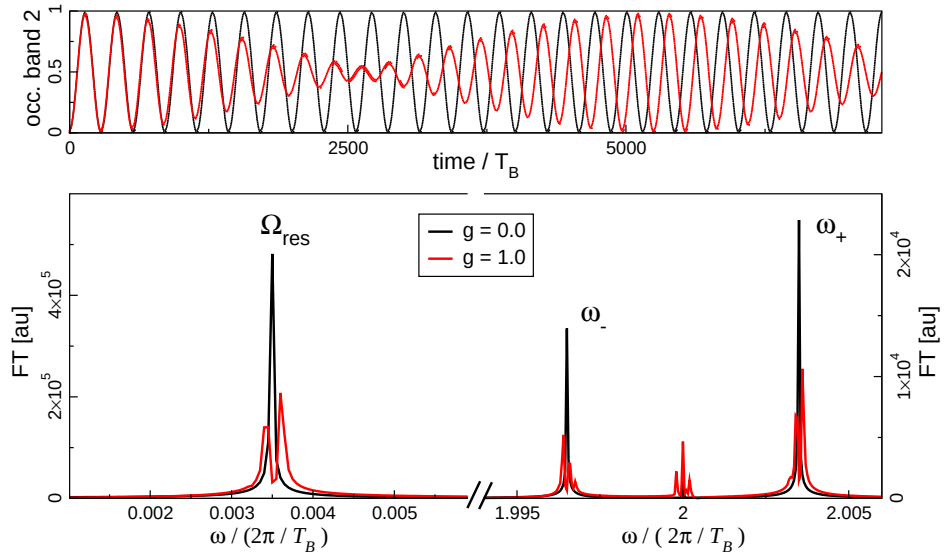

Figure 4.10: *Upper panel:* Resonant occupation of band 2 as a function of time for two particles in seven wells, without (black) and with (red) interaction for an optical lattice of depth $V_0 = 4$ and resonance $m = 2$. *Lower panel:* Fourier spectrum of the signal in the upper panel. There is a clear peak for the resonant oscillations at $\Omega_{\text{res}} = 3.51 \cdot 10^{-3}$ and two peaks for the non-resonant onsite oscillations at $\omega_\pm = 2 \pm \Omega_{\text{res}}$. The peak at Ω_{res} splits when the interaction between the two particles present in the system is turned on (*lower left panel*). Again combinations of the various frequencies are visible in the Fourier spectrum (*lower right panel*).

But the main point of the discussion concerns the interaction. Numerically, the easiest case beyond single-particle physics is to take two particles. This is also shown in the Fourier

spectrum in figure 4.10. We find that the interaction splits the resonance peak into two. This might be understood from the two possible values the interaction term can take, when only two particles are in the system, namely, the operator $n_l^s(n_l^s-1)$ (with $s=a,b$) yields either 0 or 2 when acting on a Fock state in real space. The actual eigenstates might be close to these states, since the band gap and the external force are the largest energy scales in the system and are both diagonal in the real space Fock basis. However, this argument ignores the interband interaction which plays a major role in the weakly interacting resonant regime as we will see in section 4.1.5 below. Let us therefore not go into detail for the two-particle case, but study the Fourier spectrum of the resonant oscillations with more particles.

We performed similar numerical simulations for higher particle numbers. We also apply a Fourier analysis and the effect on the frequency peak for the resonant interband oscillations is shown in figure 4.11. The resonance frequency splits into as many frequencies as there are particles in the system. This is demonstrated in figure 4.11. We see that the interaction

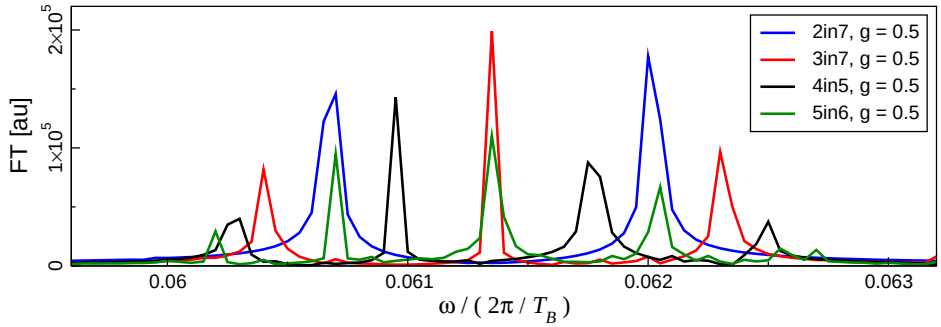

Figure 4.11: Change and splitting of the resonance frequency when including interaction with different number of particles $N=2,\dots 5$. The peak for the resonance frequency splits up into as many peaks as there are particles. Parameters: $V_0=2, m=1, g=0.5$.

indeed induces new frequencies to the system. These lead to a splitting of the resonance frequency into as many sub-frequencies as there are particles in the system. At the moment, we can state this only as a numerical observation, but it will be explained by an effective model to be introduced later in section 4.3.3. Let us further check numerically how the splitting of the resonance frequency depends on the global interaction strength g. The right hand side of figure 4.12 shows a clear linear dependence of the frequency splitting on the overall strength of the interaction for the strong resonances $m=1,2$ shown in the figure. We observed a similar behaviour for higher order resonances, however, with an additional complication. When turning to higher resonances, as e.g. $m=5$ and deeper lattices, a interaction-induced shift of the resonance becomes important. Then, the interaction might move the system out of resonance (depending on the strength of the interaction and width of the resonance as discussed in section 3.4.1) and one needs to vary the force to get into resonance again. We will not discuss this behaviour here, but stick to resonances up to order $m=3$ which are sufficiently stable against this effect.

Up to now, we have found that the interaction introduces new time scales into the system and, to be more precise, leads to splitting of the resonance frequency proportional to the strength of the interaction. So far we have only discussed the general influence of the interaction, let us also check numerically if the different interaction terms cause different effects. We computed the occupation of the upper band for a system with two particles and

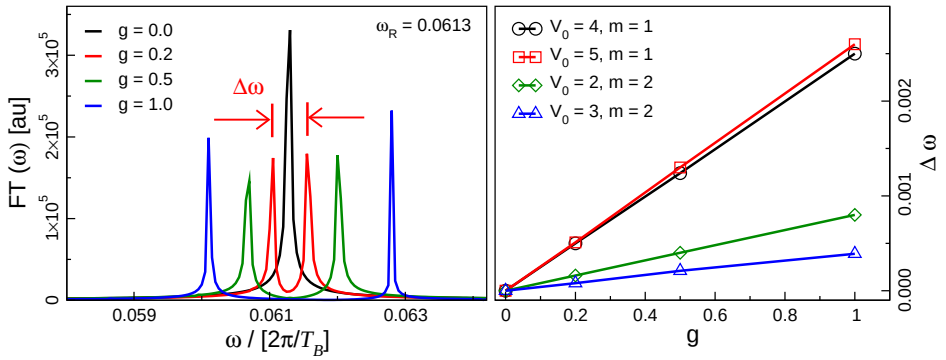

Figure 4.12: *Left panel:* Splitting of the resonance frequency when including interaction of increasing strength. *Right panel*: The splitting of the resonance frequency is linear in the total interaction strength g with different slopes for different resonances.

included only one of the three different interaction terms W_a, W_b, W_x in each computation. The occupation of the upper band shows again a beating between two frequencies and the associated periods are shown in figure 4.13 for different interaction processes and the first two resonances. These interaction-induced times scales differ strongly, some by more

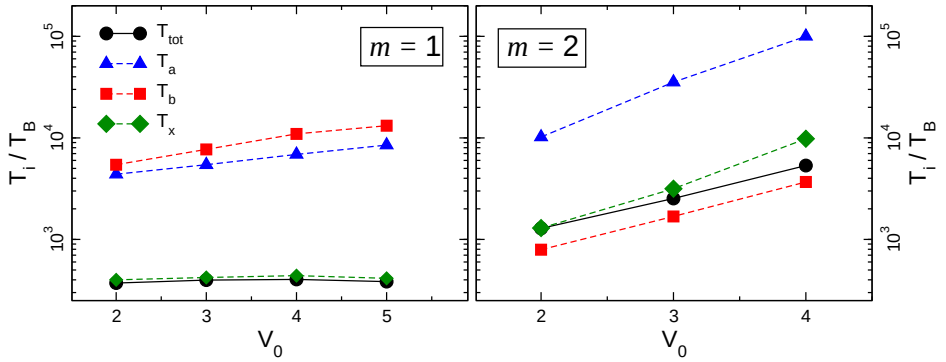

Figure 4.13: Periods of the interband oscillations introduced by the different interaction types for the first (*left panel*) and second (*right panel*) for 2 particles in 7 sites and $g = 1.0$. The periods of oscillations slightly increases with increasing depth of the optical lattice, but the time scales are very different for the different interaction types. However, in all cases, the effect of all interactions together is very similar to the effect of the interband interaction W_x only.

than one order of magnitude. For the first and strongest resonance ($m = 1$), the time scales for interactions within the upper or lower band are by one order of magnitude larger then the scale for interband interaction. Interestingly, the latter almost coincides with the interaction time scale for the completely interacting system T_{tot} (we will come back to this in figure 4.15 and 4.16). The same holds for the second resonance: The interband interaction dominates the oscillations in the fully interacting system. Why is this? Let us study the basis states contributing strongest to the time evolution to gain a qualitative understanding of this effect. This will be done in the next section.

4.1.5 Eigenbasis Expansions

To understand which states and frequencies play a major role for the collapse and revival in the resonant occupation of the upper band, we can use different types of eigenbasis expansions.

Distribution of Initial State in Eigenbasis

For the time evolution of a given initial state, we can use either a direct numerical integration or an eigenbasis expansion after diagonalising the problem (for both see the footnote on page 107 and appendix A):

$$|\psi(mT_B)\rangle = \sum_n c_n \mathrm{e}^{-\mathrm{i}\varepsilon_n mT_B}|\varepsilon_n\rangle, \quad c_n = \langle\varepsilon_n|\psi_0\rangle. \tag{4.1.9}$$

Here we use the eigenstates $U(T_B)|\varepsilon_n\rangle = \mathrm{e}^{-\mathrm{i}\varepsilon_n T_B}|\varepsilon_n\rangle$ of the Floquet-Bloch operator ($\mathcal{T}$ denotes time-ordering)

$$U(T_B) = \mathcal{T}\exp\Big[-\mathrm{i}\int_0^{T_B}\mathcal{H}(t)\,\mathrm{d}t\Big], \tag{4.1.10}$$

since the Hamiltonian eq. (4.1.1) is explicitly time-dependent with a periodicity of T_B. A necessary ingredient in such a procedure are the coefficients $c_n = \langle\varepsilon_n|\psi_0\rangle$ given by the overlap of the initial state with the eigenstates. This gives us the full spectrum and enables access to the relevant energy scales of the problem and allows an identification of the most important states participating in the time evolution. But for a physical interpretation of the relevant eigenstates, we need to project them into a basis having a clear meaning, such as the original Fock basis.

We computed the Floquet–Bloch operator and its eigenvectors numerically for $V_0 = 4$ and resonance of order $m = 2$ for $N = 4 = L$. The $\kappa = 1$-subspace is of dimension $\dim\mathcal{H} = 86$ and the initial state completely delocalised over the lattice is the Fock state $|1111;0000\rangle$. We computed the overlap of this state with all eigenstates of the Floquet–Bloch operator, i.e. the coefficients c_n, and the absolute value of these are shown in the top left panel of figure 4.14. We show them on a logarithmic scale that has been truncated at 0.1 to emphasize the largest of the 86 coefficients. We find that only a small number of approximately 10 state has large values in an eigenbasis expansion of the initial state. This allows us to hope, that the actual time evolution can be understood from a limited number of states or, as will been shown later, in a possibly truncated basis expansion.

In the other panels of figure 4.14 we try to elucidate the properties of the relevant eigenstates. We therefore show the projections of the seven most important eigenstates (those that have the largest overlap with the initial state, the absolute values are given in the axis description) onto the Fock basis. By closer inspection, we find again that some Fock basis states play a more important role than others. We look up the Fock basis used in the computation (the algorithm for creation of the Fock basis is given in appendix A) and find that the following seed states appear repeatedly with large overlap in the basis expansion of the most relevant eigenstates:

$$\begin{aligned}
|s_{10}\rangle &= |1111;0000\rangle & |s_{22}\rangle &= |1101;1000\rangle\\
|s_{47}\rangle &= |1100;1100\rangle & |s_{72}\rangle &= |0101;1010\rangle\\
|s_{79}\rangle &= |0100;1110\rangle & |s_{82}\rangle &= |0000;2110\rangle\\
|s_{85}\rangle &= |0000;1120\rangle & |s_{86}\rangle &= |0000;1111\rangle.
\end{aligned}$$

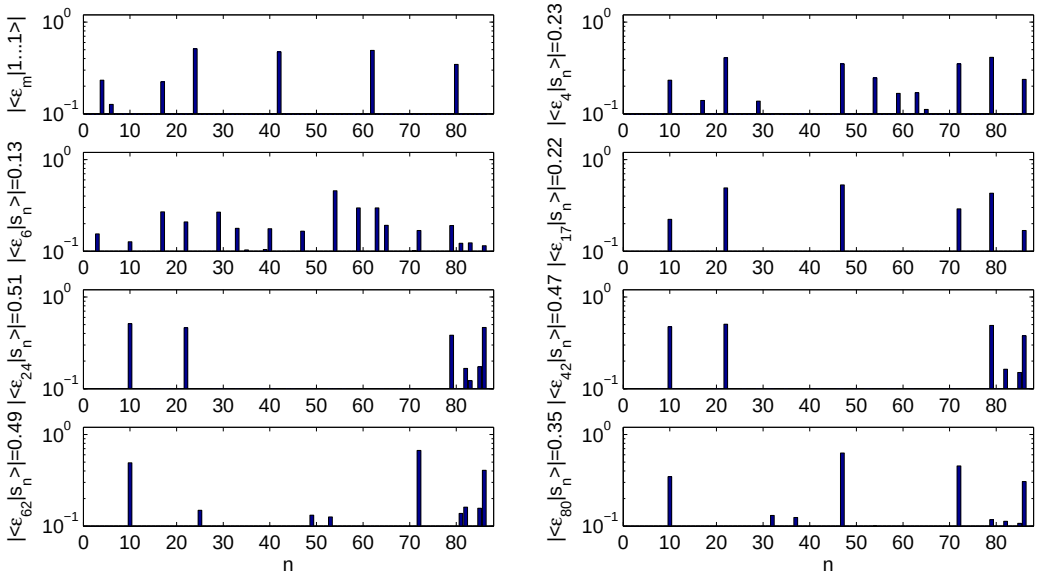

Figure 4.14: Overlap of initial state with eigenbasis (*top left*) and distribution of important eigenstates in the original Fock basis (*remaining panels*). Parameters: $V_0 = 4$, resonance of order $m = 2$, $N = 4 = L$ and $g = 1.0$.

These are several fock states that play an important role in the eigenbasis expansion with particles in the lower and upper band. Comparing these states with the total Fock basis, we see that mainly states with a small number of particles per site contribute. Put differently, double occupancy or even higher occupancy of single lattice sites seems to be avoided. This is rather clear, since we are considering repulsive interaction. However, this is not trivial since we are working in a specific regime where the system is in resonance. That is to say, to truncate the Fock basis right away can easily destroy the resonant oscillations as we shall see below.

Taking into account that the system avoids double occupancy, what does this mean for the collapse and revival effect we are interested in? Let us discuss the four interaction terms present in the Hamiltonian:

$$\frac{W_a}{2}\sum_l n_l^a(n_l^a-1)+\frac{W_b}{2}\sum_l n_l^b(n_l^b-1)+\frac{W_x}{2}\sum_l (b_l^\dagger b_l^\dagger a_l a_l + \text{h.c.}) + 2W_x\sum_l n_l^a n_l^b.$$

The first three of these involve at least two particles per site in a Fock basis expansion and the last one gives a non-zero contribution already when there is a single particle at the same site in either band, as e.g. in $|010;010\rangle$ but not in $|100;010\rangle$. Yet the system tries to avoid this repulsive interaction as far as possible. However, we are driving the system with a strong force and bring it exactly into resonance, where a level from the upper band and the lower band are energetically degenerate. Taking only these two, the lower eigenstate of such a degenerate two-level system is the coherent superposition $|\phi\rangle = (|1;0\rangle - |0;1\rangle)/\sqrt{2}$

of both states.[4] This takes place at all lattice sites. But since the system is in resonance and shows such a superposition on all sites, it cannot avoid that two particles are on top of each other in either band. This is schematically shown in figure 4.15.

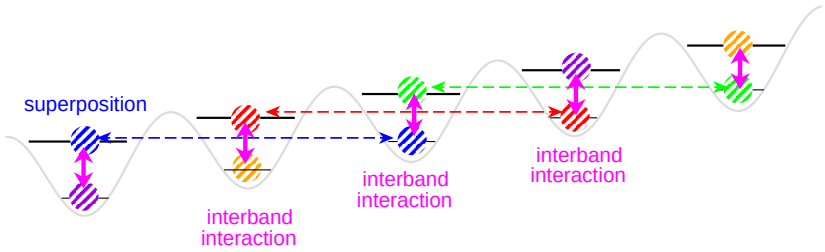

Figure 4.15: Schematical view of the effect of the interband interaction on the system in resonance of order $m = 2$ for $N = 5 = L$. In resonance, the system is forced into a superposition of states from both bands. This happens on all lattice sites and the system cannot avoid to pay an interaction price $2W_x \sum_l n_l^a n_l^b$. However, it is possible for the system to avoid double occupancy per site and band. The atoms are shaded to indicate the superposition they are in.

If our reasoning is correct, the very last interaction term $2W_x \sum_l n_l^a n_l^b$, which is contributing already for single occupancy, should be most important for the collapse and revival effect. We verified this by computing the occupation of the upper band with the same initial state as before but only this interaction term active. Our interpretation is confirmed in figure 4.16, where the collapse and revival of the resonant interband oscillations are shown with all interaction terms and only the latter one.

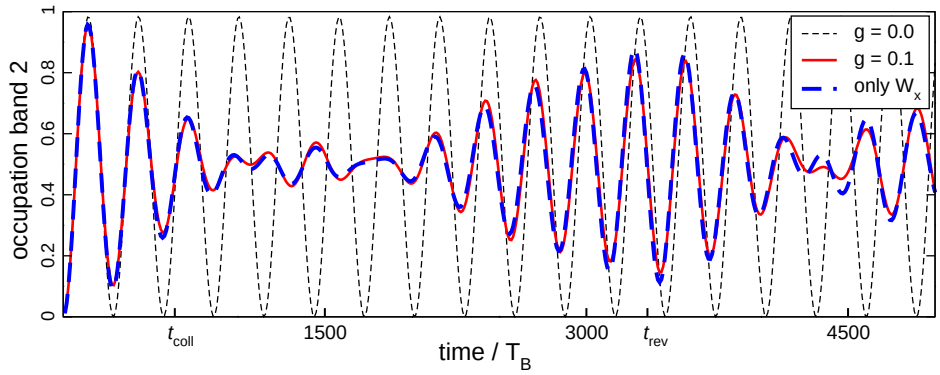

Figure 4.16: Occupation of the upper band as a function of time for a resonance of order $m = 2$ as in figure 4.4 above. Shown are the cases: vanishing two-body interaction ($g = 0$, thin dashed line), weak two-body interaction ($g = 0.1$) with all interaction terms (thick line) and only one interaction term $2W_x \sum_l n_l^a n_l^b$ (thick dashed line) included. The latter two are almost identical, indicating that this is the most relevant two-body process for the collapse and revival observed.

Let us summarise our understanding of the most relevant interaction processes. Clearly, the repulsive two-body interaction disfavours double occupancy of sites since this will always

[4] This is superposition with two degrees of freedom. In a simple Hilbert space of two two-level system, this is just one of the four Bell states [Hor09], which are maximally entangled. We thus expect the two degrees of freedom "upper band" and "lower band" to be entangled. However, there is a significant subtlety here which requires an accurate analysis: the indistinguishability of the bosonic atoms. Steps in this direction have been taken [Ami08], but a longer and more careful discussion is necessary than time and space allow us here.

cost an interaction energy W_a (W_b) for two particles occupying the same site in the lower (upper) band. Starting from an initial state with population of the ground band only, the strong force leads to a significant occupation of the upper band. Double occupied sites are also suppressed there, but two particles may sit at the same site in either band, i.e. "on top of each other". Indeed, the most important interaction term in the time evolution is $2W_x \sum_l n_l^a n_l^b$, since it already gives a non-zero contribution when there is only one particle per site in each of the two bands. This is clearly visible in comparing the time evolution of the initial state with all interaction terms and only the one mentioned. They show almost no difference (cf. figure 4.16) and the previous results for the interaction time scales in figure 4.13 need to be interpreted in the same way. We will use the fact that $2W_x \sum_l n_l^a n_l^b$ is the most important interaction term for the collapse and revival effect in the derivation of an analytical model below.

Truncated Fock Basis Time Evolution

When analysing which Fock basis states play the most important role in the collapse and revival effect of the resonant interband oscillations, we found that double occupancy is suppressed by the repulsive interaction and that states with only a single particle per site are relevant. This was supported by the fact that the collapse and revival effect is beautifully reproduced when only the interband interaction $2W_x \sum_l n_l^a n_l^b$ is present in figure 4.16. However, this does not imply that ignoring higher occupancy right from the beginning leads to the same effect. To check this, we used a truncated Fock basis to compute the time evolution of our delocalised initial state $|1, \ldots, 1; 0, \ldots, 0\rangle$. To be specific, we set up a basis with Fock states including maximally n_{max} particles per site in either band. We computed the Hamiltonian in this reduced Fock basis and the corresponding time evolution according to the time-dependent Schrödinger equation. If this truncation reproduced the physical results, it would be particularly useful for numerical computations, since an acceptable truncation of the Hilbert space would allow the computation of larger physical system (i.e., higher N, L) or faster computation for the same parameters. A truncation scheme for the Bose–Hubbard model has for instance been used in [Sch07, Cla06]. There are furthermore different time-adaptive Hilbert space truncation schemes [Dal04, Whi04] based on Vidal's time evolving block decimation idea [Vid03]. However, the numerical results shown in figure 4.17 demonstrate that such a truncation is not reasonable in our case.

We compare the time evolution of the same initial state as before using a truncated Hilbert space for a system with $N = 6 = L$ in figure 4.17. We find that using Fock basis states with at least 3 particles per site still reproduces the time evolution fairly well, but when allowing only up to two particles per site in the Fock basis, the collapse and revival effect is not all present. The different frequencies dephase very quickly and are not able to rephase for a revival. We thus see, that the collapse and revival effect cannot be obtained in a simple truncated Fock basis, but that almost the full basis is needed to describe the resonant behaviour of the many-body system where several particles are forced to oscillate between the two bands.

Another approach for theoretical modelling would be to follow an argument by Kolovsky [Kol03a] that the strong force and large band gap are dominant and diagonal in the Fock basis. Thus, so the idea, the Floquet–Bloch operator should be almost diagonal in the Fock basis. This has been used by Kolovsky to compute an additional period imposed on the system by adding a weak onsite intraband interaction. Let us check the validity of this argument for the collapse and revival phenomenon under consideration numerically. Many

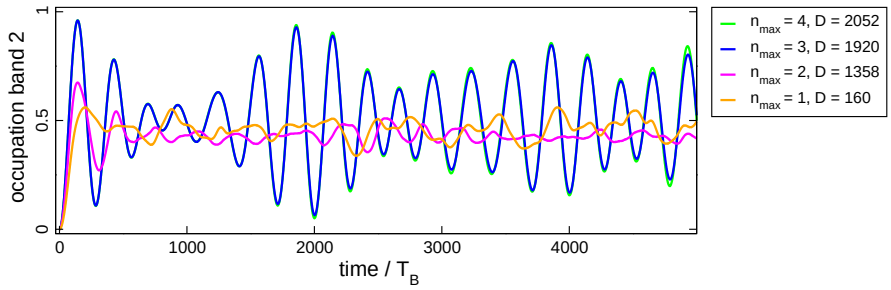

Figure 4.17: Occupation of the upper band as a function of time using a reduced Fock basis for the time evolution. Shown are time evolutions keeping Fock basis states with maximally 4 (green), 3 (blue), 2 (magenta), or 1 (orange) particle per site. This corresponds to a reduction of the Hilbert space size to 98.8%, 92.5%, 65.4%, and 7.7% of the original size. We see that a truncation of the Fock basis is not a good tool since the revival effect is not reproduced for a stronger truncation although higher occupation of the basis is suppressed by the repulsive interaction. Parameters: $V_0 = 4, m = 2$, $N = 6 = L$ and $|\psi_0\rangle = |111111, 0 \dots 0\rangle$.

of the matrix elements of the time evolution operator are indeed very small and only some of them have considerable weight. Let us set the small elements to zero and check the time evolution keeping only dominant elements. This is done in figure 4.18 where we kept only matrix elements larger than a certain threshold, i.e. $[U(T_B)]_{ij} > \eta$, and set all others to zero.

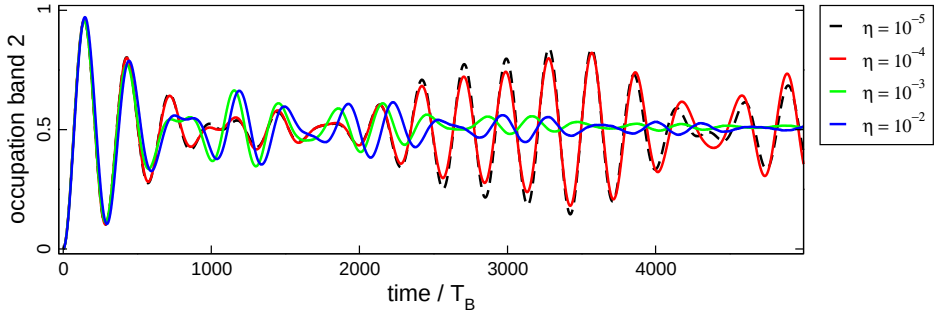

Figure 4.18: Occupation of the upper band in a truncated time evolution. The time evolution has been performed by computing the one-period time evolution operator and taking only the largest matrix elements. We set to zero all matrix elements smaller than η with $\eta = 10^{-5}$ (black dashed), 10^{-4} (red), 10^{-3} (green), 10^{-2} (blue). We see that even comparatively small matrix elements are needed to reproduce the revival effect in the time evolution. The system in resonance is sensitive to small changes. Parameters: $N = 5 = L$, $V_0 = 4$, $m = 2$, $g = 0.1$, $|\psi_0\rangle = |11111, 0 \dots 0\rangle$.

We observe that dropping already quite small matrix elements destroys the collapse and revival effect. This means that although the force might be dominant and diagonal in the Fock basis, the resonance is a special situation and is not reproduced by this approximation. The argument by Kolovsky can thus not be used to estimate the revival time in our system.

Truncated Eigenbasis Time Evolution

Despite the results from the last paragraph, studying the time-dependent signal for the occupation of the upper band itself, one is guided to believe that it should be possible to "synthesize" the signal by using only very few frequencies. These should be the most

relevant eigenfrequencies. That is, a truncated eigenbasis instead of a truncated Fock basis should be more efficient. Certainly, the sensitive dependence of the signal on even small matrix elements of the time evolution operator implies that it will be difficult to compute these eigenstates and eigenfrequencies with pen and pencil even approximately. However, we can perform a truncated eigenbasis expansion numerically to see how many eigenstates are needed to reproduce the signal.

We thus return to a time evolution using the eigenbasis, but take only those eigenstates with a contribution above a certain threshold τ. Explicitly, we are going to perform a reduced time evolution of the initial state according to

$$|\psi(mT_B)\rangle \approx \sum_n \tilde{c}_n \mathrm{e}^{-\mathrm{i}\varepsilon_n m T_B}|\varepsilon_n\rangle, \quad \tilde{c}_n = \begin{cases} \langle\varepsilon_n|\psi_0\rangle & \text{for } \langle\varepsilon_n|\psi_0\rangle \geq \tau \\ 0 & \text{otherwise} \end{cases} \tag{4.1.11}$$

The result of such a numerical simulation using a truncated eigenbasis expansion is shown in figure 4.19. Shown are three curves with different values for the threshold τ.

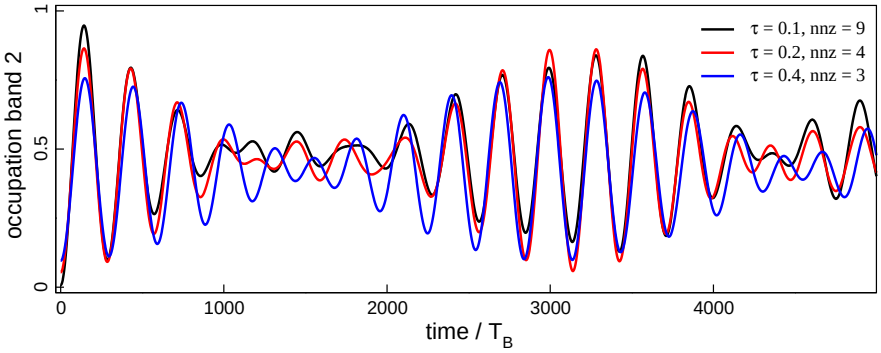

Figure 4.19: Occupation of the upper band in a truncated time evolution. The time evolution has been performed by diagonalising the one-period time evolution operator and keeping only the largest eigenfrequencies, i.e. those larger then a threshold τ. For the figure we chose $\tau = 0.1$ (black), 0.2 (red), and 0.4 (blue) corresponding to a number of nonzero (nnz) frequencies 9, 4, and 3 respectively, out 402 eigenfrequencies in total. We see that even a small number of eigenstates is sufficient to reproduce the revival effect in the time evolution. Parameters as in the last figure: $N = 5 = L$, $V_0 = 4$, $m = 2$, $g = 0.1$, $|\psi_0\rangle = |11111, 0 \ldots 0\rangle$.

The smallest threshold shown in the figure is already rather large (compared to the truncation of matrix elements performed earlier) with a value of $\tau = 0.1$ and leads to the reduced sum of 9 terms instead of the full 402 (the size of the subspace for the chosen system). We do not show smaller values for the threshold since they basically coincide with the shown curve. This is a surprising result: Only 9 of 402 eigenstates are sufficient to reproduce the collapse and revival in the resonant interband oscillations. These 2.2% are in stark contrast to a truncation of the Fock basis directly where more than 90% of the basis states were needed to reproduce the signal. A further increase of the threshold shows that the three or four largest eigenvalues preproduce the signal qualitatively well. We will use this in section 4.2.4 to estimate the revival time from the result of a numerical diagonalisation using the three most important eigenfrequencies (cf. section 4.2.4 below). Note, however, that a further reduction to even two states is not meaningful in the present context. With only two eigenstates there is only one energy difference, that is only one frequency in the system and one obtains simple sinusoidal oscillations between the two bands without any collapse, revival or beating.

Despite this surprising numerical result, that a very small number of eigenstates allows a reproduction of the collapse and revival signal, it does not give an analytical estimate for the revival time since a complete diagonalisation (and projection of the eigenstates on the initial state) is needed to "synthesize" the interband oscillations with a truncated eigenbasis expansion.

Summary of the Numerical Results

This first section of the present chapter was devoted to introducing the system under consideration, the two-band Bose–Hubbard model with an external force, and to the numerical analysis of a collapse and revival in the resonant interband oscillations present in that system. We discussed the Hamiltonian and the parameter regime we are interested in. This regimes is mainly given by the resonant interband oscillations and the effect of a weak interaction on these oscillations. We found a dephasing of different resonant oscillations seen as a collapse of the resonant interband population dynamics with partial revivals at later times. We went on with a numerical study of this effect. Firstly, we showed that it is stable against variation of several parameters as the initial state, the number of particles or lattice sites in the system as long as the particles are mainly delocalised in the initial state and the system is not too small. The time scale for the occurrence of the revival had a fixed order of magnitude under these changes, but the details varied.

Another important result of our many numerical experiments was a first glance at the physical cause leading to the effect. The strong and resonant Stark force compels the system to be in a superposition of lower and upper band states. This was also the result of the effective model for the resonance introduced previously in chapter 3. We found that the system tries to avoid double or higher occupancies in this process since all interactions are repulsive. But, being split between the lower and the upper band, the system is not able to avoid a situation with two particles "sitting on top of each other" in the course of its time evolution. The corresponding interaction process gives the dominant contribution to the collapse and revival effect in the resonant interband oscillations. We will use this understanding in order to estimate the revival time theoretically in the next section.

4.2 Theoretical Understanding

We have introduced the system and the collapse and revival effect for our two-band Bose–Hubbard model in the previous section and want to find a theoretical description in the following. The aim of the present section is easily stated but difficult to fulfill: We want to derive an expression for the revival time as a function of all system parameters

$$\text{wanted: } t_{\text{rev}} = t_{\text{rev}}(\Delta, J_i, W_j, C_0, F, N, L)$$

which should be in good agreement with our numerical results. This should ideally be done by derivation of an effective model from the original problem. Taking into account that we are dealing with an interacting many-body system in resonance and that the effect we want to describe is actually a many-body effect (it does not appear for only two particles, and is stable for several particles), this is not an easy task. In the following, we will nevertheless find an approximate expression for the revival time that gives the right scaling with (i.e., the qualitative dependence when varying one or more of) the parameters in the Hamiltonian. We will rely heavily on the numerical understanding obtained in the previous section which gives us hints which elements an approximate analytical model should contain. Comparing possible effective models to our numerical results, we will be able to develop two models that allow an analytical understanding of the collapse and revival effect in the resonant interband oscillations.

4.2.1 Introduction

Let us recover the physical situation we want to describe. We are studying a two-band Bose–Hubbard model with a strong external force. Whenever the force induced tilt of the lattice in the non-interacting case is such that an energy level from the lower band and the upper become energetically degenerate, we find a strongly enhanced transport between the two bands, which we study as the occupation of the upper band as a function of time. We call this behaviour resonant and focus precisely on this situation. Preparing an initial state that is only occupying the lower band and is delocalised over the lattice there, we find that a weak interaction leads to a collapse and revival of these resonant interband oscillations. The time scale of this revival depends on the depth of the optical lattice and the order of the resonance. We find a clear revival signal when the number of particles in the system is not too small and in this case the time scale of the revival varies only slowly with the particle number.

Taken together, we can thus distinguish three different time-scales in the process of resonant interband oscillations from our study of the occupation of the upper band:

- The period of non-resonant interband oscillations, $T_0 \approx 2\pi/\Delta$, which does not play a role for the collapse and revival effect,
- the period of resonant interband oscillations, $T_{\text{res}}^{(m)} = \pi/|V J_m(\Delta x)|$, for a resonance of order m, and
- the revival time from a superposition of several frequencies close to $\Omega_{\text{res}}^{(m)} = 2\pi/T_{\text{res}}^{(m)}$.

The last two time scales are of relevance for the present section and our aim is to find an analytical expression for the last one.

A Few Effective Models That Did Not Work

Since the oscillations appear to be a superposition of a few frequencies, one could try the following ansatz in terms of a single-particle picture: The interaction W_a splits up the lower band into sublevels and instead of one resonance frequency Ω_{res} a number of closely neighbouring resonance frequencies appears. Then we had effectively a slightly splitted bandgap: $\Delta \rightarrow \{\Delta, \Delta - gW_a\}$ and expect the superposition of Rabi-oscillations with neighbouring frequencies $\Omega_{\text{res}} = |V \cdot J_m(\Delta x)|$ and Ω_g. Remembering $V = C_0 F$ and taking $F \approx \Delta/m$ in resonance, the new frequency should be $\Omega_g = |C_0(\Delta - gW_a)J_m(\Delta x)/m|$. The period for the complete oscillations is then periodic with

$$T_\Delta = \frac{\pi}{\Omega_{\text{res}} - \Omega_g} = \frac{2T_{\text{res}}T_g}{T_g - T_{\text{res}}} = \frac{mFT_B}{|C_0|J_m(\Delta x)W_a}\,\frac{1}{g}.$$

Which is proportional to $1/g$ as found numerically, but gives the wrong scaling. By scaling we mean the dependence of the revival time on the parameters of the Hamiltonian (which are $J_a, J_b, W_a, W_b, W_x, \Delta, N, L$). This is a crude estimate and might serve to get the right order of magnitude for the oscillation period. But it ignores that we are dealing with a many-body problem, where more than two frequencies are generated by the interaction and the actual signal is not a superposition of two frequencies but strongly reminds of a collapse and revival phenomenon. Instead, it assumes the existence of a third level from the splitting of one of the two single-particle levels. The question is, however, does this simple estimate help us in understanding the collapse and revival effect in the resonant interband oscillations? The answer is no. First of all, when compared to numerical simulations with the fully interacting system, the formula does not yield the right scaling with the parameters of the Hamiltonian. Secondly, it cannot account for the numerical fact, that one of the interband interaction terms is dominating the collapse and revival effect. Substituting W_x for W_a in the formula above does not alter this fact, since the idea was to shift the band gap and a further justification of how W_x should do this is needed. But after this, the scaling would still be wrong and the many-body nature of the effect is certainly not captured. The W_x interaction terms were the dominant contribution for the collapse and revival effect, but this is not the correct way to incorporate them in an effective model.

Another, somehow similar, approach is to use our good understanding of the non-interacting single-particle system and to try an "educated guess" for an effective three or four level system. One could start with the aim of understanding a system containing two atoms only, where the system showed a real beating between only two frequencies which are very close to the unperturbed resonance frequency. In this fashion, we tried several effective three or four levels models, e.g. by allowing an additional coupling of the bands via the interband interaction. Such an extended single-particle Hamiltonian could read

$$\begin{pmatrix} -J_a\cos(Ft) & 0 & V & 0 \\ 0 & -J_a\cos(Ft) + W_a & 0 & W_x \\ V & 0 & \Delta - J_b\cos(Ft) & 0 \\ 0 & W_x & 0 & \Delta - J_b\cos(Ft) + W_b \end{pmatrix}.$$

However, such or similar Hamiltonians was never in satisfactory agreement with our numerical results and were not able to predict the actual frequencies even in the two-particle case. To conclude, there seems to be no simple account in terms of an effective small single-particle picture. In our opinion, this also excludes a good description using a mean-field

approach. Being an effective single-particle model, any mean-field theory would contain only two energies (for the lower and upper band states) and cannot account for the multitude of frequencies needed for a collapse and revival effect. Furthermore, any mean-field approach faces the problem of being a principally uncontrolled approximation, however useful it is in many applications. We will see later, that the two successful descriptions (to be explained below) are actually many-particle models.
Let us finally repeat that a direct application of Kolovsky's argument (for the interaction induced new period on top of the Bloch oscillations of single-band Bose–Hubbard model) does not work for our problem. Kolovsky's argument is based on the observation, that the time evolution operator is approximately diagonal in the original Fock basis. We saw numerically that this approximation destroys the collapse and revival effect and is thus not able to model it appropriately. The argument does not work in our case since does not take into account that the system we are studying is in resonance.

For our specific problem of the collapse and revival effect in the resonant interband oscillations, we draw the following conclusion. Necessary ingredients for a successful description of the effect need to take into account: the many-body nature of the problem (a bunch of frequencies), the resonances in the system (the original Fock basis states are not the proper basis), and the fact that the initial state is delocalised on the lattice (otherwise the effect is absent). Let us now come to a model including all this and allowing us to estimate the revival times and their scaling properly.

4.2.2 Coherent State Model

Bearing in mind the required ingredients for a description of the problem, we will now develop an effective description yielding good estimates for the revival time [Plö10c]. Here is an outline: We start with the fact that the system is in resonance by transforming the field operators to the eigenbasis of the resonant non-interacting system. Then, we use this in transforming our initial state to this basis and in a last step compute the effect of the interband interaction on the time evolution perturbatively. The last two steps are technically simplified by treating our initial state as a coherent state. This will be further justified in later in section 4.2.3.

Transformation to Resonant Basis

In chapter 3, we found a transformation for the non-interacting system in resonance, that led to very good agreement between the expected and observed oscillation times. The transformation removed the hopping terms but introduced a coupling of any two sites from the different bands. For the two levels being exactly degenerate, we could reduce the system to independent 2×2 models. In the following we will apply the same transformation in the interacting system, where the interaction terms (quartic in the field operators) will give rise to non-local interactions.

To start with, we rewrite the transformation for the non-interacting system to the resonant basis α_l, β_l in second quantisation and verify that it diagonalises the Hamiltonian. The non-interacting part of the Hamiltonian is given by

$$\mathcal{H}_0 = \sum_{l\in\mathbb{Z}} \epsilon_l^- a_l^\dagger a_l + \epsilon_l^+ b_l^\dagger b_l + V(a_l^\dagger b_l + b_l^\dagger a_l) - \tfrac{J_a}{2}(a_l^\dagger a_{l+1} + \text{h.c.}) - \tfrac{J_b}{2}(b_l^\dagger b_{l+1} + \text{h.c.}),$$

where $\epsilon_l^{\pm} = lF \pm \Delta/2$ and $V = C_0 F$ as before in section 3.1.1. The transformation and its inverse read

$$\alpha_n = \sum_{l\in\mathbb{Z}} J_{l-n}(x_a) a_l \quad \& \quad a_l = \sum_{n\in\mathbb{Z}} J_{l-n}(x_a)\alpha_n, \quad \text{with } x_a = J_a/F \tag{4.2.1}$$

$$\beta_n = \sum_{l\in\mathbb{Z}} J_{l-n}(x_b) b_l \quad \& \quad b_l = \sum_{n\in\mathbb{Z}} J_{l-n}(x_b)\beta_n, \quad \text{with } x_b = J_b/F. \tag{4.2.2}$$

Inserting it into the Hamiltonian and making use of $\sum_l J_{l-n}(x)J_{l-n'}(x') = J_{n-n'}(x-x')$, we obtain the result already known from chapter 3

$$\mathcal{H}_0 = \sum_{l\in\mathbb{Z}} \Big(\epsilon_l^- \alpha_l^\dagger \alpha_l + \epsilon_l^+ \beta_l^\dagger \beta_l + V \sum_{l'} J_{l'}(\Delta x)(\alpha_l^\dagger \beta_{l-l'} + \text{h.c.}) \Big).$$

In resonance of order m, i.e. $mF \approx \Delta$, between a lower band level at site $l+m$ and an upper band level at site l, only one coupling matrix elements dominates and the Hamiltonian can be reduced to independent two-level systems (depending on the order of resonance m). The eigenenergies are then given by

$$\omega_{l(m)}^{\pm} = (l - m/2)F \pm |V J_m(\Delta x)| \tag{4.2.3}$$

and the eigenvectors are symmetric and antisymmetric combinations of the original operators

$$\begin{pmatrix} \mu_l^{(m)} \\ \nu_l^{(m)} \end{pmatrix} = \frac{1}{\sqrt{2}} \begin{pmatrix} \beta_l + \alpha_{l+m} \\ \beta_l - \alpha_{l+m} \end{pmatrix} \quad \text{or} \quad \begin{pmatrix} \alpha_{l+m} \\ \beta_l \end{pmatrix} = \frac{1}{\sqrt{2}} \begin{pmatrix} \mu_l^{(m)} - \nu_l^{(m)} \\ \mu_l^{(m)} + \nu_l^{(m)} \end{pmatrix}. \tag{4.2.4}$$

We will often drop the superscript (m) since it is understood that these states are resonant basis states and the order of the resonance must be given. We verify this solution by inserting it into the reduced non-interacting Hamiltonian in resonance $\mathcal{H}_0^{(m)}$

$$\mathcal{H}_0^{(m)} = \sum_{l\in\mathbb{Z}} \omega_l^- \mu_l^\dagger \mu_l + \omega_l^+ \nu_l^\dagger \nu_l + \tfrac{1}{2}(\epsilon_l^+ - \epsilon_{l+m}^-)(\mu_l^\dagger \nu_l + \nu_l^\dagger \mu_l). \tag{4.2.5}$$

It is indeed diagonal, since $\epsilon_l^+ - \epsilon_{l+m}^-$ vanishes in resonance as demanded. For the many-particle problem we will distinguish many-particle states in different bases in our notation. Fock states with single-particle basis a_l, b_l are denoted as $|n_1^a, \ldots, n_L^a; n_1^b, \ldots, n_L^b\rangle$ (just as before) but those with single-particle basis μ_l, ν_l will be written with round parentheses $|n_1^\mu, \ldots, n_L^\mu; n_1^\nu, \ldots, n_L^\nu)$. Let us now reformulate our initial state for the collapse and revival problem with the help of these resonant basis states.

Coherent State Approximation

The ground state of the weakly interacting system without external force, i.e. in the superfluid regime, is well-known: All N particles occupy the zero-momentum mode of the cosine dispersion [Blo08b] to form the following superfluid state

$$|\Psi_0(N)\rangle^{(U\ll J)} = \frac{1}{\sqrt{N!}} (A_{k=0}^\dagger)^N |\text{Vac}\rangle = \frac{1}{\sqrt{N!}} \Big(\frac{1}{\sqrt{L}} \sum_l a_l^\dagger \Big)^N |\text{Vac}\rangle, \tag{4.2.6}$$

where $A_k^\dagger$ denotes the creation operator for a particle in the lower band with momentum k. Our focus lies on approximately unit filling $\bar{n} = N/L = 1$ and the time evolution of states of the form $|1,\ldots,1;0,\ldots,0\rangle$ which produced the collapse and revival effect in the resonant interband oscillations shown earlier. This state is clearly not an eigenstate of the system in resonance and shows a non-trivial time evolution. Note that it is the most important contribution to the superfluid ground state in an expansion in our Fock basis, as for example for $N = 5 = L$ one has

$$|\Psi_0(N=5=L)\rangle^{(U\ll J)} = \frac{1}{\sqrt{5}^5}\Big[|1\ldots1;0\ldots0\rangle + \frac{1}{8}|n^a_{\mathsf{max}}=2;0\rangle + \frac{7}{144}|n^a_{\mathsf{max}}=3;0\rangle + \ldots\Big],$$

where $|n_{\mathsf{max}};0\rangle$ denotes a translational invariant state with maximally n_{max} particles at one site in the lower band and zero particles in the upper band. This similarity increases with growing system size N (we postpone a more detailed discussion of this approximation to section 4.2.3). For large enough systems the superfluid ground state of the untilted system (and the single occupancy state $|1\ldots1;0\ldots0\rangle$ likewise) becomes indistinguishable from a coherent state [Blo08b, eq. (66)]

$$|\Psi_0(N, L\gg 1)\rangle^{(U\ll J)} = \mathrm{e}^{\sqrt{N}A^\dagger_{k=0}}|\mathrm{Vac}\rangle = \prod_l \left(\mathrm{e}^{\sqrt{\bar{n}}a_l^\dagger}|\mathrm{Vac}\rangle_l\right) \equiv |\boldsymbol{\varphi};0\rangle, \tag{4.2.7}$$

with $\bar{n} = N/L$, and factorises into a product of local coherent states $|\boldsymbol{\varphi};0\rangle \equiv \prod_l |\varphi;0\rangle_l$ with phase $\varphi = \sqrt{\bar{n}}$. Let us emphasize again, that this state is not an eigenstate of the system in resonance, neither with nor without interaction. We are going to introduce further notation for the states in this section, which is summarised in table 4.2. We are now going to rewrite this state in the resonant basis and to determine the effect of the interaction term $2W_x\sum_l n_l^a n_l^b$ when acting on this state. We start by inserting the expression for resonant basis states $a_l^\dagger = \frac{1}{\sqrt{2}}\sum_n J_{l-n}(x_a)(\mu_n^\dagger - \nu_n^\dagger)$ to get

$$\begin{aligned} |\varphi;0\rangle = &\quad \prod_l \exp\left[\sqrt{\frac{N}{2L}}\sum_n J_{l-n}(x_a)(\mu_n^\dagger - \nu_n^\dagger)\right]|\mathrm{Vac}\rangle \\ = &\quad \exp\left[\sqrt{\frac{N}{2L}}\sum_{l,n} J_{l-n}(x_a)(\mu_n^\dagger - \nu_n^\dagger)\right]|\mathrm{Vac}\rangle. \end{aligned} \tag{4.2.8}$$

state	description
$\lvert\{n\}\rangle$	general Fock state
$\lvert n_i^a; n_i^b\rangle$	two-band Fock state in standard basis
$\lvert n_i^\mu; n_i^\nu)$	two-band Fock state in resonance basis
$\lvert\alpha\rangle_l$	coherent state at site l
$\lvert\boldsymbol{\alpha}\rangle$	product of local coherent states
$\lvert\alpha)_l$	coherent state at site l in resonant basis
$\lvert\boldsymbol{\alpha})$	product of local coherent states in resonant basis

Table 4.2: Overview of different types of states appearing in the main text.

Using $\sum_m J_m(x)t^m = \exp[x(t-1/t)/2]$ for $t = 1$ and $[\mu_l^\dagger, \nu_l^\dagger] = 0$ (which follows from the commutation relations of $a_l^\dagger, b_l^\dagger$) we find that

$$|\boldsymbol{\varphi}; 0\rangle = \mathrm{e}^{\sqrt{\frac{N}{2L}}\sum_n(\mu_n^\dagger - \nu_n^\dagger)}|\mathrm{Vac}\rangle = \prod_n \mathrm{e}^{\sqrt{\bar{n}/2}\mu_n^\dagger}\mathrm{e}^{-\sqrt{\bar{n}/2}\nu_n^\dagger}|\mathrm{Vac}\rangle = \prod_n |\tilde{\varphi}; -\tilde{\varphi}\rangle_n, \quad (4.2.9)$$

with $\tilde{\varphi} \equiv \varphi/\sqrt{2}$. The coherent state of the lower band in resonance is thus a product of local coherent states for both bands in the resonant basis $\prod_l |\tilde{\varphi}; -\tilde{\varphi}\rangle_l \equiv |\tilde{\boldsymbol{\varphi}}; -\tilde{\boldsymbol{\varphi}}\rangle$. The minus sign simply accounts for the fact that the lower energy eigenstate is the anti-symmetric combination of the basis states. The time evolution of this state (for the non-interacting system in resonance) is not difficult to find since it is clear how to express a coherent state in Fock basis states (which are $|\{n_i^\mu\}; \{n_i^\nu\}\rangle$ in this case). However, we know the time evolution in the non-interacting case and continue to study the phase evolution created by the interband interaction.

Result for the Revival Time

The effect of the interaction term on the phase evolution of the system can be estimated by application of $\mathrm{e}^{\mathrm{i}2gW_x\cdot t\sum_l n_l^a n_l^b}$ to our initial state. This ignores a) that the interaction term does not commute with the non-interacting part of the Hamiltonian (we ignore the Baker–Campbell–Hausdorff rule) and b) that the Hamiltonian does not commute with itself at different times (which is valid to first order in the interaction strength, cf. section 3.2.3). But both is justified for a weakly interacting system. Applying the operator explicitly, we have

$$\mathrm{e}^{\mathrm{i}2gW_x\cdot t\sum_l n_l^a n_l^b}|\tilde{\boldsymbol{\varphi}}; -\tilde{\boldsymbol{\varphi}}\rangle = \exp\Bigg[\frac{\mathrm{i}gW_x t}{2}\sum_l \sum_{l_1,\ldots,l_4} J_{l-l_1}(x_a)J_{l-l_2}(x_a)J_{l-l_3}(x_b)J_{l-l_4}(x_b)\times$$
$$(\mu_{l_1}^\dagger - \nu_{l_1}^\dagger)(\mu_{l_2} - \nu_{l_2})(\mu_{l_3}^\dagger + \nu_{l_3}^\dagger)(\mu_{l_4} + \nu_{l_4})\Bigg]|\tilde{\boldsymbol{\varphi}}; -\tilde{\boldsymbol{\varphi}}\rangle. \quad (4.2.10)$$

Since $|\tilde{\boldsymbol{\varphi}}; -\tilde{\boldsymbol{\varphi}}\rangle$ is a product of local coherent states we can ignore the sum over l and discuss the expected behaviour. Firstly, both x_a and x_b are much smaller than unity and the main contribution in the sums over $l_1, \ldots, l_4$ will come from the zeroth-order Bessel functions J_0. Secondly, the product of operators gives 16 different combinations of the field operators. But due to the prefactors given by a product of Bessel functions, the combinations with equal indices are most important. They simply give an integer number when applied to the product of local coherent states they are acting on. Taking these two points together, the time evolution of this state should show an approximate revival at

$$\boxed{t_{\mathrm{rev}} = \frac{4\pi}{gW_x J_0^2(x_a)J_0^2(x_b)}.} \quad (4.2.11)$$

This is the main result of this chapter [Plö10c]. We derived an explicit expression for the revival time t_{rev} as a function of various parameters that has to be compared to numerical results. It is valid for large systems and cannot account for the effect of non-universal properties like a specific number of particles and lattice sites, but we expect it to yield the right order of magnitude for finite systems, and in particular the correct scaling with the parameters of external potentials. In deriving the above expression we used all ingredients

stated earlier: We transformed to the resonant eigenbasis, used a description in terms of the resonant basis, and the specific form of the initial state was used. In the derivation we applied several approximations, but we will compare the result with numerical simulations in a moment.

Comparison to Example Systems

The results of simulations for four different systems are shown in figure 4.20 with the predicted revival times according to eq. (4.2.11). This comparison should serve as a first example, we will show further results below.

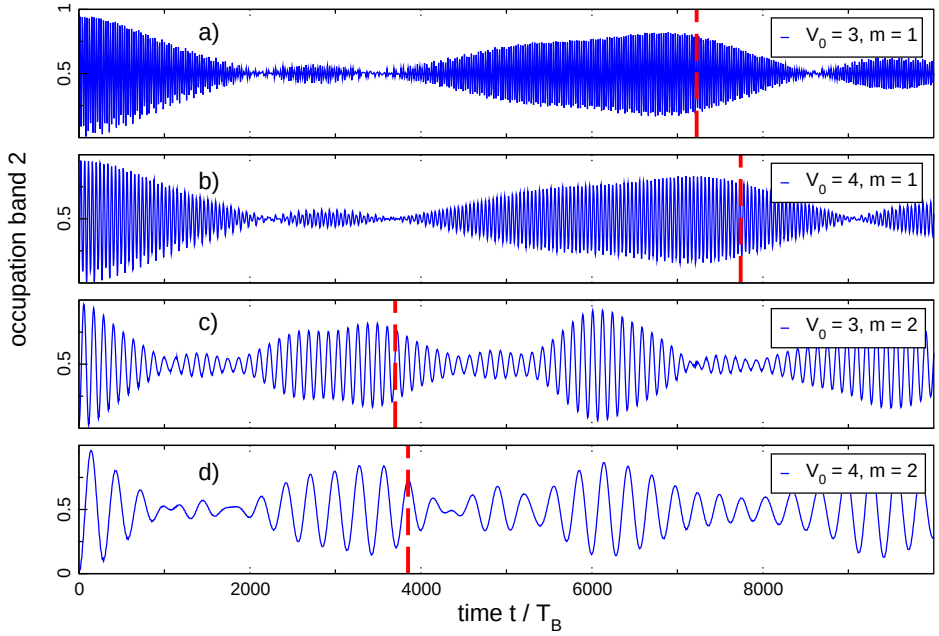

Figure 4.20: Collapse and revival in the dynamical evolution of initial states $|1,\ldots,1;0,\ldots,0\rangle$ for different potential depths and orders of resonance. Parameters: a) $V_0 = 3, m = 1$, b) $V_0 = 4, m = 1$, c) $V_0 = 3, m = 2$, d) $V_0 = 4, m = 2$, all $N = L = 5$. Our analytical result for the revival time accounts for the different orders of resonance and also for a slight shift in parameters when varying the depth of the optical lattice. In all cases, it is close to the actual maximum of the revival. Further comparison between theory and numerical simulations can be found below.

The figure shows the occupation of the upper band as function of time as computed numerically showing the familiar collapse and revival effect discussed extensively earlier. They are shown for two depths of the optical lattice (corresponding to two sets of parameters for the Hamiltonian) and the first and second resonance in the interband oscillations. A vertical dashed line shows the prediction for the revival time from our analytical analysis of the previous section.

For the parameters shown, the predicted revival time is close to the actual maximum in the revival of the interband oscillations. It follows the variation of the depth of the optical lattice as well as the order of the resonance (entering in the arguments of the Bessel functions via $x_{a,b} = J_{a,b}/F_{\text{res}}$ and $F_{\text{res}} \approx \Delta/m$) between different panels of the figure. Thus, it seems to capture something essential of the effect. In particular, it respects the order of the resonance which is a consequence of our transformation to the resonant basis

and unavoidable for a proper account of the effect. Please note that the derivation of the revival time is the same for negative g, i.e., attractive interactions. Indeed, we found the same behaviour for the occupation of the upper band for weak attractive interactions in exemplary numerical simulations.

Let us compare our analytical result to simulations for different system sizes. In contrast to the previous figure, we now fix the depth of the optical lattice and the order of the resonance, but vary the number of particles and lattice sites. This is done for $V_0 = 8$ and a first order resonance in figure 4.21. The specific size of the system has been parameterized

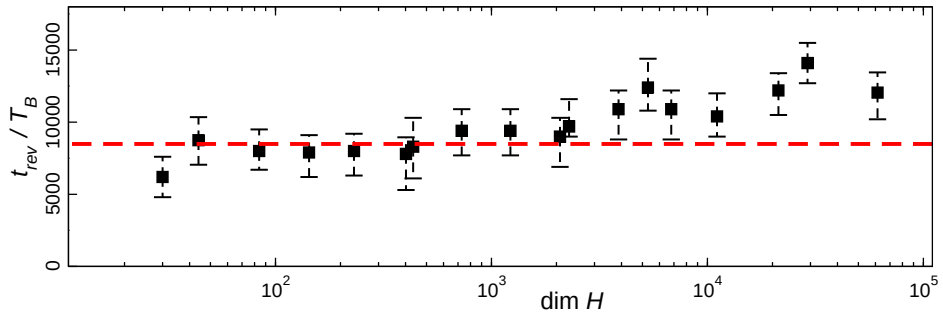

Figure 4.21: Comparison between the estimated revival time (dashed line) according to eq. (4.2.11) and numerical simulations (data points) for $V_0 = 8, m = 1$, and different system sizes, parametrised by the Hilbert space dimension. The error bars indicate the width of the revival at half maximum.

by the size of the Hilbert space under consideration (which is one subspace of fixed total quasimomentum since the quasimomentum is a constant of motion in our translational invariant system). The range of systems varies from 3 particles in 5 sites to a maximum of 8 particles in 8 lattice sites. The Hilbert space for the latter configuration is as large as $\dim \mathcal{H} = 61334$ and the initial state for the time evolution is the basis state $|s_{810}\rangle$.

The revivals in the numerical simulations are shown as black squares in the figure. The error bars do not indicate an uncertainty in the measurement of determination of the revival time (we defined it as the maximum value of the revived oscillations). Instead, the error bars indicate the width of the revived oscillations. This has been done to emphasize that the maximum is usually not in the center of the revived oscillations but slightly shifted. Furthermore we would like to indicate the complexity of the signal to a certain extent in the figure by adding these bars.

Our theoretical prediction for the revival time is given by the thick dashed line in the figure above. Since it cannot account for the specific size of the system, the prediction is given by a constant for a fixed value of the depth of the optical lattice and the order of the resonance (which is the case in figure 4.21). But we observe that it gives the right order of magnitude for the revival time as observed in the numerical simulations. The numerical data show a tendency to increase with growing system size, which the theoretical model given so far cannot explain. We will, however, learn to deal with the influence of a specific number of particles and lattice sites in two ways in sections 4.2.4 and 4.3.3.

We would like to stress that our model seems to give the right scaling when the parameters in the Hamiltonian (which are Δ, J_i, W_x, F) or the order of the resonance are changed. Let us discuss this in more detail in the next section.

Scaling in Theory and Simulations

As mentioned already, our analytical prediction for the revival time should give the right scaling when the parameters of the Hamiltonian change, e.g. by changing the depth of the optical lattice since Δ, J_i, and W_j depend on V_0.[5] Using the expression derived above for the revival time, we can discuss the dependence on V_0 here. We will discuss the scaling independent of W_x which itself is a function of the lattice depth. The remaining dependence thus describes the non-trivial scaling of the revival time for a certain order of resonance. Using the fact that the hopping is much smaller than the bandgap, we can expand the Bessel functions and obtain the leading order behaviour for a resonance of order m as

$$\frac{W_x t_{\text{rev}}}{T_B} \approx \frac{1}{g} \frac{8F^3}{4F^2 - (J_a^2 + J_b^2)} \propto 4.5 \frac{\sqrt{V_0}}{m \cdot g}. \tag{4.2.12}$$

The last result should be valid for deep lattices, since we dropped the exponentially decreasing hopping coefficients and used $F \approx \Delta/m$ as well as $\Delta \approx 2.5\sqrt{V_0}$ which is a good approximation for our units and choice of parameters. But we can of course compare the full expression for the revival time with values from numerical simulations. This is shown in figure 4.22 for different system sizes.

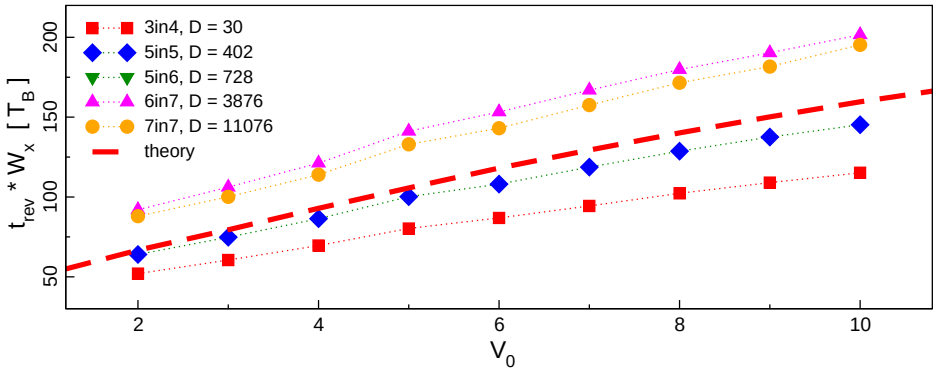

Figure 4.22: Scaling of the numerically measured revival time with varying lattice depth V_0 for resonance order $m = 1$. We multiply t_{rev} by W_x since W_x also depends on V_0. By this, we show the remaining non-trivial scaling that is not an artefact of the V_0-dependence of W_x. Filled symbols are t_{rev} from numerical simulations (the particular systems are indicated as 'Nin$L$' and D denotes the Hilbert space dimension) and the thick dashed line shows our theoretical result eq. (4.2.11).

We see that our analytical prediction correctly describes the dependence of the revival time on the parameters in the Hamiltonian, as determined by the lattice depth V_0 (see chapter 1). Again, it cannot explain the variation with increasing system size. However, the agreement in the scaling behaviour is an important result. It shows that our model captures essential aspects of the physical mechanism leading to the collapse and revival in the resonant interband oscillations.

[5] Please note, that this has also consequences for the period of the resonant interband oscillations and not only for the revival time. It means that changing the order of resonance or the depth of the lattice alters several time scales at once (cf. figure 4.20 where the resonant interband oscillations have different periods in the different panels).

Prediction: Divergence of the Revival Time

Let us discuss a peculiar effect contained in our result for the revival time. Up to now, we only discussed the simultaneous change of the Hamiltonian parameters by a change of the lattice depth. However, one can also think of changing only a single parameter. Take again the formula eq. (4.2.11) for the expected revival time

$$t_{\text{rev}} = \frac{4\pi}{gW_x J_0^2(x_a) J_0^2(x_b)},$$

it should diverge whenever we encounter a zero of either Bessel function in the denominator! How could this be achieved by a variation of parameters that is (at least in principle) experimentally feasible? The first zero of the Bessel function is approximately at $x_0 = 2.40483$. Here, the argument of the Bessel function is $x_{a(b)} = J_{a(b)}/F$, the ratio between one of the hopping coefficients and the external force. But the value of the force is determined by the order of the resonance m and the bandgap: $F \approx \Delta/m$. Altering the depth of the optical lattice changes the hopping coefficients and the band gap simultaneously.[6] For the parameters we used so far, the resonant forces (for orders $m = 1 \dots 5$) will always be greater than both hopping coefficients and we cannot reach a zero of the Bessel function. However, in experiments with so-called superlattices, which are optical lattices constructed from two lasers $V(x) = V_0 \cos(2k_L x) + V_1 \cos(4k_L x + \phi)$, it is possible to engineer the band gap of a system. In this case, the force will just vary together with the band gap (for fixed order of the resonance) and for small band gaps, one can cross zeros of the Bessel function. We are then no longer in a regime of small $x_{a,b}$ and can study the expected behaviour by approximating the zeroth order Bessel function as

$$J_0(x) \approx \sqrt{\frac{2}{\pi x}} \cos(x - \pi/4), \tag{4.2.13}$$

which is sufficient for our purposes here already for $x > 1$. It implies that the zeros of the Bessel function are equidistant with a spacing of π. In our case, the argument of the Bessel function in the denominator of the revival time is $x_s = J_s/F \propto 1/\Delta$ with $s = a, b$. We thus expect the divergences in the revival time to be equidistant when shown as a function of the inverse bandgap. Figure 4.23 shows the expected behaviour according to our prediction eq. (4.2.11) in more detail.

Before comparing to numerical simulations, there is an additional comment in place: When choosing parameters for an observation of the divergence in the revival time, one has to make sure that the period of the resonant interband oscillations does not vary too strongly in the region of the Bessel zero. There are parameter combinations where the period of the resonant interband oscillations is much larger than the revival time expected from our model. The reason is that the period of the interband oscillations in resonance of order m is given by $T_{\text{res}}^{(m)} = \pi/|V J_m(\Delta x)|$ (cf. section 3.4.1), and is itself inversely proportional to a Bessel function. In some cases zeros of the zeroth order and higher order Bessel functions come very close, e.g. around $x = 8.7$ (the third zero of the zeroth order Bessel function $J_0(x)$). Such a situation should be avoided when looking for a divergence of the revival time.

[6] The different scaling of two Hamiltonian parameters, exponential for the hopping strength and with an exponent of $-1/2$ for the interaction strength, has in fact been used to study the superfluid-Mott insulator phase transition experimentally [Blo08b].

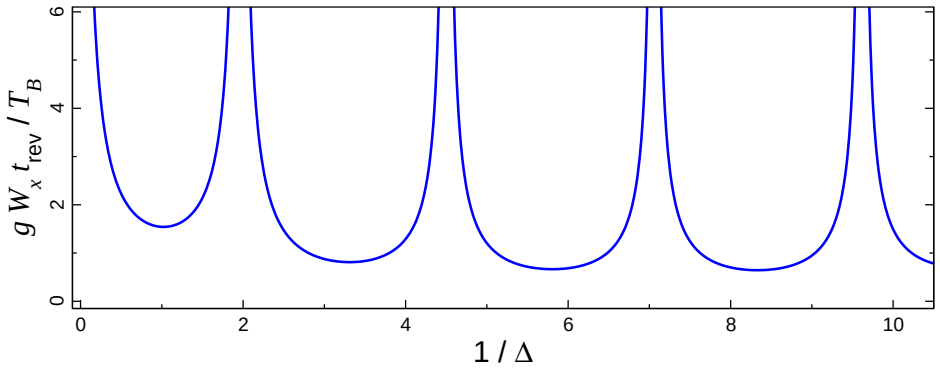

Figure 4.23: Predicted divergence of the revival time according to eq. (4.2.11). Since the revival time in our prediction is inversely proportional to Bessel functions, we expect a divergence of the revival time at the Bessel function zeros. The solid line shows our prediction for the revival time as a function of the inverse band gap. Parameters (except the band gap) for $V_0 = 4, m = 2$.

We performed numerical simulations to verify our prediction for the revival time divergence. We chose all parameters as for $V_0 = 4$, except for the band gap. Motivated by the possibility to engineer the band gap, we varied the width of the band gap and chose small values in order to cross zeros of the lowest order Bessel function. We chose a resonance of second order and varied the force together with the band gap to ensure the resonance condition. The resulting revival times as a function of the changing band gap are shown in figure 4.24. The numerical results in figure 4.24 clearly indicate the existence of diver-

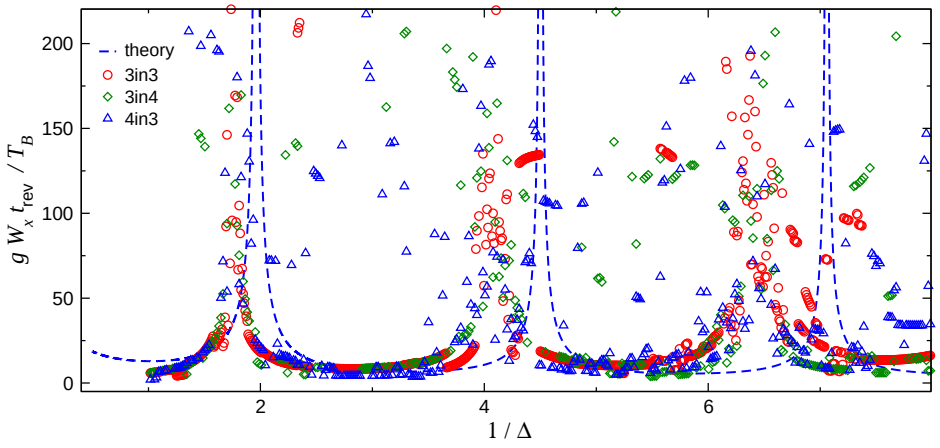

Figure 4.24: Numerically measured revival times (with the method of section 4.2.4) for small systems (data points) and expected revival time (dashed line) according to our coherent state model eq. (4.2.11) as a function of the inverse bandgap. The expected divergence of the revival time at the Bessel function zeros is confirmed by our numerical simulations. However, the positions of the divergences are shifted compared to the expected positions. Parameters: $V_0 = 4, m = 2$, and 'Nin$L$' indicated in the legend.

gencies in the revival time. However, the divergences are not at the positions predicted by our coherent state model. We do not have a clear explanation for this discrepancy at the moment. We will later introduce an effective model that reproduces the collapse and revival effect very well and is numerically more efficient (cf. section 4.3, especially figure 4.36).

The expected divergence of the revival time can be studied in more detail then and we will find a systematic deviation between the expected and numerically observed position of divergence. The reasons for this deviation are probably the approximation to an effective two-level system and the inclusion of only the dominant interaction.

Nevertheless, our numerical simulations show the presence of a divergence of the revival time when varying the band gap and indicate again, now in a completely different fashion, that our coherent state model captures the essential physics of the collapse and revival effect despite its drawbacks.

4.2.3 Details of the Coherent State Approximations

We derived an analytical expression for the revival time earlier and postponed a detailed discussion of the approximation until now.

Examples for Superfluid Ground States

We described our initial state as being similar to a coherent state and used this in calculations. In fact, there are two approximations being made here. The first one is the assumptions that our initial state is similar to the superfluid ground state of the system without force and the second one is the claim that this superfluid state becomes practically indistinguishable from a coherent state. We are going to discuss both now.

Let us start with the second assumption. We are well aware of the fact, that there is a striking difference between the following two states: a coherent state does not have definite particle number whereas our simulations are always performed for a state with fixed number of particles. The remedy for this conflict is that the particle number fluctuations (expressed in the moments $\langle (a^\dagger a)^m \rangle$) in the latter system approaches the former as the number of particles in increased. From a theoretical point of view this is described by $SU(N)$ coherent states [Per77, Mat02] (for an application to the Bose–Hubbard model see [Tri08]), which allow a description of states that have a finite particle number but behave as coherent states. The identification of both for large system sizes is also supported by the fact that the ground state is known to be superfluid and that a theoretical description of this state as a coherent state has proven successful [Blo08b].

The second claim is that the used initial state is most important in the superfluid ground state of the system without external force. In this ground state, all N particles occupy the zero-momentum mode and the ground state can be directly translated to real space by using its Fourier transform

$$|\Psi_0(N)\rangle = \frac{1}{\sqrt{N!}} \left(A^\dagger_{k=0}\right)^N |\mathrm{Vac}\rangle = \frac{1}{\sqrt{N!}} \left(\frac{1}{\sqrt{L}} \sum_{l=1}^{L} a^\dagger_l\right)^N |\mathrm{Vac}\rangle. \tag{4.2.14}$$

We can use this expression for a direct computation of this state and a comparison with our initial state. Since we are only interested in states with occupation of the lower band, we will drop the upper band quantum numbers for this section.

Let us compute the above expression for a few simple examples and discuss the general case afterwards. To keep the expressions simple, we ignore the normalisation for a moment. It is not important for the computation since we are only interested in the relative contribution of different (types of) states. For the smallest non-trivial system of two sites and

two particles we have

$$\begin{aligned}(a_1^\dagger + a_2^\dagger)^2|\mathrm{Vac}\rangle &= \left((a_1^\dagger)^2 + 2a_1^\dagger a_2^\dagger + (a_2^\dagger)^2\right)|\mathrm{Vac}\rangle = |20\rangle + 2|11\rangle + |02\rangle \\ &= 2|11\rangle + 1(|20\rangle + |02\rangle) \equiv 2|11\rangle\!\rangle^{(1)} + 1|20\rangle\!\rangle^{(2)}\end{aligned} \tag{4.2.15}$$

where the last line is written in translational-invariant combinations of the states, denoted by a double ket $|\ .\ \rangle\!\rangle^{(M)}$ with multiplicity M. The multiplicity was discussed already in chapter 1, it is basically the answer to the question *"How many different states can one create by subsequent application of the shift operator?"*. We use it here, to shorten notation and to remind ourselves that we are working in the translational invariant seed basis. For the next larger system we find after a short computation

$$(a_1^\dagger + a_2^\dagger + a_3^\dagger)^3|\mathrm{Vac}\rangle = 6|111\rangle\!\rangle^{(1)} + 3|210\rangle\!\rangle^{(3)} + 3|201\rangle\!\rangle^{(3)} + 1|300\rangle\!\rangle^{(3)} \tag{4.2.16}$$

with translational-invariant combinations of Fock states as above. A similar computation for a system with four particles and lattice sites yields (we skip again the details of the computation which is a simple application of creation operators and reorganisation of states)

$$\begin{aligned}(a_1^\dagger + a_2^\dagger + a_3^\dagger + a_4^\dagger)^4|\mathrm{Vac}\rangle = 24 \cdot |1111\rangle\!\rangle^{(1)} + \\ 12 \cdot \left(|2110\rangle\!\rangle^{(4)} + |2011\rangle\!\rangle^{(4)} + |2101\rangle\!\rangle^{(4)}\right) + 6 \cdot \left(|2200\rangle\!\rangle^{(4)} + |2020\rangle\!\rangle^{(2)}\right) + \\ 4 \cdot \left(|3100\rangle\!\rangle^{(4)} + |3010\rangle\!\rangle^{(4)} + |3001\rangle\!\rangle^{(4)}\right) + 1 \cdot |4000\rangle\!\rangle^{(4)}.\end{aligned} \tag{4.2.17}$$

In all of the simple cases computed so far, we found the coefficient of the state $|1\ldots1\rangle$ to be the largest in the expansion of the superfluid ground state.

What about the general case? Taking a closer look at the expansion, we note that the prefactors are nothing but the coefficients in a multinomial expansion

$$(x_1 + x_2 + \ldots + x_L)^N = \sum_{k_1+\ldots+k_L=N} \binom{N}{k_1, \ldots, k_L} \cdot x_1^{k_1} \cdots x_L^{k_L}, \tag{4.2.18}$$

where the expansion coefficients are given by a multinomial distribution, i.e.

$$\binom{N}{k_1, k_2, \ldots, k_L} = \frac{N!}{k_1!\, k_2! \cdots k_L!}. \tag{4.2.19}$$

We are interested in the relative weight between a state with only single occupied sites and states with one double occupied site. Their prefactors read simply

$$\binom{N}{1, 1, \ldots, 1} = \frac{N!}{1!\,1! \cdots 1!} = N! \qquad \text{and} \qquad \binom{N}{2, 0, 1 \ldots, 1} = \frac{N!}{2!\,0!1! \cdots 1!} = N!/2, \tag{4.2.20}$$

such that the ratio of the prefactors is always $1/2$ as seen in all the examples above. But the number of possible states with only one double occupancy is $N-1$ for a system of size $N = L$, which implies that the state $|1\ldots1\rangle$ has a $2(N-1)$-times larger weight than any state with one double occupied site. In this sense, our initial state is the most important contribution to the superfluid ground state of this finite system. We verified by a simple numerical test where we used an initial state that is closer to the superfluid ground state that the resulting effect is not altered. Namely, we incorporated the second largest contributions including double occupied sites (as outlined above) and still observed the discussed collapse and revival phenomenon. A more detailed theoretical analysis should certainly take into account that our initial state is not a coherent state. This could be done by repeating the computations for the derivation of an approximate revival time with $SU(N)$ coherent states.

Details for the Revival Time Estimate

In the derivation of the revival time, we discussed the action of an interband interaction term on a coherent state. We expressed the original operators a_l, b_l by operators of the resonant eigenbasis $\alpha_l\, \beta_l$ and encountered the following expression including several sums over Bessel functions:

$$\mathrm{e}^{\mathrm{i}2gW_x t\sum_l n_l^a n_l^b}|\tilde{\varphi};-\tilde{\varphi}) = \exp\Bigg[\frac{\mathrm{i}gW_x t}{2}\sum_l \sum_{l_1,\ldots,l_4} J_{l-l_1}(x_a)J_{l-l_2}(x_a)J_{l-l_3}(x_b)J_{l-l_4}(x_b)\times \\ (\mu_{l_1}^\dagger - \nu_{l_1}^\dagger)(\mu_{l_2} - \nu_{l_2})(\mu_{l_3}^\dagger + \nu_{l_3}^\dagger)(\mu_{l_4} + \nu_{l_4})\Bigg]|\tilde{\varphi};-\tilde{\varphi}). \quad (4.2.21)$$

We then argued that the most important term in the sum of Bessel functions is the ones including only zero order Bessel functions.

Let us discuss this in more detail. We define a coefficient matrix $\mathbf{M}$ with four indices $(ijkl = -L/2,\ldots,L/2 \in \mathbb{Z})$ with all products as entries

$$M_{ijkl} = J_i(x_a)J_j(x_a)J_k(x_b)J_l(x_b). \quad (4.2.22)$$

This matrix has $[2(L+1)]^4 \equiv D^4$ elements but is symmetric in the first two and last two indices, i.e. $M_{ijkl} = M_{jikl}$ and $M_{ijkl} = M_{ijlk}$, such that the number of independent elements is only $[D(D+1)/2]^2 = (2L+1)^2(L+1)^2$.

We can estimate the size of the matrix elements by using the fact that we are in a regime of $x_{a,b} \ll 1$ and inserting the leading order behaviour of the Bessel functions (cf. appendix C). If all indices are zero, the product will still be of order one, namely $M_{0000} \propto (1-x_a^2/4)^2(1-x_b^2/4)^2$. On the other hand, if none of the indices is equal to zero we find

$$M_{ijkl} \propto \frac{x_a^{i+j}x_b^{k+l}}{2^{i+j+k+l}i!j!k!l!} \quad \text{for} \quad ijkl \neq 0, \quad (4.2.23)$$

which is clearly much smaller than one and rapidly decreasing with all of the indices $ijkl$. The remaining coefficients with only some of the indices being equal to zero should thus be the next largest after M_{0000}. Let us take a specific example to understand their magnitude. We use $V_0 = 4$ and $m = 2$ for the order of the resonance. Then we have $x_a = 0.028$ and $x_b = -0.280$, such that we obtain as largest matrix elements

$$M_{0000} = 0.961, \quad M_{\pm1\pm1,00} = \pm0.0134, \text{ and } \quad M_{00,\pm1\pm1} = \pm0.0136. \quad (4.2.24)$$

We see that the matrix element M_{0000} used in our computation is by more than one order of magnitude larger than any other of the quickly decreasing contributions. To compare with further matrix elements, we plotted the absolute value of these elements on a logarithmic scale in figure 4.25. The absolute values of the matrix elements decrease rapidly away from M_{0000}.

This clearly supports our approximation of ignoring all terms except the strongly leading term. In particular, we found good agreement in the predicted and observed scaling of the revival time with the Hamiltonian parameters. The main drawback of our computation lies in the effect of a particular number of particles or lattice sites. We are now going to discuss one way to understand additional finite-size corrections.

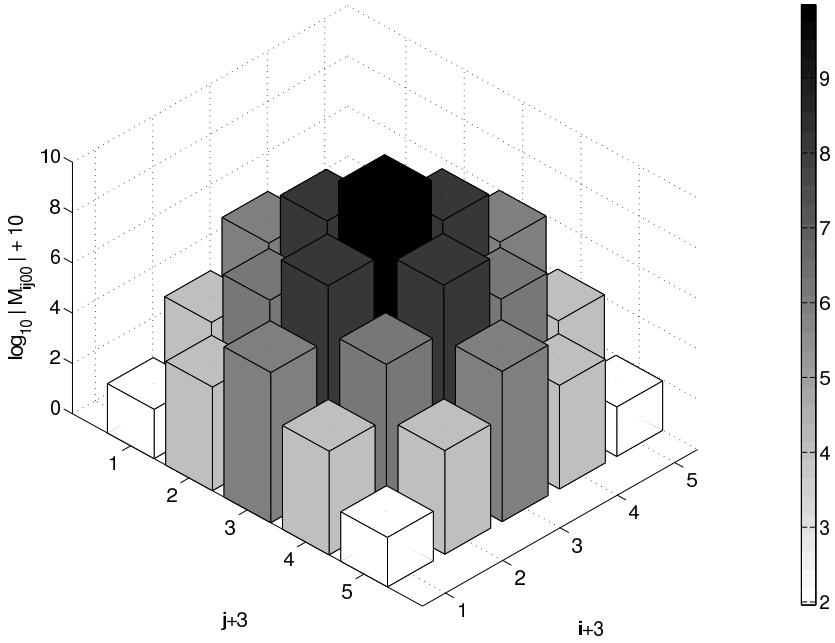

Figure 4.25: Absolute values of M_{ij00} with $i, j = -2, -1, \ldots, 2$ on a logarithmic scale. The largest matrix element M_{0000} is almost unity and the others decrease very radidly.

4.2.4 Exact Diagonalisation: Eigenfrequencies

In our numerical analysis of the collapse and revival effect, we found that a surprisingly small number of eigenstates is able to reproduce the collapse and revival signal quite well. Using such a decomposition into the eigenbasis, eq. (4.1.9) which read

$$|\psi(mT_B)\rangle = \sum_n c_n \mathrm{e}^{-\mathrm{i}\varepsilon_n mT_B} |\varepsilon_n\rangle, \quad c_n = \langle \varepsilon_n | \psi_0 \rangle,$$

the initial state dependence of the occupation of the upper band is taken into account by studying the weights c_n of the initial state expanded in the eigenbasis.

The result of a numerical diagonalisation for a system in resonance is depicted in 4.26, where the absolute values of the expansion coefficients with their corresponding quasienergies are shown. For vanishing two-body interaction strength $g = 0$, the quasienergies from the states with different occupation numbers are degenerate as expected. The energy difference between neighbouring lines of constant quasienergies corresponds to the time-scale of the resonant interband oscillations and follows from the diagonalisation of the resonant non-interacting system as $\Omega_{\text{res}} = 2\pi/T_{\text{res}} = 2|C_0 F J_m(\Delta x)|$. In the non-interacting system ($g = 0$), two coefficients are dominating and the difference of the quasienergies yields a single time-scale T_{res}.

When the interaction is turned on, the degeneracy of different eigenstates is lifted. The weight of states with many contributions from double or higher occupancies of sites decrease significantly (since they are energetically disfavoured) and their quasienergies are shifted. But, surprisingly, only a limited number of additional coefficients c_n contributes significantly in the eigenbasis expansion for $g \neq 0$ and they are all shifted simultaneously by only slightly differing energies. These states are still very similar to the non-interacting case and the observed collapse and revival signal is now determined by a this small number

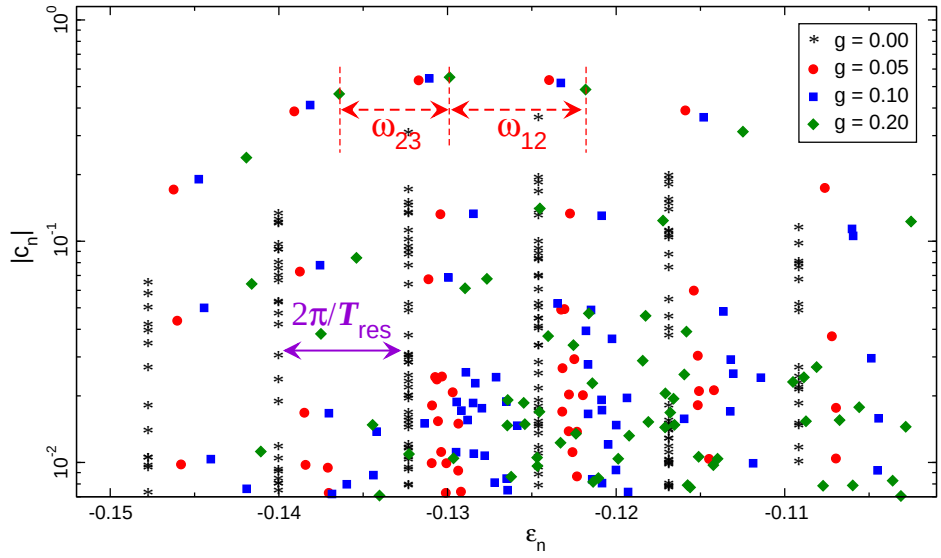

Figure 4.26: Absolute values of expansion coefficients $|c_n|$ versus the corresponding quasienergies ε_n in an expansion in the eigenbasis of the Floquet–Bloch operator, cf. eq. (4.1.9). Shown are different interaction strengths: $g = 0.0$ (*), $g = 0.05$ (circle), $g = 0.1$ (square), and $g = 0.2$ (diamond); other parameters: $V_0 = 4$, $m = 2$, $N = 5 = L$. We observe that different quasienergies are shifted at different rates when increasing the interaction strength.

of expansion coefficients that are much larger than the others. If we focus on the three largest coefficients, denoted as c_1, c_2, c_3 and sorted by their quasienergies $\varepsilon_1, \varepsilon_2, \varepsilon_3$, we find that the latter are shifted by the interaction by different amounts. The differences between neighbouring quasienergies, $\omega_{12} = |\varepsilon_2 - \varepsilon_1|$ and $\omega_{23} = |\varepsilon_3 - \varepsilon_2|$ (shown for the example $g = 0.2$ in figure 4.26), lead to a beating between two oscillations with periods $T_{12}, T_{23} \approx T_{\text{res}}$ and the revival time will thus be given by

$$t_{\text{rev}} \approx \frac{2\pi}{\omega_{23} - \omega_{12}} = \frac{T_{12} T_{23}}{T_{23} - T_{12}}. \tag{4.2.25}$$

This estimate requires a numerical diagonalisation but gives a clear physical interpretation to the revival time observed in a specific realisation with N atoms on L lattice sites.

We can perform such an analysis for different system sizes and compare the result to the full time evolution. The revival times as predicted by eq. (4.2.25) are compared to full numerical simulations in figure 4.27.

We find that our second prediction for the revival time, based on only the three largest coefficients in an eigenbasis expansion, is very close to the revival times observed numerically. The drawback of the method is the requirement of a full numerical diagonalisation of the Floquet–Bloch operator.[7] It is a full, i.e. not sparce, matrix and the diagonalisation of large matrices requires much time and working memory. Nevertheless, the approach gives

[7] The squares in the figure have been obtained from direct integration of the time-dependent Schrödinger equation. Only the non-zero matrix elements of the Hamiltonian are necessary for this and their number scales linearly with the Hilbert space dimension (see appendix A for details). To obtain the eigensystem, one needs to diagonalise the Floquet–Bloch operator which is a full matrix and all $(\dim \mathcal{H})^2$ matrix elements need to be stored. The computational system available allowed to use up to 20 GB of memory and $N = 7 = L$ was the largest system of approximately integer filling to be computable. See also table 1.1

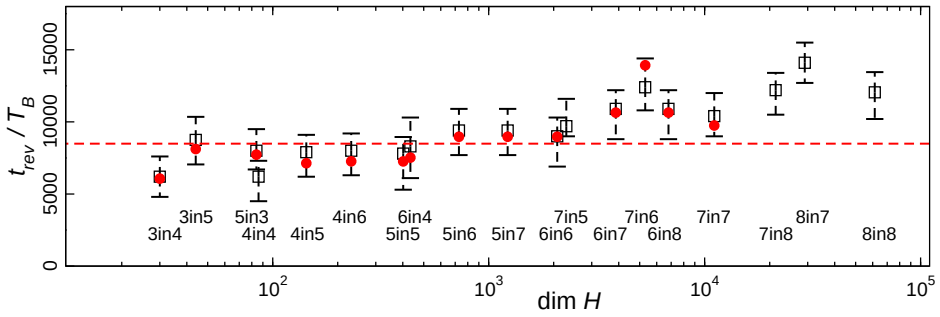

Figure 4.27: Comparison between estimated revival times according to eq. (4.2.25) (red circles) with numerical simulations (black squares) for $V_0 = 8, m = 1$, and different system sizes, parametrised by the Hilbert space dimension of the $\kappa = 1$-subspaces. The physical system sizes are indicated as 'Nin$L$' in the figure. The error bars indicate the width of the revival at half maximum. The available computational resources did not allow an exact diagonalisation for the three largest systems.

another useful interpretation of the physical process: The eigenstates are linear combinations of Fock basis states which contain single, double, or higher occupancies. When the interaction is turned on, eigenstates with large contributions from the latter basis states are strongly suppressed. Additionally, all eigenstates are shifted in energy by the repulsive inter-particle interactions by different amounts, depending on their composition of basis states. It is possible to estimate the revival time from the (differences in) energy shifts experienced by the most important eigenstates. Namely, the revival time can be predicted as the time for a complete beating between the three most important eigenfrequencies.

Summary

After introducing the effect of collapse and revival of the resonant interband oscillations and analysing it numerically, we tried to find an analytical description in the present section. We discussed different approaches that did not work and understood the necessity of several ingredients for a successful model: A proper description must rely on the many-body nature of the effect, and use the specific form of the initial state as well as the fact that the system is in resonance. We presented such a model, by transforming the most relevant interband interaction term to the eigenbasis of the resonant system and computing its effect on the time evolution of our initial state perturbatively. We compared the result to numerical simulations and found that it reproduces the scaling behaviour of the revival time when varying the parameters of the Hamiltonian. Additionally, our result predicts a divergence of the revival time for certain parameter values, which we have also detected numerically, however, with additional details the model did not explain. Both are strong indications that our model captures essential features of the complicated many-body effect. This is a nontrivial result for an interacting many-body system even for the regime of weak interactions discussed here. Furthermore, our description aimed at large systems and was thus not able to give an account for additional finite-size corrections. We presented an approach to circumvent this deficiency, which relied on a full diagonalisation of the system. In the following section, we will develop an effective model, that uses essential ingredients from both these approaches and allows an exact solution including an analytical estimate for the finite-size effects of the revival time.

4.3 Effective Spin Model

We were able to obtain the right scaling behaviour for the revival time in eq. (4.2.11) by describing the delocalised (and translationsal invariant) initial state as a coherent state and deriving the main effect of the dominant interband interaction term perturbatively. In this section, we are going to introduce an effective spin model, that allows an additional understanding of finite-size effects [Plö]. This is based on the idea developed in section 3.4.1 where we kept only the coupling between nearly degenerate levels from either band in a description of independent two-level systems. This can be interpreted as many independent spins and the effect of the interband interaction will be incorporated as an interaction between the effective spins.

4.3.1 The Effective Model and First Results

Idea for the Effective Model

So far, we gained a general understanding of the physical process leading to the collapse and revival effect in our system. Let us repeat this as a motivation for an effective model. We are working in a resonant regime, where two energy levels are degenerate, leading to strong interband oscillations. Due to this degeneracy, the eigenstates of the system in resonance are superpositions of lower and upper band states. We are using weak repulsive interaction and the system avoids double or higher occupancy of lattice sites as far as possible. But having superpositions between lower and upper level on all lattice sites, the system cannot circumvent two particles "sitting on top" of each other, that is one particle per band and site. This leads to a contribution from one of the interband interaction terms and is again shown schematically in figure 4.28.

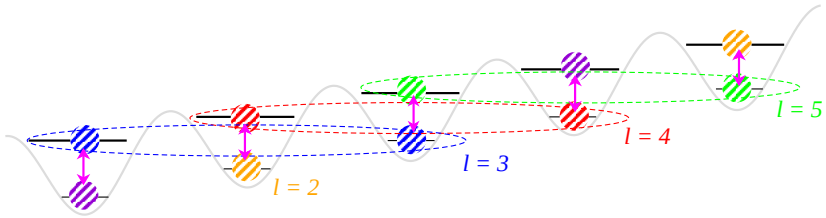

Figure 4.28: Schematical view of the effect of the interband interaction on the system in resonance of order $m = 2$. In resonance, the system is forced into a superposition of states from both bands (the sites forming a superposition are indicated by dashed ellipses). This happens on all lattice sites and the system cannot avoid to pay an interaction price $2W_x \sum_l n_l^a n_l^b$. A new fictitious lattice labeling scheme is also indicated in the figure.

Let us just try to model the physical situation from a different perspective. We have a superposition of always two energy levels. Let us enumerate them such that two degenerate levels have the same site number. This is indicated by choosing the same colours in figure 4.28 for those particles that form a superposition and should be considered on one lattice site in the fictitious lattice. The new site labels follow the same colours in the figure. We still want to use periodic boundary conditions and gave the atoms at the beginning and end of the chain accordingly colours (we did not draw ellipses around them to keep the illustration understandable). Thinking of only one of these new sites, what would be the Hamiltonian giving us a superposition of the upper and lower state? This would clearly

be proportional to the σ_x-matrix $\left(\begin{smallmatrix} 0 & 1 \\ 1 & 0 \end{smallmatrix}\right)$. The prefactor is determined by the oscillation frequency, which we know to be $\Omega_{\text{res}}^{(m)} = C_0 F J_m(\Delta x)$ for a resonance of order (m). This part is rather clear and straightforward, it is simply a reorganisation of the basis for the non-interacting resonant system.

The more interesting part concerns the effective interaction. Since we have always two levels per lattice site and the number of particles and lattice sites per band, we can think of a spin-$1/2$ sitting at each lattice site. We used the σ_z basis respresentation for the off-diagonal elements above and thus, the lower level at each site corresponds to a spin-down state $|\downarrow\rangle$ and the upper level to a spin-up state $|\uparrow\rangle$. The interband interaction should give a contribution when (remember we reorganised the basis) a down-spin and an up-spin are separated on the lattice by the order of the resonance. In figure 4.28 above, this is for example the case for the spin-up at $l = 4$ (in red) an spin-down at $l = 2$ (in yellow). This is, in essence, a way of rephrasing our understanding of the physical mechanism at work in terms of spins. The effective Hamiltonian we use (for a resonance of order m) is accordingly given by

$$\mathcal{H}_{\text{eff}} = \sum_{l=1}^{L} \left(V_m \sigma_l^x + U \sigma_l^{\uparrow} \sigma_{l+m}^{\downarrow} \right) \tag{4.3.1}$$

where $V_m = C_0 F J_m(\Delta x)$ and $U = \frac{1}{2} g W_x J_0^2(x_a) J_0^2(x_b)$. The first part is as in the non-interacting resonant system, which was also a sum of independent two-level system. We only changed the ordering of the levels to bring degenerate levels close together. The second part reflects the repulsion of two particles when sitting in different bands or different spin states respectively. Accordingly, we used our knowledge of the resonant basis for the coefficients of this effective Hamiltonian. Since we are using spin-$1/2$ matrices in this effective description it can only be applied to the case of integer filling, i.e. $N = L$. The number of lattice sites is per definition identical with the number of spins. The effective Hamiltonian is also translational invariant, such that one could use a reduction to subspaces of fixed total quasimomentum.

In the following sections we will compare the results of the effective Hamiltonian, to those from the full two-band Bose–Hubbard model. We will start again with numerical results and study analytical approaches afterwards.[8]

Numerical Results of the Effective Spin Model

First of all, we observe that the effective spin model is much easier to treat numerically, since the needed Hilbert space is much smaller than in the original two-band Bose–Hubbard model. Specifically, their Hilbert spaces for integer filling grow with the number of particles as

$$\dim \mathcal{H}_{\text{eff}} = 2^L \qquad \text{and} \qquad \dim \mathcal{H}_{\text{full}} \approx 0.26 \cdot 6^L, \tag{4.3.2}$$

where the last relation is a fit to the full Hilbert space sizes of the two-band Bose–Hubbard model for $L \lesssim 15$. Thus the numerical effort for simulating the spin model is highly reduced when compared to the bosonic system. It is also rather easy to implement, about 50 lines of MATLAB code where needed to produce the curve shown below.

[8] In an earlier footnote, we discussed the possibility of studying the entanglement between the lower and upper band states. Please note, that the additional complication caused by the indistinguishability of the bosons is not present for spins. This means, the effective model is an easy playground for studying entanglement in spin systems. The quantum Ising model for example, has been studied in [Ami08, Gri08].

To compare the original system and the effective model, we have to translate our observable to the spin picture. the total spin in z-direction does not—as one might guess—correspond to the occupation of the upper band. Instead, what we actually need to do, is to count the number of up-spins in the system:

$$\mathcal{N}_b(t) = \tfrac{1}{N}\langle\psi(t)|\sum_l n_l^b|\psi(t)\rangle \quad \longrightarrow \quad \mathcal{N}_\uparrow(t) = \tfrac{1}{L}\langle\psi(t)|\sum_l \sigma_l^\uparrow|\psi(t)\rangle \tag{4.3.3}$$

which is nothing else than projecting onto the spin-up state at all lattice sites. The initial state for the Bose–Hubbard model was characterised by occupation of the lower band only and a delocalisation of particles there. Our typical initial state for the Bose–Hubbard model reads $|1\ldots1;0\ldots,0\rangle$. The initial state for the spin system is thus the product of all spins down, i.e. $|\downarrow\ \cdots\ \downarrow\rangle$. We have computed the time-dependent expectation value of our observable for the parameters from the two-band Bose–Hubbard model. An example for $V_0 = 10$ and a resonance $m = 1$ is shown in figure 4.29 where we compare the population dynamics in the two-band Bose–Hubbard model and the effective spin model.

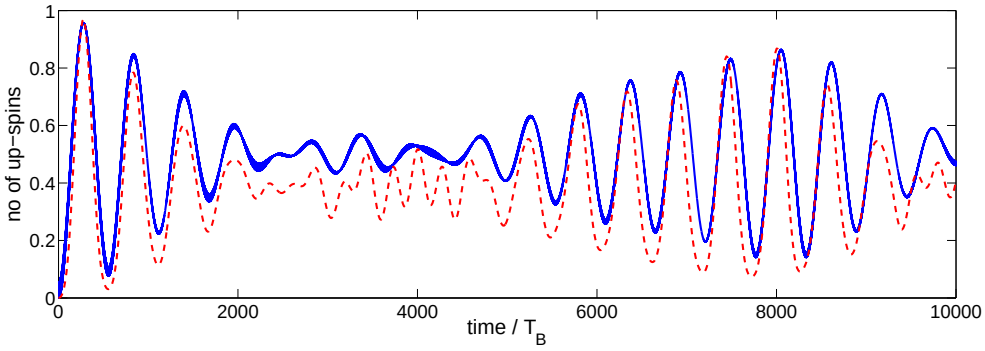

Figure 4.29: Occupation of the upper band in the two-band Bose–Hubbard model (solid blue line) and number of up-spins in the effective spin model (dashed red line) for the same parameters. The spin model reproduces most features of the complex time signal, first and foremost the collapse and revival are in very good agreement between both models. Only the mean occupation (averaged over time) in the spin model has a smaller value than in the Bose–Hubbard model. Parameters: $V_0 = 10$, $m = 1$, $g = 0.1$ and $N = 5 = L$.

We observe a very high similarity between the oscillations in both models. The Bose–Hubbard and spin model show the very same collapse and revival effect. The two signals are very close, a slight difference only in their mean value. But the maximum of the revival in the oscillations is at exactly the same position and the width of the revivals are also identical. This is an amazing result. These two very different model system show almost the same behaviour in the respective observable. This is a strong indicator, that a) our reasoning about the basic physical mechanism is a good description and b) that the effective spin model is a good effective model as far as the occupation of the upper band is concerned.

Let us compare the results from the spin model and the full two-band Bose–Hubbard model for different system sizes to check the scaling of this good agreement. Figure 4.30 shows the revival times obtained from numerical simulation of the Bose–Hubbard model and the effective spin model for a deep optical lattice $V_0 = 8$ and resonance $m = 1$. The spin model allows only integer filling and we can only compare with integer filling in the Bose–Hubbard model. The system is described by the size of the Hilbert space for the Bose–Hubbard system, i.e., the results for the spin system are *not* plotted versus the size

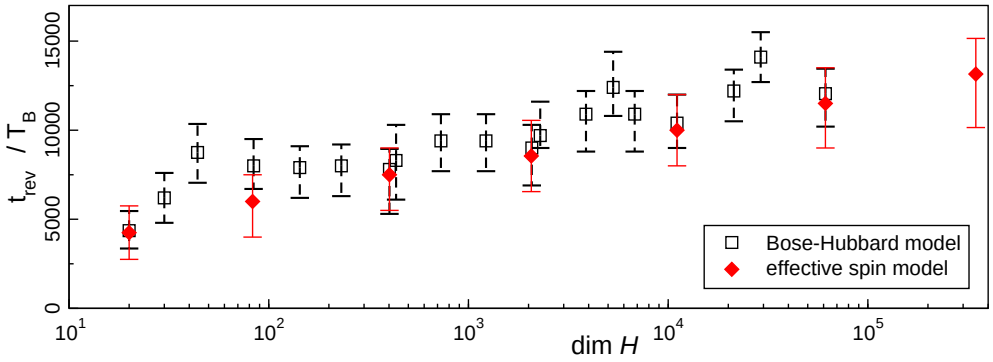

Figure 4.30: Revival times for systems of different sizes as indicated by the dimensionality of their Hilbert space for the two-band Bose–Hubbard model (empty squares) and the effective spin model (full red diamonds). The data points for the effective spin model are *not* shown for their Hilbert space size, but for the case of the full Bose–Hubbard system they should model, e.g., the spin system for $L = 5$ is at the same abscissa as the Bose–Hubbard system with $N = 5 = L$. By definition, the spin model can only describe integer filling and there are thus less data points shown for the spin model than for the Bose–Hubbard system. Note that bars in the figure indicate the width of the revival, not an error in its determination.

of their Hilbert spaces. Instead, they are shown at the same position as the system they should model, e.g., the result from a system of $L = 5$ spins is shown together with the $N = 5 = L$ Bose–Hubbard system. Similar to figure 4.29 above, we observe a very good agreement between the results from the effective model and the Bose–Hubbard model. Also the widths of the revivals (indicated by bars in the figure) are very similar. The only exception forms the small system with $L = 4$, where the revival time in the spin model lies below the results of the Bose–Hubbard model.

Overall, the agreement is astonishing, especially when compared to the drastic simplification from the two-band Bose–Hubbard model to the effective model of eq. (4.3.1). It is not only the repulsive interaction that allows this strong reduction of the Hilbert space, since we saw in section 4.1.5 that a direct truncation of the Hilbert space to only single (or even double) occupancy per site does not at all reproduce the collapse and revival effect. Such a reduction is also called "hard-core bosons" [Gir60, Rig04] and only valid in the limit of strong interaction, whereas we are in a regime of weak interactions. The incorporation of the resonance for the effective model, seems to be another important aspect of its good agreement with the original system.

Besides the very good agreement for not too small systems, we observe an additional linear increase in the revival time with growing system size L (the Hilbert space grows with a power of L which is linear on the logarithmic scale in the figure). There is an increasing trend in the revival times for the Bose–Hubbard system, too. But it is more evident in the spin model, where one can only treat exactly unit filling. So far, it is only a numerical observation. Let us try to understand the revival time theoretically and we will come back to this seemingly linear increase later.

4.3.2 Exact Solution of the Effective Spin Model

Rewriting the Hamiltonian

The smaller Hilbert space of the effective model proved advantageous for numerical computations. Let us now take a closer look at the Hamiltonian itself. The effective spin Hamiltonian reads

$$\mathcal{H}_{\text{eff}} = \sum_{l=1}^{L} \left(V_m \sigma_l^x + U \sigma_l^{\uparrow} \sigma_{l+m}^{\downarrow} \right) \qquad \text{with} \qquad \sigma_l^{\uparrow\downarrow} = \tfrac{1}{2} \left(1_l \pm \sigma_l^z \right). \tag{4.3.4}$$

We can insert the expressions for the spin-up and -down projectors given on the right. This results in four terms, the first one is simply a constant (namely $L/4$) and can be dropped since it will only shift the zero of energies. The second and third terms are the same but with opposite sign and cancel each other, such that the remaining Hamiltonian reads

$$\mathcal{H}_{\text{eff}} = \sum_{l=1}^{L} \left(V_m \sigma_l^x - \tfrac{1}{4} U \, \sigma_l^z \sigma_{l+m}^z \right). \tag{4.3.5}$$

This Hamiltonian is known (for $m = 1$) as the quantum Ising model in a transverse magnetic field [Sac01]. It describes coupled spins that tend to align in z-direction but are under the force of an applied magnetic field in x-direction.

Let us discuss the physics of this model for $m = 1$ following [Sac01]. We are in a regime with weak interaction, i.e. $V_m \gg U/4$. The ground state for $U = 0$ is given by

$$|0\rangle = \prod_l |-\rangle_l \qquad \text{with} \qquad |\pm\rangle_l = \left(|\uparrow\rangle_l \pm |\downarrow\rangle_l \right) / \sqrt{2}, \tag{4.3.6}$$

where $|\pm\rangle$ are the two (symmetric and antisymmetric) eigenstates of σ^x. Thus, in the non-interacting ground state all spins are in the same state, the lower eigenstate of σ^x which we called $|-\rangle$. What about the excitations? For the first excited state, one of the spins will be flipped to the upper eigenstate of σ^x, say the one at site i, it reads

$$|i\rangle = |+\rangle_i \prod_{l \neq i} |-\rangle_l, \tag{4.3.7}$$

and is L-fold degenerate for $U = 0$. The second excited state would contain two spin-flipped states (with degeneracy $\binom{L}{2}$) and so on. But what is the effect of the exchange term $\sigma_l^z \sigma_{l+1}^z$? In first order, it leads to a coupling of spin-flips at different sites

$$\langle i | \sum_l \sigma_l^z \sigma_{l+1}^z | i+1 \rangle = 1. \tag{4.3.8}$$

The exchange term hopps the spin-flip from one site to its neighbour. Such a tight-binding system with nearest neighbour hopping is easily diagonalised by changing to momentum space $|k\rangle = \frac{1}{\sqrt{L}} \sum_j \mathrm{e}^{\mathrm{i}kj} |j\rangle$, such that the energy of the first excited state reads in first order perturbation theory:

$$\varepsilon_k = V_m - \tfrac{1}{2} U \cos k. \tag{4.3.9}$$

We see that the perturbation lifts the degeneracy of the first excited state. The possible excitations of the system are delocalised spin-flips travelling through the system with momentum k, we will therefore call them *magnons*. If we ignore scattering between these

excitations, i.e., we treat them as non-interacting, the second excited state contains two magnons, say with momenta k_1 and k_2, such that the state has total momentum $k = k_1 + k_2$ and its energy is the sum of both single-particle energies $E(k) = \varepsilon_{k_1} + \varepsilon_{k_2}$. Within this perturbative approach the rest of the spectrum can also be understood qualitatively. However, the Hamiltonian allows much more than perturbation theory.

Exact Solution via Jordan–Wigner Transformation

Interestingly, it is possible to solve the quantum Ising model exactly. This has been achieved by Pfeuty [Pfe70] in 1971 and is quite remarkable, since the quantum Ising model with transversal field shows a quantum phase transition. To solve the model, let us further apply a rotation of π around the y-axis. This seems unnecessary at the moment, but will turn out useful later. Such a rotation leads to a replacement of $\sigma^x \to \sigma^z$ and $\sigma^z \to -\sigma^x$. The final effective spin Hamiltonian therefore reads

$$\mathcal{H}_{\text{eff}} = \sum_{l=1}^{L} \left(V_m \sigma_l^z - \tfrac{1}{4} U \, \sigma_l^x \sigma_{l+1}^x \right). \tag{4.3.10}$$

The diagonalisation of this Hamiltonian involves several steps. First, we apply a Jordan-Wigner transformation which maps the interacting spin system onto a gas of non-interacting fermions. For the formionic system, we will go to momentum space in a second step and finally perform a Bogolyubov transformation to actually obtain the eigenstates. Let us discuss the single steps first and the physical content afterwards.

The basic idea of the Jordan-Wigner transformation is, that the raising and lowering operators for a one-dimensional spin system behave locally, i.e. at the same site, like fermionic operators $c_l^\dagger$ (we assume $l \neq l'$ here):

$$\{\sigma_l^-, \sigma_l^+\} = 1 \qquad \{c_l, c_l^\dagger\} = 1 \tag{4.3.11a}$$

$$[\sigma_l^-, \sigma_{l'}^+] = \delta_{ll'} \qquad \{c_l, c_{l'}^\dagger\} = 0. \tag{4.3.11b}$$

But we already stated an important difference between spins and fermions in the second line: Spins at differente sites commute (they are independent), but fermions anti-commute! The solution to map spins to fermions that was found by Jordan and Wigner in 1928 [Jor28] is to make the spins aware of the presence of other spins. This can be achieved by giving the raising and lowering operators an additional phase involving all spin operators left of them

$$c_l^\dagger = \sigma_l^+ \mathrm{e}^{-\mathrm{i}\pi \sum_{k<l} (1+\sigma_k^z)/2} = \sigma_l^+ \prod_{k<l} \sigma_k^z \tag{4.3.12a}$$

$$c_l = \sigma_l^- \mathrm{e}^{+\mathrm{i}\pi \sum_{k<l} (1+\sigma_k^z)/2} = \sigma_l^- \prod_{k<l} \sigma_k^z. \tag{4.3.12b}$$

The operators $c_l^{(\dagger)}$ defined by these equations have indeed the correct fermionic commutation relations, as can be verified explicitly. They inherit them from the properties of the spin matrices by the help of the clever phase factor. The Jordan–Wigner representation of the spin operators therefore reads

$$\sigma_l^z = 2 c_l^\dagger c_l - 1, \quad \sigma_l^+ = c_l^\dagger \mathrm{e}^{\mathrm{i}\pi \sum_{k<l} c_k^\dagger c_k}, \quad \sigma_l^- = c_l \mathrm{e}^{-\mathrm{i}\pi \sum_{k<l} c_k^\dagger c_k}. \tag{4.3.13}$$

We need to rewrite our effective spin Hamiltonian in terms of σ^z and $\sigma^\pm$ by using $\sigma^x = \sigma^+ + \sigma^-$ and can then insert the fermionic representation. The result reads

$$\mathcal{H}_{\text{eff}} = \sum_{l=1}^{L} \Big[2V_m c_l^\dagger c_l - \tfrac{1}{4} U \left(c_l^\dagger c_{l+1} + c_{l+1}^\dagger c_l + c_l^\dagger c_{l+1}^\dagger + c_{l+1} c_l \right) \Big], \tag{4.3.14}$$

where we dropped a constant term (namely $-LV_m$). This fermionic Hamiltonian does not conserve the number of particles just as the original spin Hamiltonian did not conserve the total z-component of the spin.[9] In this fermionic representation, the resonant interband oscillations correspond to an onsite energy and the interband interaction induces hopping between neighbouring fermionic sites but can also create or annihilate two particles at neighbouring sites.

The nearest neighbour coupling suggests again to switch to momentum space via $c_k = \frac{1}{\sqrt{L}} \sum_l \mathrm{e}^{\mathrm{i}kl} c_l$ to obtain

$$\begin{aligned} \mathcal{H}_{\text{eff}} &= \sum_k \left(2V_m - \tfrac{1}{2} U \cos(k) \right) c_k^\dagger c_k - \tfrac{\mathrm{i}}{4} U \sin(k) \left(c_{-k}^\dagger c_k^\dagger + c_{-k} c_k \right) \\ &= \frac{U}{4} \sum_k 2 \left(\tfrac{4V_m}{U} - \cos(k) \right) n_k - \mathrm{i} \sin(k) \left(c_{-k}^\dagger c_k^\dagger + c_{-k} c_k \right). \end{aligned} \tag{4.3.15}$$

This Hamiltonian involves a creation and annihilation of two fermions with momenta of opposite direction, like one encounters in the BCS theory of superconductivity. It can similarly be diagonalised by a Bogolyubov transformation, the final step in solving the quantum Ising model in a transverse field, which is equivalent to our effective spin model.

We introduce new operators as linear combinations of the ones from above

$$c_k = u_k d_k + \mathrm{i} v_k d_{-k}^\dagger \qquad d_k = u_k c_k - \mathrm{i} v_k c_{-k}^\dagger \tag{4.3.16a}$$

$$c_{-k} = u_k d_{-k} + \mathrm{i} v_k d_k^\dagger \qquad d_{-k} = u_k c_{-k} - \mathrm{i} v_k c_k^\dagger, \tag{4.3.16b}$$

and the coefficients need to be chosen such that the operators are still fermionic

$$\{ d_k, d_{k'}^\dagger \} = \delta_{kk'} \qquad \text{and} \qquad \{ d_k^\dagger, d_{k'}^\dagger \} = 0 = \{ d_k, d_{k'} \} \tag{4.3.17}$$

which implies $u_k^2 + v_k^2 = 1$. They can be chosen such that $u_{-k} = u_k$ and $v_{-k} = -v_k$. One can thus use a representation of the coefficients $u_k = \cos(\theta_k/2)$ and $v_k = \sin(\theta_k/2)$. The final step is to insert the Bogolyubov transformation, eq. (4.3.16), into the quadratic Hamiltonian of eq. (4.3.15) and to demand that terms violating particle number conservation (like $d^\dagger d^\dagger$ and dd) vanish. This is achieved by the right choice of the free phase in the transformation

$$\tan \theta_k = \frac{\sin k}{\cos k - 4V_m/U}, \tag{4.3.18}$$

as can be verified by a making use of standard trigonometric identities. The final result in terms of the Bogolyubov quasi-particles is

$$\mathcal{H}_{\text{eff}} = \sum_k \epsilon(k) \big(d_k^\dagger d_k - 1/2 \big), \text{ with } \epsilon(k) = V_m \Big[1 - \tfrac{U}{V_m} \cos k + \big(\tfrac{U}{4V_m} \big)^2 \Big]^{1/2}. \tag{4.3.19}$$

[9] It is now clear why we performed the additional rotation around the y-axis. Without this rotation, one can also apply the Jordan–Wigner transformation, but one would obtain a Hamiltonian with interacting fermions ($\sigma_l^z \sigma_{l+1}^z \to c_l^\dagger c_l c_{l+1}^\dagger c_{l+1}$ + quadratic terms) which is not solvable via Fourier and Bogolyubov transforms.

This is the exact solution of our effective spin model. The elementary excitations of the system are non-interacting fermions with a cosine dispersion, which we identified qualitatively as magnons earlier. We recover the excitation energy $\varepsilon_k = V_m - \frac{1}{2}U\cos k$ as was discussed in perturbation theory in the limit of weak interactions (which is exactly the regime we are interested in). It was thus justified to treat the elementary excitations as independent, since they are actually given by non-interacting fermions. However, the fermionic nature of the solution implies an important constraint for the excitations. When several magnons are present, they must all have different momenta due to Pauli's exclusion principle. The spectrum of possible single-particle energies is shown for the parameters of $V_0 = 4$ is shown in figure 4.31.

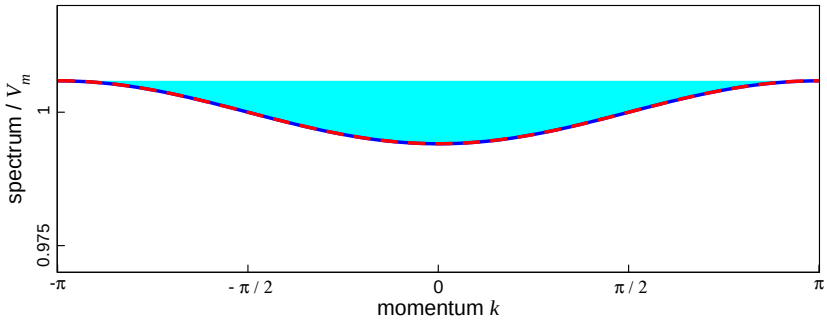

Figure 4.31: Single-particle spectrum for the effective spin model. Shown is the exact solution (solid line) and the approximation for weak interactions (dashed red line). Parameters correspond to $V_0 = 4$ and $g = 0.1$, such that $U/V_m \approx 0.0118$.

There is a constant contribution V_m for each excitation and a momentum dependent contribution from the interaction that led to hopping in the fermion representation. The many-particle state can be generated as usual as $d^\dagger_{k_1} d^\dagger_{k_2} \cdots d^\dagger_{k_n}|\mathrm{Vac}\rangle$ with all $k_1, k_2, \ldots, k_n$ distinct and has an energy of $E(k) = \epsilon_{k_1} + \epsilon_{k_1} + \cdots + \epsilon_{k_n}$ with possible momenta $k_j = 2\pi \cdot j/L$ and $(j = 1, \ldots, L)$ for our system with periodic boundary conditions.

4.3.3 Results for the Revival Time

Identification of Contributing States

Now, that we have solved the effective model exactly and know that the excitations are magnons with distinct momenta, we would like to understand the implications for the revival time in the effective model. The exact solution allows the computation of any correlation function for the system. But this is not of interest to us here. We want to perform the exact time evolution of a given initial state. Since we know the eigenstates of the system we can use an eigenbasis expansion

$$|\psi(t)\rangle = \sum_{j=1}^{2^L} c_j \mathrm{e}^{-\mathrm{i}\varepsilon_j t}|\varepsilon_j\rangle, \tag{4.3.20}$$

with the many different many-magnon states forming the complete eigenbasis. Similar to the truncated eigenbasis expansion in section 4.2.4, we can now determine the most relevant coefficients and use their energies to estimate the revival time. This is done in figure 4.32

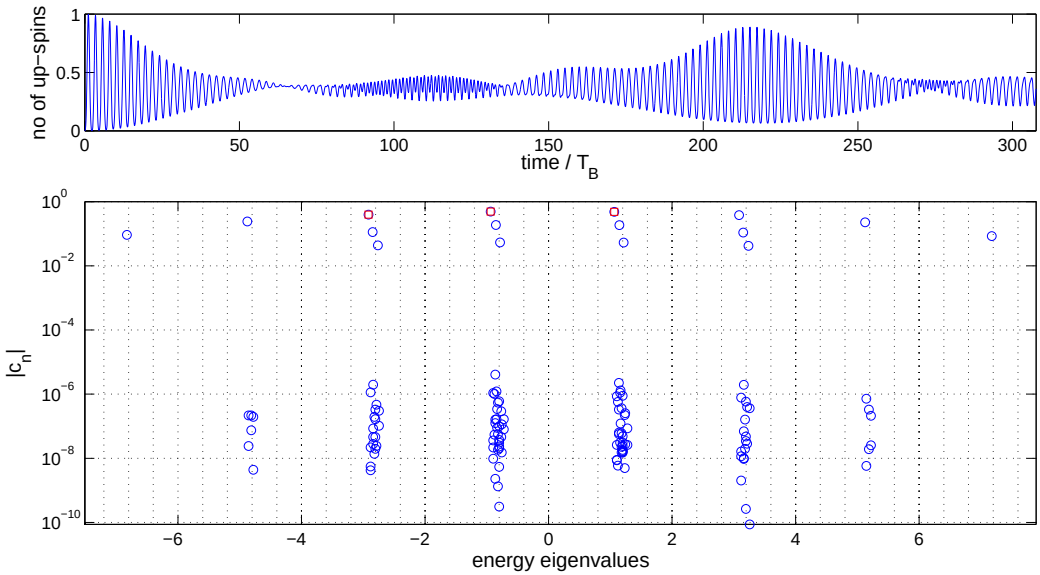

Figure 4.32: Eigenbasis expansion in the effective spin model. *Upper panel:* Number of up-spins as a function of time for initial state $|\downarrow \cdots \downarrow\rangle$ showing the collapse and revival effect. *Lower panel:* Coefficients of eigenbasis expansion versus the corresponding eigenenergies. The three largest coefficients are marked by red squares and have the smallest energy in their respective subspace. Parameters: $V_m = 1$ which sets $T_{\text{res}} = \pi$, $L = 7$ and $F = 4.6020$.

where we show the time evolution of our specific initial state together with the expansion sorted by their energies.

The time evolution in the upper panel shows the well-known collapse and revival effect for the number of up-spins for a system of size $L = 7$. In the lower panel, we show the coefficients for the eigenbasis expansion of our initial state $|\downarrow \cdots \downarrow\rangle$ sorted by their eigenenergies. The three largest coefficients (i.e. with greatest absolute value) have been marked by red squares. We will later use them for an approximate estimate of the revival time as has been very successful in the truncated eigenbasis expansion for the full two-band problem.

As expected, the spectrum of the effective spin model is divided into regions or subspaces of $0, 1, \ldots, L$ magnons which are separated by an energy V_m (set to unity in the figure) and the n-th subspace is $\binom{L}{2}$-fold degenerate. We see that the most relevant expansion coefficients are those from the center of the complete spectrum. More precisely, the three largest coefficients (marked by red squares in the figure) for a system of size L are from the subspaces with

$$M-1,\ M,\ M+1 \text{ magnons, where } M = \begin{cases} L/2 & \text{for } L \text{ even} \\ (L-1)/2 & \text{for } L \text{ odd} \end{cases}. \tag{4.3.21}$$

To estimate the revival time for the spin system, we need to know the exact energies of the dominant coefficients. An important observation from figure 4.32 is: In each of the three central energy bunches, it is *always the energetically lowest* eigenenergy that yields the largest coefficient. We added a horizontal grid to make this clearer visible in figure 4.32. We observed exactly the same behaviour in systems of any (numerically accessible) size and parameter values. Therefore, we need to determine the exact values of these eigenenergies

from our understanding of the spectrum in order to estimate the revival time from a truncated eigenbasis expansion using the three dominant coefficients. We are going to do this in a surprisingly simple way now.

Computation of the Revival Time

We know that the energy of a many-body state with M magnons is given by

$$E_M = \sum_{l=1}^{M} \left(V_m - \tfrac{1}{2}U\cos(k_{j_l})\right) \tag{4.3.22}$$

with $k_{j_l} = 2\pi j_l/L$ and each j_l can take a value between $1, \ldots, L$. The energies for a given number of magnons M thus arise from different choices of the momenta k_{j_l}. To obtain the smallest possible value, we need to minimise the sum of M cosine functions with possible arguments k_{j_l} under the constraint of all j_l being different. This is an optimisation in several variables of a nonlinear function and in general a difficult task. But, we can give a clear physical picture, how the state of minimal energy is achieved. Starting with only one k, the state to be filled is certainly the one closest to the minimum of the dispersion relation, $k = 0$, the next k must be different and will take a state with slightly higher energy and momentum, but still close to $k = 0$. This process will go on gradually until we have a many-body state with half of the possible magnons. But this is nothing else, than having a cosine energy band that is half filled. This is shown schematically in figure 4.33.

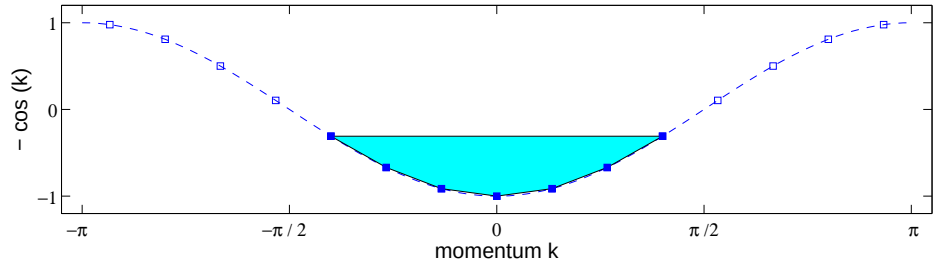

Figure 4.33: The magnon sea at half filling. Show is the cosine dispersion of the single-particle excitations. It is resolved by a finite number of points since momentum is discrete in a finite system. We need the states of lowest energy with l magnons. This is achieved by filling the sea of possible single-particle excitations from below. This is shown in the figure.

We show a cosine dispersion, that is resolved by L points and filled up from the center. Since the energies we are adding up are the energies of the delocalised spin-flip excitations, we take an analogy to solid-state physics and refer to it as the *magnon sea*. The total energy in the half-filled sea is thus the lowest energy of a state containing M magnons, with M according to eq. (4.3.21).

The revival time can then be estimated from the difference between the energies of states with $M-1$, M, and $M+1$ magnons. That is we need

$$\Delta\omega = (E_{M+1} - E_M) - (E_M - E_{M-1}) = E_{M+1} + E_{M-1} - 2E_M. \tag{4.3.23}$$

In the picture of having a half-filled magnon sea, this means that the revival time can be obtained by comparing the energies for the complete magnon sea (at half filling) with the energies for one single-particle and one single-hole excitation of the magnon sea, i.e., adding

or removing one magnon. Inserting explicitly that the energy of M magnons is proportional to the sum of M cosine functions (the constant terms cancel) with different arguments filling the magnon sea from below, we obtain the following frequency difference

$$\begin{aligned}\Delta\omega &= -\frac{1}{2}U\left(\sum_{j=1}^{M+1}\cos(k_j)+\sum_{j=1}^{M-1}\cos(k_j)-2\sum_{j=1}^{M}\cos(k_j)\right)\\ &= -\frac{1}{2}U\left(\cos k_{M+1}-\cos k_M\right)\approx -\tfrac{1}{2}U\frac{2\pi}{L}(M+1-M)=-\frac{\pi}{L}\,U,\end{aligned} \tag{4.3.24}$$

where we expanded the cosine around its zero. Using our expression for U, we find that the revival time as estimated by oscillations between the dominant frequencies, is altered by a size-dependent prefactor

$$\boxed{t_{\text{rev}}=\frac{L}{2\pi}\frac{4\pi}{gW_xJ_0^2(x_a)J_0^2(x_b)}\,.} \tag{4.3.25}$$

This is an important result, adding a finite-size correction of $L/2\pi$ to our previous prediction eq. (4.2.11) for the revival time. We also see clearly here, that a direct analogy to quantum optics is not sufficient to explain the collapse and revival effect in the two-band Bose–Hubbard system. The reason is simply that the revival time in the Jaynes–Cummings model converges quickly to a finite value, already for a small number of photonic modes (see appendix B). But we just understood, that this is not the case for two-band Bose–Hubbard model.

Comparison to Numerical Results

Let us compare this prediction to numerical data. First of all, the formula should describe the result of a truncated eigenbasis expansion. There, one can estimate the revival also numerically by using the differences between the three dominant frequencies numerically instead of analytically, as has been done above. A comparison between a numerical estimate using full diagonalisation of the spin model and our analytical result is shown in figure 4.34.

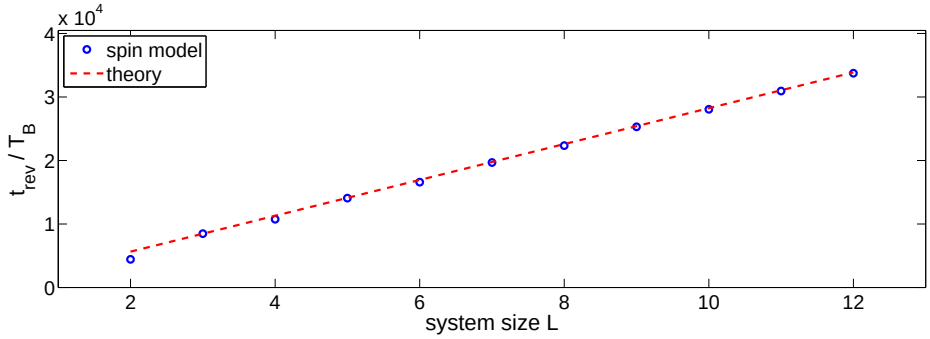

Figure 4.34: Comparison of numerical and analytical estimate of revival time in the effective spin model. Shown are the numerical estimate using full diagonalisation of the spin model (data points) and our analytical result (dashed line). The numerical result agrees well with the numerical estimate, indicating that the linearisation of the cosine is a good approximation already for small systems. The agreement is better for larger systems.

We observe very good agreement between the purely numerical result of a truncated basis expansion and our analytical estimate for a basis truncation. This basically validates that approximating the cosine gives surprisingly good results even for small systems and supports the claim of a finite-size correction as given by eq. (4.3.25). Keeping in mind the good agreement between the numerical prediction for the revival within a truncated basis expansion as demonstrated in section 4.2.4, we expect a good agreement between the actual maximum of the revival and the numerical estimate.

Let us compare our prediction with actual revival times as observed in the full Bose–Hubbard model. This can be done by applying a finite-size scaling, using the analytical prediction for the finite-size behaviour. This means, when we rescale the numerical results for the revival time by a size-dependent factor $2\pi/L$, the curves for different sizes should coincide. The result of such a rescaling of numerical data as a function of the lattice depth is shown in figure 4.35.

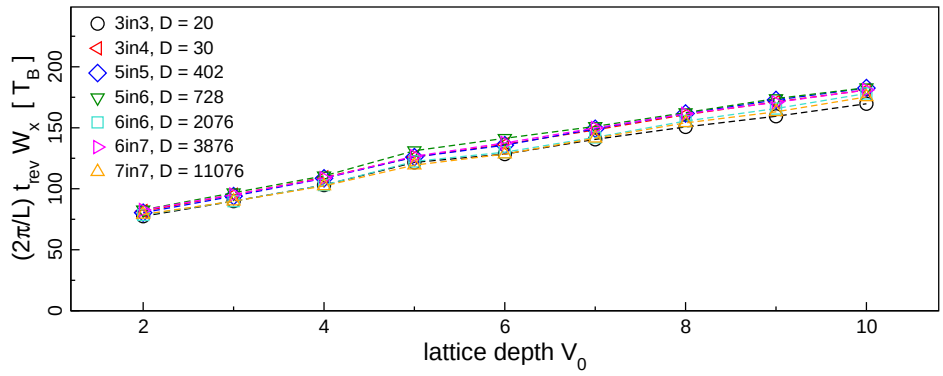

Figure 4.35: Finite-size scaling of the revival times. We show the revival times from different numerical simulations of the full two-band Bose–Hubbard model (the corresponding system sizes 'Nin$L$' and the dimension of the Hilbert spaces D are indicated in the legend). The numerical values have been rescaled by the size-dependent prefactor $2\pi/L$ according to our improved analytical prediction. The data points for different system sizes basically coincide, indicating the validity of our analytical prediction eq. (4.3.25).

We show a rescaling of several systems that have exactly integer or slightly smaller filling. The curves coincide up to some small deviations that seem to increase with the lattice depth. Nevertheless, the agreement is very good. The size-dependent prefactor in eq. (4.3.25) as a correction to our earlier result eq. (4.2.11) for the revival time thus explains our numerical data for integer and nearly integer filling remarkably well. We thus have a single result describing complex systems with Hilbert spaces sizes ranging over three orders of magnitude (as shown in figure 4.35). This is of course only possible for integer filling, where the presented effective spin model is applicable. We believe, however, that one can estimate the effect of slightly higher filling, corresponding to one or two more atoms in the system, by either adding a larger spin to the effective model or using a description with larger spins, e.g. spin 1, right from the beginning. The former is easily achieved numerically and the latter could serve as a refined analytical model.

Divergence of Revival Time

We find that the effective spin model describes the collapse and revival effect very well. Let us come back to the expected divergence of the revival time whenever the denominator in

our analytical result eq. (4.3.25) is vanishing. We studied this effect already in section 4.2.2 on page 134 for the full two-band Bose–Hubbard model, but the spin model is much easier to treat numerically and allows us to study a larger parameter range.

Motivated by the experimental possibilities with superlattices, we varied the band gap of the system which included a variation of the external force $F \approx \Delta/m$ since the system has to be in resonance. However, the band gap does not enter as parameter into our effective spin model eq. (4.3.1), since it is by definition set-up to work in resonance only (see the discussion and motivation of the spin model in section 4.3.1). Therefore we vary the external force to study the expected divergence whenever one of the two Bessel functions $J_0^2(J_a/F)J_0^2(J_b/F)$ in the denominator for the revival time vanishes. The result is shown in figure 4.36 for a system of $L = 8$ spins.

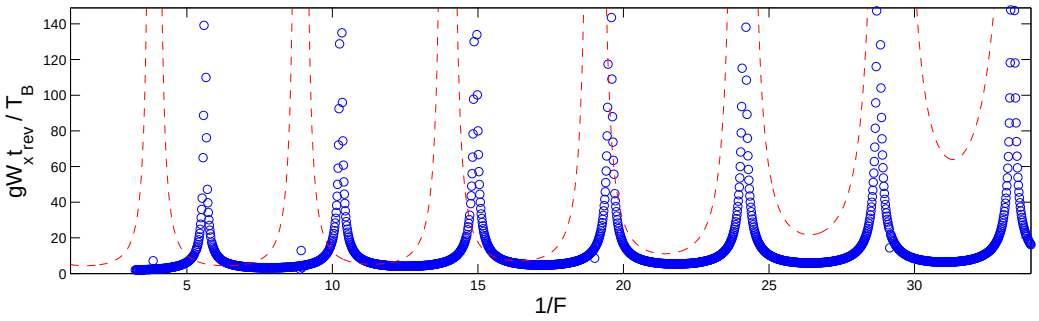

Figure 4.36: Comparison of numerical simulations and analytical estimate for the revival time in the effective spin model. Shown are the numerical results using full diagonalisation of the spin model similar to the procedure in section 4.2.4 (data points) and our analytical result eq. (4.3.25) (dashed line) as a function of the inverse force. We observe very clear equidistant divergencies in the revival time both in numerics and in the analytical result. The form of the divergencies is in qualitative agreement but the distance between neighbouring peaks is different in the numerical and analytical result. Parameters correspond to $V_0 = 4$.

We find clear divergencies of the revival time in the numerical simulations. The form of the divergencies is in good agreement with our theoretical expectation according to eq. (4.3.25), however, our theory and numerics differ in the exact position of the peaks. The peaks are equidistant in both cases, but the spacings between neighbouring peaks differ. A possible explanation for this might be that we used only the three largest coefficients to predict the revival whereas an improved theoretical estimate should include the contribution from more or even all eigenstates to the time evolution of the initial wave function.

Additionally, the minima in the revival times as expected from our theory (the dashed line in figure 4.36) show an upwards trend in the parameter range shown. This increase in the minmal values stems from the two Bessel functions in the denominator as figure 4.37 clearly shows where we compare the reciprocals of the two Bessel functions and their product. This increase of the minima is not present in the numerical data for the revival time in figure 4.36 and the explanation might be the same as above.

Nevertheless, the existence of divergencies in the revival times is clearly visible in the spin model and support the use of our effective model for a good qualitative understanding of the collapse and revival effect in the resonant interband oscillations.

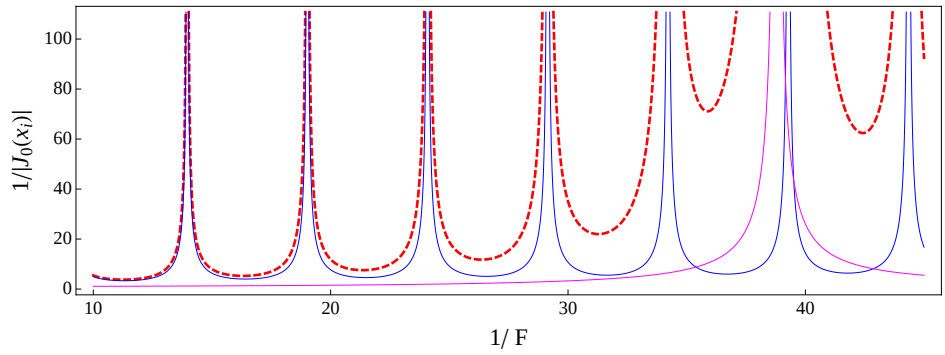

Figure 4.37: Reciprocals of two Bessel functions and of their product. Shown are the absolute values of $1/J_0(x_a)$ (thin magenta line), $1/J_0(x_b)$ (thin blue line), and $1/[J_0(x_a)J_0(x_b)]$ (thick dashed red line) where $x_{a(b)} = J_{a(b)}/F$ as a function of $1/F$. The figure clearly shows that increase in the minima height is due to a divergence of the Bessel function $J_0(x_a)$ at $x_a = J_a/F = 38.79$. Parameters J_a and J_b correspond to $V_0 = 4$.

Summary

After an extensive numerical study and a theoretical analysis based on a delocalised initial state and the resonant basis in earlier sections, we developed an effective spin model in the present section, that is—quite remarkably—an exactly solvable interacting many-body model. With the help of this model we were able to obtain an analytical prediction for the revival time in eq. (4.3.25) adding a correction to our previous result of eq. (4.2.11) which accounts also for the size of the system. We motivated this effective spin model in detail, performed numerical simulations and sketched its analytical solution, as well as the consequences for our analytical estimate of the revival time. The latter was found to be in very good agreement with earlier numerical results and could explain all numerically observed features of the revival for (nearly) integer filling, including finite-size effects.

4.4 Summary

We studied a system of weakly interacting bosons in deep optical lattices under the influence of a constant external force within a two-band Bose–Hubbard model. We used our knowledge of resonances in the interband coupling as the force is varied and studied the effect of repulsive inter-particle interactions on the resonant interband oscillations. Using an initial state with population of the lower band only and being delocalised there, we found a collapse and partial revival of the interband oscillations due to the inter-particle interaction. An extensive numerical study revealed that this effect is stable against variation of various external parameters as the system size and the particular structure of the initial state, provided the latter is delocalised in the lower part of the lattice. Further numerical analysis showed that the interband interaction is the main cause for this collapse and revival effect. The reason for this is that the resonant force brings the system into a superposition between lower and upper band states at all sites and it is thus unavoidable to have two particles repelling each other in either bands at the same sites ("on top of ech other"). The other terms of the repulsive interaction play a minor role, since double occupancy of sites is not necessary for the resonant interband oscillations.

After this numerical understanding of the system we presented different analytical approaches. They all relied on several inevitable ingredients: the presence of resonances, the many-body nature of the effect, and the special form of the initial state. We were able to find the right scaling with the parameters present in the Hamiltonian, by approximating the initial state as a coherent state and computing the effect of the interband interaction perturbatively. Later, we motivated and studied an effective spin model in order to describe the system. This is non-trivial, since it compromises a drastic reduction of the Hilbert space in a regime where a direct truncation, e.g. in terms of hard-core bosons, is not applicable. The effective model is still an interacting many-body model, however with the great and rare advantage of being exactly solvable. We used the analytical solution to derive an improved analytical prediction for the revival time, including also the effects of finite-size of the system. This allowed us to explain basically all details of the collapse and revival effect, we observed numerically until now.

Summary and Outlook

Complex dynamics of ultracold atoms: the subject of this thesis has been twofold. We started with a survey of ongoing experiments involving ultracold atomic gases in optical lattices and described the amazing possibilities to realise different quantum mechanical systems. For instance, periodic optical lattices are easily created and lead to energy bands in the spectrum. An additional external force entails several interesting phenomena, for example a coupling of energy bands. The situation for deep optical lattices is well described by Bose–Hubbard models. In this thesis, we focused on the single- and two-band Bose–Hubbard model and studied the complex dynamics of energy levels in the quantum chaotic regime and the complex time evolution of the wave function as reflected in the population dynamics of the two-band model. In this respect, the present work forms a contribution to the theoretical study of cold atomic gases and also of complex quantum dynamics. We would like to emphasize both aspects of our work.

Let us discuss these two sides in more detail. In chapter 1 we described the experimental realisation of ultracold atoms in optical lattices including also additional external forces on the atoms. This allows to build a many-body Wannier–Stark system. Throughout this work, we concentrated on deep optical lattices and chose to model this with a tilted Bose–Hubbard model. We derived it explicitly from first principles in chapter 1 and discussed the different possible physical processes, in particular the force-induced interband coupling. That chapter was intended to lay the foundation in terms of ultracold atoms for studying possible sides of complex dynamics in the following chapters.

The statistical approach to a complex many-level system has been used in our discussion of quantum chaos in the single-band Bose–Hubbard model in chapter 2. There, we developed and analysed a new tool for the detection and characterisation of avoided crossings in quantum spectra. We used it to compare random matrix theory predictions to the spectral behaviour of the chaotic Bose–Hubbard model, as detected by the fidelity. We believe that the fidelity provides an experimentally feasible and reliable tool to analyse quantum spectra, even complex ones as encountered in quantum chaos. It allowed us to detect remarkable details of the spectrum: a few regular solitonic levels crossing the chaotic sea.

The third and longest part of this thesis was dedicated to the interband coupling in a two-band Bose–Hubbard model. We discussed the non-interacting two-band system in chapter 3 and found that the force-induced interband coupling leads to a complex time evolution of the wave function. As a direct sign of this, we have studied the horizontal and vertical transport in this two-band model. To gain a quantitative understanding of the system's dynamics, we applied different perturbative expansions in real space and in momentum space. A particular feature discussed were resonant interband oscillations that take place on long time scales and with large amplitude.

We used our knowledge of the resonant non-interacting system to study the effect of a

weak inter-particle interaction on these resonant interband oscillations in chapter 4. The complexity of the problem, including the many-body nature of it, with many levels contributing significantly to the time evolution of a given initial state, forced us to rely heavily on numerical results in that chapter. The weak inter-particle interaction leads to a collapse and revival of the resonant interband oscillations, the main contribution stemming from the onsite interaction between single particles in either band. These numerical results put us in a position to develop two effective descriptions of the dynamics of collapse and revival in the interband oscillations. The second of these descriptions is an extension of an effective two-level system to include interaction which led us to build an interacting spin system that could even been solved analytically. Here, the numerical results were an important backbone for our analytical modelling and chapter 4 could stand as a fortunate example of how a collaboration between numerical and analytical calculations can create effective models for complex dynamics.

To summarise, we studied complex dynamics in the Bose–Hubbard model, with focus on the spectral structure of the single-band model and the complex dynamics of the interband coupling in the two-band model.

Future directions

Our findings certainly stimulate many further questions and several problems have been left unsolved. Concerning the complex single-band spectrum, it is desirable to give a theoretical estimate for the small regular component which we found by application of our fidelity measure. This might be possible by studying a classical phase space corresponding to very high filling, as exemplified in [Kol07]. Furthermore, the fidelity should be applied to other systems as well for a better understanding of its behaviour in different contexts.

We studied the force-induced interband coupling in the two-band Bose–Hubbard model. The non-interacting system is rather well understood now and sufficient precision for different observables should be achievable with nearly degenerate perturbation theory of higher order as pointed out in section 3.4.2. However, concerning the effect of inter-particle interactions, we only took the first step. We discussed the band coupling for weak interactions and strong forces. The regimes of stronger interactions and weaker forces remain an open problem, where the effect of the interaction is difficult to predict. There is an additional band-coupling due to the interaction and one might imagine a situation where this interaction-induced interband coupling might become the dominant band-coupling mechanism. But even within the regime of weak inter-particle interactions, we discussed mainly a single observable: the occupation of the upper band. This is a simple and intuitive quantity, but it ignores many details of the problem. A further study of the wave function itself is needed as well as the computation of other observables, for instance different measures of correlation. We mentioned the possibility for entanglement in the 'band'-degree of freedom, which would open many applications in the field of quantum information and is itself an interesting problem due to the indistinguishability of the bosonic atoms. Our study of the interband coupling revealed the existence of field induced resonances. One could also take a rather different perspective and try to engineer a certain occupation as a function of time or even a desirable quantum state by applying carefully chosen time-dependent fields. For example, an external force modulated by a simple sine function was shown to allow a dynamical transition of the superfluid-Mott-insulator phase transition in the single-band Bose–Hubbard model [Eck05, Lig07]. A future study investigating these possibilities for complex dynamics with ultracold atoms would be very interesting.

Appendices

Appendix A

Remarks on Numerical Implementation

Many of the results in this thesis have been obtained by numerical computation. We would like to use this appendix to give a few details on the numerical side of the problem and to state a few of the parameters used in computations. In a last section we would like to comment further on the statistical χ^2-test used in chapter 2.

Contents

A.1 Remarks on the Algorithms

The numerical results obtained in this work have been obtained by using mainly our own C routines, MATLAB and external libraries. Routines for the single-band Bose–Hubbard model have been written by Andrea Tomadin (see [Tom06] for many details about the code and its properties) and we extended them to a two-band model. Furthermore, we were able to speed up the code significantly by 1) storing only the non-zero matrix elements of the Hamiltonian and 2) by changing matrix-vector multiplication to vector-vector multiplication (needed for the time-integration using a Runge-Kutta algorithm [Pre92]) and 3) partly parallelised the code. A numerical runs usually performs the following steps: Creation of the Fock basis; Creation of the seed basis for given quasimomentum κ; computation of the Hamiltonian matrix elements. Depending on the problem under consideration, either the Hamiltonian is used to compute the Floquet–Bloch operator which is afterwards diagonalised (and the eigensystem is used for further analysis of for the computation of physical observables) or the Hamiltonian is used to solve the time-dependent Schrödinger equation for a given initial state. The former is mainly applied in chapter 1 and the latter in chapter 4. Additionally, we wrote a code for computation of the Hamiltonian without application of the gauge-transformation, i.e., using the original Fock basis instead of the seed basis and applied fixed boundary conditions (see chapter 1). Let us discuss several important parts of the code and also these three new ingredients in more detail.

Basis Creation We need to create the Fock basis for N atoms in L lattice site for B bands. The following algorithm creates all Fock basis vectors recursively. It has been developed by Andrea Tomadin [Tom06] and we modified it slightly to include an arbitrary number of bands and to start the basis as $|N,0,0\ldots\rangle, |N-1,1,0,0\ldots\rangle, \ldots$ which seems a natural ordering. The code stores the Fock basis vectors in a large vector (of length $\dim H$) containing integer vectors (each of length $B \cdot L$). After allocation of the necessary memory, a routine is called for creation of the basis, that takes the total number of lattice sites for all bands and the total number of atoms as parameters. It calls itself recursively and is given here with short comments:

```
void fock_basis_grow(int N, int L, Fock_basis f){
   int i;
   if(L == 1){   // if only one site is left
      f->buffer[0] = N;   // put all remaining atoms there
      // and copy it into the current basis vector:
      vector_copy(f->buffer, f->vector[f->current[0]], f->sites);
      f->current[0]++;    // go to next basis vector
   }
   else {   // if more than one site is left
      for(i = 0; i <= N; i++){   // loop over atoms
         f->buffer[L-1] = i;    // put 0...N atoms on the last site
         // start over with less atoms and L-1 sites:
         fock_basis_grow(N - i, L - 1, f);
      }
   }
}
```

Based on the basis created in this way, we now loop over all Fock basis states to find their multiplicity in order to be able to say to which quasimomentum subspace they can contribute. This is done by subsequent application of the shift operator and comparison with other states of the Fock basis that have already been used for shifts. This can take rather long for bigger systems, since all Fock basis states are shifted and afterwards compared to many other already earlier shifted states. It can take several days for large systems, say, $N = 10 = L$ and two bands. To parallelise this is not straightforward since to find new vectors and compare them with older ones is not independent of the order in which it is performed.

Computation of Matrix Elements For any analysis of the system, it is inevitable to compute the matrix elements of the Hamiltonian in a given basis. For a reduction of the Hilbert space to subspaces we introduced periodic boundary conditions and the translational invariant seed basis. Numerically, we use the original Fock basis and create the matrix elements for the seed basis (for given total quasimomentum) explicitly. That means, a list of seed vectors $\{|s_i\rangle\}$ is computed and the corresponding seed basis states are constructed as

$$|\mathbf{s}_i, \kappa\rangle = \frac{1}{\sqrt{M_s}} \sum_{l=1}^{M_s} \mathrm{e}^{\mathrm{i}2\pi\kappa l} \hat{S}^l |\mathbf{s}_i\rangle. \tag{A.1}$$

Let us first check the orthogonality of these basis states. We compute the scalar product directly

$$\begin{aligned}\langle \mathbf{s}', \kappa' | \mathbf{s}, \kappa \rangle &= \frac{1}{\sqrt{M_s M_{s'}}} \sum_{m=1}^{M_{s'}} \sum_{n=1}^{M_s} \mathrm{e}^{\mathrm{i}2\pi(\kappa n - \kappa' m)} \langle \mathbf{s}' | \hat{S}^{m+n} | \mathbf{s} \rangle \\ &= \frac{1}{\sqrt{M_{s'}}} \sum_{m=1}^{M_{s'}} \mathrm{e}^{-\mathrm{i}2\pi\kappa' m} \langle \mathbf{s}' | \underbrace{\hat{S}^{-m} | \mathbf{s}, \kappa \rangle}_{\mathrm{e}^{\mathrm{i}2\pi\kappa m} | \mathbf{s}, \kappa \rangle} = \frac{1}{\sqrt{M_{s'}}} \sum_{m=1}^{M_{s'}} \mathrm{e}^{\mathrm{i}2\pi m(\kappa - \kappa')} \langle \mathbf{s}' | \, \mathbf{s} \rangle \\ &= \frac{M_s}{\sqrt{M_{s'}}} \, \delta_{\kappa\kappa'} \langle \mathbf{s}' | \, \mathbf{s}, \kappa \rangle = \sqrt{\frac{M_s}{M_{s'}}} \, \delta_{\kappa\kappa'} \sum_{n=1}^{M_s} \mathrm{e}^{\mathrm{i}2\pi\kappa n} \langle \mathbf{s}' | \hat{S}^n | \, \mathbf{s} \rangle = \sqrt{\frac{M_s}{M_{s'}}} \, \delta_{\kappa\kappa'} \, \delta_{ss'}.\end{aligned}$$

In the second line we made use of the fact that the seed basis state are eigenstates of the shift operator and the very last step was obtained $\langle \mathbf{s}' | \hat{S}^n | \, \mathbf{s} \rangle$ is equal to 1 for $n = M_s$ and $s = s'$ and zero otherwise. The seed basis states are thus orthonormal as expected. In the numerical procedures we used, the Fock basis is stored plus the relevant information to create seed basis states out of these. To compute matrix elements $\langle \mathbf{s}', \kappa | \sum_l (a^\dagger_{l+1} a_l) | \mathbf{s}, \kappa \rangle$, we expand both seed basis states in Fock states and then compute the expectation value of the hopping operator. The straightforward way of computing these matrix elements uses five loops (over left and right vector, the expansion of each, and a loop over the sites for the hopping). However, by using the fact that the application of an operation on each lattice site and a shift of the sites commute, i.e. $[\sum_l \hat{O}_l, \hat{S}^m] = 0$, one can reduce the number of loops by one and save computation time [Tom06]. The idea is, that the application of the hopping operator $a^\dagger_{l+1} a_l$ onto a seed state $|\mathbf{s}\rangle$ will give a prefactor $[n^\alpha_l (n^\alpha_{l+1} + 1)]^{1/2}$ and result in a different state which can of course be obtained from another seed state $\hat{S}^m | \mathbf{s}' \rangle$. The additional shift operator can be combined with the shift operator from the expansion of the left seed basis state and by this allowing a reduction of the necessary loops, see [Tom06] for details.

Storing the Hamiltonian To speed up the computation (see below) we want to change matrix-vector multiplication which is required for the Runge-Kutta time integration to a vector-vector multiplication. The first step is to use a one-dimensional array (i.e. a vector) for the Hamiltonian matrix. We just cycle through the upper triangle of the matrix and record only the nonzero matrix-elements in their order of appearance. Additionally, we store the original indices in two vectors of integers `indexi[n]` and `indexj[n]` which give the original index i and j for the n-th nonzero matrix-element (counted in order of appearance). Besides it is not necessary to allocate the `hamiltonian` vector (and the vectors `indexi`, `indexj`) with length $(\dim H)^2$, but smaller. We can estimate the maximal number of non-zero elements as follows. Consider the one-band Hamiltonian

$$H = -\frac{J}{2} \sum_{l=1}^{L} (\mathrm{e}^{\mathrm{i}Ft} a^\dagger_{l+1} a_l + \mathrm{h.c.}) + \frac{W}{2} \sum_{l=1}^{L} n^a_l (n^a_l - 1). \tag{A.2}$$

Inspecting the matrix element of two arbitrary states shows that the very first term can give maximally L non-zero elements per fixed right vector, where L is the number of sites. Another L elements for the 'h.c.' and one diagonal element. Alltogether we can have maximally $(2L + 1) \cdot \dim H$ non-zero elements which is of course much smaller than

$(\dim H)^2$. Applying the same reasoning for the two-band model, we find the maximal number of non-zero matrix elements is given by $(8L+1)\dim H$ there. The big advantage from the numerical point of view is, that we save a lot of memory by allocating and storing only the non-zero matrix-elements. In particular, this number scales only linearly with the Hilbert space dimension and we can compute the time-evolution of a given initial state (as shown very often in chapter 4) for larger systems. This cannot be applied to the Floquet–Bloch operator which is a full matrix and one needs all $(\dim H)^2$ matrix-elements. One could also make use of the Lanczos algorithm to find the eigenvalues and eigenvectors of the Floquet–Bloch operator. There, one can apply Floquet theory to solve an equivalent but larger time-independent problem. But the memory needed to obtain the eigenstates of the Floquet–Bloch operator scales again quadratic with the Hilbert space dimension, but the prefactor is even larger than 1, since one needs to store several copies of the lower triangle of the Hamiltonian [Par10]. However, one can gain in computation time, but at the cost of physical size of the system: instead of $N = 10 = L$ one is then only able to compute smaller systems since more memory is needed. A massive parallelisation does not ease this limitation, since the problem grows exponentially in memory (needed for the matrix elements) and in time (for the integration) with a factor of about 6 when increasing both N and L by 1 in the two-band case. The only solution to go to much larger sizes, will be to use a reduced but time-adaptive basis as in t-DMRG or other methods. But these methods have their own restrictions and simulability of complex systems with such methods is also known to be limited [Ven09].

Speed up the Integration We use a fourth-order Runge–Kutta algorithm [Pre92] with adaptive step-size and an internal estimation of the error. The integration is performed at small stepsizes such as to remain below the error bound given by the user (see [Pre92] for Details). It is known that the Runge–Kutta integration is not a strictly unitary time evolution but we checked that the norm of the wave function was always close to one even for very long integration times (as applied in chapter 4). As mentioned before, we modified the code from [Tom06] to make it faster. The step described in the previous paragraph is most important for this: We use the vectors just described and replace matrix-vector multiplication for the time-integration by vector-vector multiplication. To illustrate this, let us take the above mentioned vectors and a matrix-vector product, say `dpsi = hamiltonian*psi`, can be written with these vectors as

```
for(n=0; n<numtot; n++){
        i = indexi[n];
        j = indexj[n];
        dpsi[i] = dpsi[i] + H[n]*psi[j];
        dpsi[j] = dpsi[j] + H[n]*psi[i];
}
```

Note that one does not calculate the i-th component of `psi` and loops over i as is usually done, but directly computes the whole vector `psi`. The second line is needed, since only the upper triangle part of the Hamiltonian has been stored. In our case of a time-dependent Hamiltonian, we can implement the time-dependent phase factors directly in this matrix-vector product. This saves the computation of $H(t)$ out of H in every product for the Runge–Kutta algorithm. The amount of time saved scales non-linear with the matrix size, for large systems we found this algorithm for the integration of the time-dependent

Schrödinger equation to be up to a factor of 10 faster (when compiled with the `intel` compiler on our `intel` machine). This vectorisation is thus an immense gain in computation time.

PARALLELISATION The third step to speed up the computation of single runs is parallelisation. Please keep in mind that one can always run different parameters (like various values of κ) independently. This will in all cases be faster than implementing a loop over this parameter and parallelising that code (Amdahl's law). However, when one is interested in a single parameter set and wants a fast result, it is useful to parallelise the code. For our system, we used the fact that the different columns of the Floquet–Bloch operator can be integrated independently and the loop was parallelised with OpenMP (Open Multi-Processing, see `http://openmp.org/`). It is a programming interface that allows to implement shared-memory multiprocessing by simply adding compiler directives to the `C` code.
We used external libaries to diagonalise the Floquet–Bloch operator. These were taken from the `LAPACK` package, available online (`http://www.netlib.org/lapack/`). However, we also had intel specific version of these libaries from the so called `Intel Math Kernel Libary` package (`http://software.intel.com/en-us/intel-mkl/`). They can directly be used in parallel without special attention by the programmer and have also been used in some cases for this thesis to speed up single runs.

A.2 More Numbers

COEFFICIENTS OF THE BOSE–HUBBARD MODEL For completeness, we give the Hamiltonian parameters that have been used throughout this for numerical computations with the Bose–Hubbard model. The numbers have been obtained by computing the Wannier functions for an optical lattice and using them for coefficients of the Hubbard model as described in section 1.3.2. They are summarised in table A.1.

V_0	Δ	C_0	J_a	J_b	W_a	W_b	W_x
2.0	2.97	−0.184	0.1710	−0.9239	0.0237	0.0142	0.0100
3.0	3.68	−0.164	0.1015	−0.7685	0.0274	0.0162	0.0111
4.0	4.39	−0.150	0.0616	−0.6204	0.0301	0.0180	0.0123
5.0	5.05	−0.140	0.0384	−0.4871	0.0323	0.0199	0.0135
6.0	5.68	−0.133	0.0245	−0.3744	0.0342	0.0216	0.0146
7.0	6.26	−0.126	0.0160	−0.2839	0.0359	0.0231	0.0156
8.0	6.79	−0.122	0.0107	−0.2137	0.0373	0.0252	0.0165
9.0	7.30	−0.117	0.0072	−0.1605	0.0386	0.0258	0.0173
10.0	7.77	−0.114	0.0050	−0.1205	0.0398	0.0269	0.0180

Table A.1: Parameters of the Bose–Hubbard model for different depths of the optical lattice. All parameters are given in recoil energies E_R.

Resonant Forces and Interband Oscillations We found that the resonant values of the force can in a good approximation as in equation (3.4.2). It is then given by

$$F_m = |\Delta|/\sqrt{m^2 - 4C_0^2}.$$

We computed the first five resonances for the non-interacting two-band model for the parameters given in the table above. They are summarised in table A.2. Furthermore, we

V_0	$F_{m=1}$	$F_{m=2}$	$F_{m=3}$	$F_{m=4}$	$F_{m=5}$
2.0	3.1941	1.5108	0.9975	0.7457	0.5956
3.0	3.8955	1.8653	1.2341	0.9231	0.7375
4.0	4.6020	2.2201	1.4707	1.1006	0.8796
5.0	5.2604	2.5501	1.6907	1.2656	1.0116
6.0	5.8923	2.8655	1.9008	1.4232	1.1376
7.0	6.4636	3.1526	2.0924	1.5669	1.2526
8.0	7.0029	3.4219	2.2718	1.7014	1.3602
9.0	7.5069	3.6739	2.4398	1.8274	1.4610
10.0	7.9804	3.9109	2.5978	1.9459	1.5558

Table A.2: Periods of resonant oscillations of the non-interacting two-band system. Numerical values are given in units of Bloch periods for different lattice depths V_0 and orders of resonance r. The periods increase rapidly with the order of resonance.

found that the periods of the resonant interband oscillations can be described quite well by an effective two-level system in degenerate perturbation theory, see chapter 3. They are then computed as

$$T_{\text{res}}^{(m)} = \frac{F}{2|VJ_m(\Delta x)|}\, T_B.$$

The full list of periods of the resonant oscillations is given in table A.3 below.

A.3 Short Remark on the Statistical χ^2-test

In chapter 2 we used a statistical χ^2-test to quantify how close a numerically obtained level spacing distribution approaches the expected prediction. We showed the values of the weighted deviation between the observed values o_i and the expected values e_i, where the χ^2 deviation shown in chapter 1 is defined as [Pre92, chap. 14-3]

$$\chi^2 \equiv \sum_i \frac{(o_i - e_i)^2}{e_i}. \tag{A.1}$$

Please note that the denominator is not squared. To obtain the probability for the the measured distribution to be drawn from the expected distribution for k degrees of freedom ($k = 1$ in our Wigner-Dyson test), one computes the so-called p-value. To avoid confusion with the statistical χ-distribution, we will denote the numerical χ^2-deviation by x in the

V_0	$T_{\text{res}}^{m=1}/T_B$	$T_{\text{res}}^{m=2}/T_B$	$T_{\text{res}}^{m=3}/T_B$	$T_{\text{res}}^{m=4}/T_B$	$T_{\text{res}}^{m=5}/T_B$
2.0	16.09	43.25	106.39	250.18	572.84
3.0	27.44	113.91	429.43	1544.55	5404.77
4.0	45.11	284.82	1626.25	8849.97	46835.47
5.0	71.66	676.50	5760.15	46716.18	368359.33
6.0	111.13	1554.42	19578.81	234802	2737310
7.0	171.10	3510.82	64773.90	1137480	19414841
8.0	256.88	7658.01	205088.13	5226720	129457966
9.0	381.32	16355.25	629715.33	23068493	821249099
10.0	558.80	34136.77	1870804.83	97534614	4941339172

Table A.3: Periods of resonant oscillations of the non-interacting two-band system. Numerical values are given in units of Bloch periods for different lattice depths V_0 and orders of resonance r. The periods increase rapidly with the order of resonance.

following. The probability for the measured distrubution to be drawn from the expected distribution is given by the p-value

$$p = 1 - \mathrm{CDF}[\chi(k,x)] = 1 - \frac{\gamma(k/2, x/2)}{\Gamma(k/2)}, \tag{A.2}$$

where we used the statistical χ-distribution for k degrees of freedom and the lower incomplete gamma function

$$\chi(k,x) = \frac{1}{2^{k/2}\Gamma(k/2)} x^{k/2-1}\mathrm{e}^{-x/2} \qquad \text{and} \qquad \gamma(s,x) = \int_0^x t^{s-1}\mathrm{e}^{-t}\mathrm{d}t$$

Since we have one degree of freedom, we can make use of $\Gamma(1/2) = \sqrt{\pi}$ and $\gamma(1/2, x) = \sqrt{\pi}\mathrm{erf}(\sqrt{x})$ to get an approximate formula

$$p = 1 - \mathrm{erf}(\sqrt{x/2}) = 1 - \sqrt{x}\sqrt{\tfrac{2}{\pi}}\left(1 - \frac{x}{6} + \mathcal{O}(x^2)\right). \tag{A.3}$$

Another possibility to characterise the measured level spacing distribution would be to use the best fit (by minimisation of some cost function) for an interpolating distribution. An example for such a distribution interpolating a regular and quantum chaotic level spacing distribution is given by the Brody distribution

$$P(s,w) = a\, s^w \mathrm{e}^{-a\, s^{w+1}} \quad \text{where} \quad a = \Gamma\left(\frac{w+2}{w+1}\right)^{w+1}, \tag{A.4}$$

with the Gamma function $\Gamma(x)$. It contains only one free parameter w and interpolates between a Poissonian distribution for $w = 0$ and a Wigner–Dyson distribution for $w = 1$. However, by applying a golden-mean fit to a given Brody distribution on which we added some noise, we found that the fit is preferring more regular distributions. This means, that this is not a solution to the problem of determining the degree of regularity for a given level spacing distribution and has thus not been applied in the main text of chapter 2.

Appendix B

The Rabi Problem & Collapse and Revival in Quantum Optics

The models and phenomena discussed in the context of the tilted two-band model (chapters 3 and 4) bear strong similarity to classical effects encountered in quantum optics. The so-called Rabi problem and the observed collapse and revival in the Jaynes–Cummings model play a paradigmatic role there. The present appendix should serve to review these phenomena and to compare them to our system. We therefore apply the same methods as in the main chapters of this thesis and point out similarities and differences.

The Rabi Problem

The original Rabi problem treated a spin-1/2-particle with magnetic moment μg in a magnetic field $\vec{B}$. This field should have a constant part B_0 in z-direction and an oscillating part $B_1 \cos \omega t$ in x-direction. The Hamiltonian is $-\vec{\mu}\vec{B} = \frac{1}{2}\mu g \vec{B} \cdot \vec{\sigma}$. That is, the constant part leads to Zeeman-splitting $\pm \mu g B_0$ and the oscillating field couples these two Zeeman-levels. The Schrödinger equation reads

$$\mathrm{i}\frac{\mathrm{d}}{\mathrm{d}t}\begin{pmatrix} a(t) \\ b(t) \end{pmatrix} = \begin{pmatrix} -\Delta/2 & 2V\cos(\omega t) \\ 2V\cos(\omega t) & \Delta/2 \end{pmatrix}\begin{pmatrix} a(t) \\ b(t) \end{pmatrix}, \tag{B.1}$$

where we set $\Delta \equiv \mu g B_0$ and $V = 4\mu g B_1$ to connect to our notation. We are now going to solve this problem in the rotating wave approximation (RWA) to obtain the well-known Rabi result.

If the coupling was absent, the amplitudes $a(t)$ and $b(t)$ would evolve in time with phases $\mathrm{e}^{\pm \mathrm{i}\Delta t/2}$, respectively. Let us therefore go to a reference frame rotating with these phases, i.e. to the interaction picture (not altering transition probabilities like $P_{a\to b}(t)$)

$$\tilde{a}(t) = \mathrm{e}^{-\mathrm{i}\Delta t/2}\, a(t) \qquad \text{and} \qquad \tilde{b}(t) = \mathrm{e}^{+\mathrm{i}\Delta t/2}\, b(t) \tag{B.2}$$

obtaining a new Schrödinger equation that is purely off-diagonal (cf. eq. (3.2.7))

$$\mathrm{i}\frac{\mathrm{d}}{\mathrm{d}t}\begin{pmatrix} \tilde{a}(t) \\ \tilde{b}(t) \end{pmatrix} = V\begin{pmatrix} 0 & \mathrm{e}^{\mathrm{i}(\omega-\Delta)t} + \mathrm{e}^{-\mathrm{i}(\omega+\Delta)t} \\ \mathrm{e}^{-\mathrm{i}(\omega-\Delta)t} + \mathrm{e}^{\mathrm{i}(\omega+\Delta)t} & 0 \end{pmatrix}\begin{pmatrix} \tilde{a}(t) \\ \tilde{b}(t) \end{pmatrix}. \tag{B.3}$$

If we are not too far from resonance, the terms $\mathrm{e}^{\pm\mathrm{i}(\omega-\Delta)t}$ oscillate very slowly, and $\mathrm{e}^{\pm\mathrm{i}(\omega+\Delta)t}$ very quickly. The latter are therefore expected to average out after a few cycles. We will neglect them and this approximation is the RWA. The problem is now easily solved: we differentiate the equation for one of the amplitudes and insert the other one to obtain:

$$0 = \ddot{\tilde{a}} + \mathrm{i}(\Delta - \omega)\dot{\tilde{a}} + V^2\tilde{a}. \tag{B.4}$$

This linear differential equation can readily be solved, leading to an occupation of the upper level if initially zero, i.e. initial conditions $a(0) = 1$ and $b(0) = 0$, given by

$$|b(t)|^2 = \frac{4V^2}{(\Delta-\omega)^2 + 4V^2}\ \sin^2\left[\frac{1}{2}\sqrt{(\Delta-\omega)^2+4V^2}\ t\right]. \tag{B.5}$$

This is the Rabi formula. It describes an oscillation between two states, similar to to a time-independent two-level system prepared in the lower level (which is not an eigenstate due to the coupling of the states), where the detuning $\Delta - \omega$ has to be replaced by the bandgap $\Delta = E_1 - E_0$. The frequency of the oscillation $\Omega_R \equiv \frac{1}{2}\sqrt{(\Delta-\omega)^2+4V^2}$ is called *Rabi frequency*. This concludes the standard solution known from various textbooks.

Performing the same steps as above without the RWA leads to a second order differential equation with coefficients explicitly depending on time (cf. eq. (3.2.10) of section 3.2)

$$0 = \ddot{\tilde{a}} + 2\mathrm{i}\Delta\cdot\dot{\tilde{a}} - 4V^2\cos^2(\omega t)\cdot\tilde{a} = 0 = \ddot{\tilde{a}} + 2\mathrm{i}\Delta\dot{\tilde{a}} - 2V^2(1+\cos 2\omega t)\,\tilde{a}.$$

Introducing dimensionless variables $\tau = \omega t$ with $\partial_t = \partial_{\tau/\omega} = \omega\partial_\tau$ and measuring energies in units of ω, i.e. $\delta \equiv \Delta/\omega$ and $v \equiv V/\omega$, we recognize the similarity to the Mathieu equation

$$0 = a'' + 2\mathrm{i}\delta\, a' - 2v^2(1+\cos 2\tau)\, a. \tag{B.6}$$

This equation is exactly solveable and the solution (with constants of integration $c_{1,2}$) reads

$$y(\tau) = c_1\mathrm{e}^{-\mathrm{i}\tau\delta}C\left(\delta^2-2v^2, v^2, \tau\right) + c_2\mathrm{e}^{-\mathrm{i}\tau\delta}S\left(\delta^2-2v^2, v^2, \tau\right).$$

Here, $C(a,q,x)$ and $S(a,q,x)$ denote the even an odd Mathieu functions [Abr68, chap. 20]. When including the appropriate initial condition the explicit time-dependent solution reads

$$\begin{aligned} a(\tau) = \mathrm{e}^{-\mathrm{i}\tau\delta}\Big[&S(\epsilon^2,v^2,\tau)C'(\epsilon^2,v^2,0) - C(\epsilon^2,v^2,\tau)S'(\epsilon^2,v^2,0) + \\ &\mathrm{i}\delta\big[C(\epsilon^2,v^2,\tau)S(\epsilon^2,v^2,0) - C(\epsilon^2,v^2,0)S(\epsilon^2,v^2,\tau)\big]\Big] \\ &\times\Big[C'(\epsilon^2,v^2,0)S(\epsilon^2,v^2,0) - C(\epsilon^2,v^2,0)S'(\epsilon^2,v^2,0)\Big]^{-1} \end{aligned} \tag{B.7}$$

where $\epsilon^2 = \delta^2 - 2v^2$ and the prime indicates the first derivative with respect to the third variable, i.e. $C'(a,q,x) = \partial C(a,q,x)/\partial x$. The Mathieu functions are well known from various problems of physics (e.g. the motion of elliptical membranes or problems with periodic potentials) and have the special values $C(a,0,z) = \cos(\sqrt{a}z)$ and $S(a,0,z) = \sin(\sqrt{a}z)$. However, they are difficult to use "mainly because of the impossibility of analytically representing them in a simple and handy way" [Fre01]. We see that the Rabi-Problem is exactly solveable in terms of known functions, but the physical content of the solution is not obvious. Hill's equation can be seen as an extension of the Mathieu equation involving two (or more) periodic functions instead of one. There are relations between the Fourier expansions for the solutions of both equations, discussed in [Olv10]. We will not discuss this further but we have found that the Rabi problem even beyond the RWA is exactly solveable. However, the solution cannot be expressed in a simple way and shows already features of more complex dynamics (cf. chapter 3).

The Jaynes–Cummings Model: Collapse and Revival

The quantised version of the Rabi problem with linear polarization is called the Jaynes–Cummings model. Using again the RWA, the Hamiltonian is given by [Scu97]:

$$H_{\text{JCM}} = \hbar\nu a^\dagger a + \tfrac{1}{2}\hbar\omega\sigma_z + \frac{\hbar\Omega}{2}\left(a\sigma_+ + a^\dagger\sigma_-\right). \tag{B.8}$$

The Jaynes–Cummings model in the RWA can easily be solved, see [Scu97] for instance. One is then able to compute the probability for an atom to be excited when exposed to a beam of coherent light. The result is a sum of many Rabi floppings weighted by the coherent state photon number distribution

$$p(t) = \sum_n p_n |b(t)|^2 = \mathrm{e}^{-|\alpha|^2} \sum_n \frac{|\alpha|^{2n}}{n!} \cos^2(g\sqrt{n+1}\, t). \tag{B.9}$$

An example for the collapse and revival observed in this observable has been shown in figure 4.5 in the main text.

What happens if we take a finite number of field modes, starting from 1 and increasing it slowly? How quickly does the system approach the state of large n? Figure B.1 shows the results of simple numerical computations. It appears that the limit of large n is approached

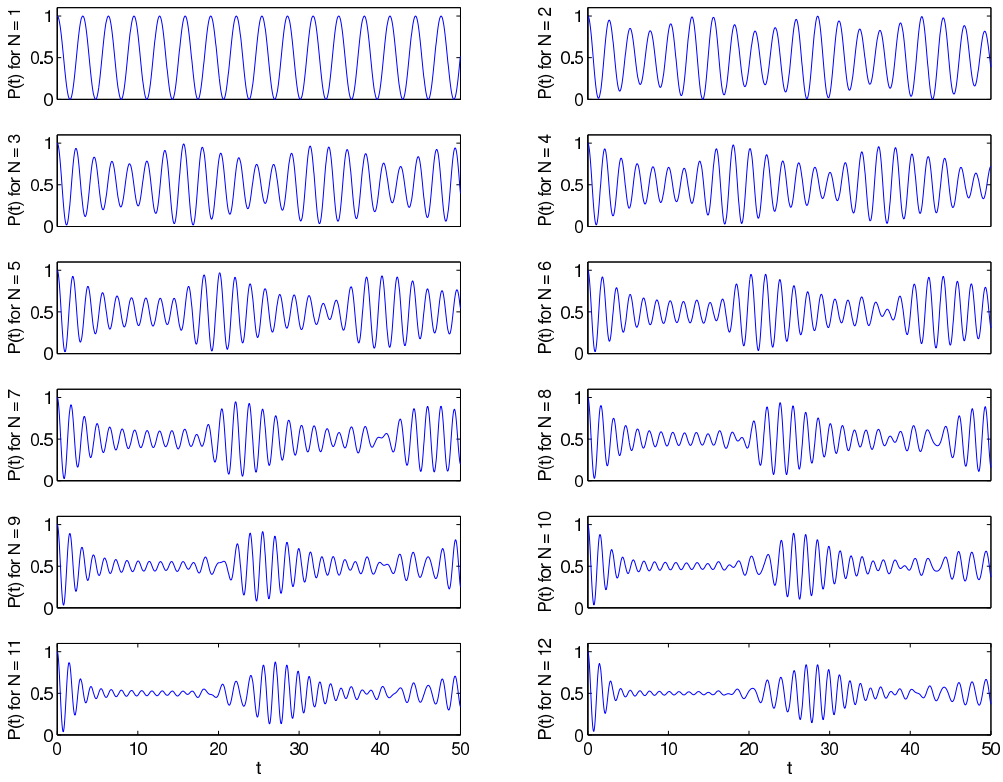

Figure B.1: (Normalized) occupation of upper state as a function of time in Jaynes–Cummings model of different finite number of field modes $N = 1 \ldots 12$ according to Eq. (B.9). The parameters are amplitude $\alpha = 3$ and coupling $g = 0.7$ as in fig. 4.5 where the limit of large N is realized. Also shown is the predicted Gaussian envelope (dashed line).

very quickly, already for about $n > 10$ the occupation is very close to the limiting behaviour.

Let us derive approximate expressions for the three time-scales of the system in the limit of large n. These are the period of the Rabi oscillations t_R, the decay time for the oscillations t_c, and the revival time t_r. To be slightly more general (and following [Scu97, chap. 6.2]), we consider detuned oscillations where the frequency of the light mode ν (the value of the external force times the order of the resonance nF in the two-band model) is not exactly equal to the separation Ω of the two states in the atom (the band gap Δ in the two-band model). We call this detuning $\nu - \Omega = \delta$ (i.e. $\Delta - nF$ for the two-band model). Then the Rabi frequency for a mode with $\langle\hat{n}\rangle = n$ photons is given by

$$\Omega_n = \sqrt{\delta^2 + 4g^2\langle\hat{n}\rangle}, \quad \text{such that} \quad t_R = \frac{2\pi}{\Omega_n} = \frac{2\pi}{\sqrt{\delta^2 + 4g^2\langle\hat{n}\rangle}}.$$

The oscillations corresponding to different $\langle\hat{n}\rangle$ become uncorrelated when the deviation $\Delta\hat{n}$ in the photon number distribution is equal or larger then $\sqrt{\langle\hat{n}\rangle}$. One can thus estimate the collapse time from

$$\left(\Omega_{\langle\hat{n}\rangle+\sqrt{n}} - \Omega_{\langle\hat{n}\rangle-\sqrt{n}}\right) t_c \approx 1.$$

Using $n \gg \sqrt{n}$ in the limit $n \gg 1$ one arrives at [Scu97]

$$t_c \approx \frac{2\pi}{2g}\left(1 + \frac{\delta^2}{4g^2\langle n\rangle}\right)^{1/2}. \tag{B.10}$$

In exact resonance, the collapse time is equal to $1/2g$ and independent of the number of photons. The revivals, on the other hand, take place when the phases of neighbouring terms differ by (an integral multiple of) 2π, i.e.

$$\left(\Omega_{\langle\hat{n}\rangle} - \Omega_{\langle\hat{n}\rangle-1}\right) t_r \approx 2\pi m \qquad \text{with} \qquad m = 1, 2, \ldots$$

Using again Taylor expansions for $\langle\hat{n}\rangle \gg 1$, one obtains [Scu97]

$$t_r \approx \frac{2\pi m}{g}\sqrt{n}\left(1 + \frac{\delta^2}{4g^2\langle n\rangle}\right)^{1/2} \qquad \text{for } \delta \neq 0. \tag{B.11}$$

For the values in the figures, this amounts to $t_r = 2\pi\sqrt{\alpha^2}/g = 26.9$ which is quite good for the first revival. A refined analysis shows, that the revivals are not equidistant, and there are improved predictions to overcome this limitation of the above mentioned simple model [Fer09]. However, the main effect for us is the quick convergence of the revival time with growing number of photonic modes included as has been demonstrated in figure B.1. There is no such convergence in the two-band model of chapter 4 with growing number of atoms. A direct explanation of the effect described there is therefore not possible by reference to the Jaynes–Cummings model discussed.

Appendix C

Bessel Functions of the First Kind

DEFINITION The Bessel functions of the first kind, denoted as $J_\alpha(x)$, are solutions of Bessel's differential equation [Abr68]

$$x^2\frac{\mathrm{d}^2y}{\mathrm{d}x^2} + x\frac{\mathrm{d}y}{\mathrm{d}x} + (x^2-\alpha^2)y = 0. \tag{C.1}$$

They are finite at the origin $(x = 0)$ for non-negative integer α, and diverge as x approaches zero for negative non-integer α. For integer order solutions, it is possible to define the function by its Taylor series expansion around $x = 0$ which can be expressed in terms of the hypergeometric series as

$$J_\alpha(x) = \sum_{m=0}^{\infty}\frac{(-1)^m}{m!\Gamma(m+\alpha+1)}\left(\frac{x}{2}\right)^{2m+\alpha} = \frac{(x/2)^\alpha}{\Gamma(\alpha+1)}\,{}_0F_1(\alpha+1;-x^2/4) \tag{C.2}$$

where $\Gamma(z)$ is the gamma function. The first four Bessel functions are shown in fig. C.1.

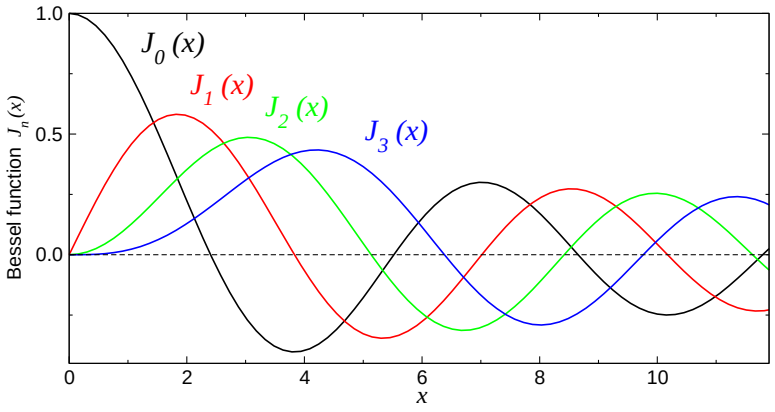

Figure C.1: Ordinary Bessel functions of the first kind $J_n(x)$ for integer values $n = 0, 1, 2, 3$.

INTEGRAL REPRESENTATIONS For integer values of n, is possible to use an integral representation:

$$J_n(x) = \frac{1}{\pi}\int_0^\pi \cos(n\tau - x\sin\tau)\,\mathrm{d}\tau = \frac{1}{2\pi}\int_{-\pi}^{\pi} \mathrm{e}^{-\mathrm{i}\,(n\tau - x\sin\tau)}\,\mathrm{d}\tau. \tag{C.3}$$

These lead to the relations used in the main text the integrals

$$\begin{aligned}\frac{2}{\pi}\int_0^\pi \cos(\Delta x \sin t)\sin(kt)\mathrm{d}t &= \begin{cases} 2J_k(\Delta x) & \text{for } k \text{ even} \\ 0 & \text{for } k \text{ odd} \end{cases} \\ \frac{2}{\pi}\int_0^\pi \sin(\Delta x \sin t)\sin(kt)\mathrm{d}t &= \begin{cases} 0 & \text{for } k \text{ even} \\ 2J_k(\Delta x) & \text{for } k \text{ odd} \end{cases}\end{aligned} \tag{C.4}$$

RECURRENCE The Bessel function J_α satisfies the recurrence relations:

$$\frac{2\alpha}{x}J_\alpha(x) = J_{\alpha-1}(x) + J_{\alpha+1}(x) \qquad \text{and} \qquad 2\frac{\mathrm{d}J_\alpha}{\mathrm{d}x} = J_{\alpha-1}(x) - J_{\alpha+1}(x). \tag{C.5}$$

For integer order n, the following relationship is valid

$$J_{-n}(x) = (-1)^n J_n(x). \tag{C.6}$$

ASYMPTOTICS The Bessel functions have the following asymptotic expansion for non-negative α:

$$J_\alpha(x) \approx \begin{cases} \frac{1}{\Gamma(\alpha+1)}\left(\frac{x}{2}\right)^\alpha & \text{for } 0 < x \ll \sqrt{\alpha+1} \\ \sqrt{\frac{2}{\pi x}}\cos\left(x - \frac{\alpha\pi}{2} - \frac{\pi}{4}\right) & \text{for } x \gg |\alpha^2 - 1/4| \end{cases} \tag{C.7}$$

SUM FORMULAE For integer order n, J_n is often defined via a Laurent series for a generating function:

$$\mathrm{e}^{(x/2)(t-1/t)} = \sum_{n=-\infty}^{\infty} J_n(x)t^n, \tag{C.8}$$

This leads directly to the so-called Jacobi-Anger identity:

$$\mathrm{e}^{\mathrm{i}z\cos\phi} = \sum_{n=-\infty}^{\infty} \mathrm{i}^n J_n(z)\,\mathrm{e}^{\mathrm{i}n\phi} \quad \Rightarrow \quad \mathrm{e}^{\mathrm{i}z\sin\phi} = \sum_{n=-\infty}^{\infty} J_n(z)\,\mathrm{e}^{\mathrm{i}n\phi}. \tag{C.9}$$

Sums over products of Bessel functions can also be calculated

$$\sum_{l=-\infty}^{\infty} J_{n-l}(x)J_{n'-l}(x') = J_{n-n'}(x-x'), \quad \sum_{l=-\infty}^{\infty} J_{n\mp l}(x)J_l(x') = J_n(x-x') \tag{C.10}$$

$$\sum_{l=-\infty}^{\infty} \tau^l J_l(x)J_{n+l}(x') = \left[\frac{x' - x/\tau}{x' - x\tau}\right]^{n/2} J_n(g), \tag{C.11}$$

with $g = \sqrt{x^2 + x'^2 - xx'(\tau + 1/\tau)}$ in the last line.

TAYLOR EXPANSION The ordinary Bessel functions of integer order have the Taylor expansions

$$J_0(x) = 1 - \frac{1}{4}x^2 + \frac{1}{64}x^4 + \mathcal{O}(x^6), \quad J_1(x) = \frac{1}{2}x - \frac{1}{16}x^3 + \mathcal{O}(x^5) \tag{C.12}$$

$$J_2(x) = \frac{1}{8}x^2 - \frac{1}{96}x^4 + \mathcal{O}(x^6), \quad \ldots \quad J_m(x) = \frac{x^m}{2^m m!} + \mathcal{O}(x^{m+2}). \tag{C.13}$$

Basically all these relations have been used in the main text and have been taken from [Abr68].

Appendix D

Degenerate Perturbation Theory

Introduction

Following [Shi63], we consider the eigenvalue problem

$$(H^0 + V)A = EA \tag{D.1}$$

where H^0 and V are hermitian matrices, E is a diagonal matrix of eigenvalues and A the matrix of eigenvectors. As usual, H^0 is assumed to be diagonal and we are seeking a solution A in a series expansion in V. Taking the transposed equation $AE - H^0A = VA$, in components given by

$$\sum_k (A_{ik}E_k\delta_{kp} - E_i^0\delta_{ik}A_{kp}) = \sum_k V_{ik}A_{kp},$$

we look at the element A_{ip} on the left hand side and can write

$$A_{ip}(E_p - E_i^0) = \sum_k V_{ik}A_{kp} \quad \Rightarrow \quad A_{ip} = \sum_k \frac{V_{ik}A_{kp}}{E_p - E_i^0}. \tag{D.2}$$

The wanted eigenvalue and eigenvector are E_p and A_{ip}, we have two distinguish between non-degenerate and degenerate eigenvalues:

- non-degenerate: $E_p - E_i^0 \gg V_{ik}$ for $\forall i \neq p$
- degenerate: $E_p - E_i^0 \gg V_{ik}$ for $\forall i \neq p, q$.

Let us discuss these two cases now. The first one is well known and repeated as illustration.

Non-degenerate Perturbation Theory: $E_p - E_i^0 \gg V_{ik}$ for $\forall i \neq p$

The above condition implies that all components of the eigenvector are small except for one: $A_{ip} \ll 1\ \forall i \neq p$. The only large component is A_{pp} and we extract it from the summation

$$A_{ip}(E_p - E_i^0) = \frac{V_{ip}A_{pp}}{E_p - E_i^0} + \sum_{k\neq p} \frac{V_{ik}A_{kp}}{E_p - E_i^0}.$$

The last term is small and allows a perturbative solution

$$A_{ip} = \Big(\frac{V_{ip}}{E_p - E_i^0} + \sum_{j\neq p} \frac{V_{ij}V_{jp}}{(E_p - E_i^0)(E_p - E_j^0)} + \dots\Big)A_{pp}$$

We want to find E_p and therefore take the case $i = p$ in the last equation. Multiplication with $(E_p - E_p^0)$ yields the result

$$E_p = E_p^0 + V_{pp} + \sum_{i \neq p} \frac{V_{pi}V_{ip}}{(E_p - E_i^0)} + \sum_{i,j \neq p} \frac{V_{pi}V_{ij}V_{jp}}{(E_p - E_i^0)(E_p - E_j^0)} + \ldots,$$

possibly easier to recognize in the form

$$E_n = E_n^{(0)} + \langle n^0|V|n^0\rangle + \sum_{m \neq n} \frac{|\langle m^0|V|n^0\rangle|^2}{E_n^0 - E_m^0} + \ldots.$$

The components of the eigenvector shall not be discussed here, see [Shi63] for details.

Degenerate Perturbation Theory: $E_p - E_i^0 \gg V_{ik}$ for $\forall i \neq p, q$

In this case, all components of the eigenvector are small except for two: $A_{ip} \ll 1 \; \forall i \neq p, q$, such that we have to exclude two components from the summation

$$A_{ip} = \frac{V_{ip}A_{ip}}{E_p - E_i^0} + \frac{V_{iq}A_{iq}}{E_p - E_i^0} + \sum_{k \neq p,q} \frac{V_{ik}A_{kp}}{E_p - E_i^0}.$$

The iterative solution reads

$$\begin{aligned} A_{ip} \;=\; & \Big(\frac{V_{ip}}{E_p - E_i^0} + \sum_{j \neq p,q} \frac{V_{ij}V_{jp}}{(E_p - E_i^0)(E_p - E_j^0)} + \ldots\Big)A_{pp} \\ & + \Big(\frac{V_{iq}}{E_p - E_i^0} + \sum_{j \neq p,q} \frac{V_{ij}V_{jq}}{(E_p - E_i^0)(E_p - E_j^0)} + \ldots\Big)A_{qp}. \end{aligned}$$

By introducing the following matrices

$$\mathcal{V}_{lm}(E) = V_{lm} + \sum_{i \neq m} \frac{V_{li}V_{im}}{E - E_i^0} + \sum_{i \neq l} \sum_{j \neq m} \frac{V_{li}V_{ij}V_{jm}}{(E - E_i^0)(E - E_j^0)} + \ldots, \tag{D.3}$$

the solution can be cast in form of a block matrix equation

$$\begin{pmatrix} E_p^0 + \mathcal{V}_{pp}(E) & \mathcal{V}_{pq}(E) \\ \mathcal{V}_{qp}(E) & E_q^0 + \mathcal{V}_{qq}(E) \end{pmatrix} \begin{pmatrix} A_{pp} \\ A_{qp} \end{pmatrix} = E \begin{pmatrix} A_{pp} \\ A_{qp} \end{pmatrix}. \tag{D.4}$$

This eigenvalue problem for the nearly eigenvalues E_p and E_q has the solutions

$$\begin{aligned} E_\pm = & \frac{1}{2}\Big(E_p^0 + \mathcal{V}_{pp}(E) + E_q^0 + \mathcal{V}_{qq}(E)\Big) \\ & \pm \frac{1}{2}\sqrt{\Big(E_p^0 + \mathcal{V}_{pp}(E) - E_q^0 - \mathcal{V}_{qq}(E)\Big)^2 + 4|\mathcal{V}_{pq}|^2}, \end{aligned} \tag{D.5}$$

where $E = E_p$ or E_q, the distinction is only a third order effect [Shi63]. The eigenstates of the effective two-level system can also be computed by standard methods.

List of Figures

Bibliography

We included backreferences to the main text for all citations. These are given by the blue page numbers at the end of each bibliographic entry. We furthermore included direct hyperlinks to the cited documents where possible.

[Abr68] M. Abramowitz and I. Stegun, editors. *Handbook of Mathematical Functions*. Dover Publications (1968). 170, 173, 174

[Abu07] P. Abumov and D. W. L. Sprung. *Interminiband Rabi oscillations in biased semiconductor superlattices*. Phys. Rev. B **75** (2007), 165421. URL http://dx.doi.org/10.1103/PhysRevB.75.165421. 22, 68, 78, 93

[Aku06] V. M. Akulin. *Coherent Dynamics of Complex Quantum Systems*. Springer-Verlag, Berlin (2006). 1, 2

[Ami05] L. Amico, A. Osterloh, and F. Cataliotti. *Quantum Many Particle Systems in Ring-Shaped Optical Lattices*. Phys. Rev. Lett. **95** (2005), 063201. URL http://dx.doi.org/10.1103/PhysRevLett.95.063201. 72

[Ami08] L. Amico, R. Fazio, A. Osterloh, and V. Vedral. *Entanglement in many-body systems*. Rev. Mod. Phys. **80** (2008), 517–576. URL http://dx.doi.org/10.1103/RevModPhys.80.517. 119, 142

[And95a] M. H. Anderson, J. R. Ensher, M. R. Matthews, C. E. Wieman, and E. A. Cornell. *Observation of Bose-Einstein Condensation in a Dilute Atomic Vapor*. Science **269** (1995), 198–201. URL http://www.sciencemag.org/cgi/content/abstract/269/5221/198. 1

[And95b] M. H. Anderson, J. R. Ensher, M. R. Matthews, C. E. Wieman, and E. A. Cornell. *Observation of Bose-Einstein Condensation in a Dilute Atomic Vapor*. Science **269** (1995), 198–201. URL http://www.sciencemag.org/cgi/content/abstract/269/5221/198. 7

[Aub96] S. Aubry, S. Flach, K. Kladko, and E. Olbrich. *Manifestation of Classical Bifurcation in the Spectrum of the Integrable Quantum Dimer*. Phys. Rev. Lett. **76** (1996), 1607–1610. URL http://dx.doi.org/10.1103/PhysRevLett.76.1607. 59

[Bar09] T. Barthel, C. Kasztelan, I. P. McCulloch, and U. Schollwöck. *Magnetism, coherent many-particle dynamics, and relaxation with ultracold bosons in optical superlattices*. Phys. Rev. A **79** (2009), 053627. URL http://dx.doi.org/10.1103/PhysRevA.79.053627. 21

[Ber01] G. P. Berman *et al.* *Delocalization border and onset of chaos in a model of quantum computation*. Phys. Rev. E **64** (2001), 056226. URL http://dx.doi.org/10.1103/PhysRevE.64.056226. 36

[Bla00] S. Blanes, F. Casas, and J. Ros. *Improved High Order Integrators Based on the Magnus Expansion*. BIT Numerical Mathematics **40** (2000), 434–450. URL http://www.springerlink.com/content/m066815725k48682. 79

[Bla09] S. Blanes, F. Casas, J. Oteo, and J. Ros. *The Magnus expansion and some of its applications*. Physics Reports **470** (2009), 151 – 238. URL http://dx.doi.org/10.1016/j.physrep.2008.11.001. 79, 84

[Blo08a] I. Bloch. *Quantum coherence and entanglement with ultracold atoms in optical lattices*. Nature **453** (2008), 1016. URL http://dx.doi.org/10.1038/nature07126. 1

[Blo08b] I. Bloch, J. Dalibard, and W. Zwerger. *Many-body physics with ultracold gases*. Rev. Mod. Phys. **80** (2008), 885. URL http://dx.doi.org/10.1103/RevModPhys.80.885. 1, 3, 7, 8, 9, 14, 17, 23, 24, 50, 68, 127, 128, 133, 135

[Boh84] O. Bohigas, M. J. Giannoni, and C. Schmit. *Characterization of Chaotic Quantum Spectra and Universality of Level Fluctuation Laws*. Phys. Rev. Lett. **52** (1984), 1–4. URL http://dx.doi.org/10.1103/PhysRevLett.52.1. 2, 30

[Bos24] S. Bose. *Plancks Gesetz und Lichtquantenhypothese*. Zeitschrift für Physik **26** (1924), 178–181. URL http://dx.doi.org/10.1007/BF01327326. 7

[Bra95] C. C. Bradley, C. A. Sackett, J. J. Tollett, and R. G. Hulet. *Evidence of Bose-Einstein Condensation in an Atomic Gas with Attractive Interactions*. Phys. Rev. Lett. **75** (1995), 1687–1690. URL http://dx.doi.org/10.1103/PhysRevLett.75.1687. 7

[Bra08] D. Bradley, S. Fisher, A. Gunault, R. Haley, J. Kopu, H. Martin, G. Pickett, J. Roberts, and V. Tsepelin. *Relic topological defects from brane annihilation simulated in superfluid ^{3}He*. Nature Physics **4** (2008), 46–49. URL http://dx.doi.org/10.1038/nphys815. 1

[Bre06] B. M. Breid, D. Witthaut, and H. J. Korsch. *Bloch–Zener oscillations*. New Journal of Physics **8** (2006), 110. URL http://stacks.iop.org/1367-2630/8/i=7/a=110. 68, 74

[Bre07] B. M. Breid, D. Witthaut, and H. J. Korsch. *Manipulation of matter waves using Bloch and Bloch–Zener oscillations*. New Journal of Physics **9** (2007), 62. URL http://stacks.iop.org/1367-2630/9/i=3/a=062. 74

[Buo04] P. Buonsante, R. Franzosi, and V. Penna. *Persistence of mean-field features in the energy spectrum of small arrays of Bose–Einstein condensates*. Journal of Physics B: Atomic, Molecular and Optical Physics **37** (2004), S229. URL http://stacks.iop.org/0953-4075/37/i=7/a=067. 59

[Buo07] P. Buonsante and A. Vezzani. *Ground-State Fidelity and Bipartite Entanglement in the Bose–Hubbard Model*. Phys. Rev. Lett. **98** (2007), 110601. URL http://dx.doi.org/10.1103/PhysRevLett.98.110601. 24, 25

[Cla06] S. R. Clark and D. Jaksch. *Signatures of the superfluid to Mott-insulator transition in the excitation spectrum of ultracold atoms*. New Journal of Physics **8** (2006), 160. URL http://stacks.iop.org/1367-2630/8/i=8/a=160. 120

[Cou06] E. Courtade, O. Houde, J.-F. Clément, P. Verkerk, and D. Hennequin. *Dark optical lattice of ring traps for cold atoms*. Phys. Rev. A **74** (2006), 031403. URL http://dx.doi.org/10.1103/PhysRevA.74.031403. 72

[Dal04] A. J. Daley, C. Kollath, U. Schollwöck, and G. Vidal. *Time-dependent density-matrix renormalization-group using adaptive effective Hilbert spaces*. Journal of Statistical Mechanics: Theory and Experiment **2004** (2004), P04005. URL http://stacks.iop.org/1742-5468/2004/i=04/a=P04005. 120

[Dav95] K. B. Davis, M. O. Mewes, M. R. Andrews, N. J. van Druten, D. S. Durfee, D. M. Kurn, and W. Ketterle. *Bose-Einstein Condensation in a Gas of Sodium Atoms*. Phys. Rev. Lett. **75** (1995), 3969–3973. URL http://dx.doi.org/10.1103/PhysRevLett.75.3969. 7

[Eck05] A. Eckardt, C. Weiss, and M. Holthaus. *Superfluid-Insulator Transition in a Periodically Driven Optical Lattice*. Phys. Rev. Lett. **95** (2005), 260404. URL http://dx.doi.org/10.1103/PhysRevLett.95.260404. 158

[Els99] N. Elstner and H. Monien. *Dynamics and thermodynamics of the Bose-Hubbard model*. Phys. Rev. B **59** (1999), 12184–12187. URL http://dx.doi.org/10.1103/PhysRevB.59.12184. 24, 25

[Ess91] F. H. L. Essler, V. E. Korepin, and K. Schoutens. *Complete solution of the one-dimensional Hubbard model*. Phys. Rev. Lett. **67** (1991), 3848–3851. URL http://dx.doi.org/10.1103/PhysRevLett.67.3848. 28

[Fan61] U. Fano. *Effects of Configuration Interaction on Intensities and Phase Shifts*. Phys. Rev. **124** (1961), 1866–1878. URL http://dx.doi.org/10.1103/PhysRev.124.1866. 78

[Fer09] I. Feranchuk and A. Leonov. *Analytical analysis of the 'collapse-revival' effect in the Jaynes–Cummings model*. Physics Letters A **373** (2009), 517 – 520. URL http://dx.doi.org/10.1016/j.physleta.2008.12.006. 172

[Fet71] A. Fetter and J. Walecka. *Quantum Theory of Many-Particle Systems*. McGraw-Hill, New York (1971). 13

[Fis89] M. P. A. Fisher, P. B. Weichman, G. Grinstein, and D. S. Fisher. *Boson localization and the superfluid-insulator transition*. Phys. Rev. B **40** (1989), 546–570. URL http://dx.doi.org/10.1103/PhysRevB.40.546. 23

[Fra01] R. Franzosi and V. Penna. *Spectral properties of coupled Bose-Einstein condensates*. Phys. Rev. A **63** (2001), 043609. URL http://dx.doi.org/10.1103/PhysRevA.63.043609. 58, 59

[Fre01] D. Frenkel and R. Portugal. *Algebraic methods to compute Mathieu functions*. Journal of Physics A: Mathematical and General **34** (2001), 3541. URL http://stacks.iop.org/0305-4470/34/i=17/a=302. 170

[Fuk73] H. Fukuyama, R. A. Bari, and H. C. Fogedby. *Tightly Bound Electrons in a Uniform Electric Field*. Phys. Rev. B **8** (1973), 5579–5586. URL http://dx.doi.org/10.1103/PhysRevB.8.5579. 68, 69, 86

[Gat07] R. Gati and M. K. Oberthaler. *A bosonic Josephson junction*. Journal of Physics B: Atomic, Molecular and Optical Physics **40** (2007), R61. URL http://stacks.iop.org/0953-4075/40/i=10/a=R01. 1

[Gir60] M. Girardeau. *Relationship between Systems of Impenetrable Bosons and Fermions in One Dimension*. Journal of Mathematical Physics **1** (1960), 516–523. URL http://link.aip.org/link/?JMP/1/516/1. 144

[Glü99] M. Glück, A. R. Kolovsky, and H. J. Korsch. *Lifetime of Wannier-Stark States*. Phys. Rev. Lett. **83** (1999), 891–894. URL http://dx.doi.org/10.1103/PhysRevLett.83.891. 99, 107

[Glü02] M. Glück, A. R. Kolovsky, and H. J. Korsch. *Wannier-Stark resonances in optical and semiconductor superlattices*. Physics Reports **366** (2002), 103–182. URL http://dx.doi.org/10.1016/S0370-1573(02)00142-4. 10, 11, 13, 22, 70

[Gre02a] M. Greiner, O. Mandel, T. Esslinger, T. W. Hänsch, and I. Bloch. *Quantum phase transition from a superfluid to a Mott insulator in a gas of ultracold atoms*. Nature **415** (2002), 39–44. URL http://dx.doi.org/10.1038/415039a. 1

[Gre02b] M. Greiner, O. Mandel, T. W. Hänsch, and I. Bloch. *Collapse and revival of the matter wave field of a Bose–Einstein condensate*. Nature **419** (2002), 51–54. URL http://dx.doi.org/10.1038/nature00968. 102, 103

[Gri08] G. R. Grimmett, T. J. Osborne, and P. F. Scudo. *Entanglement in the Quantum Ising Model*. Journal of Statistical Physics **131** (2008), 305–339. URL http://dx.doi.org/10.1007/s10955-008-9502-6. 142

[Haa91] F. Haake. *Quantum signatures of chaos*. Springer-Verlag, Berlin (1991). 28, 30, 36, 38, 43, 44, 47, 62

[Har04] T. Hartmann, F. Keck, H. J. Korsch, and S. Mossmann. *Dynamics of Bloch oscillations*. New Journal of Physics **6** (2004), 2. URL http://stacks.iop.org/1367-2630/6/i=1/a=002. 69, 71

[Hau10] J. Hausinger and M. Grifoni. *Dissipative two-level system under strong ac driving: A combination of Floquet and Van Vleck perturbation theory*. Phys. Rev. A **81** (2010), 022117. URL http://pra.aps.org/abstract/PRA/v81/i2/e022117. 68, 99

[He01] L. He and D. Vanderbilt. *Exponential Decay Properties of Wannier Functions and Related Quantities*. Phys. Rev. Lett. **86** (2001), 5341–5344. URL http://dx.doi.org/10.1103/PhysRevLett.86.5341. 14, 17

[Heu07] S. Heusler, S. Müller, A. Altland, P. Braun, and F. Haake. *Periodic-Orbit Theory of Level Correlations*. Phys. Rev. Lett. **98** (2007), 044103. URL http://dx.doi.org/10.1103/PhysRevLett.98.044103. 30

[Hil06] M. Hiller, T. Kottos, and T. Geisel. *Complexity in parametric Bose-Hubbard Hamiltonians and structural analysis of eigenstates*. Phys. Rev. A **73** (2006), 061604. URL http://dx.doi.org/10.1103/PhysRevA.73.061604. 39

[Hor09] R. Horodecki, P. Horodecki, M. Horodecki, and K. Horodecki. *Quantum entanglement*. Rev. Mod. Phys. **81** (2009), 865–942. URL http://dx.doi.org/10.1103/RevModPhys.81.865. 119

[Jor28] P. Jordan and E. Wigner. *Über das Paulische Äquivalenzverbot*. Zeitschrift für Physik **47** (1928), 631–651. URL http://dx.doi.org/10.1007/BF01331938. 146

[Kit04] C. Kittel. *Introduction to Solid State Physics*. Wiley VCH, New York (2004). 3

[Kla08] M. Klaiber, D. Dimitrovski, and J. S. Briggs. *The Magnus expansion for interaction of atoms with attosecond laser pulses*. Journal of Physics B: Atomic, Molecular and Optical Physics **41** (2008), 175002. URL http://stacks.iop.org/0953-4075/41/i=17/a=175002. 79

[Koh59] W. Kohn. *Analytic Properties of Bloch Waves and Wannier Functions*. Phys. Rev. **115** (1959), 809–821. URL http://dx.doi.org/10.1103/PhysRev.115.809. 14

[Kol03a] A. R. Kolovsky. *New Bloch Period for Interacting Cold Atoms in 1D Optical Lattices*. Phys. Rev. Lett. **90** (2003), 213002. URL http://dx.doi.org/10.1103/PhysRevLett.90.213002. 120

[Kol03b] A. R. Kolovsky and A. Buchleitner. *Floquet-Bloch operator for the Bose–Hubbard model with static field*. Phys. Rev. E **68** (2003), 056213. URL http://dx.doi.org/10.1103/PhysRevE.68.056213. 16, 26, 27, 28, 31, 36, 50, 60, 72

[Kol04] A. R. Kolovsky and A. Buchleitner. *Quantum chaos in the Bose–Hubbard model*. EPL **68** (2004), 632–638. URL http://dx.doi.org/10.1209/epl/i2004-10265-7. 28, 31, 36, 50, 57

[Kol07] A. R. Kolovsky. *Semiclassical analysis of the Bogoliubov spectrum in the Bose-Hubbard model*. Phys. Rev. E **76** (2007), 026207. URL http://dx.doi.org/10.1103/PhysRevE.76.026207. 29, 158

[Lan81] L. D. Landau and E. M. Lifshitz. *Quantum Mechanics*. Butterworth Heinemann, 3. edition (1981). 37

[Leg01] A. J. Leggett. *Bose-Einstein condensation in the alkali gases: Some fundamental concepts*. Rev. Mod. Phys. **73** (2001), 307–356. URL http://dx.doi.org/10.1103/RevModPhys.73.307. 8

[Lie61] E. Lieb, T. Schultz, and D. Mattis. *Two soluble models of an antiferromagnetic chain*. Annals of Physics **16** (1961), 407 – 466. URL http://dx.doi.org/10.1016/0003-4916(61)90115-4. 69

[Lie99] E. H. Lieb. *Some problems in statistical mechanics that I would like to see solved*. Physica A **263** (1999), 491 – 499. URL http://dx.doi.org/10.1016/S0378-4371(98)00517-2, proceedings of the 20th IUPAP International Conference on Statistical Physics. 8

[Lig07] H. Lignier, C. Sias, D. Ciampini, Y. Singh, A. Zenesini, O. Morsch, and E. Arimondo. *Dynamical Control of Matter-Wave Tunneling in Periodic Potentials*. Phys. Rev. Lett. **99** (2007), 220403. URL http://dx.doi.org/10.1103/PhysRevLett.99.220403. 158

[Lin06] J. Links and K. E. Hibberd. *Bethe Ansatz Solutions of the Bose-Hubbard Dimer*. SIGMA **2** (2006), 95. URL http://dx.doi.org/10.3842/SIGMA.2006.095. 57, 58

[Lon10] S. Longhi. *Field-induced decay of the quantum vacuum: Visualizing pair production in a classical photonic system*. Phys. Rev. A **81** (2010), 022118. URL http://dx.doi.org/10.1103/PhysRevA.81.022118. 68

[Lub09] M. Lubasch. *Private communication* (2009). 41

[Mag54] W. Magnus. *On the exponential solution of differential equations for a linear operator*. Commun. Pure Appl. Math. **VII** (1954), 649673. URL http://dx.doi.org/10.1002/cpa.3160070404. 79

[Mag69] W. Magnus and S. Winkler. *Hill's equation*. Interscience Publishers, John Wiley (1969). 75

[Mat02] M. Mathur and H. S. Mani. *SU(N) coherent states*. Journal of Mathematical Physics **43** (2002), 5351–5364. URL http://link.aip.org/link/?JMP/43/5351/1. 135

[McN97] A. D. McNaught and A. Wilkinson, editors. *International Union of Pure and Applied Chemistry: Compendium of Chemical Terminology*. Blackwell, Oxford, second edition (1997). 44

[Meh04] M. L. Mehta. *Random Matrices*. Elsevier, Amsterdam (2004). 2

[Mey91] P. Meystre and M. Sargent. *Elements of Quantum Optics*. Springer, Berlin (1991). 109

[Mil97] G. J. Milburn, J. Corney, E. M. Wright, and D. F. Walls. *Quantum dynamics of an atomic Bose-Einstein condensate in a double-well potential*. Phys. Rev. A **55** (1997), 4318–4324. URL http://dx.doi.org/10.1103/PhysRevA.55.4318. 57

[Mon93] G. Montambaux, D. Poilblanc, J. Bellissard, and C. Sire. *Quantum chaos in spin-fermion models*. Phys. Rev. Lett. **70** (1993), 497–500. URL http://dx.doi.org/10.1103/PhysRevLett.70.497. 36

[Mor01] O. Morsch, J. H. Müller, M. Cristiani, D. Ciampini, and E. Arimondo. *Bloch Oscillations and Mean-Field Effects of Bose-Einstein Condensates in 1D Optical Lattices*. Phys. Rev. Lett. **87** (2001), 140402. URL http://dx.doi.org/10.1103/PhysRevLett.87.140402. 3

[Mor06] O. Morsch and M. Oberthaler. *Dynamics of Bose-Einstein condensates in optical lattices*. Rev. Mod. Phys. **78** (2006), 179. URL http://dx.doi.org/10.1103/RevModPhys.78.179. 10, 68

[Mül04] S. Müller, S. Heusler, P. Braun, F. Haake, and A. Altland. *Semiclassical Foundation of Universality in Quantum Chaos*. Phys. Rev. Lett. **93** (2004), 014103. URL http://dx.doi.org/10.1103/PhysRevLett.93.014103. 30

[Nak01] Y. Nakamura, Y. A. Pashkin, and J. S. Tsai. *Rabi Oscillations in a Josephson-Junction Charge Two-Level System*. Phys. Rev. Lett. **87** (2001), 246601. URL http://dx.doi.org/10.1103/PhysRevLett.87.246601. 91

[Ols98] M. Olshanii. *Atomic Scattering in the Presence of an External Confinement and a Gas of Impenetrable Bosons*. Phys. Rev. Lett. **81** (1998), 938–941. URL http://dx.doi.org/10.1103/PhysRevLett.81.938. 13

[Olv10] F. W. J. Olver *et al.*, editors. *Digital Library of Mathematical Functions*. National Institute of Standards and Technology. http://dlmf.nist.gov/ (2010). 75, 170

[Par10] C. Parra-Murillo. *Private communication* (2010). 164

[Pec66] P. Pechukas and J. C. Light. *On the Exponential Form of Time-Displacement Operators in Quantum Mechanics*. The Journal of Chemical Physics **44** (1966), 3897–3912. URL http://link.aip.org/link/?JCP/44/3897/1. 79

[Pec83] P. Pechukas. *Distribution of Energy Eigenvalues in the Irregular Spectrum*. Phys. Rev. Lett. **51** (1983), 943–946. URL http://dx.doi.org/10.1103/PhysRevLett.51.943. 40

[Per77] A. M. Perelomov. *Generalized coherent states and some of their applications*. SOV PHYS USPEKHI **20** (1977), 703–720. 135

[Per84] A. Peres. *Stability of quantum motion in chaotic and regular systems*. Phys. Rev. A **30** (1984), 1610–1615. URL http://dx.doi.org/10.1103/PhysRevA.30.1610. 38, 39

[Pet02] C. J. Pethick and H. Smith. *Bose–Einstein Condensation in Dilute Gases*. Cambridge University Press, Cambridge (2002). 8

[Pfe70] P. Pfeuty. *The one-dimensional Ising model with a transverse field*. Annals of Physics **57** (1970), 79 – 90. URL http://dx.doi.org/10.1016/0003-4916(70)90270-8. 146

[Plö] P. Plötz, P. Schlagheck, and S. Wimberger. *Complex dynamics of a two-band Bose–Hubbard model*. In preparation. 81, 89, 141

[Plö10a] P. Plötz. *On Rabi oscillations between Bloch bands*. to appear as Conference Proceedings in the Journal of Siberian Federal University (2010). 75, 77, 91, 92

[Plö10b] P. Plötz, M. Lubasch, and S. Wimberger. *Detection of avoided crossings by fidelity*. submitted to Phys. Rev. E (2010). 40, 43, 47, 60, 61, 62

[Plö10c] P. Plötz, J. Madroñero, and S. Wimberger. *Collapse and revival in inter-band oscillations of a two-band Bose–Hubbard model*. Journal of Physics B: Atomic, Molecular and Optical Physics **43** (2010), 081001. URL http://stacks.iop.org/0953-4075/43/i=8/a=081001. 126, 129

[Pon08] A. V. Ponomarev. *Dynamics of Cold Fermi atoms in one-dimensional Optical Lattices*. Ph.D. thesis, University of Freiburg (2008). 28, 47

[Pre92] W. Press *et al. Numerical Recipes in C*. Cambridge University Press, Cambridge (1992). 107, 113, 161, 164, 166

[Ram07] J. Rammer. *Quantum Field Theory of Non-equilibrium States*. Cambdrige University Press, Cambridge (2007). 106

[Rap07] A. Rapp, G. Zaránd, C. Honerkamp, and W. Hofstetter. *Color Superfluidity and "Baryon" Formation in Ultracold Fermions*. Phys. Rev. Lett. **98** (2007), 160405. URL http://dx.doi.org/10.1103/PhysRevLett.98.160405. 1

[Rig04] M. Rigol and A. Muramatsu. *Universal properties of hard-core bosons confined on one-dimensional lattices*. Phys. Rev. A **70** (2004), 031603. URL http://dx.doi.org/10.1103/PhysRevA.70.031603. 144

[Roj10] A. G. Rojo. *Matrix exponential solution of the Landau–Zener problem*. arXiv:1004.2914v1 (2010). URL http://arxiv.org/abs/1004.2914. 73, 80, 84

[Rot95] J. Rotvig, A.-P. Jauho, and H. Smith. *Bloch Oscillations, Zener Tunneling, and Wannier-Stark Ladders in the Time Domain*. Phys. Rev. Lett. **74** (1995), 1831–1834. URL http://dx.doi.org/10.1103/PhysRevLett.74.1831. 68

[Sac01] S. Sachdev. *Quantum Phase Transitions*. Cambridge University Press, Cambridge (2001). 25, 36, 145

[Sch07] F. Schmitt, M. Hild, and R. Roth. *Bose–Fermi mixtures in 1D optical superlattices using full and truncated single-band bases*. Journal of Physics B: Atomic, Molecular and Optical Physics **40** (2007), 371. URL http://stacks.iop.org/0953-4075/40/i=2/a=010. 120

[Scu97] M. O. Scully and S. M. Zubairy. *Quantum Optics*. Cambridge University Press, Cambridge (1997). 171, 172

[Sha86] B. S. Shastry. *Infinite Conservation Laws in the One-Dimensional Hubbard Model*. Phys. Rev. Lett. **56** (1986), 1529–1531. URL http://dx.doi.org/10.1103/PhysRevLett.56.1529. 30

[Shi63] J. H. Shirley. *Interaction of a quantum system with a strong oscillating field*. Ph.D. thesis, California Institute of Technology. URL http://resolver.caltech.edu/CaltechETD:etd-05142008-103758 (1963). 87, 175, 176

[Shi65] J. H. Shirley. *Solution of the Schrödinger Equation with a Hamiltonian Periodic in Time*. Phys. Rev. **138** (1965), B979–B987. URL http://dx.doi.org/10.1103/PhysRev.138.B979. 87

[Sia07] C. Sias, A. Zenesini, H. Lignier, S. Wimberger, D. Ciampini, O. Morsch, and E. Arimondo. *Resonantly Enhanced Tunneling of Bose-Einstein Condensates in Periodic Potentials*. Phys. Rev. Lett. **98** (2007), 120403. URL http://dx.doi.org/10.1103/PhysRevLett.98.120403. 3, 11, 12, 13, 99, 107

[Stö99] H.-J. Stöckmann. *Quantum Chaos: an introduction*. Cambridge University Press, Cambridge (1999). 28, 30

[Tab89] M. Tabor. *Chaos and Integrability in Nonlinear Dynamics*. Wiley-Interscience, New York (1989). 30

[Tom06] A. Tomadin. *Quantum Chaos with Ultracold Atoms in Optical Lattices*. Master's thesis, Università di Pisa (2006). 13, 17, 19, 26, 27, 31, 32, 161, 162, 163, 164

[Tom07] A. Tomadin, R. Mannella, and S. Wimberger. *Many-Body Interband Tunneling as a Witness of Complex Dynamics in the Bose–Hubbard Model*. Phys. Rev. Lett. **98** (2007), 130402. URL http://dx.doi.org/10.1103/PhysRevLett.98.130402. 21, 31, 32, 54

[Tom08] A. Tomadin, R. Mannella, and S. Wimberger. *Many-body Landau–Zener tunneling in the Bose-Hubbard model*. Phys. Rev. A **77** (2008), 013606. URL http://dx.doi.org/10.1103/PhysRevA.77.013606. 21, 31, 32

[Tri08] F. Trimborn, D. Witthaut, and H. J. Korsch. *Exact number-conserving phase-space dynamics of the M-site Bose–Hubbard model*. Phys. Rev. A **77** (2008), 043631. URL http://dx.doi.org/10.1103/PhysRevA.77.043631. 135

[Urw70] K. M. Urwin and F. M. Arscott. *Theory of the Whittaker-Hill equations*. Proc. R. Soc. Edinburgh **69** (1970), 28. 75

[Ven09] H. Venzl, A. J. Daley, F. Mintert, and A. Buchleitner. *Statistics of Schmidt coefficients and the simulability of complex quantum systems*. Phys. Rev. E **79** (2009), 056223. URL http://dx.doi.org/10.1103/PhysRevE.79.056223. 164

[Ven10] H. Venzl, T. Zech, B. Ole, M. Hiller, F. Mintert, and A. Buchleitner. *Solitonic eigenstates of the chaotic Bose–Hubbard Hamiltonian*. Applied Physics B: Lasers and Optics **98** (2010), 647–652. URL http://dx.doi.org/10.1007/s00340-009-3858-4. 60, 61, 62

[Vid03] G. Vidal. *Efficient Classical Simulation of Slightly Entangled Quantum Computations*. Phys. Rev. Lett. **91** (2003), 147902. URL http://dx.doi.org/10.1103/PhysRevLett.91.147902. 120

[Voi88] P. Voisin, J. Bleuse, C. Bouche, S. Gaillard, C. Alibert, and A. Regreny. *Observation of the Wannier-Stark Quantization in a Semiconductor Superlattice*. Phys. Rev. Lett. **61** (1988), 1639. H. Schneider, H.T. Grahn, K.v. Klitzing, and K. Ploog, *Resonance-induced delocalization of electrons in GaAs-AlAs superlattices*. Phys. Rev. Lett. **65** (1990), 2720; J. Feldmann, K. Leo, J. Shah, D.A.B. Miller, J.E.

Cunningham, T. Meier, G. von Plessen, A. Schulze, P. Thomas, and S. Schmitt-Rink. *Optical investigation of Bloch oscillations in a semiconductor superlattice*. Phys. Rev. B **46** (1992), 7252 ; B. Rosam, D. Meinhold, F. Loser, V.G. Lyssenko, S. Glutsch, F. Bechstedt, F. Ross, K. Kohler, and K. Leo. *Field-Induced Delocalization and Zener Breakdown in Semiconductor Superlattices*. Phys. Rev. Lett. **86** (2001), 1307. 22

[Wan00] S.-J. Wang and Q. Jie. *General features of quantum chaos and its relevance to nuclear physics*. Phys. Rev. C **63** (2000), 014309. URL http://dx.doi.org/10.1103/PhysRevC.63.014309. 36

[Whi04] S. R. White and A. E. Feiguin. *Real-Time Evolution Using the Density Matrix Renormalization Group*. Phys. Rev. Lett. **93** (2004), 076401. URL http://dx.doi.org/10.1103/PhysRevLett.93.076401. 120

[Wil07] F. Wilczek. *Quantum chromodynamics: Lifestyles of the small and simple*. Nature Physics **3** (2007), 375. URL http://dx.doi.org/10.1038/nphys635. 1

[Wil10] S. Will, T. Best, U. Schneider, L. Hackermüller, D.-S. Lühmann, and I. Bloch. *Time-resolved observation of coherent multi-body interactions in quantum phase revivals*. Nature **465** (2010), 197–201. URL http://dx.doi.org/10.1038/nature09036. 1

[Yan93] X. Yang and J. Burgdörfer. *Statistics of avoided crossings for generic quantum systems*. Phys. Rev. A **48** (1993), 83–87. URL http://dx.doi.org/10.1103/PhysRevA.48.83. 31, 47, 61

[Zak91] J. Zakrzewski and M. Kuś. *Distributions of avoided crossings for quantum chaotic systems*. Phys. Rev. Lett. **67** (1991), 2749–2752. URL http://dx.doi.org/10.1103/PhysRevLett.67.2749. 30, 31, 36, 39, 44, 47, 58

[Zen09] A. Zenesini, H. Lignier, G. Tayebirad, J. Radogostowicz, D. Ciampini, R. Mannella, S. Wimberger, O. Morsch, and E. Arimondo. *Time-Resolved Measurement of Landau-Zener Tunneling in Periodic Potentials*. Phys. Rev. Lett. **103** (2009), 090403. URL http://dx.doi.org/10.1103/PhysRevLett.103.090403. 3, 11, 73

[Zha96] X.-G. Zhao, G. A. Georgakis, and Q. Niu. *Rabi oscillations between Bloch bands*. Phys. Rev. B **54** (1996), R5235–R5238. URL http://dx.doi.org/10.1103/PhysRevB.54.R5235. 68, 73, 74, 75